APPENDIX A

COMPARATIVE BEHAVIOR OF LATERALLY LOADED GROUPS OF BORED AND DRIVEN PILES

INTRODUCTION

The soil modelling approach that has been adopted in this research is to simulate lateral group behavior by

(1) using p-y curves for statically loaded single piles from well-know criteria [e. g., 1, 2]. These criteria are resident in many design-level computer codes and are easy for the designer to implement [e. g., 3, 4, 5];

(2) converting the static p-y curves into dynamic p-y curves if seismic or impact loading is being modelled (Appendix B); and

(3) modifying single-pile curves for lateral group action by using a p-multiplier, which may be either a static factor, discussed in this appendix, or a dynamic factor, discussed in Appendix B. The p-multiplier approach is used in FLPIER [4, 5], modified for dynamic loading as described in Appendix C.

Values for p-multipliers have been evaluated through detailed numerical or analytical modelling or by performing load tests on pile groups, or by a combination of both numerical / analytical modelling and field or centrifuge tests [6, 7, 8, 9, 10]. However, none of these studies has been specific to the construction method that is used to install the piles. The contribution of this appendix is to describe a major field load test program in which the effect of the piling construction method on p-multipliers was evaluated.

TEST SITE AND TEST ARRANGEMENT

Site Conditons

In its planning for the construction of foundations for numerous viaducts to support rail traffic through the west central coastal plain of Taiwan, the High Speed Rail Authority of Taiwan contracted with several universities, consulting firms and contractors to construct and load test and two large, full-scale pile groups. The west central coastal plain of Taiwan is in a geographical area that is prone to large seismic events, and it was considered necessary to design the viaducts to resist large horizontal loads.

The objective of the test program was to measure the capacity and stiffness of groups of vertical piles of different designs that were loaded laterally with a quasi-static ground-line shear. Two test groups were selected for construction and testing. The cost of construction for each group was estimated to be approximately equal. These groups were constructed and loaded to the capacity of the loading system, 1000 metric tons ("T") (9.8 MN). One pile group consisted of bored piles (drilled shafts), and one consisted of round, displacement-type prestressed concrete piles, which were driven into position.

The test site was located about 5 km west of the town of Chaiyi, Taiwan, on a flat coastal plain. Soil conditions at the test site are summarized in Figure A-1. The ground surface shown in that figure is the elevation of the ground surface at the base of the pile caps of the tested groups after minor excavation. Detailed soil data are available in Reference 11. Numerous geophysical tests, soil borings and CPT, SPT and DMT soundings were made on the test site, within 5 m of each test group. The Unified classifications of the soil layers and the various parameters listed in the "Properties"

column of Figure A-1 were deduced from the borings and soundings [11]. The piezometric surface was located at 3 m below the ground surface. The soils in the top 8 m of the profile are considered to be "sands" with a relative density of 50 to 60 per cent in the following analysis.

Testing Arrangement

The layouts of the test groups are shown in Figures A-2 and A-3. All piles were plumb to the tolerances permitted by the High Speed Rail Authority (2 per cent). The lateral load tests were conducted essentially by jacking the two test groups apart. That is, the test groups served as mutual reactions for each other.

Bored Pile Group

The bored pile group (Figure A-2) consisted of six, 1.5-m-diameter piles installed to a depth of 33 - 34 m below the ground surface. All six of the group piles were constructed using the slurry displacement method of construction, in which a bentonite slurry was used to maintain borehole stability. Several other bored piles were constructed, as shown in Figure A-2. Piles B1 and B2 served as reference piles for lateral loading (tested as single, isolated piles). They were tested individually with free heads. Pile B10 served as a reference pile for axial loading. (Piles B9 and B11 served as anchor piles for the axial loading test on Pile B10. The group cap served as the reaction for the lateral load tests on Piles B1 and B2.) Only Pile B1 was constructed by the slurry displacement method, as per the group piles. Piles B2 and B10 (highlighted in Figure A-2 with boldface and underlining) were constructed using the oscillated casing method, in which casing is oscillated into the soil continuously for the full depth of the borehole, and the soil within the casing is excavated while maintaining a balance on the water head at

the base of the casing throughout the process. The reinforcing steel is then set and the borehole concreted using temie techniques as the casing is withdrawn, similar to the way in which a borehole is concreted during the construction of bored piles by the slurry displacement method. Because Pile B2 was constructed in a manner different from the group piles, results from the test on Pile B1 were used exclusively in the analysis that is described in this appendix. The axial load test results on Pile B10 were used only in a general way to confirm the approximate correctness of the axial load model that is needed for the analysis of laterally loaded pile groups with non-pinned heads.

A potentially important detail is the order in which the piles were installed. In very general terms, the bored piles in the group were installed from the front, or leading, row (first) to the back, or trailing, row (last). It is speculated that this installation order might have resulted in reduced effective stresses in the coarse-grained soil surrounding the piles that were installed first — those in the leading row — by the later installation of piles behind the leading row. Reduced effective stresses in the soil mass around the front-row piles should have produced softer soil response behavior of the leading-row piles compared to the behavior that might have occurred if the leading row of piles had been installed last.

Driven Pile Group

The driven pile group consisted of 12, 0.80-m-diamter, closed-toe, hollow, circular prestressed concrete piles. They were likewise driven to a penetration of 33 to 34 m. These piles can be considered to be "displacement piles." The hollow core of each pile was filled with an instrument package and concrete after all of the piles were installed. A single, isolated pile, denoted P13 in Figure A-3, was tested laterally in a

free-headed state by reacting off the group pile cap. Before the cap was constructed, Piles P6 and P7 were subjected to axial load tests. Because of the assumptions concerning head fixity in the driven pile group, discussed later, it was not necessary to model the axial load behavior of the group piles with close accuracy.

The installation order of the driven piles is also shown in Figure A-3. The order of installation was somewhat more random than that in the bored pile group, but in general the piles on the leading row were installed prior to the piles on the second (first trail) row, which were in turn installed in general prior to the piles in the third (second trail) row. The piles on the fourth (third trail) row were in general installed last. With displacement-type piles in coarse-grained soil, it can be speculated that the effect of installing the leading row first was opposite to that of installing the leading row first in the bored pile group. That is, installing displacement piles in a row behind a row of piles already installed would increase effective stresses around the piles already installed and result in stiffer soil response in those piles than in the piles installed later.

Instrumentation

Both the bored and driven piles were instrumented thoroughly. Those piles that were subjected to individual-pile axial load tests were instrumented with a toe load cell, a family of telltales and rebar stress meters (referred to in the United States as "sister bars"). Those piles that were subjected to lateral load tests, including all of the group piles and the lateral reference piles, were instrumented with inclinometer tubing on approximately the neutral axis of the pile. Deviations in lateral deflection from the pile toes (considered to be stationary) were measured with precision inclinometers during the load tests. Some of the piles that were loaded laterally also contained sister bars. The

translations and rotations of the group caps were measured by using LVDT's suspended from reference frames supported in the soil as far from the test groups as possible. The load was applied to the group by multiple hydraulic jacks whose loads were controlled so as to "steer" the group on an approximately straight path. Each jack was equipped with a calibrated electronic load cell.

The instruments for the bored piles were affixed to the reinforcing steel cages prior to inserting the cages into the boreholes and concreting the piles. The instruments for the driven piles were installed in the hollow core of each pile by attaching the instruments to a carrier and lowering the carrier into the core after the piles were driven. The operation was completed by concreting the instruments into the core.

The interpretations that are given here are based on the jack load cell, cap deflection and inclinometer readings. Sister bar readings, although available, were not used because not all piles had sister bars and because initial review of the readings revealed some inconsistencies that could not be explained by the individuals reviewing the data.

More information on the instrumentation and pile group arrangements can be found in Reference 12.

SİNGLE PILE TESTS

General Description

The single, reference piles (B1, B2 and P13) were all tested statically, free-headed, by applying a horizontal load approximately 0.5 m above the ground surface. The geomaterials from that level to the ground surface were removed in the analyses that follow. The individual test piles were all subjected to forced vibration tests to load

amplitudes as high as 44.5 kN (5 tons) prior to the static load tests. Since these loads were comparatively small, it has been assumed that they had minimal effect on the load-movement behavior that was measured in the static tests. The loads were applied to the single piles by reacting off the respective group pile caps, prior to loading the pile groups, in a direction perpendicular to the direction of group loading. Again, it was assumed that the loading of the single piles in this manner had no effect on the measured response of the pile groups.

The single-pile load tests were performed on May 29 - 31, 1997, approximately five months after the piles were installed. Loads were applied semi-monotonically. That is, loads were applied in increments until the load reached approximately one-seventh of the expected capacity, upon which the load was removed. The process was repeated for loads equal to about two-sevenths of the expected capacity, three-sevenths of the expected capacity, and so forth until the final capacity was reached. Readings that were made near the peak loads on each cycle are reported in this appendix, as it was assumed that the lateral pile response at such loads was not significantly influenced by cycling at lower load amplitudes.

The load-deformation-depth relations that were measured for Piles B1 (reference for the bored pile group test) and P13 (reference for the driven pile group test) are shown in Figures A-4 and A-5, respectively. The symbol "T" in those figures represents metric tons ("tonnes") rather that U. S. tons, where 1 T = 9.8 kN. As stated previously, Pile B2 was not used as a reference because it was installed with the oscillated casing procedure rather than the slurry displacement procedure that was used for all of the group piles. As would be expected intuitively, the bored pile, B1, carried considerably more load at a

given head deflection than did the driven pile, P13, because of its much larger moment of inertia. For the same reason significant lateral pile movement occurred to a greater depth in the reference bored pile (about 7 m) than in the reference driven pile (about 5 m).

Analysis of Single Pile Test Results

From the perspective of the objective of this appendix the main purpose of the single pile tests was to establish site-specific, pile-geometry-specific and construction-method-specific p-y curves for the reference piles. The pile and soil profile that was assumed for the analysis of the single-pile load tests is shown in Figure A-6. The soil was modelled initially by using standard p-y curve formulations — "Reese" [1] for coarse-grained soil layers ("sand") and "Matlock" [13] for fine-grained ("clay") soil layers. In preliminary analyses the "O'Neill" p-y criterion [2] was also used for the sand layers, in place of the Reese criterion; however, the predictions of deformed pile shape was better with the Reese criterion, so the Reese criterion was used as the starting point for the analysis.

Modelling of the structural properties of the piles is at least as important as modelling the resistance-deformation behavior of the soil (i. e., through p-y curves). Simplified design drawings for a typical bored pile and a typical driven (prestressed concrete) pile are shown in Figures A-7 and A-8, respectively. Material properties of the concrete and steel are given in Table A-1. (These were the target properties that were verified from concrete cylinder tests for cast-in-place concrete and steel coupon tests on reinforcing steel. No verification was available for the properties of the concrete in the prestressed outer shell of the driven piles or for the prestressing steel.) The concrete-steel model was the model proposed by Andrade [14] and implemented in the version of

FLPIER used in this study [15]. This model computes bending stiffness along the pile by first computing strains across the cross-section of a bending element (representing the pile) and assigns corresponding stresses based on uniaxial stress-strain curves for concrete and steel in compression and tension. The gapping-unloading-reloading (hysteretic) structural model described in Appendix C was not resident in the version of FLPIER used in these analyses (Version 5.1); however, because of the procedure by which the tests were conducted, the gapping-unloading-reloading phenomenon should have had little effect on the pile deflections at the loads at which the tests, both single pile and group, were analyzed (at or near the peak load in a cycle).

When the tests were first analyzed with FLPIER using the Reese and Matlock p-y criteria for the soil and the Andrade structural model for the piles, relatively poor comparisons with the measurements were achieved. Modifications to the p-y criteria in the upper 12.0 m of the soil profile were then made in order to improve the match in measured versus computed displaced configuration at several selected loads; that is, site-specific p-y curves were determined. The diameters of all bored piles (including the group piles discussed later) were increased in FLPIER from 1.5 to 1.60 m to account for oversizing of the borehole that commonly occurs when excavating a bored pile in coarse-grained soil under a drilling slurry. The p-y curves derived from the original published criteria are compared with the modified p-y criteria that were necessary to provide acceptable matches with the measured data in Figures A-9 through A-11, for Piles B1, B2 and P13.

One modification to the p-y curves was to prescribe a non-zero resistance at the soil surface. This is contrary to the Reese sand criterion, which provides for zero soil

resistance at the surface. It is not clear what physical phenomenon this change reflected. The surface soil (Figure A-1) was described as a "sandy silt with some clayey silts," even though it classified as an SM. It is possible that the need to give the soil surface resistance could reflect a cohesion component to shear strength of the soils not reflected by the Reese sand criteria. However, a more likely condition was that the bored piles were greater than 1.6 m in diameter at the surface because of the effects of auger drilling, and that the need to give the soil non-zero surface resistance actually simulated increased bending stiffness in a pile with a "mushroom" top. The salutary effect of using a non-zero surface resistance p-y curve, as shown at the soil surface in Figures A-9 through A-11, versus using null p-y curves at the surface, is demonstrated in Figure A-12.

The original and modified p-y curves necessary to model Pile B2 (Figure A-10) were included, even though the data from Pile B2 were not used in modelling the bored pile group, because a comparison of Figure A-9 for the slurry bored pile with Figure A-10 for the full-depth casing pile shows that, although there are local, depthwise differences in the p-y curve corrections, the mean correction is about equal for both methods of construction. This suggests that there was no advantage from the point of view of maintaining soil properties around the piles in using one construction method over the other.

On the other hand, comparison of Figures A-9 (bored pile B1) and A-11 (driven pile P13) indicates that smaller modifications had to be made to the p-y curves for the driven piles than had to be made for the bored piles. The modifications that were made were generally to stiffen the p-y curves for the driven piles, whereas the p-y curves had to be softened, in general, for the bored piles.

Two numerical models (computer codes) were used to analyze the single-pile test results: LPILE [3] and FLPIER [15]. Both codes simulate nonlinear bending and axial load effects in laterally loaded concrete piles using similar procedures, and both use p-y curves to represent the soil in an identical manner. The results from both codes were essentially identical, as is demonstrated for Pile B2 in Figure A-13. However, FLPIER was selected for further use in this study because it was desired ultimately to develop p-multipliers that could be used in FLPIER.

The modified p-y curves shown in Figures A-9 through A-11 were accepted as the correct set of p-y curves for the test site for bored and driven piles, respectively, of the sizes used in the test groups. p-y curves below a depth of 12 m were taken as the curves predicted by the standard p-y criteria. These curves were used without any site-specific modifications. Any deviations from these families of p-y curves that were needed to model the group tests were considered to be the results of (a) pile group construction, including installation order, and (b) pile-soil-pile interaction during lateral loading.

PILE GROUP TESTS

Effects of Pile Construction on Soil Property Indexes

When the pile group construction was completed, but prior to load testing of the groups, soundings were made though small access holes in the pile caps to assess the index properties of the soil within the pile groups compared to index properties before the piles were installed. Several different types of probes were used. Two will be considered here: The seismic piezocone (SCPTU) and the dilatometer (DMT). Locations of the probes within each group are shown in Figures A-2 and A-3. Changes from initial values prior to construction to values obtained by probing the soil within the

groups for q_c (cone tip reading corrected for pore pressure) and E_d (the dilatometer modulus) are shown in Figures A-14 through A-17 for both the bored pile group and the driven pile group [16]. The differences in initial and post-construction readings are denoted by the symbol "Δ" in those figures.

Comparing Figures A-14 and A-15, it is obvious that there was a tendency for q_c to decrease due to pile installation in the upper 12 m in the bored pile group, while in the same depth range in the driven pile group the tendency was for q_c to increase due to pile installation. Similarly, from Figures A-16 and A-17, the dilatometer modulus decreased within the bored pile group, while there was a slight tendency for it to increase in the driven pile group above a depth of 12 m. These data strongly suggest that the installation of bored piles loosened the soil between the piles within the bored pile group, or perhaps reduced lateral effective stresses, or both. On the other hand, the installation of the driven piles increased the soil density or lateral effective stresses, or both. These data suggest that the p-multipliers that are necessary to simulate group behavior using the site-specific (modified) single-pile p-y curves as a baseline will likely be different in the two groups.

Lateral Load Tests

The groups were tested approximately two months after the single, reference piles were tested, using a quasi-monotonic loading procedure that was very similar to the procedure used for the single piles. The groups were loaded by essentially jacking them apart. The results of the load tests, in terms of cap translation versus lateral load (applied 0.5 m above the ground surface), are shown in Figures A-18 and A-19. A maximum load of 1000 tonnes (17.8 MN) was applied to each group. It is obvious that the bored pile

group, consisting of six, 1.5-m-diameter piles, was much stiffer than the driven pile group, consisting of twelve, 0.8-m-diameter piles, despite the fact that the installation method seemed to weaken the soil around the bored piles within the group.

This seemingly anomalous behavior (from a soil mechanics perspective) was likely caused by two important factors. First, the bored piles were tied into the pile cap through heavy, hooked rebars, with full development lengths extending into the pile cap, which were assumed to provide a moment connection between the pile cap and the pile heads. No such moment connection existed between the pile cap and the driven piles, in which the cast-in-place concrete for the steel-reinforced pile cap was merely poured over the extended heads of the driven piles. The driven group piles therefore behaved more as free- or pinned-headed piles than as fixed-headed piles. Moment connections stiffen the group response considerably relative to pinned connections. Second, the sum of the moments of inertia of the six bored piles was higher than that of the 12 driven piles, further stiffening the bored pile group. The fact that the bored pile group was stiffer despite the obvious disadvantages of using bored piles with regard to the stiffness of the soil between the piles indicates the significance of the behavior of the structural components of the pile-soil-cap system and the importance of modelling correctly the structural performance of the pile group system.

On the other hand, a measure of the effects of soil softening due to lateral pile group action in both groups is evident in Figures A-20 and A-21. The depths of significant lateral pile deflection are much deeper in these figures, from the group tests, than from the corresponding figures for the single pile tests, A-4 and A-5, recalling that the loads shown on Figures A-4 and A-5 are loads per pile, whereas those shown on

Figures A-20 and A-21 are loads for the entire group. Note that there is some discrepancy in measured head deflections among piles in Figure A-20. The lateral deflections at the head of each pile (base of pile cap) should be equal; hence, the differences in head deflections in Figures A-20 and A-21 are indications of the reliability of the deflection readings, which seemed to be comparable in both groups.

Modelling Group Behavior

Both group tests were modelled in a preliminary step using Program GROUP 4 [17] and FLPIER, Version 5.1. Both codes gave similar results for the group load tests at small loads; however, it is necessary to model nonlinear bending in the piles at higher loads, which is not done automatically in GROUP 4. This made it difficult to account for the effects of the prestress on bending stiffness of the driven piles at higher loads. The prestressing force is applied as a uniform axial load along the pile in FLPIER. This force retards the onset of tensile cracking and the resulting reduced bending stiffness in the piles. Eventually, however, the piles develop tensile cracks, which reduces bending stiffness. FLPIER handles this effect automatically. GROUP 4 gave a stiffer response than FLPIER for the bored pile group at higher loads because it did not automatically adjust pile stiffness when cracking moments were applied. (In both cases — bored and driven piles — bending stiffness can be reduced by the user in GROUP 4, making multiple runs when combinations of computed bending moments and axial loads indicate that there will be cracking in the cross section, but this process is slow and inconvenient compared to using FLPIER, which makes the stiffness adjustments for flexural cracking automatically.) FLPIER also allows the user to model the bending flexibility of the pile cap, whereas GROUP 4 assumes that the pile cap undergoes rigid body motion. Since

the diameters of the piles in the bored pile group were large relative to the thickness of the cap, cap bending was a possibility, and the ability to simulate this phenomenon was a virtue in the group model. For these reasons, and because it was desired to compute the p-multipliers directly for FLPIER, further work with GROUP 4 was abandoned.

The pile head and group cap conditions that were modelled by FLPIER are shown in Figures A-22 and A-23. All soil that had surrounded the bottom parts of the pile caps was removed physically prior to the tests, so that there was no passive resistance or side shearing resistance against either cap. However, both caps were cast on the ground. No measurements of the shearing stresses between the bottoms of the caps and the soil were made, and no reliable measurements of shear load distribution among the piles were available. Therefore, it was assumed that the contribution of cap base shear to the total group resistance was very small, and it was neglected in the FLPIER analyses.

A less obvious, but no less important, phenomenon that had to be modelled with FLPIER in the simulation of the behavior of the fixed-headed bored pile group was the rotational stiffness of the group, or the axial "push-pull" couples that resist the applied moment (applied load times 0.5 m, as shown in Figures A-22 and A-23.) and the "fixing" moments that are produced at the pile heads as the cap translates. These latter moments cause the cap to rotate and the fixing moments to relax, thus softening the lateral response of the pile group. The degree to which the cap rotates under loading from the fixing moments depends upon the stiffness of the group piles in the axial push-pull mode. It is therefore important to model the axial stiffnesses of the piles when the pile heads are assumed to be fixed into the pile cap because these stiffnesses directly influence the p-y

curves that are required to be used to provide a match with the lateral deflection measurements.

Unfortunately, the only axial load test that was available for direct determination of unit axial load transfer curves for the bored piles, which can also be supplied to FLPIER to simulate axial pile stiffness, was the test on Pile B10. That pile, however, was installed using the full-depth-casing technique, rather than the direct slurry displacement technique used in the group piles. Therefore, unit axial load transfer curves (sometimes called "t-z" and "q-z" curves) were generated using an internal routine in FLPIER, which uses an approximate method based on principles given by Randolph and Wroth [18]. The axial stiffness calculations are carried out by using a simple discrete element model to which t-z and q-z springs area attached. In order to generate the t-z and q-z curves in FLPIER, it is only necessary to specify a value of soil shear modulus in the free field, G, and the ultimate value of unit side shear f_{max} and of base resistance q_{max}. G was estimated in the coarse-grained soil layers from Eqs. A-1 and A-2,

$$G = \frac{E}{2(1+v)}, \qquad \text{where} \qquad \text{(A-1)}$$

$$E(psf) = 10,000 \, N_{60} \qquad \text{(A-2)}$$

In Eq. A-2, N_{60} is the standardized SPT blow count (average value in a given layer). Poisson's ratio (v) was taken to be 0.3. For fine-grained soil layers, Eq. A-1 was used to estimate G, whereas E was obtained from Eqs. A-3 and A-4.

$$G = \frac{50 \, s_u}{(1+v)}, \qquad \text{where} \qquad \text{(A-3)}$$

$$s_u(tsf) = 15 \, N_{60} \qquad \text{(A-4)}$$

In Eq. A-4, s_u is the undrained shear strength of the fine-grained soil. Poisson's ratio (ν) was taken to be 0.5.

The ultimate unit side and base resistances were obtained from API [19], which is strictly valid only for driven piles but which was assumed to give appropriate values for bored piles, as well. In coarse-grained soils f_{max} is set equal to σ'_v K tan $\delta \leq f_{max}$ (limit), where σ'_v is the vertical effective stress at the center of a given soil layer, K is an earth pressure coefficient taken equal to 0.8 and δ is an angle of pile-soil wall friction prescribed by API RP2A based on the fines content and relative density of the soil. f_{max} (limit) is based on the same properties. q_{max} in compression is defined by σ'_v (base) N_q, where N_q is a function of fines content and relative density $\leq q_{max}$ (limit). q_{max} (limit) is likewise given by API to be a function of fines content and relative density, and is set equal to zero for uplift loading.

In fine-grained soils f_{max} is determined in API RP2A from the ratio of s_u to σ'_v, and q_{max} is taken to be 9 s_u at the base of the pile for compression loading and zero for uplift loading.

Once the axial load-movement behavior of single piles was simulated in FLPIER, that value was used for each bored pile in the group without modification for axial group effects. The argument for making this simplifying assumption was that the front (leading) row of piles would settle, the back (trailing) row of piles would go into tension, and the middle row of piles would essentially remain stationary axially. The tendency for one pile on the front row to soften the behavior of its neighbor on that row is approximately offset by the tendency for the uplift in both piles in the back row to stiffen the behavior of the piles on the front row, with similar effects for piles on the back row.

No strong concern about modelling of axial behavior existed for the driven pile group, since no fixing moments develop with pinned-headed piles, and the lateral stiffness is essentially decoupled from the axial push-pull behavior. Nonetheless, the same procedure was used for simulating axial response in the driven pile group that was used in the bored pile group.

With the modelling of axial behavior accomplished, the main effort in modelling the test groups with FLPIER was to determine how the site-modified, single-pile p-y curves (Figure A-9 and Figure A-11) were required to be modified again to produce the p-y curves best suited to modelling group behavior. The second-step modification (for group action) was made by multiplying the site-modified p-y curves in Figures A-9 (bored piles) and A-11 (driven piles) by appropriate p-multipliers specific to each row of piles, from the leading row to the last trailing row.

The concept of the p-multiplier, as applied in this study, is briefly explained in Figure A-24. For each pile on a given row in the group (leading, first trailing, second trailing, and so forth), all of the p-values on all of the p-y curves at every depth are multiplied by a single factor ρ (the p-multiplier for that row in the group). ρ was varied in the FLPIER model until an acceptable match was found between the computed and measured load-deformation behavior of the pile cap for both group tests. By following the procedure outlined in this appendix the factor ρ describes the combined effect of group construction and group loading on lateral pile group action.

The ρ values (p-multipliers) were ascertained by varying ρ on a row-by-row basis and comparing the computed cap translations at seven values of cap load, ranging from 150 T (1.47 MN) to 1000 T (9.8 MN). The number of loads at which the absolute value

of the computed deflection minus the measured deflection divided by the measured value of deflection exceeded 15 per cent was considered a measure of the accuracy of the selected family of ρ values. The results of a subset of analyses of the effects of families of ρ values on cap displacement in the bored pile group are summarized in Table A-2. The most accurate family of ρ values for the bored pile group is shown in Column (8) of Table A-2, although the families of values in Columns (2) and (10) of Table A-2 are essentially of equal accuracy.

The optimum set of ρ values (p-multipliers) for each group is presented in Table A-3. Also shown in Table A-3 are values that have been cited by Peterson and Rollins [8] as being appropriate for laterally loaded pile groups based on information available in 1996. The p-multipliers for the bored pile group in the current study were, on the average, lower than those cited by Peterson and Rollins, while the p-multipliers for the driven pile group were higher, row by row and on the average, than those of Peterson and Rollins. Considering the independent soil data of Huang in Figures A-14 through A-17, these trends appear to be clearly related to installation methods.

The measured lateral load versus lateral translation relations for both pile groups are compared with the relations predicted by FLPIER using the site-specific (modified) p-y curves for both bored and driven piles (Figures A-9 and A-11) and the p-multipliers tabulated in Table A-3 are shown in Figure A-25. The predictions are excellent.

Finally, a typical comparison of computed and measured deflected shapes for group piles is shown in Figure A-26. The FLPIER model with the modified p-y curves and the deduced p-multipliers appears to give good predictions of pile shape under loading.

Further details on the field tests and the analysis of the field tests can be found in Reference 20.

CONCLUSIONS AND RECOMMENDATIONS

Conclusions

Although the knowledge obtained from the Chaiyi field tests and their analysis is site specific, the general conclusions stated below are expected to be valid for other sites where similar soil conditions exist (loose to medium dense silty sands and sandy silts near the surface) and at which piles are installed with a similar geometry (rectangular groups with three-diameter center-to-center pile spacing) by casting the piles in place or by driving displacement piles. It is pointed out that these conclusions cannot be extended to sites where liquefaction will occur, nor is it likely that these conclusions apply to predominantly clay sites. The conclusions can be stated as follows:

1. Single-pile p-y curves needed to be softer (reduced p values for given values of y) than the prescribed curves (Reese criteria for sand layers; Matlock criteria for clay layers) for large-diameter (1.5 m) bored piles. See Figure A-9.

2. Single-pile p-y curves did not require overall softening relative to the prescribed curves (Reese criteria for sand layers; Matlock criteria for clay layers) for smaller-diameter (0.80 m) driven displacement piles; but some modification at individual depths, both softening and stiffening, was needed to optimize the simulation of measured single pile behavior. See Figure A-11.

3. The ratio of the deduced p-multipliers for the quasi-static loading of bored piles, averaged over all rows, was approximately 0.65 times that for the quasi-

static loading of driven displacement piles. The ratio of the average p-multiplier for the bored piles to the average "standard" value recommended by Peterson and Rollins was 0.85, whereas the ratio of the average p-multiplier for the driven displacement piles was 1.33 times the value recommended by Peterson and Rollins. See Table A-3.

4. The row-wise pattern of p-multipliers for both the driven and bored pile groups, tabulated in Table A-3, was similar to that observed by others. That is, the highest values appeared on the leading (front) row, the next highest on the first trailing row, etc. [When the extreme event loading has a predictable direction, it is appropriate to use row-wise p-multipliers in the design process. In seismic events, however, loading direction likely varies, and loading is cyclic, making it more reasonable from a design perspective to use average p-multipliers for all piles in the group.] The exact row-to-row ratios of p-multipliers is likely a function of the order of pile installation. In this study, the installation order was generally from front (leading) row to back (last trailing) row.

5. The differences in p-multipliers for bored and driven piles apparently largely reflect the effects of the differing effects of boring and driving displacement piles on the density and stress state in the mass of soil within the pile group.

6. The reduced soil stiffness around the bored piles was overshadowed by the effects of head fixity and pile diameter (higher moment of inertia) in the bored pile group.

The applicability of the results summarized in this appendix to p-multipliers for dynamic loading (e. g., Appendix B) is not clear. However, the results suggest that for low frequencies of seismic loading (low predominant frequency of the seismic event) the average p-multiplier for groups of bored piles should be lower than those for driven displacement piles by a factor in the range of 0.65.

Recommendations for Further Research

The following additional research is recommended:

1. Further research is needed to understand the frequency range to which the ratio of p-multipliers for bored piles to those for driven piles, deduced from static tests such as these tests, applies.

2. It is possible that p-multipliers will be different for bored piles installed with continuous, full-depth casing than for bored piles installed by slurry displacement. Further research into this phenomenon is warranted if full-depth casing construction methods become common on DOT projects in the United States.

REFERENCES — APPENDIX A

1. Reese, L. C., Cox, W. R., and Koop, F. C, "Analysis of Laterally Loaded Piles in Sand," Offshore Technology Conference, Houston, Texas, Proceedings (1974), pp. 473 - 484.

2. Murchison, J., and O'Neill, M. W., "Evaluation of p-y Relationships in Cohesionless Soil," *Analysis and Design of Pile Foundations*, Ed. by J. R. Meyer, ASCE (1984), pp. 174 - 191.

3. Reese, L. C., and Wang, S. T., *Computer Program LPILE Plus, Version 3.0 — A Program for the Analysis of Piles and Drilled Shafts Under Lateral Loads, Technical Manual* (1997), Ensoft, Inc., Austin, TX.

4. Hoit, M., Hays, C., and McVay, M., "The Florida Pier Analysis Program: Methods and Models for Pier Analysis and Design," *Transportation Research Record No. 1569* (1997), Transportation Research Board, pp. 1- 7.

5. PMB Engineering, Inc., PAR: *Pile Analysis Routines, Theoretical and User's Manuals* (1988), PMB Engineering, Inc., San Francisco, CA.

6. Brown, D. A., Morrison, C., and Reese, L. C., "Lateral Load Behavior of Pile Group in Sand," *Journal of Geotechnical Engineering*, ASCE, Vol. 114, No. 11 (1988), pp. 1326 - 1343.

7. McVay, M., Casper, R., and Shang, T-I, "Lateral Response of Three-Row Groups in Loose to Dense Sands at 3D and 5D Pile Spacing," *Journal of Geotechnical Engineering*, ASCE, Vol. 121, No. 5 (1995), pp. 436 - 441.

8. Peterson, K., and Rollins, K. M., "Static and Dynamic Lateral Load Testing of a Full-Scale Pile Group in Clay," *Research Report No. CEG.96-02* (1996), Department of Civil Engineering, Brigham Young University, Provo, UT, 223 pp.

9. Pinto, P., McVay, M., Hoit, M., and Lai, P., "Centrifuge Testing of Plumb and Battered Pile Groups in Sand," *Transportation Research Record No. 1569* (1997), Transportation Research Board, pp. 8 - 16.

10. Brown, D. A., and Shie, C. F., "Modification of p-y Curves to Account for Group Effects on Laterally Loaded Piles," Geotechnical Engineering Congress, *Geotechnical Special Publication No. 27*, ASCE, Vol. 2 (1991), pp. 479 - 490.

11. Chen, C-H, "Data for Planned Pile Group Tests at Chaiyi Test Site," *Workshop Report* (1996), Department of Civil Engineering, National Taiwan University, Taipei, Taiwan.

12. Huang, A. B., *Midterm Report of the Lateral Test of Group Piles* (1997), Department of Civil Engineering, National Chao-Tung University, Hsinchu, Taiwan.

13. Matlock, H., "Correlations for Design of Laterally Loaded Piles in Soft Clays," Second Annual Offshore Technology Conference, Houston, Texas, Proceedings (1970), pp. 578 - 588.

14. Andrade, P., "Materially and Geometrically Nonlinear Analysis of Laterally Loaded Piles Using a Discrete Element Technique," *Final Report* (1994), Department of Civil Engineering, University of Florida.

15. McVay, M., Hays, C., and Hoit, M., *User's Manual for Florida Pier, Version 5.1* (1996), Department of Civil Engineering, University of Florida.

16. Huang, A. B., "The Effect of the Installation of Group Piles on the Properties of the Soil in the Vicinity," *Final Report* (1997), Department of Civil Engineering, National Chao-Tung University, Hsinchu, Taiwan.

17. Reese, L. C., and Wang, S. T., *GROUP 4.0 for Windows*: Technical Manual (1996), Ensoft, Inc., Austin, TX.

18. Randolph, M. F., and Wroth, C. P., "Analysis of Deformation of Vertically Loaded Piles," *Journal of the Geotechnical Engineering Division*, ASCE, Vol. 104, No. GT12 (1978), pp. 1465 - 1488.

19. American Petroleum Institute, *Recommended Practice for Planning, Designing and Constructing Fixed Offshore Platforms — API Recommended Practice 2A (RP2A)*, 17th Edition (1993), API, Washington, D. C.

20. Zhang, Xianfeng, "Comparison of Lateral Group Effect between Bored and PC Driven Pile Groups in Sand," Master of Science Thesis (1999), Department of Civil and Environmental Engineering, University of Houston, Houston, Texas.

Table A-1. Concrete and Steel Properties for Chaiyi Load Tests

Property	Bored Piles and Cap	Prestressed Concrete Piles
f'_c (concrete)	27.5 MN/m^2	78.4 MN/m^2 (shell) 20.59 MN/m^2 (core)
E_c (concrete)	2.5×10^4 MN/m^2	3.35×10^4 MN/m^2 (shell) No data for core (2.0×10^4 MN/m^2 used)
f_y (steel)	411.6 MN/m^2	1421 MN/m^2 (cable)
E_s (steel)	199.8 GN/m^2	199.8 GN/m^2

Table A-2. Effect of Varying p-Multipliers on Cap Deflection for the Bored Pile Group

Load (T)	Measured cap deflection (mm)	Computed cap deflection (mm)											
		(1)	(2)	(3)	(4)	(5)	(6)	(7)	(8)	(9)	(10)	(11)	(12)
		0.8	0.6	0.6	0.6	0.7	0.7	0.5	**0.5**	0.5	0.5	0.65	0.55
		0.4	0.3	0.3	0.2	0.2	0.3	0.3	**0.4**	0.4	0.3	0.35	0.47
		0.333	0.3	0.2	0.3	0.3	0.2	0.3	**0.3**	0.2	0.4	0.2	0.13
150	1.38	1.81 +31%	2.15 +55%	2.32 +68%	2.31 +67%	2.19 +59%	2.20 +59%	2.28 +65%	**2.14 +55%**	2.31 +67%	2.13 +54%	2.18 +58%	2.26 +64%
300	4.34	3.48 -20%	4.17 -4%	4.58 +6%	4.56 +5%	4.24 -2%	4.27 -2%	4.57 +5%	**4.22 -3%**	4.61 +6%	4.20 -3%	4.24 -2%	4.51 +4%
450	8.05	6.09 -24%	7.55 -6%	8.21 +2%	8.17 +2%	7.62 -5%	7.65 -5%	8.06 +0%	**7.49 -7%**	8.19 +2%	7.43 -8%	7.65 -5%	7.95 -1%
600	12.96	7.85 -39%	9.8 -24%	10.8 -17%	10.8 -17%	10.0 -23%	10.0 -23%	10.6 -18%	**9.7 -25%**	10.7 -17%	9.67 -25%	10.0 -23%	10.4 -20%
800	10.1	11.8 +17%	15.3 +52%	17.0 +68%	17.0 +68%	15.6 +55%	15.7 +55%	16.7 +65%	**15.2 +50%**	16.9 +67%	15.2 +50%	15.5 +55%	16.4 +62%
900	18.69	14.6 -22%	19.1 +2%	21.5 +15%	21.5 +15%	19.5 +4%	19.5 +4%	21.1 +13%	**18.9 +1%**	21.3 +14%	18.9 +1%	19.3 +3%	20.5 +10%
1000	23.15	19.5 -16%	26.6 +15%	30.1 +30%	30.1 +30%	27.2 +18%	27.2 +18%	29.6 +28%	**26.4 +14%**	29.9 +29%	26.4 +14%	27.0 +17%	29 +25%
Average difference ratio		-10%	+13%	+25%	+24%	+15%	+15%	+23%	**+12%**	+24%	+12%	+15%	+21%
Error probability		7/7	3/7	4/7	4/7	4/7	4/7	4/7	**3/7**	4/7	3/7	4/7	4/7

Note: The percentage below each computed deflection is the ratio of the difference between a computed and measured deflection to the measured deflection; "Average difference ratio" is the value of the sum of all the difference ratios in a column divided by the number of total loads, i.e., 7; "Error probability" is defined as the ratio of the number of the loads whose corresponding difference ratios exceed ±15% to the number of total loads.

Table A-3. p-Multipliers for Chaiyi Lateral Group Load Tests

Pile Row	Inferred p-Multipliers from Chaiyi Load Tests		p-Multipliers from Peterson and Rollins S / D = 3	Default p-Multipliers from FLPIER S/D = 3
	Bored Pile Group	Driven Pile Group		
Lead	0.5	0.9	0.6	0.8
First Trail	0.4	0.7	0.4	0.4
Second Trail	0.3	0.5	0.4	0.2
Third Trail	-	0.4	-	0.3
Average	*0.4*	*0.63*	*0.47*	*0.43*

Depth m	Boring Log	Description	SPT N averaged	Properties
0 ▽		Fine sandy silt; yellowish brown loose with some clayey silts (SM)	5	$k=27.14$ MN/m^3 $\phi=35°$ $\gamma=19$ kN/m^3
3		Silty fine sand; grey; medium dense; occasionally with sandy silt layers. (SM)	6	$k=18.86$ MN/m^3 $\phi=35°$ $\gamma=9.2$ kN/m^3
8		Silty clay; greyish brown; medium stiff, occasionally with coarse sand seams (2-3 mm) (CL)	10	$S_u=60$ kN/m^2 $\varepsilon_{50}=0.007$ $\gamma=9.2$ kN/m^3
12		Silty fine sand; grey; loose with fine sandy silt layer (SM)	10	$k=18.32$ MN/m^3 $\phi=34°$ $\gamma=9.4$ kN/m^3
17		Clayey silts; grey; medium dense with little sandy silts (ML/ CL) Silty clay; grey; medium dense with silty fine sand layer	17	$k=20.36$ MN/m^3 $\phi=34°$ $\gamma=9.2$ kN/m^3
25		Silty clay; grey; very stiff with little fine sand (CL)	18	$S_u=115$ kN/m^2 $\varepsilon_{50}=0.005$ $\gamma=9.2$ kN/m^3
32 43		Silty clay; grey; very stiff with silty fine sand layer (SM/CL)	19 45	$S_u=121.3$ kN/m^2 $\varepsilon_{50}=0.005$ $\gamma=9.2$ kN/m^3

Figure A-1. Subsurface Profile at Chaiyi, Taiwan, Test Site

3 @ 4.5 m

B1 (Lateral reference)

B9

B6

B3

SCPTU-N1

DMT-N2

B10 (Axial reference)

12.0 m

B7

B4

2 @ 4.5 m

SCPTU-N2

DMT-N1

B11

B8

B5

B2 (Lateral reference)

8.5 m

Cap Thickness = 2.0 m
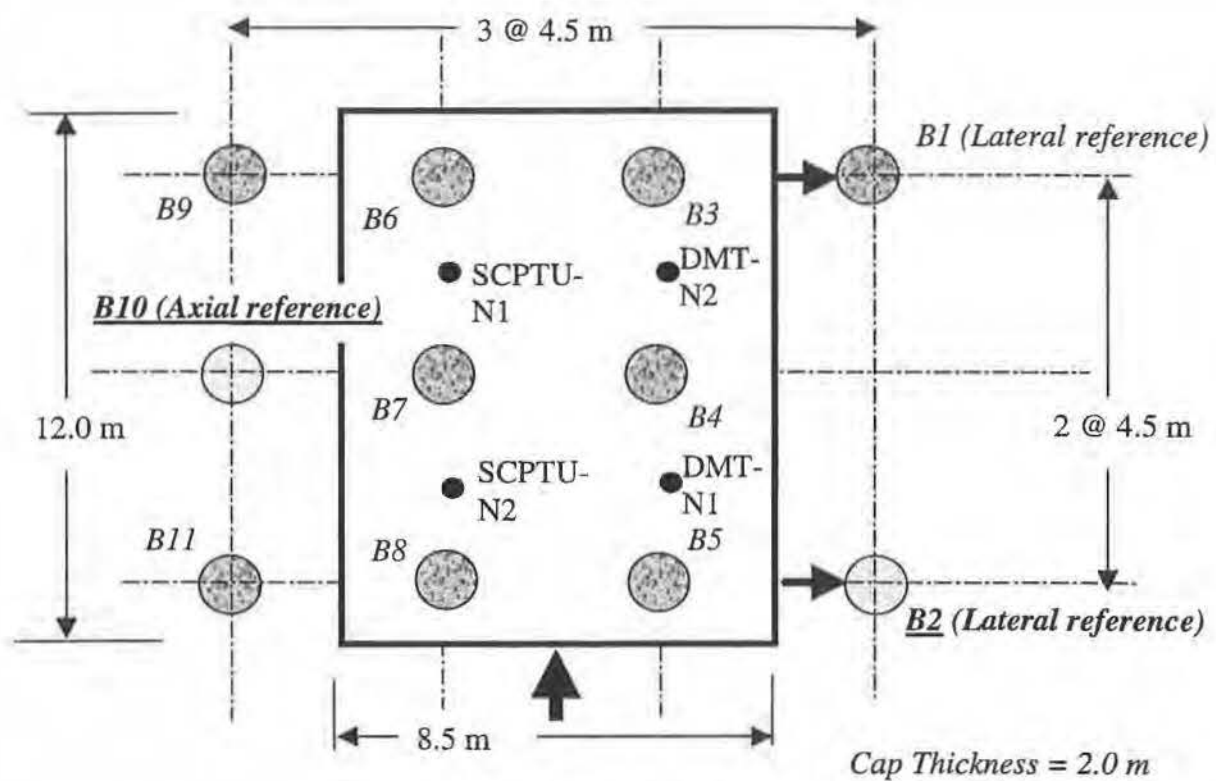
(a) Bored Pile Group Layout

B6 (# 1)

B3 (# 2)

B7 (# 4)

B4 (# 5)

B8 (# 3)

B5 (# 6)
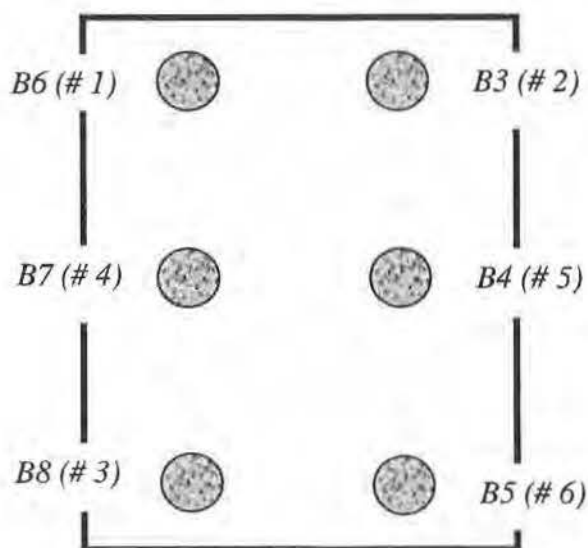
(b) Order of Installation for Bored Piles in Test Group

Figure A-2. Plan View of Test Group for Bored Piles and Reference Piles (Not to Scale)

8.0 m

2 @ 2.4 m

P4   P8   P12

SCPTU-N3

P3   P7*   P11

3 @ 2.4 m

DMT-N3

9.0 m

P2   P6*   P10

P13 (lateral reference)

3.0 m

P1

P5   P9

Cap thickness = 2.0 m

* —Axial reference pile
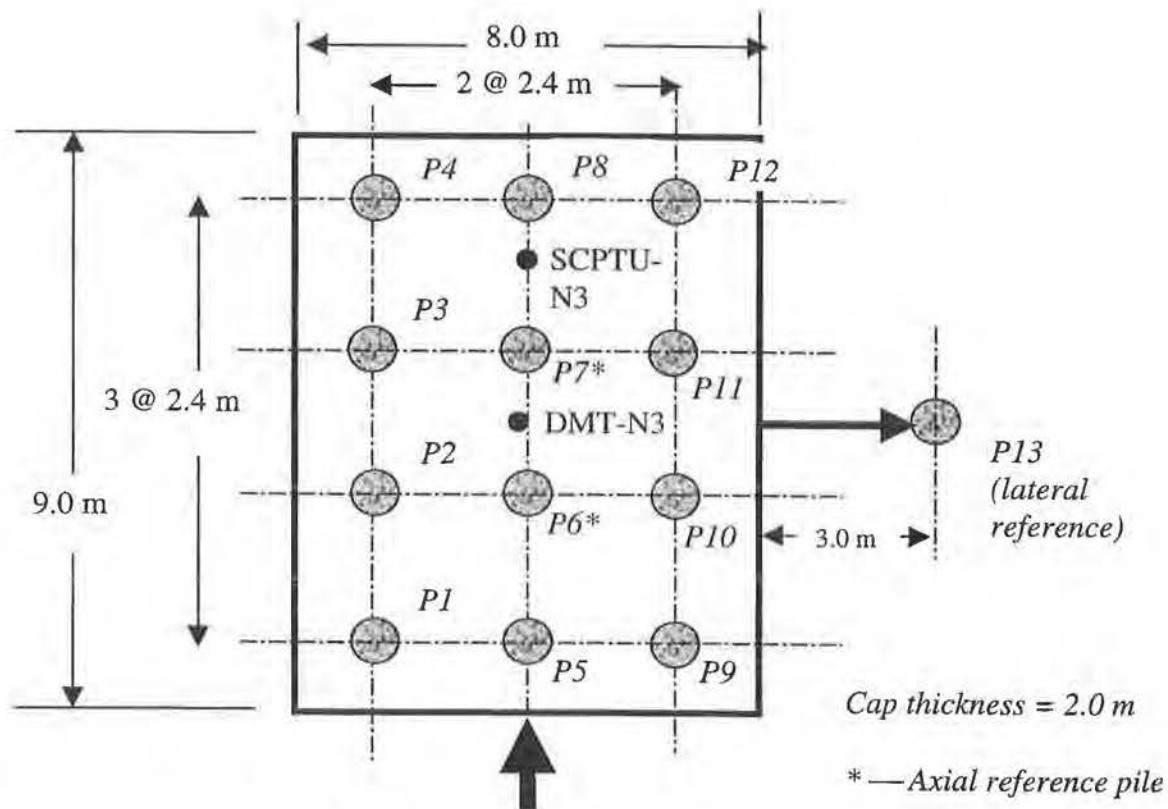
(a) Driven Pile Group Layout

P4 (# 9)   P8 (# 1)   P12 (# 2)

P3(# 10)   P7 (# 3)   P11 (# 5)

P2 (# 11)   P6 (# 4)   P10 (# 6)

P1 (# 12)   P5 (# 8)   P9 (# 7)
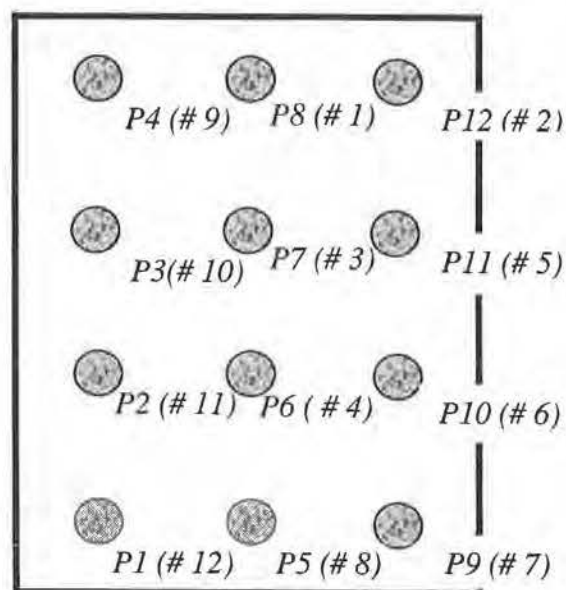
(b) Order of Installation for Driven Piles in Test Group

Figure A-3. Plan View of Test Group for Driven Piles and Reference Piles (Not to Scale)
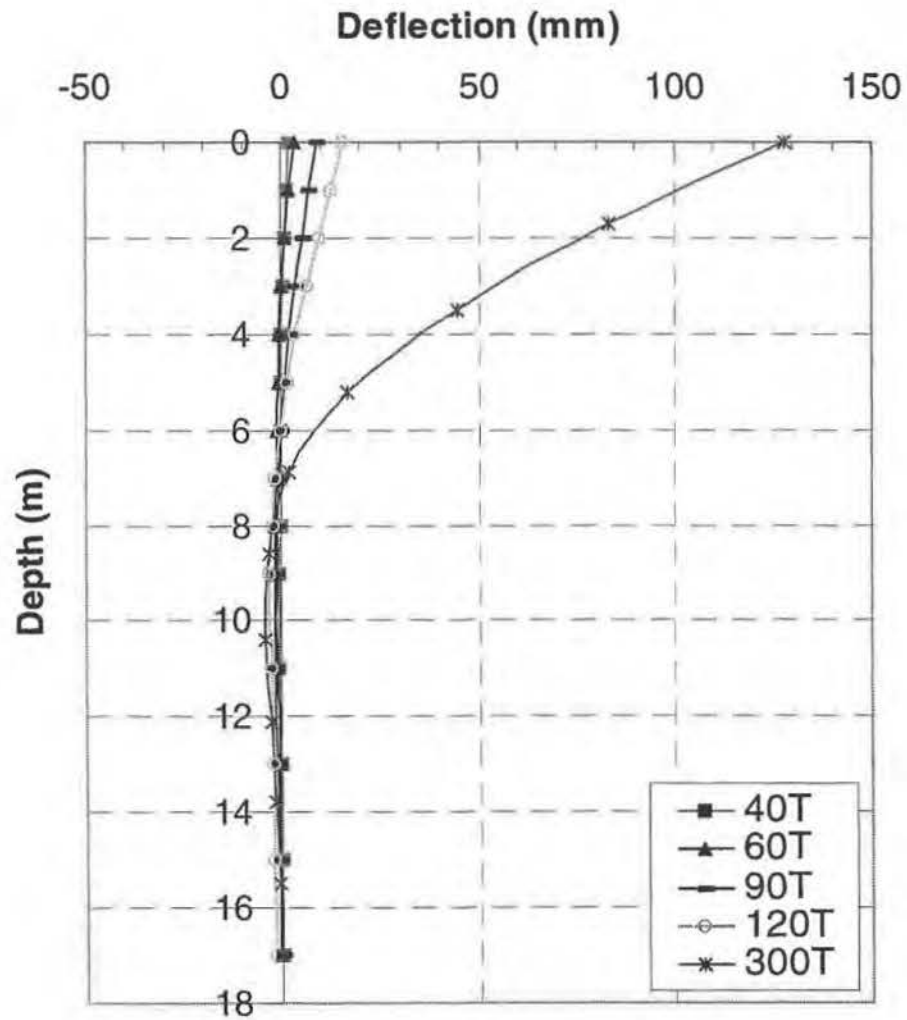
Figure A-4. Measured Load-Deflection-Depth Relations for Pile B-1
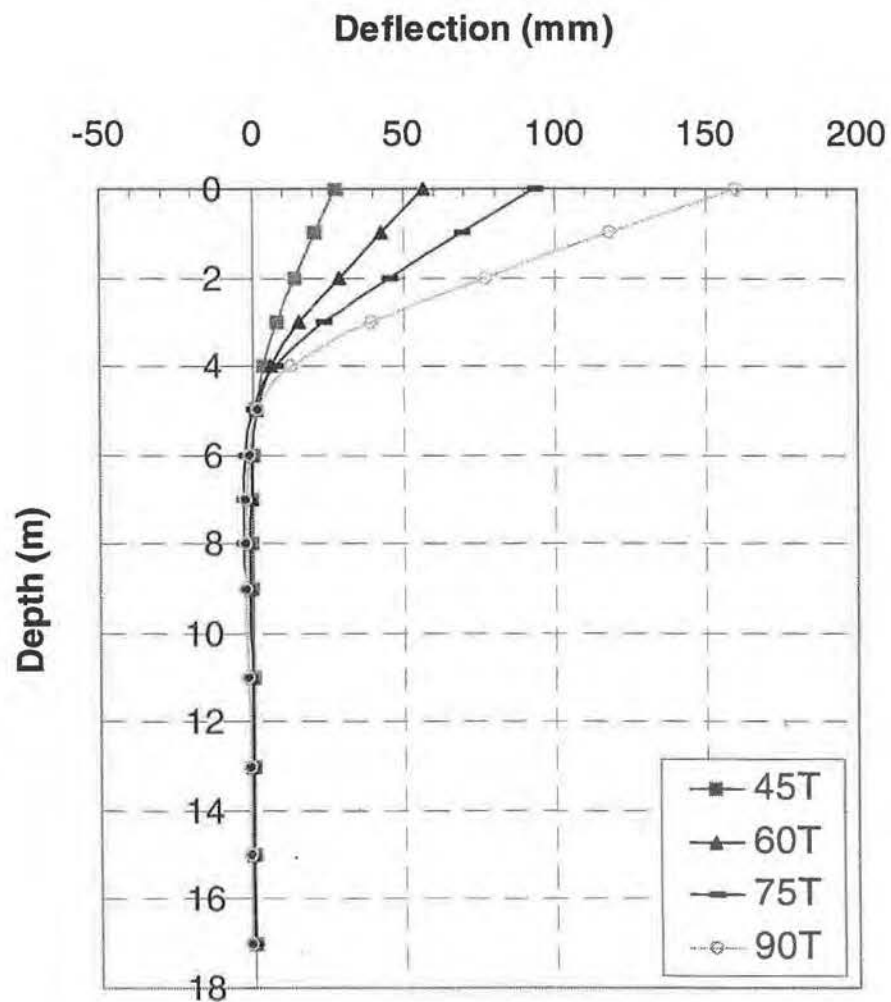
Figure A-5. Measured Load-Deflection-Depth Relations for Pile P-13
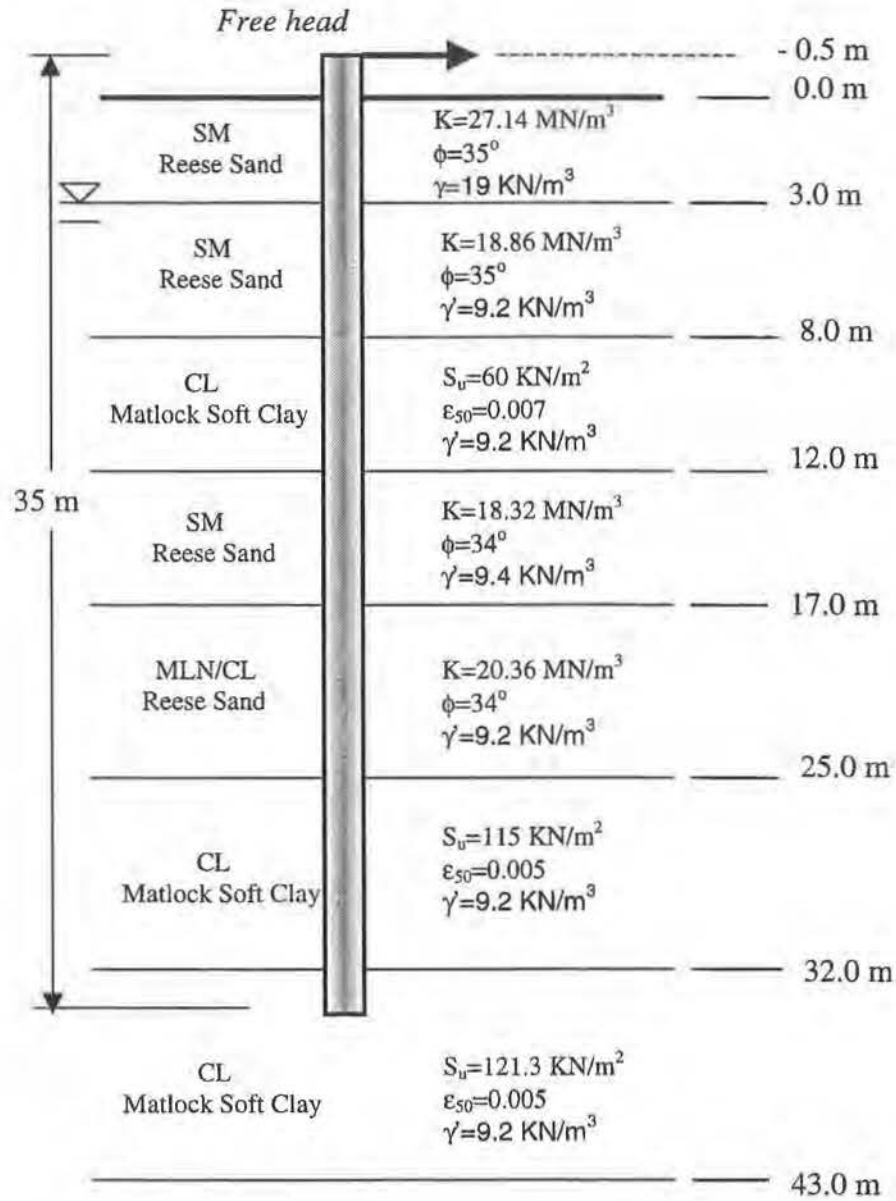
Figure A-6. Soil Properties Used in Developing Initial p-y Curves

Cast-in-place Bored Pile Details

Designated pile top
Bottom of Pile cap
Plain concrete
PD1
PD2
Spacer
PD3

Section A

Type A: 2D16 PD4@100
Type B: D16 PD4@150
Type C: D16 PD4@150

PD1 Equal space

Section B

Spacer @3000 vertical height of pile

Type A: D16 PD4@100
Type B: D16 PD4@150
Type C: D16 PD4@150

PD2 Equal space

Section C

Type A: D16 PD4@200
Type B: D16 PD4@300
Type C: D16 PD4@300

PD3 Equal space

2D16 PD4@100
Footing reinforcement
Plain concrete
Bolt of pile cap

Pile&Pile Cap Connection Detail

Table of Reinforcement A,B,C

NO.	Nominal Diameter	Reinforcement Type	Remark
PD1	D32		Type A: 26x3 B: 34 C: 26
PD2	D32		Type A: 26x2 B: 34 C: 26
PD3	D32		Type A: 26 B: 17 C: 13
PD4	D16	◯	

Notes

1 unit: mm except those denoted
2 E_c of concrete=27500 kN/m^2 ; f_y of steel =41600 kN/m^2
3 The reinforcement of bored piles B3~B8 & 12,13 is type A;
   B1,2,9&11 is type B; B10 is type C

4 L: the length of bored piles were described inconsistently in the series of
   reports of this project, in this analysis, they are assumed to
   be 35 m for the single bored pile and 1.5 m shorter for the group piles
   according to the graphs in the data report.
5 E_s =2x10^8 kN/m^2 ; E_c =2.5x10^7 kN/m^2

Figure A-7. Structural Details for Bored Piles

Figure A-8. Structural Details for Driven (Prestressed Concrete) Piles
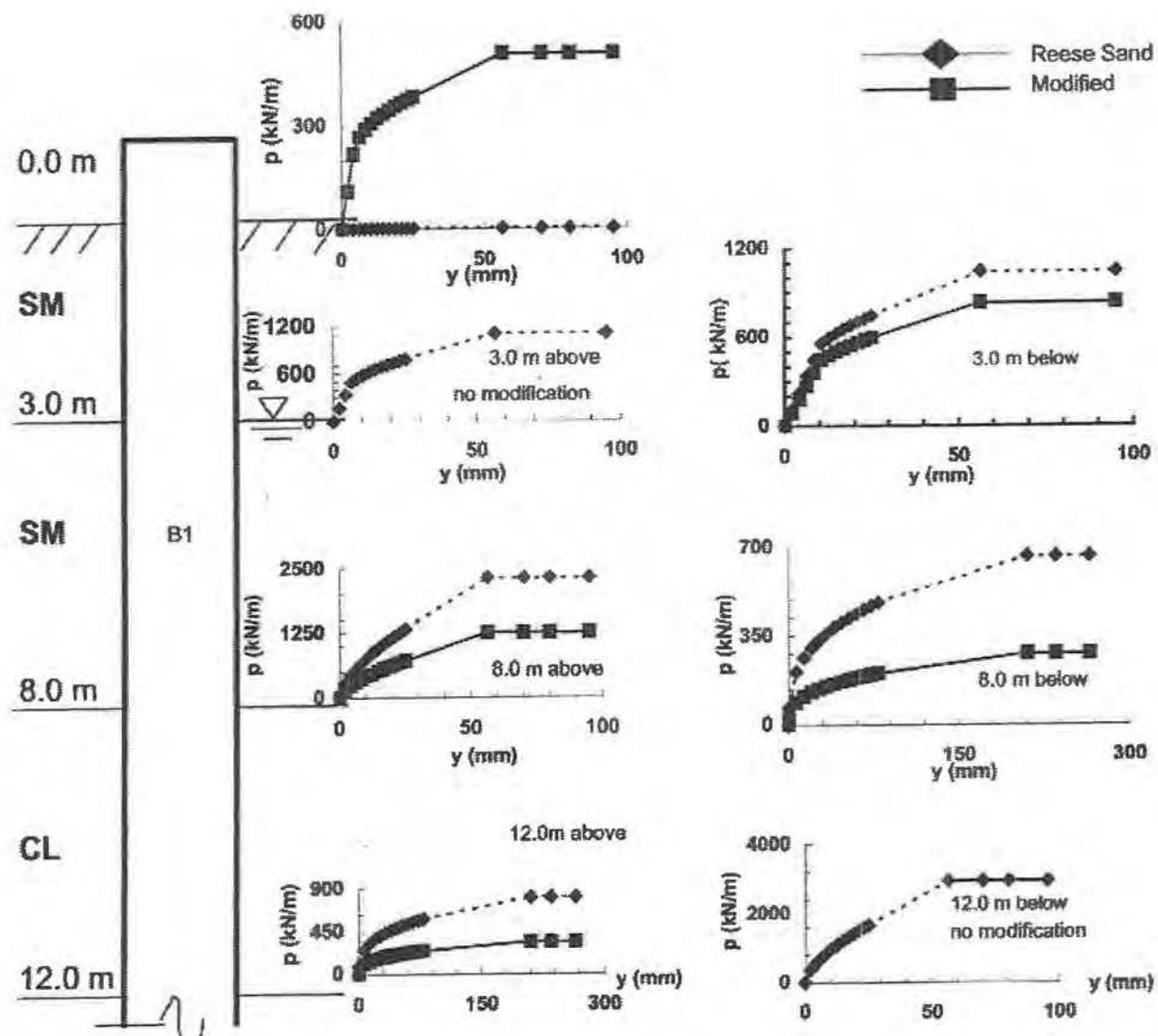
Figure A-9. *Original and Modified p-y Curves for Bored Pile B-1 (Slurry Drilled)*
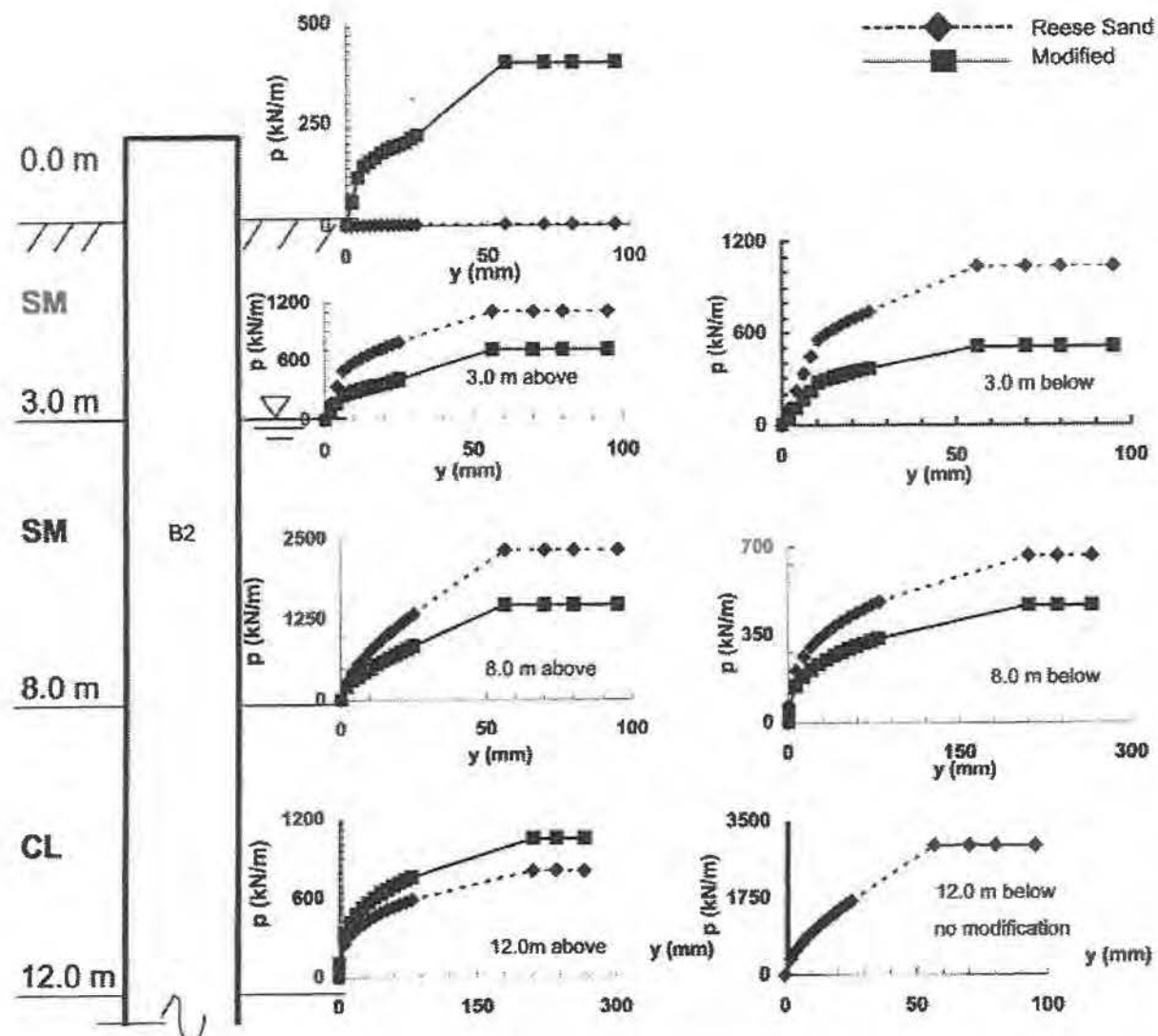
Figure A-10. Original and Modified p-y Curves for Bored Pile B-2 (Full-Depth Casing)
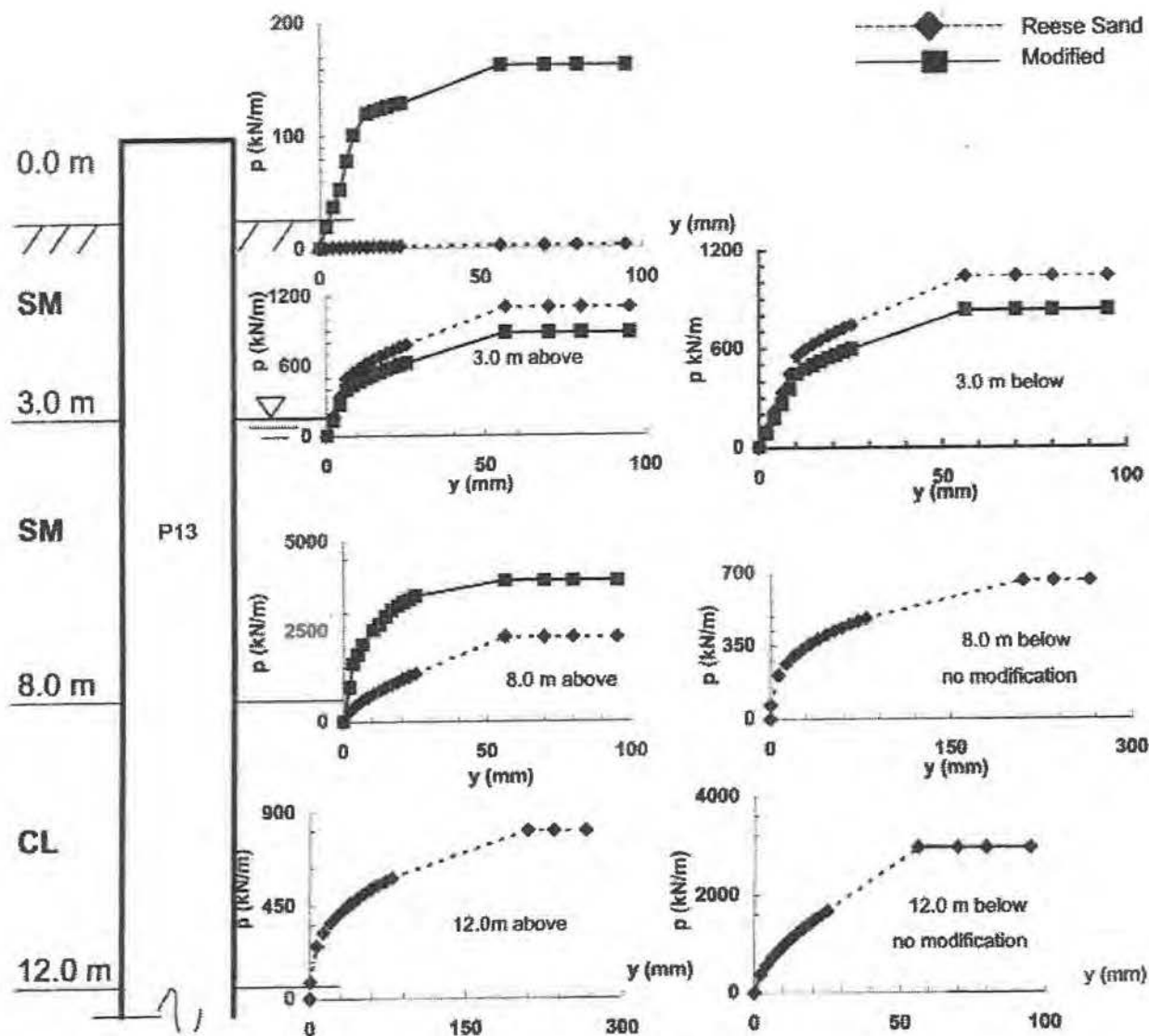
Figure A-11. Original and Modified p-y Curves for Driven Pile P-13 (Prestressed Concrete)
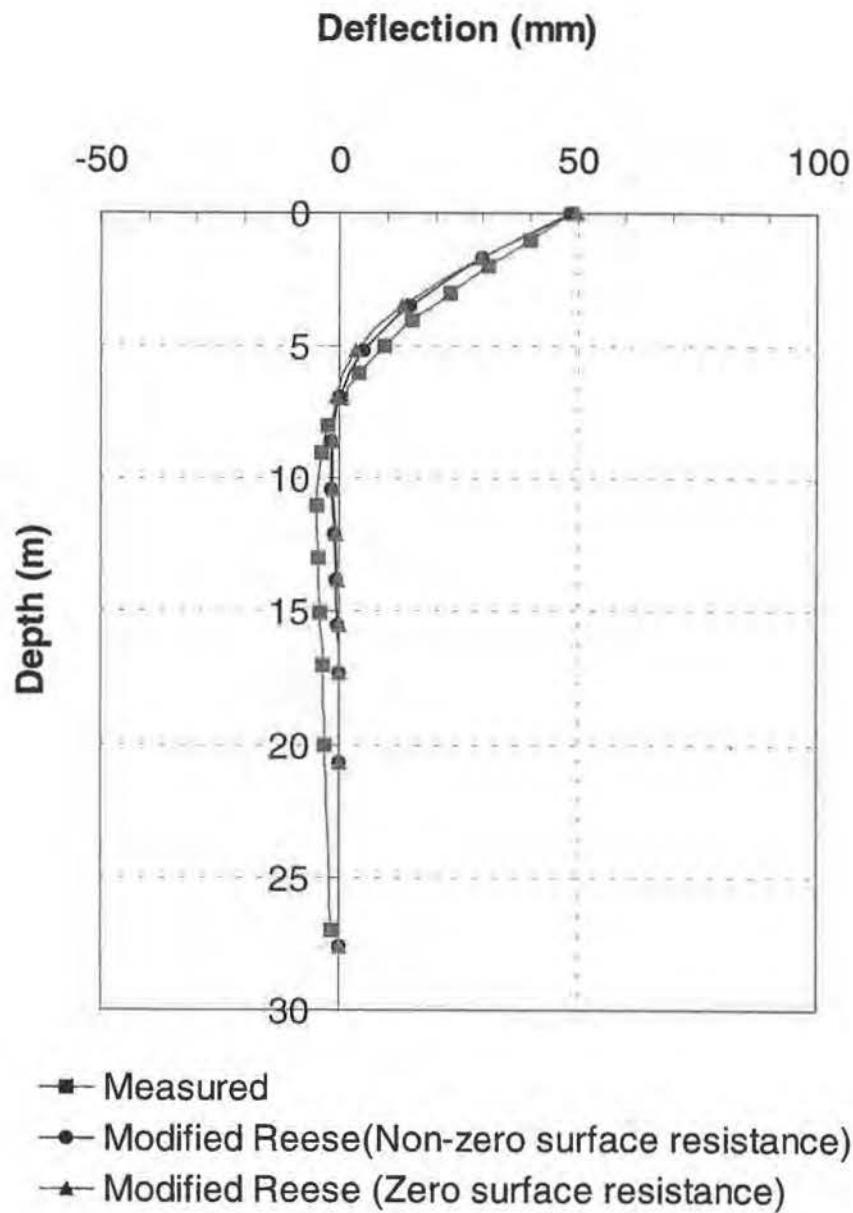
Deflection (mm)

Figure A-12. *Effect of p-y Formulation on deflected Shape of Bored Pile B1 —*
Load = 200 T (1.96 MN)
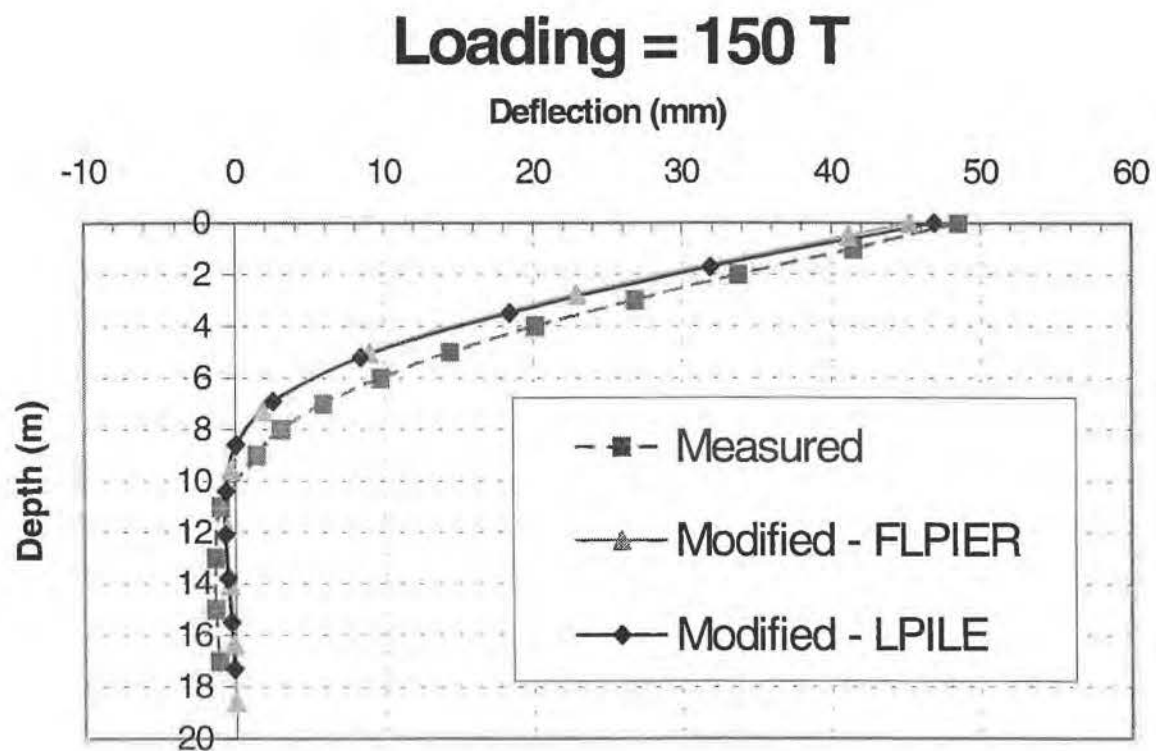
Figure A-13. Predictions of Deflected Shape of Bored Pile B2 Using FLPIER and
LPILE Plus with Modified p-y Criteria — Load = 150 T (1.47 MN)
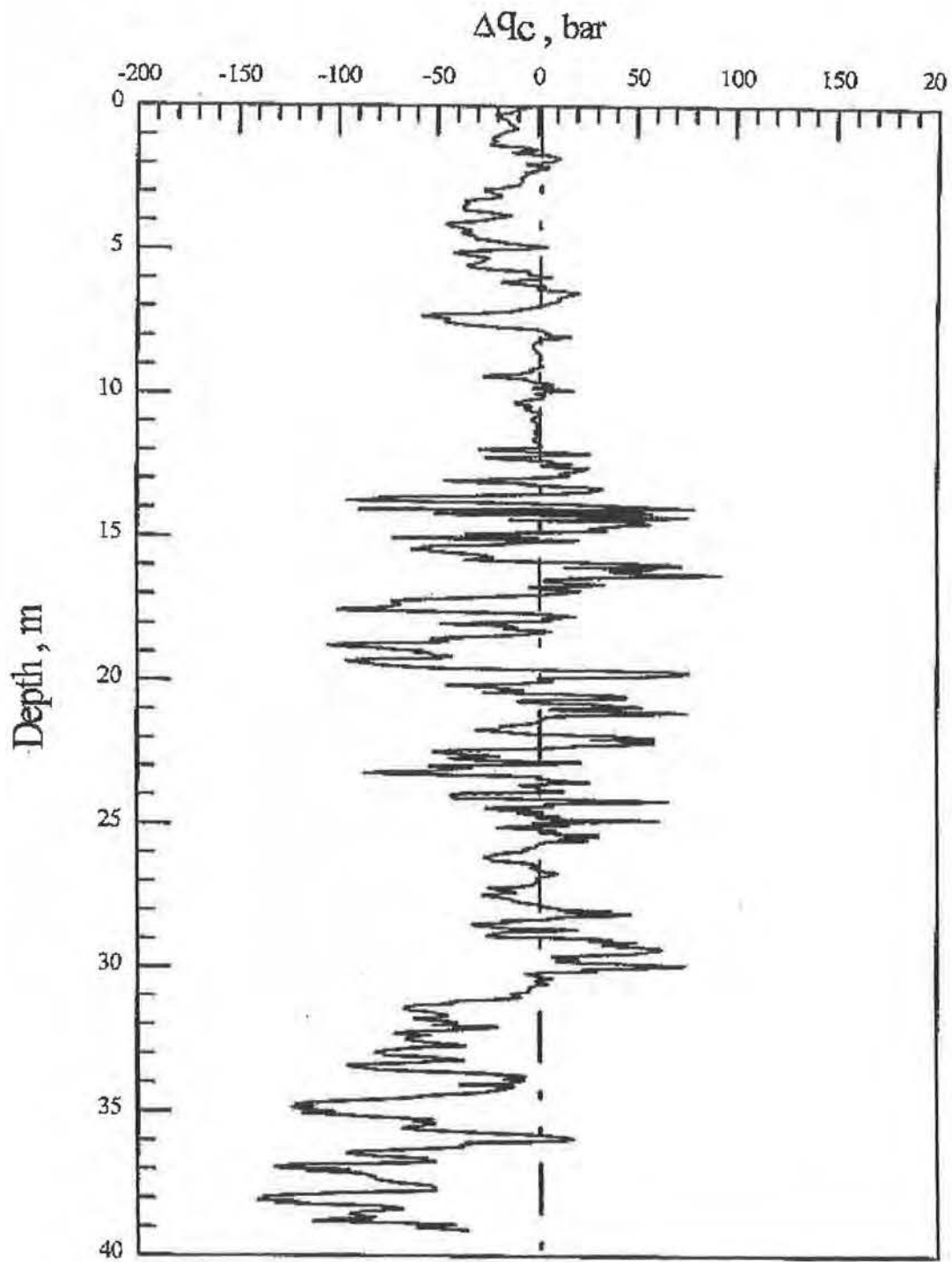
Figure A-14. Change in Cone Tip Reading (q_c) within Bored Pile Group from Pre-Installation Value to Value Obtained after Piles Installed (SCPTU-N1)
(after Huang [16])
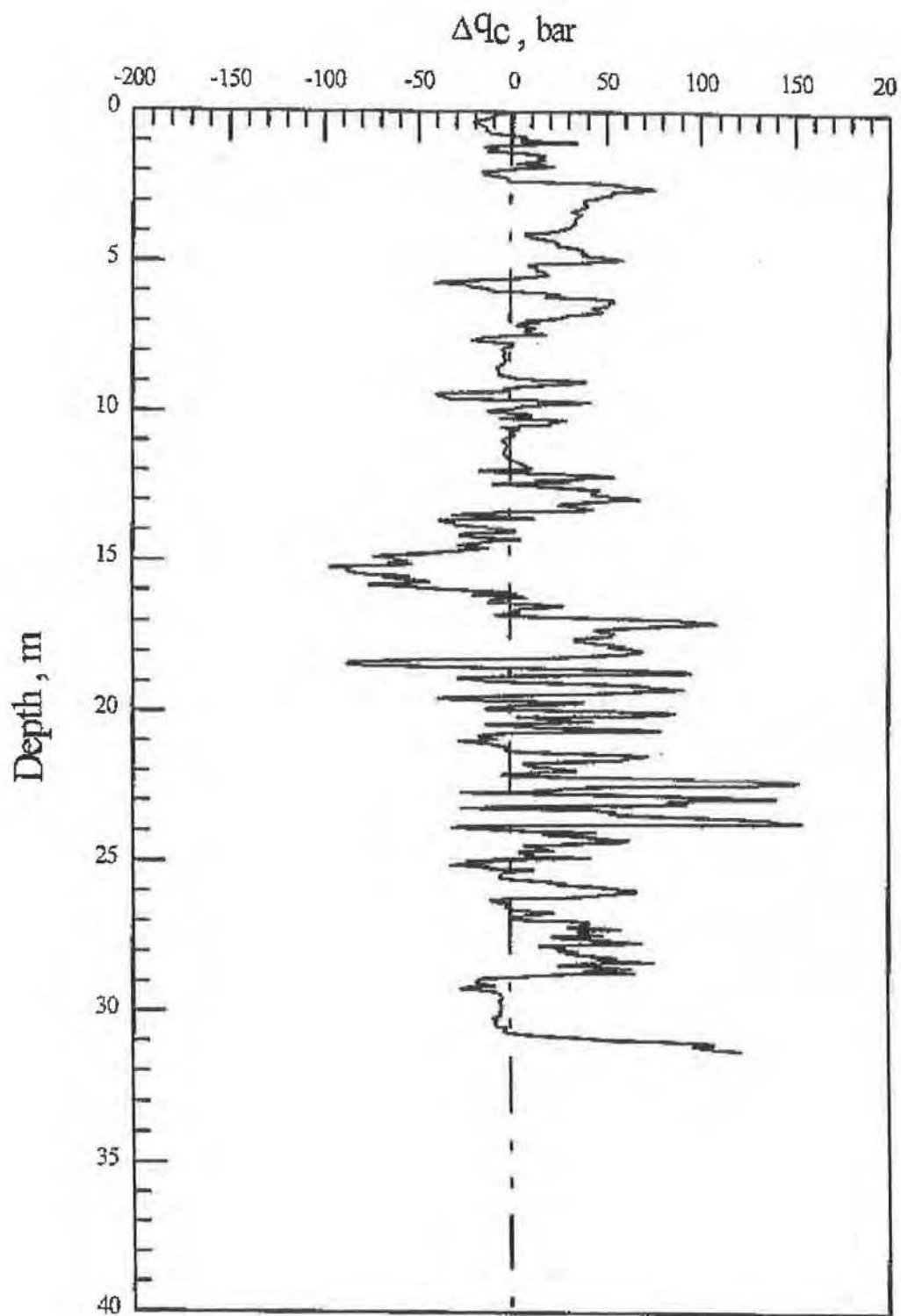
Figure A-15. Change in Cone Tip Reading (q_c) within Driven Pile Group from Pre-Installation Value to Value Obtained after Piles Installed (SCPTU-N3) (after Huang [16])
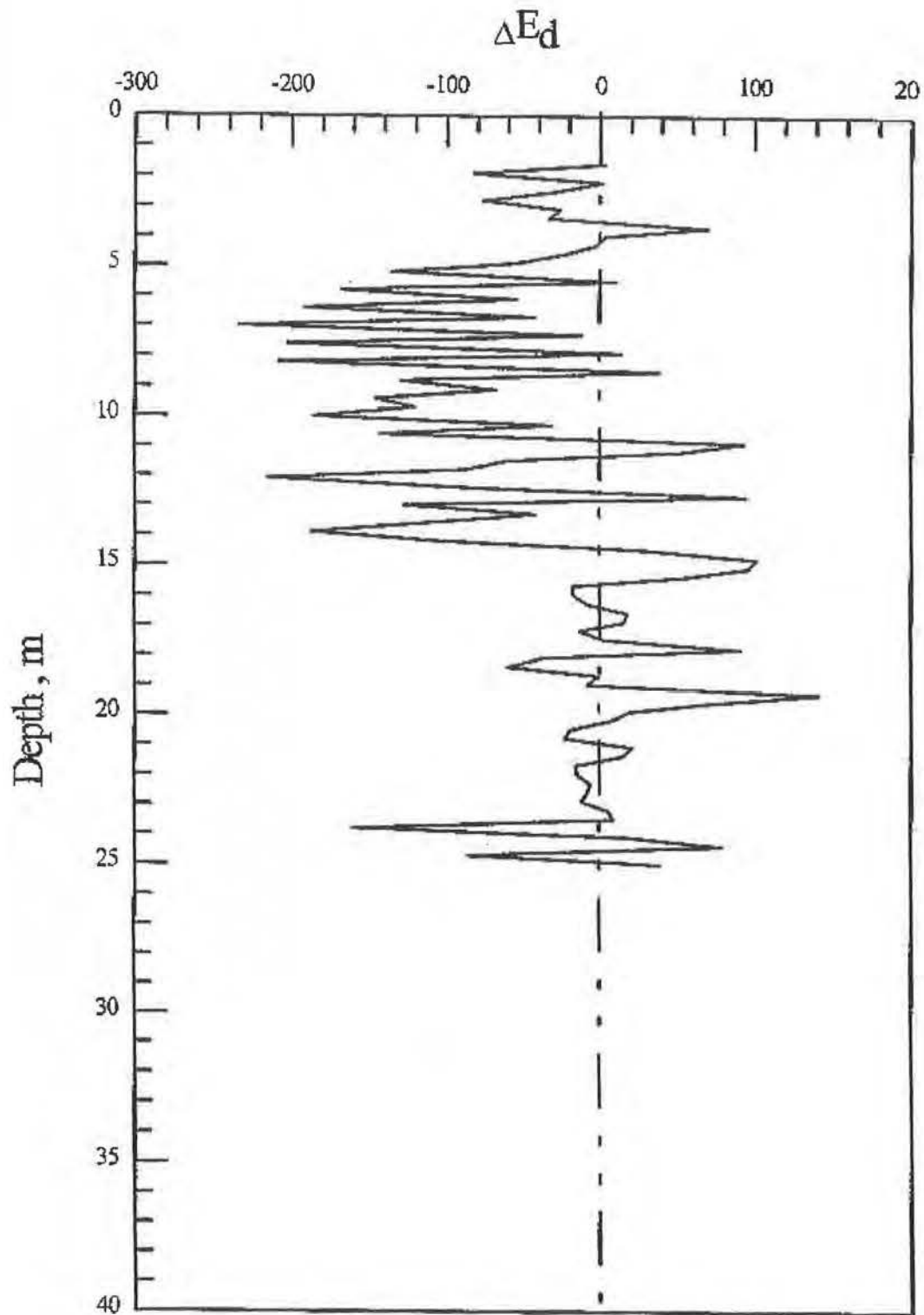
*Figure A-16. Change in Dilatometer Modulus (E_d) within Bored Pile Group from Pre-Installation Value to Value Obtained after Piles Installed (DMT-N1)
(after Huang [16])*
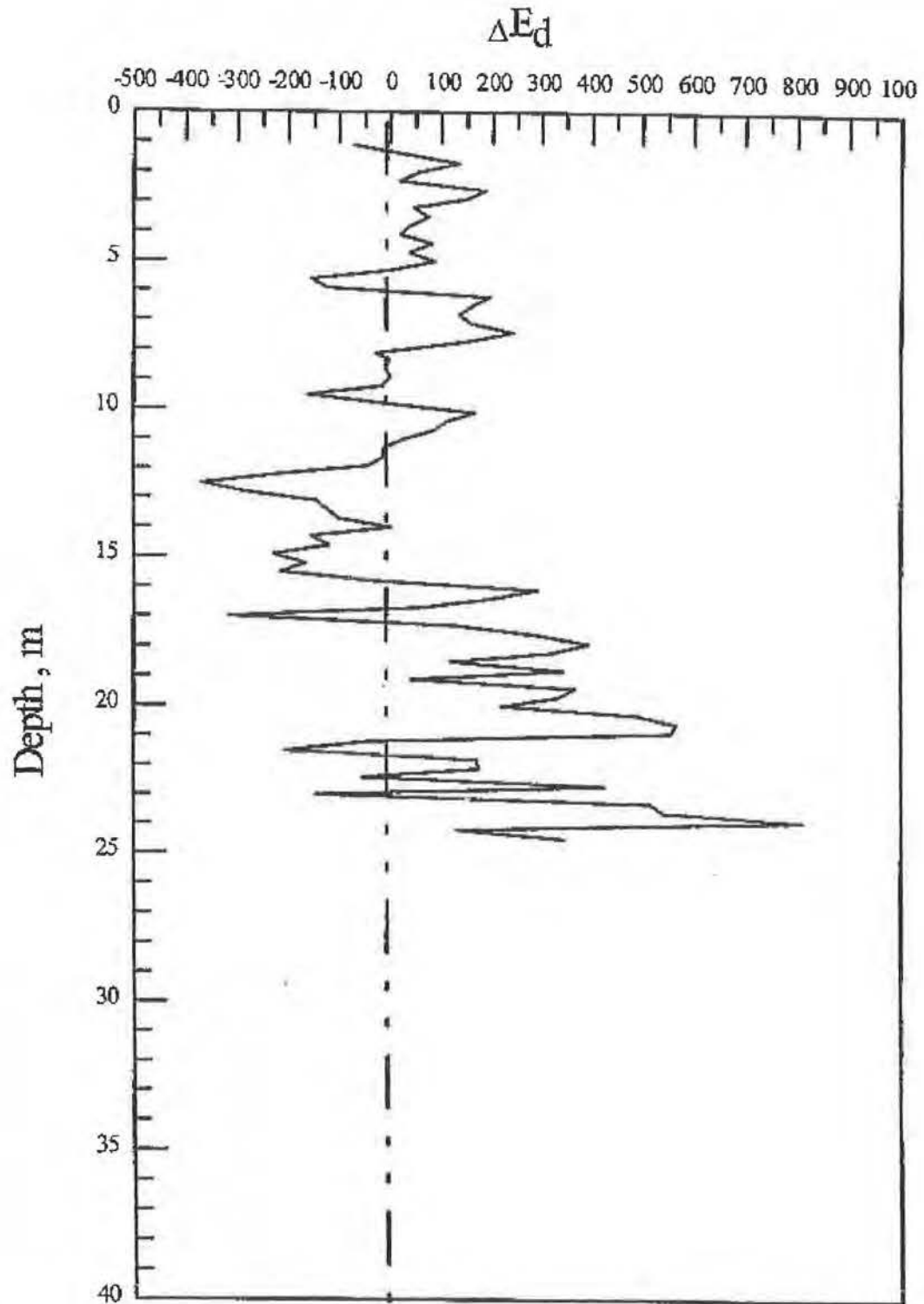
Figure A-17. *Change in Dilatometer Modulus (E_d) within Driven Pile Group from Pre-Installation Value to Value Obtained after Piles Installed (DMT-N3) (after Huang [16])*
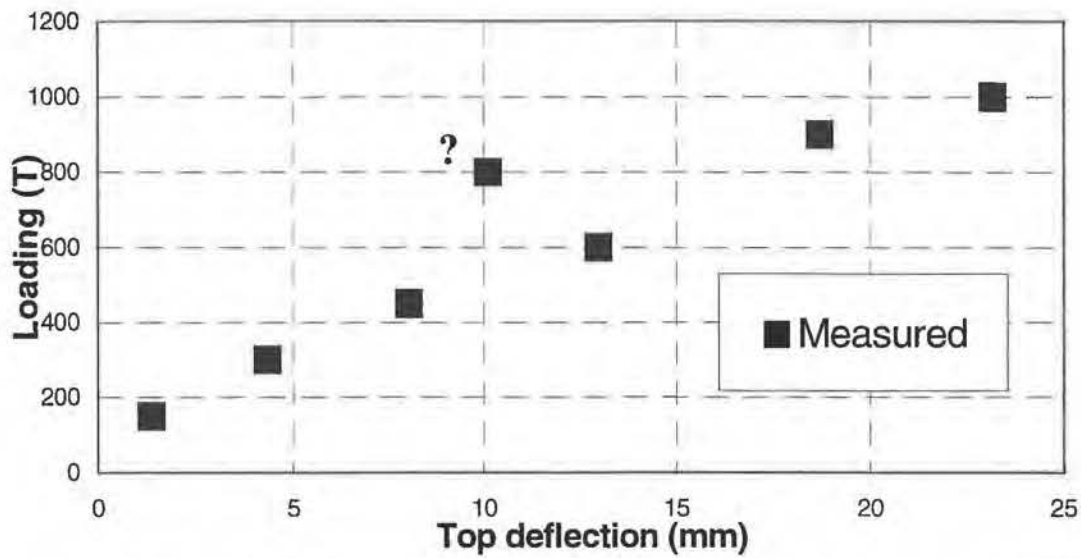
Figure A-18. Cap Shear Load Versus Lateral Cap Deflection — Bored Pile Group
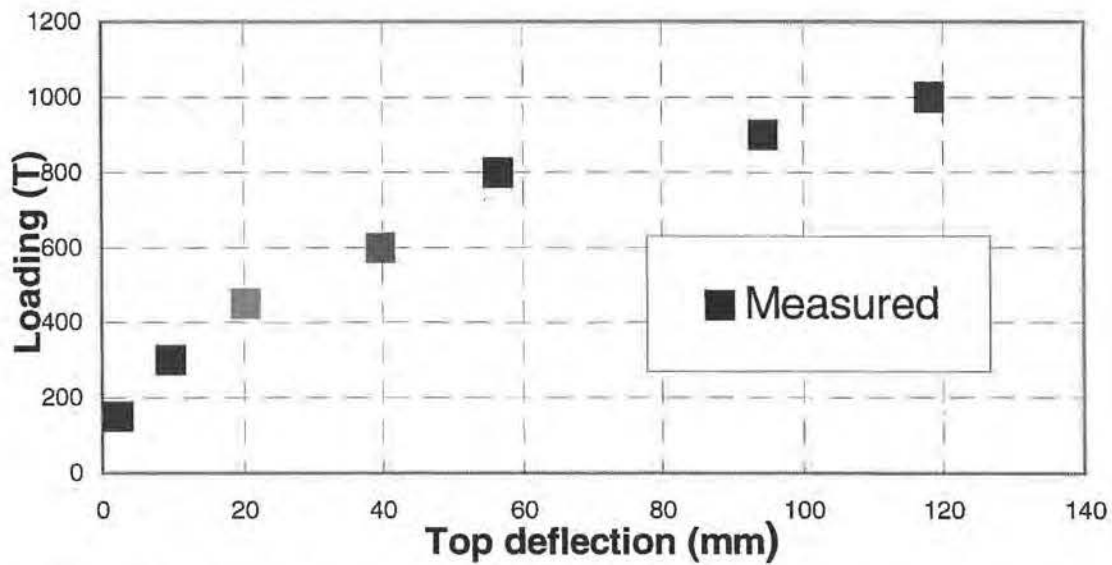
Figure A-19. Cap Shear Load Versus Lateral Cap Deflection — Driven Pile Group
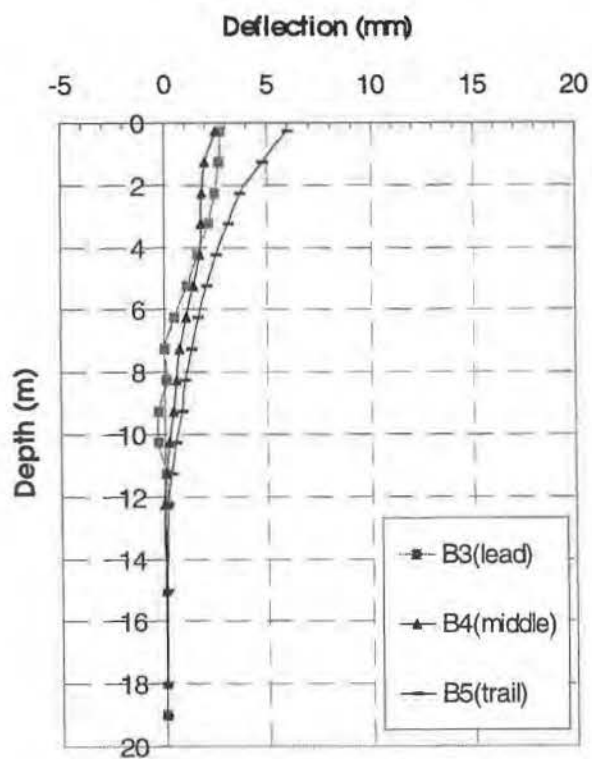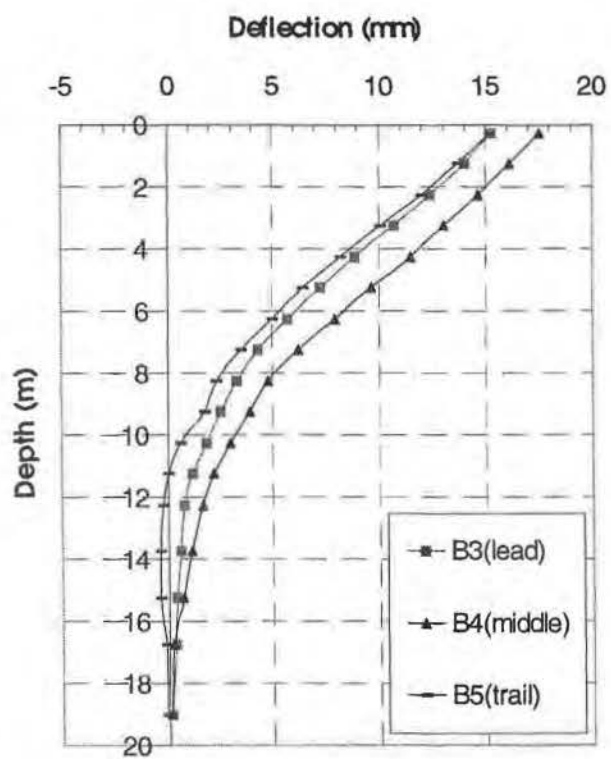
(a) Load = 300 T   (b) Load = 800 T

Figure A-20. Measured Deflected Shapes along Selected Piles in Bored Pile Group
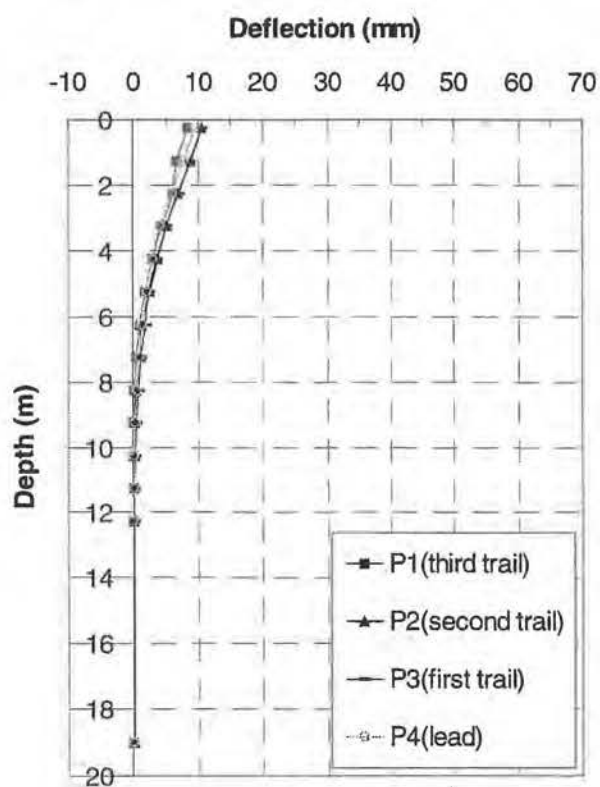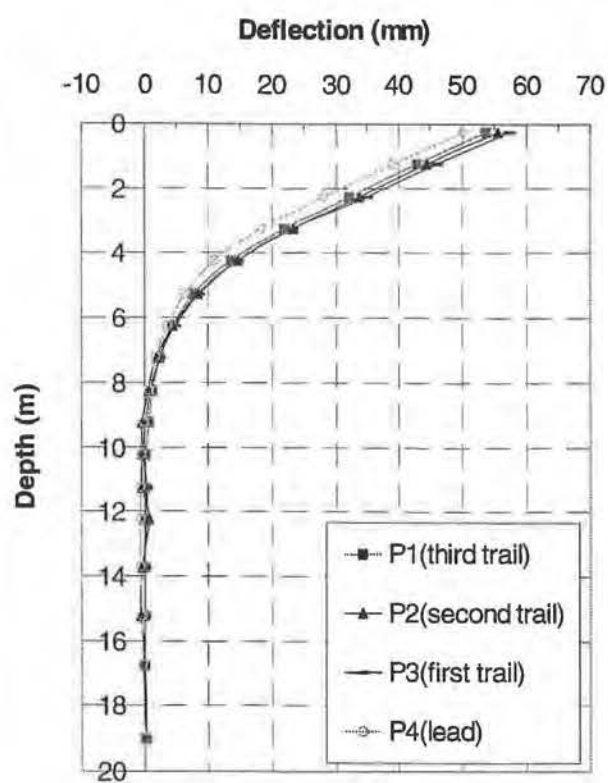
(a) Load = 300 T   (b) Load = 800 T

Figure A-21. Measured Deflected Shapes along Selected Piles in Driven Pile Group
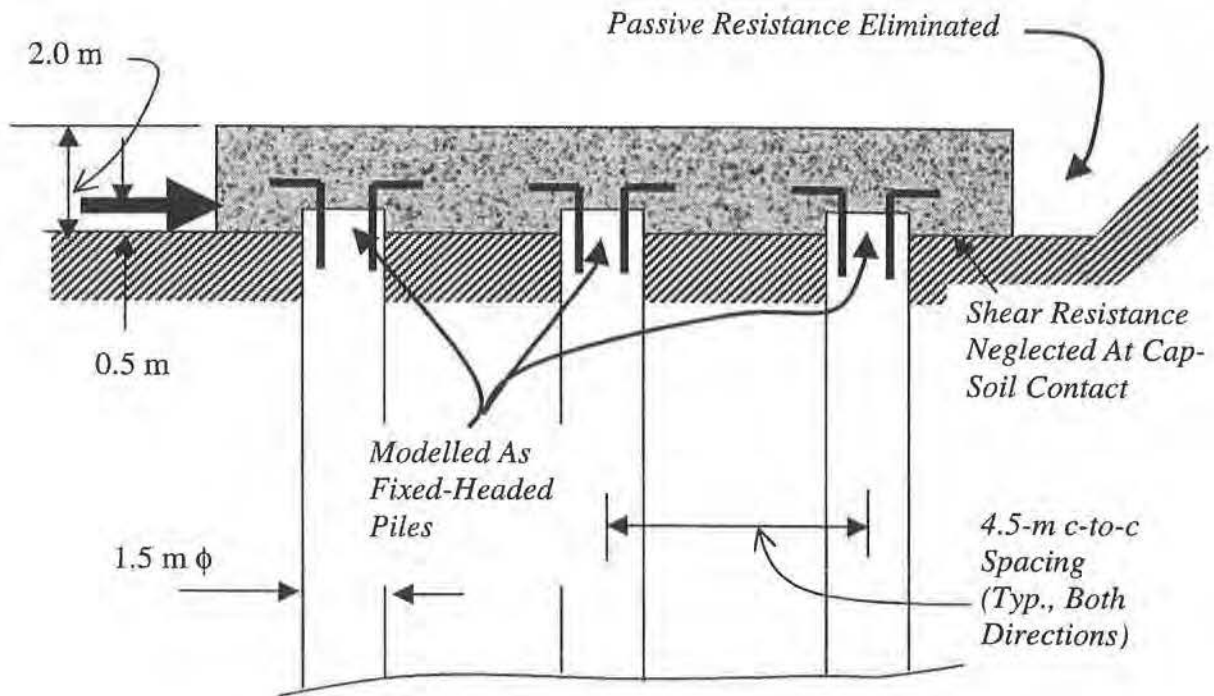
Figure A-22. FLPIER Modelling for Arrangement for Bored Pile Group
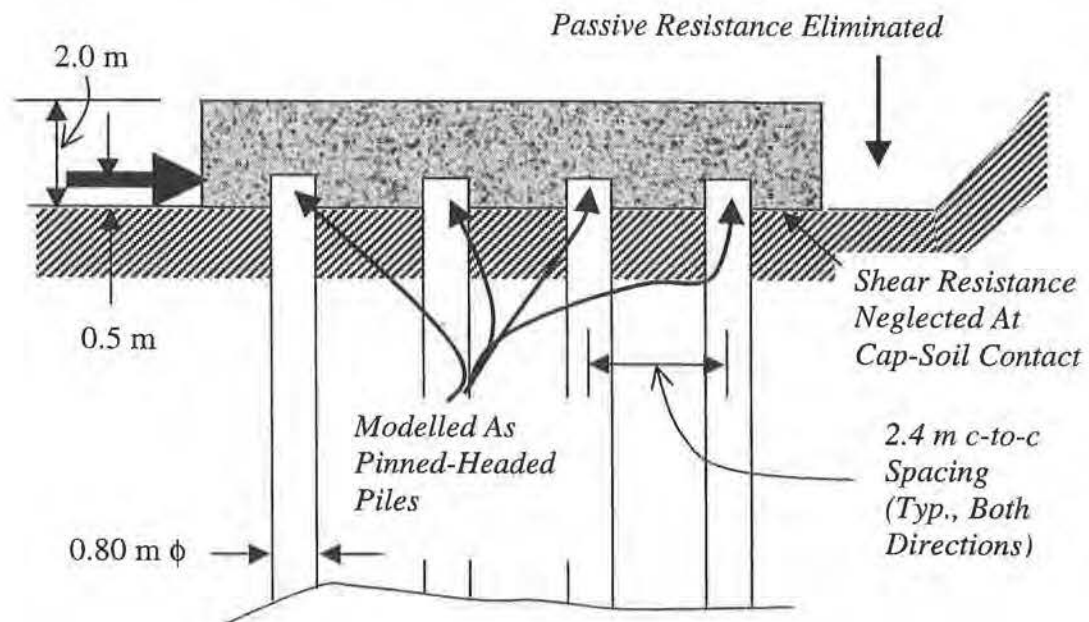
Figure A-23. FLPIER Modelling Arrangement for Driven Pile Group

p (F/L)

p-y curve for <u>single pile</u> at depth x

p (single pile)

p (group pile)

p-y curve for group pile at depth x and at common values of y —

$p_{group} = \rho \; psingle \; pile$

y (common to both curves)

y (L)
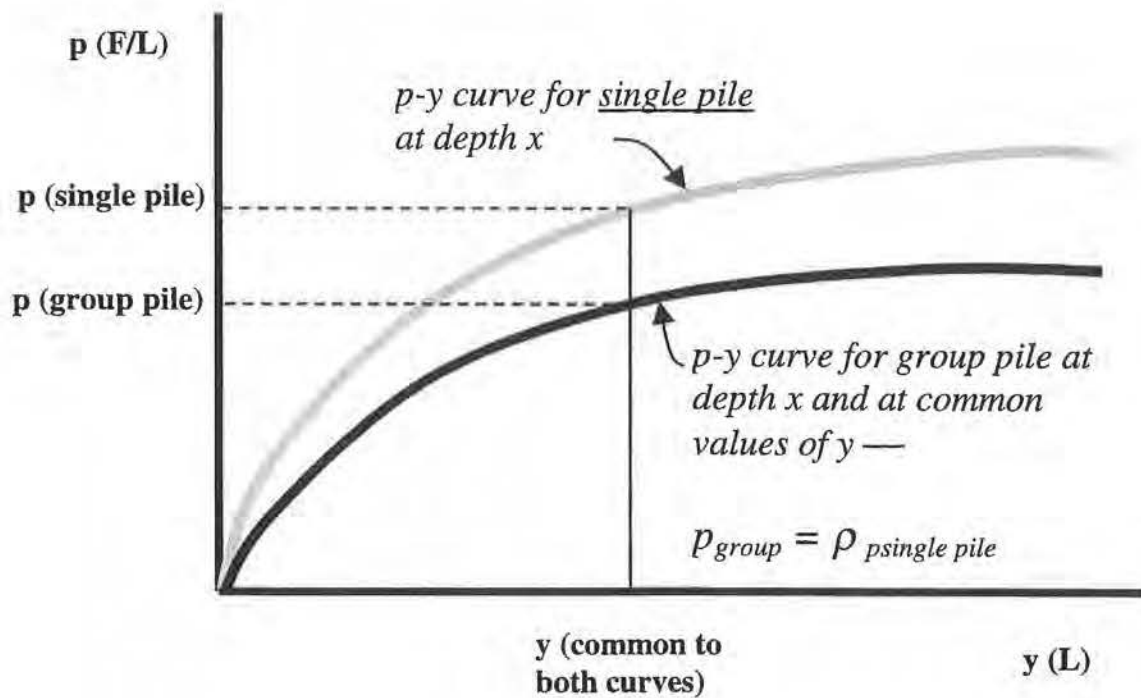
Figure A-24. Definition of the p-Multiplier (ρ) for Simulating Lateral Group Behavior
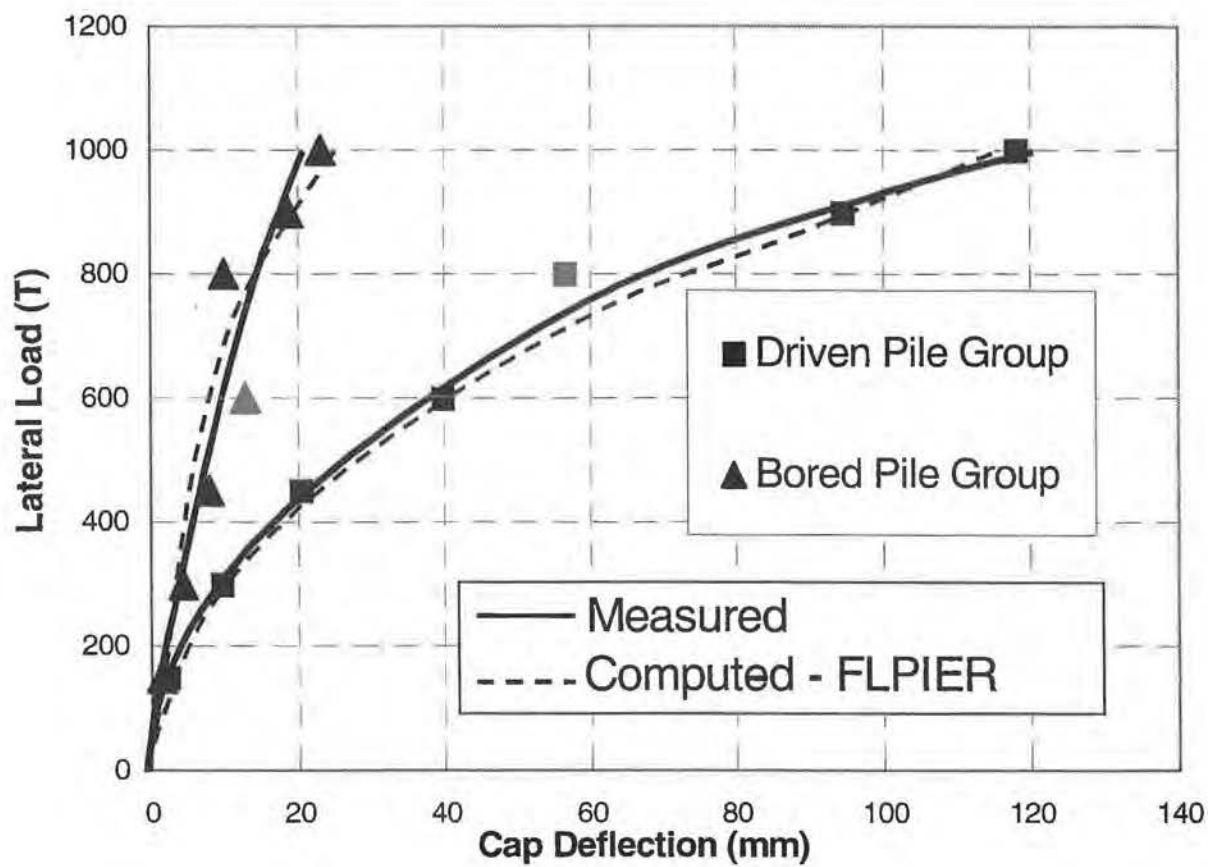
Figure A-25. Measured Lateral Load-Cap Deflection Relationships for Driven and Bored Pile Groups
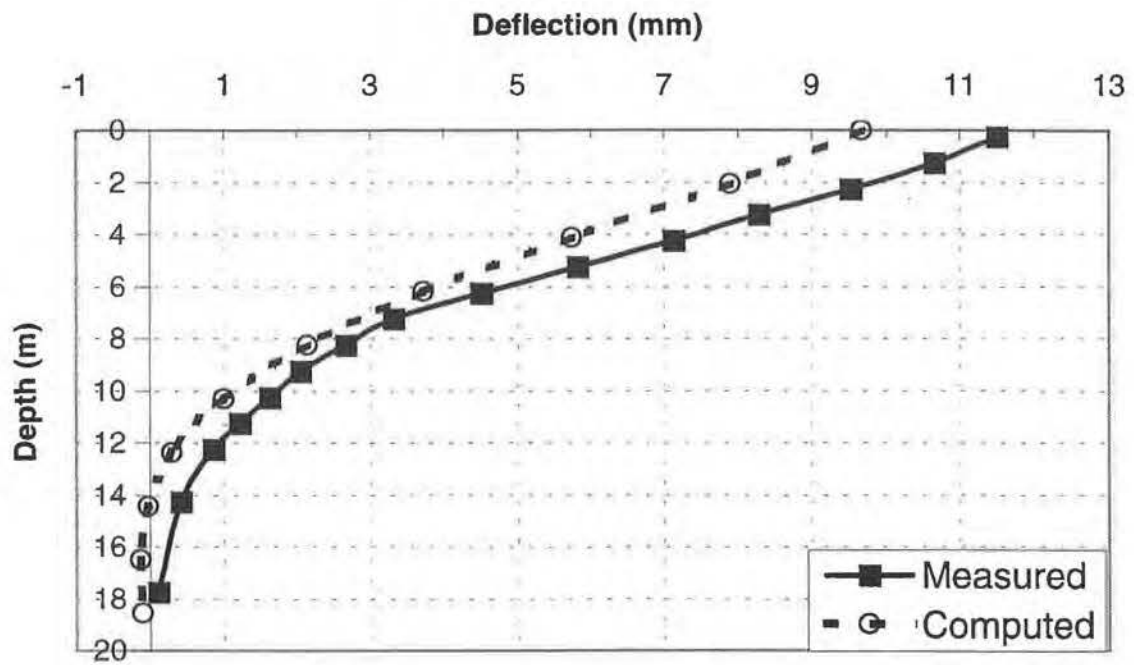
Figure A-26. Measured and Predicted Deformed Shape of Pile B3 on Lead Row of the Bored Pile Group — Load = 600 T

APPENDIX B

DYNAMIC RESPONSE OF PILES TO EARTHQUAKE LOADING — ANALYTICAL

INTRODUCTION

Catastrophic damage that has resulted from recent earthquakes has raised concerns about the current codes and approaches used for the design of structures and foundations. In the past, free-field accelerations, velocities and displacements have been used as input ground motions for the seismic design of structures without considering the kinematic interaction of the foundation or the site effects that have resulted from the soil stratigraphy and the introduction of piles. Depending on the pile or pile group configuration and soil profile, free-field response may underestimate or overestimate actual in-situ conditions that will result in radically changed foundation and structural behavior and therefore impact design criteria.

The behavior of pile foundations during an earthquake event is influenced by the interaction of the pile foundation with the surrounding soil medium. This interaction can be categorized into (a) kinematic interaction and (b) inertial interaction. The former characterizes the response of piles to the seismic loading through the soil, while the latter describes the pile-soil interaction due to the inertial loading from the superstructure applied at the pile head. The characteristics of the pile-soil interaction in these two types of loading are different. Therefore, the kinematic interaction and the inertial interaction are addressed separately.

KINEMATIC RESPONSE OF PILES

Recent destructive earthquakes have highlighted the need for increased research into the revamping of design codes and building regulations to prevent further catastrophic losses in

terms of human life and economic assets. The present study investigated the response of single piles to kinematic seismic loading using the three-dimensional finite element program ANSYS [1].

The objectives of this study were twofold:

1. Develop a finite element model that can accurately model the kinematic soil-structure interaction of piles, accounting for the nonlinear behavior of the soil, discontinuity conditions at the pile-soil interface, energy dissipation and wave propagation.

2. Use the developed model to evaluate the kinematic interaction effects on the pile response with respect to the input ground motion. The results of a number of studies on the kinematic interaction of pile groups reported in the literature are also included.

Assumptions and Restrictions

The problem to be addressed is shown in Figure B-1. As shown, the actual system consists of a pile foundation supporting a typical bridge pier. Current design codes use the free-field motion as the input ground motion at the foundation level. The analysis described herein attempted to evaluate the interaction of the pile-soil system and how it alters the free-field motion and modifies the ground motion at the foundation level.

The dynamic loading was applied to the rigid underlying bedrock (Figure B-1) as one-dimensional horizontal acceleration (X-direction in finite element model), and only horizontal response was ascertained. Vertical accelerations were ignored because the margins of safety against static vertical forces usually provides adequate resistance to dynamic forces induced by vertical accelerations. Wu and Finn [2], using a three-dimensional elastic model, found that

deformations in the vertical direction and normal to the direction of shaking are negligible compared to the deformations in the direction of horizontal shaking.

Although the finite element analysis used in this study includes important features such as soil nonlinearity and gapping at the pile-soil interface, it does not account for build-up of pore pressure due to cyclic loading. Thus, neither the potential for liquefaction nor the dilatational effect of clays and the compaction of loose sands in the vicinity of piles is accounted for, in the current analysis. Furthermore, the inertial interaction between the superstructure and the pile-foundation system is not considered here. The analysis is limited to the response of free-headed piles with no external forces from the superstructure ("D'Alembert forces") to understand better the kinematic interaction effects in seismic events.

3-D Finite Element Model

Model Formulation

Full three-dimensional geometric models were used to represent the pile-soil systems. Exploiting symmetry, only one half of the actual model was built, thus significantly reducing computing time and cost. Figure B-2 depicts the pile-soil system considered in the analysis, showing an isometric view of the half of the model used. Figures B-2 and B-3 show the finite element mesh (Mesh No. 3) used in the analysis.

The pile and soil were modelled using eight-noded block elements. Each node had three translational degrees of freedom, i.e. X, Y and Z coordinates, as shown in Figure B-4. A three-dimensional point-to-surface contact element was used at the pile-soil interface to allow for sliding and separation in tension, but ensured compatibility in compression. The contact element had five nodes with three degrees of freedom at each node, i.e., translations in the X, Y and Z

directions as shown in Figure B-4b. Transmitting boundaries were used to allow for wave propagation and to eliminate the "box effect" (i. e., the reflection of waves back into the model at the boundaries) during dynamic loading. The element used to model the transmitting boundary consisted of a spring and a dashpot arranged in parallel, as illustrated in Figure B-4c.

Soil Properties

The soil was modelled using two approaches: a homogeneous elastic medium and an elasto-plastic material using the Drucker-Prager failure criteria, to evaluate the effect of soil plasticity on the pile response. For cases involving plasticity, the angle of dilitancy was assumed to be equal to the angle of internal friction (associated flow rule). There was no strain hardening, and therefore no progressive yielding was considered. Since pore pressures were not considered in this analysis, effective stress parameters and drained conditions were assumed. The material damping ratio of the soil, β, was assumed to be 5% (i.e. D = 10%). This soil material damping ratio is compatible with the expected strain level under earthquake loading. The governing equations of the system are given by

$$[M]\{\ddot{u}\}+[C]\{\dot{u}\}+[K]\{u\}=\{F(t)\} \qquad (B-1)$$

where $\{\ddot{u}\}, \{\dot{u}\},\ and\ \{u\}$ are the acceleration, velocity and displacement vectors, respectively, and [M], [C] and [K] are the global mass, damping and stiffness matrices. The damping matrix, $[C]=\zeta[K]$, in which the damping coefficient, $\zeta=\dfrac{2\beta}{\omega_0}$, and ω_0 is the predominant frequency of the loading (rad/s). Material damping was assumed to be constant throughout the entire seismic event, although the damping ratio varies with the strain level.

B-4

Pile Properties

Cylindrical reinforced concrete piles with linear elastic properties were considered in this study. The piles were modeled using eight-noded brick elements. The cylindrical geometry was approximately modeled using wedge shaped elements (Figure B-2a). No damping was considered within the piles and relevant parameters are listed on Figure B-5.

Pile-Soil Interface

Modelling of the pile-soil interface is crucial because of its significant effect on the response of piles to lateral loading [3]. Two cases were considered in the analysis:

1. The pile and soil were perfectly bonded, in which case the perimeter nodes of the piles coincided with the soil nodes (elastic with no separation).

2. The pile and soil were connected by frictional interface elements that are described below.

The contact surface (pile) is said to be in contact with the target surface (soil) when the pile node penetrates the soil surface. A very small tolerance was assumed to prevent penetration and to achieve instant contact as pile nodes attempt to penetrate the soil nodes (or vice versa). Coulomb friction was employed between the pile and soil along the entire pile length as well as the pile tip (for floating piles). The coefficient of friction relating shear stress to the normal stress was chosen according to API recommendations [4] and was assumed to be 0.7. The contact surface coordinates and forces were fully updated to accommodate any large or small deflections that may occur. The penalty function method was used to represent contact with a normal contact stiffness (K_n). K_n allowed the interface element to deform elastically before slippage occurred and was chosen to be equal to the shear modulus of the soil. Convergence was achieved and

over-penetration was prevented using K_n= 6800 kN/m (numerically equal to the shear modulus of the soil).

Boundary Conditions

Boundary conditions varied depending on the type of loading. For static loading, the bottom of the mesh (representing the top of the bedrock layer) was always fixed in all directions. All symmetry faces were fixed against displacement normal to the symmetry plane, but were free to move on the surface of the plane. The nodes along the top surface of the mesh were free to move in all directions. The nodes along the sides of the model were free to move vertically but were constrained in the horizontal direction by a Kelvin element in order to represent a horizontally infinite soil medium during static and dynamic analyses. The constants were calculated using the solution due to Novak and Mitwally [5], given by

$$ k_r = \frac{G}{r_o} [S_1(a_0,\upsilon,\zeta) + iS_2(a_0,\upsilon,\zeta)] \qquad (B\text{-}2) $$

where k_r = total stiffness, G = soil shear modulus, r_0 = distance to finite element boundary, S_1 and S_2 = dimensionless parameters from closed form solutions, ν = Poisson's ratio, a_o = dimensionless frequency = $r_0\omega/V_s$, ω = circular frequency of loading and V_s = shear wave velocity of the soil. The real and imaginary parts of Eq. B-2 represent the stiffness and damping, respectively, i. e.

$$ K = \frac{GS_1}{r_0} \quad and \quad C = \frac{GS_2}{\omega r_0} \qquad (B\text{-}3) $$

To determine the stiffness and damping of the Kelvin elements, the constants given by Eq. B-3 were multiplied by the area of the element face (normal to the direction of loading) because they assume constant unit area of contact. For static loading, i. e., zero frequency, the damping term vanishes and the element reduces to a spring only.

For dynamic loading, ω was taken as the predominant frequency of the earthquake load and was determined from a discrete Fourier transform of the time history of the input motion. Figure B-6 shows the Fourier amplitude (c_n) versus frequency (ω_n) content for the strong motion record used in the study. It is evident that a narrow spectrum exists at a dominant frequency of approximately 2 Hz.

Time dependent displacements were applied to the stratum base to simulate seismic loading. All other boundary conditions remained unchanged and are graphically portrayed in Figure B-3.

Loading Conditions

Initial Loading

The state of stress in the pile-soil system in actual in-situ conditions was replicated as an initial loading condition prior to any additional dynamic or static external load. That is, geostatic stresses were modelled by applying a global gravitational acceleration, g, to replicate vertically increasing stress with depth. A linearly increasing pressure with depth was applied to the periphery of the soil block to replicate horizontal stresses as shown in Figure B-3b. A coefficient of lateral earth pressure, $K_o = 0.65$, typical of many geological conditions, was used. Due to the difference in density and stiffness for the pile and soil, the soil tended to settle more than the pile in the vertical direction, resulting in premature slippage at the pile-soil interface. To eliminate

this false representation of initial conditions, the difference between the relative displacement between the soil and the pile was accounted for by adding a corresponding body load to the pile. The resulting mesh represented in-situ conditions, especially for drilled shafts.

Static Loading

All static loads were applied as distributed loads along the perimeter of the pile head that was level with the ground surface. Only one-half of the total load was applied to the pile in the finite element analysis due to the symmetric geometry of a full circular pile.

Dynamic Loading

Strong motion records from the Loma Prieta Earthquake in California (M_L=7.1) in 1989 were used in the finite element study. The accelerogram and displacement data used were from the Yerba Buena Island rock outcrop station in the Santa Cruz Mountain [6]. The measured displacements were applied to the top of the rigid bedrock layer at 0.02 sec intervals. Considering that the maximum acceleration of the measured one-dimensional motion was 0.03g, the accelerations were multiplied by a factor of seven to simulate a PHA (peak horizontal acceleration) of approximately 0.2g for the bedrock input motion. It is important to note that the acceleration data were for bedrock motions and not free-field motions that can either increase or decrease in terms of PHA due to the site effects. Motions of 20 sec duration were modelled to include all of the important features of the earthquake. The predominant frequency was approximately 2 Hz, which is typical of destructive earthquakes [7].

Verification of the Finite Element Model

The verification process followed incremental steps to ensure that pile, soil, and boundary conditions were separately accounted for in order to minimize error accumulation. The size of the mesh was mainly dependent on the loading conditions (static or dynamic) and geometry of the piles. The mesh was refined near the pile to account for the severe stress gradients and plasticity encountered in the soil, with a gradual transition to a coarser mesh away from the pile in the horizontal X and Y directions. The vertical Z-direction subdivisions were kept constant to allow for an even distribution of vertically propagating SH-waves. The maximum element size, E_{max}, was less than one-fifth to one-eighth of the shortest wavelength (λ) to ensure accuracy [7], i. e.,

$$E_{max} < (1.5 - 1.8) \times \lambda \tag{B-4}$$

where $\lambda = V_s/f$, V_s is the soil shear wave velocity and f is the excitation frequency in Hz. The minimum V_s was 60 m/s, and the dynamic loading had a cut-off frequency equal to 20Hz. Thus, a maximum element length of 0.5m was adopted. The proposed element division was verified using results from a sensitivity study focussing on vertical pile shaft discretization by El-Sharnouby and Novak [8], who found that using 12 to 20 elements gave accurate results with a minimum of computational effort. Thus, that range was adopted for this study.

The pile mesh was first verified by considering the pile as a fixed cantilever in air (no soil). Lateral deflections resulting from a static load for three different pile mesh sizes were compared to one-dimensional beam flexure theory, and the maximum difference was 8%. The results were very close, the small differences, however, could be explained by the fact that beam

theory is not exact (ignores shear deformations) and the finite model was not a perfect cylinder. Since the maximum number of elements (6000) and nodes (11000) available was limited, 180 elements were used to model the pile (accuracy within 8% of theoretical solutions). When soil and boundary elements were added, the total number of elements was close to the limit.

The soil was added to the model assuming a homogeneous soil stratum (Figure B-5). The elastic responses of socketed and floating single piles in the homogeneous soil stratum were compared to the results from two different analyses. (a) the results from Poulos and Davis [9] using Mindlin's equations and enforcing pile-soil compatibility; and (b) the results presented by Trochanis et al. [3] using a 3-D finite element analysis, although their pile had a square cross-section but the same flexural rigidity. Three different soil meshes were built with increasing refinement to determine an acceptable level of accuracy while maintaining a computationally efficient model. Mesh No. 1 consisted of 1080 elements, Mesh No. 2 consisted of 2640 elements, and Mesh No. 3 had 3280 elements. Other meshes with a total number of elements equal to 6000 were also tested but were not used due to unreasonable computer processing time.

The results for the linear elastic response under lateral loading at the pile head are shown in Fig. B-7a. The mesh that yielded the closest match (Mesh No. 3, depicted in Figures B-2 and B-3) was used in the analysis. The deflections obtained in this study were slightly greater than those from Poulos and Davis [9]. However, those authors pointed out that their solution might underestimate the response of long piles in soft soils. Figures B-7b and B-7c show pile head deflections considering separation at the pile-soil interface and soil plasticity, respectively. It can be seen that good agreement exists with the results from Trochanis et al. [3]. The differences in the plastic soil case may be attributed to the use of a different model for soil plasticity (modified Drucker-Prager model). Figures B-8a and B-8b show the elastic soil surface

displacements away from the pile compared to results from elastic theory by Poulos and Davis [9] and other finite element analyses (FEA) [3]. It can be seen from Figures B-8a and B-8b that the results obtained using Mesh No. 3 agree well with both solutions, especially close to the pile. The pressure distribution in the soil agreed equally well.

The final step in the verification process was accomplished by solving the ground response to an earthquake signal using the finite element model and comparing the elastic free-field response to that obtained using the program SHAKE91 [10]. Considering that SHAKE91 is a 1-D analysis, constraints were applied to the finite model to allow only displacements in the direction of shaking (one degree of freedom per node) to replicate 1-D results. The results from the finite element analysis and SHAKE91 are plotted in Figure B-9 for elastic response using the same parameters. A constant shear modulus and material damping ratio were used in both the SHAKE91 and the FEA models. It can be seen from Figure B-9 that the agreement is quite good along the entire time period considered. The maximum free-field accelerations for the FEA and SHAKE91 were both amplified to approximately 0.6g from 0.2g (bedrock input motion) and are compared with bedrock accelerations in Figure B-10. The same FEA model was modified to allow for three-dimensional response, and the free-field response is plotted against the one-dimensional results in Figure B-11. The maximum free-field acceleration obtained from 3-D analysis was only 0.35g (Figure B-11). The accelerations calculated from the 3-D analysis are closer to those observed during actual seismic events. Hence, it was concluded that the 3-D analysis resulted in realistic acceleration magnitudes. Therefore, all further models discussed herein assumed full 3-D capability.

Numerical Study for Kinematic Interaction

The kinematic effects of piles in a homogeneous soil medium were evaluated by comparing acceleration time histories and Fourier spectra of the pile head and the free field. The same dynamic loading was applied in all cases (i. e., Loma Prieta data) to the underlying bedrock for a homogeneous soil profile. Results from seven different pile-soil configurations were obtained and are referred to in Figures B-12 through B-18. The following notation is used throughout the graphs and literature to identify each test case (see Figure B-5 for soil and pile parameters):

- **EFH** – refers to the free-field response using linear isotropic visco-elastic constitutive relations (Elastic, Free-field, Homogeneous).

- **PFH** – refers to the free-field response using a perfect elastic-plastic soil model, Drucker-Prager criteria (Plastic, Free-field, Homogeneous).

- **ESNFH** – refers to the floating single pile head response using a linear isotropic visco-elastic soil with no separation at the pile-soil interface, $L/D = 15$, $E_p/E_s = 1000$ (Elastic Single pile, No separation, Floating, Homogeneous)

- **ESNSH** - refers to the socketed single pile head response using a linear isotropic visco-elastic soil with no separation at the pile-soil interface, $L/D = 20$, $E_p/E_s = 1000$ (Elastic, Single pile, No separation, Socketed, Homogeneous).

- **ESSFH** – same as ESNFH case, but allows for separation at the pile-soil interface (Elastic, Single pile, Separation, Floating, Homogeneous).

- **PSSFH** – refers to the floating single pile head response using a perfect plastic elastic soil model with separation allowed at the pile-soil interface, $L/D = 15$, $E_p/E_s = 1000$, $c' = 34$ kPa, $\psi = 16.5°$ (Plastic, Single pile, Separation, Floating, Homogeneous).

- **PSSSH** – refers to the socketed single pile head response using a perfect plastic elastic soil model with separation allowed at the pile-soil interface, $L/D = 20$, $E_p/E_s = 1000$, $c' = 34$ kPa, $\psi = 16.5°$ (Plastic, Single pile, Separation, Socketed, Homogeneous).

Results

Figure B-12a compares the free-field response for the elastic and plastic soil cases. The difference between the two cases is not evident over the 20 second duration, but a more detailed evaluation is presented in Figure B-15 for the 2 through 10 second interval. The acceleration response is slightly amplified using a plastic soil model. This can be attributed to the limiting ultimate effective stress and limiting shear strength. Figure B-12b compares the Fourier spectra for elastic and plastic soil profiles against the input bedrock spectrum using a cut-off frequency of 20 Hz. It is evident from the figure (Figure B-12b) that there is an amplification of the Fourier amplitudes for the free-field response compared to the bedrock. There is a notable increase in amplitude for the plastic soil model over the elastic soil model, suggesting that the reduction in soil stiffness reduces the natural frequency of the homogeneous layer. The increase in acceleration and amplitude may be attributed to the fact that the first natural frequency of the elastic homogenous layer is slightly greater than 2 Hz, whereas the natural frequency of the plastic soil layer is slightly decreased and became closer to the predominant frequency at the free-field (approximately 1.5 Hz). For higher frequencies (Figure B-11b), the small amplitude peaks seen at the bedrock level diminish as the seismic waves propagate throughout the soil until they reach the free-field. Both the elastic and plastic free-field amplitudes diminish at frequencies higher than 10 Hz, above which little response is induced in most structures.

Similar results for the floating and socketed pile head response are plotted in Figure B-13 and B-14. Figures B-13a and B-13b represent the corresponding acceleration and Fourier

spectrum for ESNFH compared to EFH. Both diagrams are almost identical, except the Fourier amplitudes are slightly greater for the floating pile (especially for a frequency above 5 Hz). Figure B-14 shows the response of the ESNSH socketed pile case. Again, the overall acceleration of the pile head is similar to that of the elastic free-field. The Fourier amplitudes of the socketed pile (no separation) show both a decrease and an increase in magnitude over the elastic free-field depending on the frequency range. At the predominant frequency amplitude (2 Hz), ESNSH seems to slightly decrease compared to EFH, and at frequencies above and below the predominant frequency the amplitudes are increased. The increased stiffness of the system due to the socketed pile may be responsible for the increased amplitude at higher frequency ranges compared to that of the free-field.

Figure B-16 introduces the effects of separation between the pile and soil for the floating pile case. Only the 2 through 10 second time interval is shown to provide a more detailed analysis. The overall response is very similar for both cases shown in Figure B-16. The floating pile with gapping seems to eliminate small fluctuations of acceleration seen when no gapping was allowed.

Figure B-17 introduces the effects of the soil plasticity in addition to separation for the floating pile. PSSFH is compared with the elastic model (ESSFH), and the results are very similar. The random scatter shown by introducing plasticity may be attributed to the solution procedure used in the finite element program. For convergence reasons, smaller time steps had to be used for the plastic soil model, which led to numerical instabilities. Figure B-18 compares the floating and socketed pile head response including both separation and soil nonlinearity. The floating pile showed slightly higher peaks over the socketed pile, but the response remained almost identical.

Kinematic Interaction in Pile Groups

Modelling the kinematic response of pile groups accounting rigorously for all the factors that influence the response is a formidable task. Therefore, most of the investigations on the seismic soil-pile interactions use linear analyses or simple idealized systems.

Analyses of the kinematic response of a single pile and of pile groups have been reported by Takemiya and Yamada [11], Flores-Berrones and Whitman [12], Gazetas [13] and Tazoh et al. [14]. However, these studies had very limited parametric results. Ahmad and Mamoon [15] and Fan et al. [16] attempted to fill this gap by providing comprehensive parametric studies for the kinematic response of piles. The results of these two studies are summarized here.

Ahmad and Mamoon [15] examined the response of single piles under vertically and obliquely incident SH, SV and P harmonic waves using a hybrid boundary element formulation. The piles were modelled using compressible beam-column elements and the soil was modelled as a hysteretic visco-elastic halfspace. They found that the pile-soil stiffness ratio, angle of incidence and the excitation frequency have significant influence on the seismic responses of piles. The results from the limited cases considered in their study suggested that in the low frequency range piles essentially follow the ground motion. This conclusion is similar to what was observed from the analyses presented earlier in this Appendix. They also found that at higher frequencies piles seem to remain relatively still, while the free-field soil mass moves considerably. This filtering effect was found to be severe for a vertically incident wave, gradually diminishing for a more obliquely incident one. Furthermore, they found that flexible piles undergo significant bending under seismic excitation, whereas rigid piles tend to show almost low, uniform rigid body motion. Obliquely incident waves produce higher displacement

than a vertically incident one throughout the pile depth. In the low frequency range, vertically incident waves produce higher rotations of the pile head; but in the higher frequency range the opposite trend was observed.

Fan et al. [16] performed an extensive parametric study using the boundary element solution proposed by Kaynia and Kausel [17] to develop dimensionless graphs for pile head deflections versus the free-field response for various soil profiles subjected to vertically propagating harmonic waves. Fan et al. [16] also used the approach developed by Makris and Gazetas [18], in which free-field accelerations are applied to a one-dimensional Beam-on-Dynamic-Winkler-Foundation model with frequency-dependent springs and dashpots to analyze the response of floating single piles and pile groups. Both approaches are essentially linear (or equivalent linear) analyses.

Makris and Gazetas [18] studied the kinematic response of single piles, one-row pile groups and as well as square groups of piles. They considered soil profiles with constant soil modulus, linearly increasing soil modulus with depth, and two distinct constant values above and below a depth $z = L/2$. Each pile-foundation-soil system was excited by vertically propagating harmonic shear free-field waves.

The results of the analyses were portrayed in the form of kinematic displacement factors (plotted versus dimensionless frequency, a_0) defined as the response of the pile cap normalized by the free-field motion. The investigated parameters were: the ratio of the effective pile modulus to the soil modulus, the piles spacing-to-diameter ratio and the pile's slenderness ratio. Inspection of the results revealed the following trends:

1. The general shape of the kinematic displacement factor, I_u, consists of three fairly distinct regions in the frequency range of greatest interest ($a_0 < 0.5$):

- A low-frequency region $(0 < a_0 < 0.1 - 0.3)$ in which $I_u \approx 1$, meaning the piles follow closely the deformations of the ground.

- An intermediate-frequency region $(0.1 - 0.2 < a_0 < 0.3 - 0.4)$ characterized by I_u declining rapidly with frequency, which showed increasing incompatibility between the movement of a pile and the surrounding soil.

- A relatively high-frequency region $a_0 > 0.3-0.4$ in which I_u fluctuates around an essentially constant value of about $0.2 - 0.4$.

2. For the low and intermediate frequency regions, pile-soil-pile interaction effects on kinematic loading are not significant, but they are significant for pile head loading (inertial interaction).

Summary and Conclusions — Kinematic Action

A 3-D finite element analysis was performed to investigate site effects and pile kinematic interaction effects from seismic loading for a single pile. The analysis considered floating and socketed piles, including nonlinear soil properties, slippage and gapping at the pile-soil interface, and dissipation of energy through damping. Based on the results from the kinematic interaction study, it was concluded that the pile head response (floating and socketed) closely resembled the free-field response for the low predominant frequency seismic loading. Fan et al. [16] reached a

similar conclusion from their parametric study using a boundary element solution.

The following specific conclusions can be drawn:

- The effect of allowing a three-dimensional behavior as opposed to a one-dimensional behavior, with seismic loading applied in one dimension, was to decrease the acceleration amplitudes by a factor of 1.6 for the for the soil profiles considered.

- The effect of soil plasticity was to increase the Fourier amplitudes at the predominant frequency but to slightly decrease the maximum acceleration amplitudes.

- The elastic kinematic interaction of single piles (both floating and socketed) has slightly amplified the bedrock motion when compared to the free-field response and slightly decreased the Fourier amplitudes of all frequencies considered (0 through 20 Hz).

- Overall, the kinematic interaction response including soil plasticity, slippage and gapping at the pile soil interface, and damping is equivalent to the free-field response. However, the conclusions are limited to the pile and soil parameters, and to the earthquake loading used in the analysis.

- For the frequency range of interest, pile-soil-pile interaction effects on kinematic loading are not significant but are significant for pile head loading (inertial interaction).

INERTIAL LOADING AND DYNAMIC p-y CURVES

Introduction

Most building and bridge codes use factored static loads to account for the dynamic effects of pile foundations. Although very low frequency vibrations may be accurately modelled using factored loads, the introduction of nonlinearity, damping, and pile-soil interaction during

transient loading may significantly alter the response. The typical frequency range of interest for earthquake loading is 0 to 10 Hz. Therefore, the emphasis in the current study is on that range.

Novak et al. [19] developed a frequency-dependent pile-soil interaction model, however, it assumes strictly linear or equivalent linear soil properties. Gazetas and Dobry [20] introduced a simplified linear method to predict fixed–head pile response accounting for both material and radiation damping and using available static stiffness (derived from finite element or any other accepted method). This method is not suitable for the seismic response analysis because of the linearity assumptions. In general, there is much controversy over advanced linear solutions (frequency domain) as they do not account for permanent deformation or gapping at the pile-soil interface.

Nogami et al. [21] developed a time domain analysis method for single piles and pile groups by integrating plane strain solutions with a nonlinear zone around each pile using p-y curves. El Naggar and Novak [22, 23] also developed a computationally efficient model for evaluating the lateral response of piles and pile groups based on the Winkler hypothesis accounting for nonlinearity using a hyperbolic stress-strain relationship, and slippage and gapping at the pile-soil interface. The model also accounts for the propagation of waves away from the pile and energy dissipation through both material and geometric damping.

The p-y curve (unit load transfer curve) approach is a widely accepted method for predicting pile response under static loads because of its simplicity and practical accuracy. In the present study, the model proposed by El Naggar and Novak [23] was modified to utilize existing or developed cyclic or static p-y curves to represent the nonlinear behavior of the soil adjacent to the pile. The model uses unit load transfer curves in the time domain to model nonlinearity, and incorporates both material and radiation damping to generate dynamic p-y curves.

Model Description

Pile Model

The pile is assumed to be vertical and flexible with circular cross-section. Non-cylindrical piles are represented by cylindrical piles with equivalent radius to accommodate any pier/pile configurations. The pile and the surrounding soil are subdivided into n segments, with pile nodes corresponding to soil nodes at the same elevation. The standard bending stiffness matrix of beam elements models the structural stiffness matrix for each pile element. The pile global stiffness matrix is then assembled from the element stiffness matrices and is condensed to give horizontal translations at each layer and the rotational degree of freedom at the pile head.

Soil Model: Hyperbolic Stress-Strain Relationship

The soil is divided into n layers with different soil properties assigned to each layer according to the soil profile considered. Within each layer, the soil medium is divided into two annular regions as shown in Figure B-19. The first region is an inner zone adjacent to the pile and accounts for the soil nonlinearity. The second region is the outer zone that allows for wave propagation away from the pile and provides for the radiation damping in the soil medium. The soil reactions and the pile-soil interface conditions are modeled separately on both sides of the pile to account for slippage, gapping and state of stress as the load direction changes.

Inner field element. The inner field is modeled with a nonlinear spring to represent the stiffness and a dashpot to simulate material (hysteretic) damping. The stiffness is calculated assuming plane strain conditions; the inner field is a homogeneous isotropic visco-elastic, massless medium; the pile is rigid and circular; there is no separation at the soil-pile interface;

B-20

and displacements are small. Novak and Sheta [24] obtained the stiffness under these conditions as:

$$k_{NL} = \frac{8\pi G_m (1-v)(3-4v)\left[(r_o/r_1)^2 + 1\right]}{(r_o/r_1)^2 + (3-4v)^2 \left[(r_o/r_1)^2 + 1\right]ln(r_1/r_0) - 1} \qquad (B\text{-}5)$$

where r_0 is the pile radius, r_1 is the outer radius of the inner zone, and v is the Poisson's ratio of the soil stratum. The ratio r_1/r_0 depends on the extent of nonlinearity, which depends on the level of loading, and on the pile's size. A parametric study showed that r_1/r_0 of 1.1 to 2 yielded good agreement between the stiffness of the composite medium (inner zone and outer zone) and the stiffness of a homogeneous medium (no inner zone) under small strain (linear) conditions. G_m is the modified shear modulus of the soil and is approximated, according to the strain level, by a hyperbolic law as

$$G_m = G_{max}\left(\frac{1-\eta}{1+\eta}\right) \qquad (B\text{-}6)$$

G_{max} is the maximum shear modulus (small strain modulus) of the soil according to laboratory or field tests. In the absence of actual measurements, maximum shear modulus for any soil layer can be calculated in this model by using the equation of Hardin and Black [25]:

$$G_{max} = \frac{3230(2.97-e)^2}{1+e}\sigma_o^{0.5} \qquad kN/m^2 \qquad (B\text{-}7)$$

where e = void ratio and σ_o (kN/m^2) = the mean principal effective stress in the soil layer.

The parameter $\eta = P/P_u$ is the ratio of the horizontal soil reaction in the soil spring, P, to the ultimate resistance of the soil element, P_u. The ultimate resistance of the soil element is

calculated using standard relations given by the American Petroleum Institute [4]. For clay, the ultimate resistance is given as a force per unit length of pile by

$$P_u = 3c_u d + \gamma x d + J c_u x \qquad \text{or} \qquad (B-8)$$

$$P_u = 9c_u d \qquad (B-9)$$

where P_u is the minimum of the resistances calculated by Eqs.B-8 and B-9, c_u is the undrained shear strength, d is the diameter of the pile, γ is the effective unit weight of the soil, and J is an empirical coefficient dependent on the shear strength. A value of J = 0.5 was used for soft clays [26] and J = 1.5 for stiff clays [27].

The corresponding criteria for the ultimate lateral resistance of sands at shallow depths P_{u1} or at large depths P_{u2} are [4]:

$$P_{u1} = A\left\{\gamma X\left[\frac{K_o X \tan\phi \sin\beta}{\tan(\beta-\phi)\cos\alpha} + \frac{\tan\beta}{\tan(\beta-\phi)}(d + X \tan\beta \tan\alpha)\right]\right\} \\ + A\gamma X\{K_o X \tan\beta(\tan\phi \sin\beta - \tan\alpha) - K_a d\} \qquad (B-10)$$

$$P_{u2} = A\gamma Xd\left[K_a\left(\tan^8\beta - 1\right) + K_o \tan\phi \tan^4\beta\right] \qquad (B-11)$$

In the these equations, A is an empirical adjustment factor dependent on the depth from the soil surface, K_o is the earth pressure coefficient at rest, ϕ is the effective friction angle of the sand, β = $\phi/2 + 45°$, $\alpha = \phi/2$, and K_a is the Rankine minimum active earth pressure coefficient defined as $K_a = \tan^2(45°-\phi/2)$.

In the derivation of Eq. B-5, the inner field was assumed to be massless [24]. Therefore, the mass of the inner field is lumped equally at two nodes on each side of the pile: node 1 adjacent to the pile and node 2 adjacent to the outer field, as shown in Fig. B-19.

Far field element. The outer (far) field is modelled with a linear spring in parallel with a dashpot to represent the linear stiffness and damping (mainly radiation damping). The outer zone allows for the propagation of waves to infinity. The complex stiffness, K, of a unit length of a cylinder embedded in a linear visco-elastic soil medium given by Novak et al [19]:

$$K = G_{max}[S_{u1}(a_o, v, D) + iS_{u2}(a_o, v, D)]$$ (B-12)

where $a_o = \omega r_1/V_s$ is the dimensionless frequency, ω = the frequency of loading, V_s = shear wave velocity of the soil layer, and D = the material damping constant of the soil layer. Figure B-20 shows the general variations of S_{u1} and S_{u2} with Poisson's ratio and material damping. Rewriting Eq. B-12, the complex stiffness, K, can be represented by a spring coefficient, k_L, and a damping coefficient, c_L, as:

$$K = k_L + ia_o c_L$$ (B-13)

It can be noted from Figure B-20 that for the dimensionless frequency range between 0.05 and 1.5, S_{u1} maintains a constant value and S_{u2} increases linearly with a_o. The predominant frequency of destructive earthquake loading falls within this range. Therefore, for the purpose of a time domain analysis, the spring and dashpot constants, S_{u1} and S_{u2}, respectively, can be considered frequency independent and to depend only on Poisson's ratio. They are given as

$$k_L = G_{max}S_{u1}(v)$$ and (B-14)

$$c_L = \frac{2G_{max}r_1}{V_s}S_{u2}(a_o = 0.5, v)$$ (B-15)

Soil-Pile Interface

The soil-pile interface is modeled separately on each side of the pile, thus allowing gapping and slippage to occur on each side independently. The soil and pile nodes in each layer

B-23

are connected using a no-tension spring. That is, the pile and soil will remain connected and will have equal displacement for compressive stresses. The spring is disconnected if tensile stress is detected in the soil spring to allow a gap to develop. This separation or gapping results in permanent displacement of the soil node that is dependent on the magnitude of the load. The development of such gaps is often observed in experiments, during offshore loading and after earthquake excitation in clays. These gaps eventually fill in again over time until the next episode of lateral dynamic loading. The pile-soil interface for sands does not allow for gap formation, but instead the sand caves in resulting in the virtual back-filling of sand particles around the pile during repeated dynamic loading. When the pile is unloaded, the sand on the tension side of the pile follows the pile with zero stiffness instead of remaining permanently displaced as in the clay model. In the unloading phase, the stiffness of the inner field spring is assumed to be linear in both the clay and sand models.

Group Effect

Since each pile in a group is affected not only by its own load, but also by the load and deflection of other piles in the group, the response of a pile group is greatly affected by the interaction between piles. For piles subjected to earthquake loading, this effect is important when considering the inertial loading, as has been pointed out by Fan et al. [16]. For this reason, the group effect was also investigated in this study. As large displacements, pile-soil separation and soil nonlinearity are expected to occur during earthquake events, the model developed by El Naggar and Novak [23], which is capable of these factors was used in this study.

Soil Model: p-y *Curve Approach*

The soil reaction to transient loading consists of stiffness and damping. The stiffness is established using the p-y curve approach, and the damping is established from analytical solutions that account for wave propagation. A similar approach was suggested by Nogami et al. [21] using p-y curves.

Based on physical tests, *p-y* curves can be used to relate pile deflections to the corresponding soil reaction at any depth (element) below the ground surface. The *p-y* curve represents the total soil reaction to the pile motion (i.e. the inner and outer zones' reactions combined). The total stiffness, k_{py}, derived from the *p-y* curve is equivalent to the true stiffness (real part of the complex stiffness) of the soil medium. Thus, referring to the hyperbolic law model, the combined inner zone stiffness (k_{NL}) and outer zone stiffness (k_L) can be replaced by a unified equivalent stiffness zone (k_{py}) as shown in Figure B-21a. Hence, to ensure that the true stiffness is the same for the two soil models, the flexibility of the two models is equated, i.e.,

$$\frac{1}{k_{py}} = \frac{1}{k_L} + \frac{1}{k_{NL}} \tag{B-16}$$

The stiffness of the nonlinear strength is then calculated as

$$k_{NL} = \frac{(k_{py})(k_L)}{(k_L - k_{py})} \tag{B-17}$$

The constant of the linear elastic spring, k_L, is established from the plane strain solution (i.e. Eq. B-14). The static soil stiffness, k_{py} represents the relationship between the static soil reaction, p, and the pile deflection, y, for a given *p-y* curve at a specific load level. The *p-y* curves are established using empirical equations [26, 28, 29] or curve fit to measured data using an accepted method such as the modified Ramberg-Osgood model [30]. In the present study, internally

generated static p-y curves are established based on commonly used empirical correlations for a range of soil types.

Damping

The damping (imaginary part of the complex stiffness) is incorporated into both the p-y approach and hyperbolic model to allow for energy dissipation throughout the soil. The nonlinearity in the vicinity of the pile, however, drastically reduces the geometric damping in the inner field. Therefore, both material and geometric (radiation) damping are modelled in the outer field. A dashpot is connected in parallel to the far-field spring, and its constant is derived from Eq. B-15. If the material damping in the inner zone is to be considered, a parallel dashpot with a constant c_{NL} to be suitably chosen may be added as shown in Figure B-21b. The addition of the damping resistance to static resistance represented by the static unit load transfer (the p-y curve) tends to increase the total resistance as shown in Figure B-22.

Static p-y curve generation for clay

The general procedure for computing p-y curves in clays both above and below the groundwater table and corresponding parameters are recommended by Matlock [26] and Bhushan et al. [27], respectively. The p-y relationship was based on the following equation:

$$\frac{p}{P_u} = 0.5 \left(\frac{y}{y_{50}} \right)^n \tag{B-18}$$

where p = soil resistance, y = deflection corresponding to p, P_u = ultimate soil resistance from Eqs. B-8 and B-9, n = a constant relating soil resistance to pier/pile deflection, and y_{50} = corrected deflection at one-half the ultimate soil reaction determined from laboratory tests. The tangent stiffness constant, k_{py}, of any soil element at time step t+Δt is given by the slope of the

tangent to the *p-y* curve at the specific load level as shown in Figure B-22. This slope is established from the soil deflections at time steps t and t-Δt and the corresponding soil reactions calculated from Eq. B-18, i.e.,

$$k_{py(t+\Delta t)} = \frac{p_t - p_{t-\Delta t}}{y_t - y_{t-\Delta t}}$$

(B-19)

Therefore, Eq. B-14 and Eq. B-19 can be substituted into Eq. B-17 to obtain the nonlinear stiffness representing the inner field element in the analysis. Thus, the linear and nonlinear qualities of the unit load transfer curves have been logically incorporated into the outer and inner zones, respectively.

Static p-y curve generation for sand

Several methods have been used to experimentally obtain *p-y* curves for sandy soils. Abendroth and Greimann [31] performed eleven scaled pile tests and used a modified Ramberg-Osgood model to approximate the nonlinear soil resistance and displacement behavior for loose and dense sand. The most commonly used criteria for development of p-y curves for sand were proposed by Reese et al. [32] but tend to give very conservative results. Bhushan et al. [33] and Bhushan and Askari [34] used a different procedure based on full-scale load test results to obtain nonlinear *p-y* curves for saturated and unsaturated sand. A step-by-step procedure for developing *p-y* curves in sands, based on Bhushan and Haley [35] and Bhushan et al. [33], was used to estimate the static unit load transfer curves for different sands below and above the water table. The procedure used to generate *p-y* curves for sand differs from that suggested for clays. The secant modulus approach is used to approximate soil reactions at specified lateral displacements. The soil resistance in the static p-y curve model can be calculated using the following equation:

B-27

$$p = (k)(x)(y)(F1)(F2) \qquad \qquad \text{(B-20)}$$

where k is a constant that depends on the lateral deflection y (i.e. k decreases as y increases) and relates the secant modulus of soil for a given value of y to depth ($E_s = kx$), and x is the depth at which the p-y curve is being generated. *F1* and *F2* are density and groundwater (saturated or unsaturated) factors, respectively, and can be determined from Meyer and Reese [36]. The main factors affecting k are the relative density of the sand (loose or dense) and the level of lateral displacement. The secant modulus decreases with increasing displacement and thus the nonlinearity of the sand can be modeled accurately. This analysis assumes linear increase of the soil modulus with depth (but varies nonlinearly with displacement at each depth), which is typical for many sands.

Equation B-20 was used to establish the p-y curve at a given depth. The tangent stiffness k_{py} (needed in the time domain analysis), which represents the tangent to the p-y curve at the specific load level, was then calculated using Eq. B-19 based on calculated soil reactions from the corresponding pile displacements for two consecutive time steps (using Eq. B-20).

Degradation of Soil Stiffness

Transient loading, especially cyclic loading, may result in a buildup of pore water pressures and/or a change of the soil structure that causes the shear strain amplitudes of the soil to increase with increasing number of cycles [37]. Idriss et al. [37] reported that the shear stress amplitude decreased with increasing number of cycles for harmonically loaded clay and saturated sand specimens under strain-controlled undrained conditions. These studies suggest that repeated cyclic loading results in the degradation of the soil stiffness. For cohesive soils, the

value of the shear modulus after N cycles, G_N, can be related to its value in the first cycle, G_{max}, by

$$G_N = \delta G_{max} \tag{B-21}$$

where the degradation index, δ, is given by $\delta = N^{-t}$ and t is the degradation parameter defined by Idriss et al. [37]. This is incorporated into the proposed model by updating the nonlinear stiffness, k_{NL}, by an appropriate factor in each loading cycle.

Time Domain Analysis and Equations of Motion

The time domain analysis was used in order to include all aspects of nonlinearity and examine the transient response logically and realistically. The governing equation of motion is given by:

$$[M]\{\ddot{u}\} + [C]\{\dot{u}\} + [K]\{u\} = \{F(t)\} \tag{B-22}$$

where $[M]$, $[C]$ and $[K]$ are the global mass, damping and stiffness matrices, and $\{\ddot{u}\}$, $\{\dot{u}\}$, $\{u\}$ and $F(t)$ are acceleration, velocity, displacement, and external load vectors, respectively. Referring to Fig. B-19, the equations of motion at node 1 (adjacent to the inner field) and node 2 (adjacent to the outer field) are:

$$m_1\ddot{u}_1 + c_{NL}(\dot{u}_1 - \dot{u}_2) + k_{NL}(u_1 - u_2) = F_1 \tag{B-23}$$

$$m_2\ddot{u}_2 - c_{NL}(\dot{u}_1 - \dot{u}_2) - k_{NL}(u_1 - u_2) = F_2 \tag{B-24}$$

where u_1 and u_2 are displacements of nodes 1 and 2, and F_1 is the force in the nonlinear spring including the confining pressure, and F_2 is the soil resistance at node 2. The equation of motion for the outer field is written as:

$$c\ddot{u}_2 + k_L u_2 = -F_2 \tag{B-25}$$

Assuming compatibility and equilibrium at the interface between the inner and outer zones leads to the following equation, which is valid for both sides of the pile:

$$\begin{bmatrix} F_1 \\ 0 \end{bmatrix} = \begin{bmatrix} Am_1 + B(c_L + c_{NL}) + k_{NL} & -k_{NL} - Bc_{NL} \\ -k_{NL} - Bc_{NL} & k_{NL} + Am_2 + B(c_L + c_{NL}) + k_L \end{bmatrix} \begin{bmatrix} u_1 \\ u_2 \end{bmatrix} + \begin{bmatrix} F_1^{i-1} \\ F_2^{i-1} \end{bmatrix}, \quad \text{(B-26)}$$

where F_1^{i-1} and F_2^{i-1} are the sums of inertia forces and soil reactions at nodes 1 and 2, respectively. The values A and B are constants of numerical integration for inertia and damping.

The linear acceleration assumption was used and the Newmark β method was implemented for direct time integration of the equations of motion. The modified Newton-Raphson iteration scheme was used to solve the nonlinear equilibrium equations.

Verification of the Analytical Model

Verification of Clay Model

Different soil profiles were considered in the analysis. Figure B-23 shows the typical pile-soil system and the soil profiles considered including linear and parabolic soil profiles. The p-y model was first verified against the hyperbolic model [12]. Figures B-24 and B-25 compare the dynamic soil reaction and pile head response for both the hyperbolic and p-y curve models for a single reinforced concrete pile in soft clay. A pile 0.5m in diameter and 15m long was used with an elastic modulus (E_p) equal to 35 GPa. A parabolic soil profile with the ratio $E_p/E_s = 1000$ at the pile base was assumed. The undrained shear strength of the clay was assumed to be 25 kPa. Figure B-24 shows the calculated dynamic soil reactions for a prescribed harmonic displacement of an amplitude equal to 0.03d at a frequency of 2 Hz at the pile head. It can be

noted from Figure B-24 that the soil reactions obtained from the two models are very similar, and approach stability after 5 cycles. The pattern shown in Figure B-24 is also similar to that obtained by Nogami et al. [27], showing an increasing gap and stability after approximately 5 cycles. Figure B-25 shows the displacement-time history of the pile head installed in the same soil profile. The load was applied at the pile head and was equal to approximately 10% of the ultimate lateral loading capacity of the pile. The hyperbolic and p-y curve models show very similar responses at the pile head, and both stabilize after approximately 5 cycles.

The dynamic soil reactions are, in general, larger than the static reactions because of the contribution from damping. Employing the same definition used for static p-y curves, dynamic p-y curves can be established to relate pile deflections to the corresponding dynamic soil reaction at any depth below the ground surface. The proposed dynamic p-y curves are frequency dependent. These dynamic p-y curves can be used in other static analyses that are based on the p-y curve approach to account approximately for the dynamic effects on the soil reactions to transient loading.

Figures B-26 and B-27 show dynamic p-y curves established at two different clay depths for a prescribed harmonic displacement at the pile head with an amplitude equal to 0.05d, for a frequency range from 0-10 Hz. The shear modulus of the soil was assumed to increase parabolically along the pile length. A concrete pile 12.5m in length and 0.5m in diameter was considered in the analysis. The elastic modulus of the pile material was assumed to be 35 GPa and the ratio E_p/E_s = 1000 (at the pile base). Both the p-y curve and hyperbolic models were used to analyze the pile response. The dynamic soil reaction (normalized by the ultimate pile capacity, P_{ult}) obtained from the p-y curve model compared well with that obtained from the hyperbolic relationship model, especially for lower frequencies, as can be noted from Figures B-

B-31

26 and B-27. It can also be observed from Figures B-26 and B-27 that the soil reaction increased as the frequency increased. This increase was more evident in the results obtained from the p-y curve model.

Verification of Sand Model

The p-y curve and hyperbolic models were used to analyze the response of piles installed in sand. The sand was assumed to be unsaturated and a linear soil modulus profile was adopted. The same pile as was used in the previous case was considered. Figure B-28 shows the calculated dynamic soil reactions at 1m depth for a prescribed harmonic displacement with an amplitude equal to 0.0375d at the pile head with a frequency of 2 Hz. As can be noted from Figure B-28, the two models feature very similar dynamic soil reactions. It should be noted that the soil reactions at both sides of the pile are traced independently. The upper part of the curve in Figure B-28 represents the reactions for the soil element adjacent to the right face of the pile when it is loaded rightward. The lower part represents the reactions of the soil element adjacent to the left face of the pile as it is loaded leftward. Both elements offer zero resistance to the pile movement when tensile stresses are detected in the nonlinear soil spring during unloading of the soil element on either side. However, the soil nodes remain attached to the pile node at the same level, allowing the sand to "cave in" and fill the gap. Observations from field and laboratory pile testing have confirmed that, unlike clays, sands usually do not experience gapping during harmonic loading. Thus both analyses model the physical behaviour of the soil realistically and logically.

The pile head displacement-time histories obtained from the p-y curve and hyperbolic models for a pile installed in a sand with linearly varying elastic modulus due to an applied

harmonic load are shown in Figure B-29. It can be noted that good agreement exists between the results from the p-y curve model and hyperbolic model.

Figures B-30 and B-31 show dynamic p-y curves established at two different depths for a prescribed harmonic displacement equal to 0.05d at the pile head for a steel pile driven in sand for a frequency range from 0 to 10 Hz. The results from both the p-y curve and hyperbolic models displayed the same trend, as can be noted from Figures B-30 and B-31.

Validation of Dynamic Model with Lateral Statnamic Tests

In order to verify that the p-y curve model can accurately predict dynamic response, it was employed to analyze a lateral Statnamic load test, and the computed response was compared with measured values.

The test site was located north of the New River at the Kiwi maneuvers area of Camp Johnson in Jacksonville, North Carolina. The soil profile is shown in Figure B-32, and consists of medium dense sand extending to the water table, underlain by a very weak, gray silty clay. There was a layer of gray sand at a depth of 7 m and a calcified sand stratum underlying that layer. The pile tested at this site was a cast-in-place reinforced concrete shaft with steel casing having an outer diameter of 0.61 m and a casing wall thickness of 13 mm. More details on the soil and pile properties and the loading procedure are presented by El Naggar [38]. Statnamic testing was conducted on the pile two weeks after lateral static testing was performed. Statnamic loading tests were performed by M. Janes and P. Bermingham, both of Berminghammer Foundation Equipment, Hamilton, Ontario.

The computed lateral response of the pile head is compared with the measured response in Figure B-33 for two separate tests with peak load amplitudes of 350 kN and 470 kN. The agreement between the measured and computed values was excellent, especially for the first load

B-33

test. The initial displacement was slightly adjusted for the computer-generated model to accommodate initial gapping that occurred due to the previous static test performed on the pile. The static *p-y* curve for the top soil layer was reduced significantly in order to model the loss of resistance due to permanent gap developed near the surface.

Dynamic p-y Curve Generation

The dynamic *p-y* curves presented in Figures B-26 through B-28, B-30 and B-31 showed that a typical family of curves exists related to depth, much like the static *p-y* curve relationships. Thus, dynamic *p-y* curves could be established at any depth and be representative of the soil resistance at this specific depth. In this study, they were obtained at a depth equal to 1.5 mm which was found to illustrate the characteristics of the dynamic *p-y* curves.

More dynamic *p-y* curves were generated using prescribed harmonic displacements applied at the pile head that allowed for the development of plastic deformation in the soil along the top quarter of the pile length. Steel pipe piles were considered in the analysis. It was assumed that sand had a linear soil profile and the clay had a parabolic profile in order to match the soil profile employed to derive the static *p-y* curves used in the analysis. The soil shear wave velocity profiles and the pile properties are given in Figure B-34. The tests were divided into two separate cases involving clays (Case I) and sandy soils (Case II). Table B-1 summarizes the characteristics of each case and relevant pile and soil parameters. The dynamic p-y curves were generated over a frequency range of 0 to 10 Hz (2 Hz intervals) for different classifications of sand and clay based on standard laboratory and field measurements (SPT-value, relative density, c_u, etc.). All results were obtained after one or two cycles of harmonic loading.

Results / Discussion

The results from the computational model showed a general trend of increasing soil resistance with an increase in the load frequency. The dynamic *p-y* curves obtained seem to have three distinct stages or regions. The initial stage (at small displacements) shows an increase in the soil resistance (compared with the static *p-y* curve) that corresponds to increasing the velocity of the pile to a maximum. This increase in the soil resistance is larger for higher frequencies. In the second stage, the dynamic *p-y* curves have almost the same slope as the static *p-y* curve for the same displacement. This stage occurs when velocity is fairly constant and consequently the damping contribution is also constant. The third stage of the dynamic *p-y* curve is characterized by a slope approaching zero as plastic deformations start to occur (similar to the static *p-y* curve at the same displacement). There is also a tendency for the dynamic curves to converge at higher resistance levels approaching the ultimate lateral resistance of the soil at depth x, P_u (determined from the American Petroleum Institute [4].

The overall relationship between the dynamic soil resistance and loading frequency for each test was established in the form of a generic equation. The equation was developed from regression analysis relating the static *p-y* curve, frequency, and apparent velocity, ωy, so that:

$$P_d = P_s\left[\alpha + \beta a_o^{\,2} + \kappa a_o\left(\frac{\omega y}{d}\right)^n\right] \qquad , \qquad P_d \leq P_u \text{ at depth x,} \qquad (B\text{-}27)$$

where P_d = dynamic value of "p" on the *p-y* curve at depth x (N/m), P_s = corresponding static soil reaction (obtained from the static *p-y* curve) at depth x (N/m), a_o is dimensionless frequency $= \omega r_o / V_s$, ω = frequency of loading (rad/s), d = pile diameter (m), y = lateral pile deflection at depth x when soil and pile are in contact during loading (m), and α, β, κ, and n are constants determined from curve fitting Eq. B-27 to the computed dynamic *p-y* curves from all cases

B-35

considered in this study. A summary of the best-fit values for the constants is provided in Table B-2. The constant α is taken equal to unity to ensure that $P_d = P_s$, for $\omega = 0$. For large frequencies or displacements, the maximum dynamic soil resistance is limited to the ultimate static lateral resistance of the soil, P_u.

Figures B-35 and B-36 show dynamic p-y curves established using Eq. B-27 and the best-fit constants (as dashed lines). The approximate dynamic p-y curves established from Eq. B-27 represented soft/medium clays and loose/medium dense sands reasonably well. However, the accuracy is less for stiffer soils (higher V_s values). The precision of the fitted curves also increases with frequency ($\omega \geq 4$ Hz) where the dynamic effects are important. The low accuracy at a lower frequency ($a_o < 0.02$) may be attributed to the application of the plane strain assumption in the dynamic analysis. This assumption is suitable for higher frequencies as the dynamic stiffness of the outer field model vanishes for $a_o < 0.02$ due to the assumption of plane strain. Case C1 was also used to obtain dynamic p-y curves at depths of 1.0 m and 2.0 m to examine the validity of Eq. B-27 to describe the dynamic soil reactions at other depths along the soil profile. The results showed that Eq. B-27 (using the constants in Table B-2) predicted the dynamic soil reactions reasonably well.

Development of a Simplified Model

For many structural dynamics programs, soil-structure interaction is modelled using static p-y curves to represent the soil reactions along the pile length. However, the use of static p-y curves for dynamic analysis does not include the effects of velocity-dependent damping forces. The dynamic p-y curves established using Eq. B-27 and the parameters given in Table B-2 allow for the generation of different dynamic p-y curves based on the frequency of loading and soil

profile. Substituting dynamic *p-y* curves in place of traditional static *p-y* curves for analysis should result in better estimates of the response of structures to dynamic loading.

Alternatively, the dynamic soil reactions can be represented using a simple spring and dashpot model. This model can still capture the important characteristics of the nonlinear dynamic soil reactions. A simplified dynamic model that can be easily implemented into any general finite element program is proposed herein.

Complex Stiffness Model

As discussed previously, Eq. B-27 can be used directly to represent the dynamic relationship between a soil reaction and a corresponding pile displacement. The total dynamic soil reaction at any depth is represented by a nonlinear spring whose stiffness is frequency dependent.

A more conventional and widely accepted method of calculating dynamic stiffness is through the development of the complex stiffness. The complex stiffness has a real part K_1 and an imaginary part K_2, i. e.:

$$P_d = Ky = (K_1 + iK_2)y \qquad (B-28)$$

The real part, K_1 represents the true stiffness, k, and the imaginary part of the complex stiffness, K_2, describes the out-of-phase component and represents the damping due to the energy dissipation in the soil element. Because this damping component generally grows with frequency (resembling viscous damping), it can also be defined in terms of the constant of equivalent viscous damping (the dashpot constant) given by $c = K_2 / \omega$. Then the dynamic *p-y* curve relation can be described as

$$P_d = (k + i\omega c)y = ky + c\dot{y} \qquad (B-29)$$

in which both k and c are real and represent the spring and dashpot constants, respectively, and $\dot{y}$= dy/dt is velocity. Using Eq. B-27, the dynamic p-y curve can be written in the form of Eq. B-28, i. e.,

$$P_d = (K_1 + iK_2)y = \left(\frac{P_s\alpha}{y} + i\frac{P_s\left(\beta a_o^2 + \kappa a_o\left(\frac{\omega y}{d}\right)^n\right)}{y} \right)y \quad . \quad \text{(B-30)}$$

The stiffness and damping constants are then calculated as

$$k = K_1 = \frac{P_s\alpha}{y} \qquad \text{and} \qquad \text{(B-31)}$$

$$c = \frac{K_2}{\omega} = \frac{P_s\left(\beta a_o^2 + \kappa a_o\left(\frac{\omega y}{d}\right)^n\right)}{\omega y} \qquad \text{(B-32)}$$

The complex stiffness can be generated at any depth along the pile using the static p-y curves and Eqs. B-31 and B-32.

Complex Stiffness Constants – Soft Clay Example

The complex stiffness constants were calculated for Test C1 (Table B-2) using the method described in the previous section. The values of the true stiffness, k, were obtained for the range of displacements experienced by the pile for the frequency range from 0 to 10 Hz. The stiffness parameter $(S_1)_{py}$ was defined as

$$(S_1)_{py} = \frac{k_{py}}{G_{max}} \qquad . \qquad \text{(B-33)}$$

The constant of equivalent damping, c, was obtained by averaging the value from Eq. B-32 for the range of velocities experienced by the pile for each frequency of loading. Then, the equivalent damping parameter $(S_2)_{py}$ was defined as

$$(S_2)_{py} = \frac{cV_s\omega}{G_{max}r_o} \qquad . \tag{B-34}$$

Figure B-37 shows the true stiffness calculated from the static p-y curve, and it can be noted that this stiffness is identical at all loading frequencies considered. There is a definite trend of decreasing stiffness with increased displacement due to the soil nonlinearity. The constant of equivalent damping presented in Figure B-38 shows a decreasing pattern with frequency that can be attributed to separation at the pile-soil interface. The values from Figsures B-37 and B-38 can be directly input into a finite element program as spring and dashpot constants to obtain the approximate dynamic stiffness of a soil profile similar to Test C1.

Implementing Dynamic p-y *Curves in ANSYS*

A pile and soil system similar to Test C1 was modelled using the *ANSYS* [1] to verify the applicability and accuracy of the dynamic p-y curve model in a standard structural analysis program. A dynamic harmonic load with peak amplitude of 100 kN at a frequency of 6 Hz was applied to the head of the same steel pipe pile used in Test C1. The soil stiffness was modelled using three procedures: (1) static p-y curves; (2) dynamic p-y curves using Eq. B-27; and (3) complex stiffness method using equivalent damping constants. The pile head response for each test was obtained and compared to the results from the two-dimensional p-y curve model.

The pile was modelled using two-noded beam elements and was descretized into 10 elements that increased in length with depth. At each pile node, a spring or a spring and a

dashpot was attached to both sides of the pile to represent the appropriate loading condition at the pile-soil interface. The pile and soil remained connected and had equal displacement for compressive stresses. The spring or the spring and dashpot model disconnects if tensile stress is detected in the soil, allowing a gap to develop.

The soil was first modelled using nonlinear springs with force displacement relationships calculated directly from static p-y curves. The soil stiffness was then modelled using the approximate dynamic p-y curve relationship calculated for Test C1 using Table B-2. The last computational test considered a spring and a dashpot in parallel.

The pile head response for each computational test is shown in Figs. B-39 and B-40, along with the calculated response from the 2-D analytical p-y model. Figure B-39a shows that the static p-y curves model computed larger displacements with increasing amplitudes as the number of cycles increased. Figure B-39b shows that the response computed using the dynamic p-y curve model was in good agreement with the response computed using the 2-D analytical model. The results obtained using the complex stiffness model are presented in Fig. B-40a and show a decrease in displacement amplitude. The overdamped response can be attributed to using an average damping constant, which overestimates the damping at higher frequencies and large nonlinearity. Figure B-40b shows the response of the 2-D model compared to the complex stiffness approach with the average damping constant reduced by 50%. The results show that the response in this case is in good agreement with the response computed using the 2-D analytical model.

DYNAMIC p-MULTIPLIERS

One reasonable approach to account for pile-soil-pile interaction for piles in a group would be to predict the loss in soil resistance relative to that of an isolated single pile. Poulos and Davis [9] introduced the interaction factors concept to reduce the soil stiffness in the context of linear elastic analysis. Focht and Koch [39] extended that linear elastic procedure to introduce the nonlinearity of soil into the evaluation of group interaction factors by applying a y-multiplier to "stretch" p-y curves. Cox et al. [40] described an alternate approach to account approximately for the group effect, in which a "p-factor" would be used to "shrink" the p values on the p-y curve rather than to stretch the y values.

The p-multiplier concept was formalized by Brown and his colleagues [41, 42]. This concept states that lateral group action reduces the p-value on the p-y curve at every point on every p-y curve for a given pile (based on its geometric position in the group) by the same amount, regardless of pile deflection. In this manner, the p-multiplier provides a means for expressing the elastic interaction that appears in the interaction factors plus an actual reduction in ultimate soil resistance. The p-multiplier assumes a different value depending upon whether a pile is in a leading position, in a trailing position and the angle between the line connecting the two piles and the load direction, θ. Using the p-multipliers would allow the analysis of the lateral response of a pile group as an ensemble of individual piles. The soil resistance to the movement of each of these individual piles would be represented by p-y curves with p values reduced by properly chosen p-multipliers. For example, FLPIER (Appendix C) uses p-multipliers as an option for considering lateral group action. The p-multipliers found in the literature are given either by row (i.e. same p-multiplier value for all piles in the same row) or

assuming different values for each pile. In the latter case, the total p-multiplier for any pile is obtained by multiplying (rather than summing) the p-mulitpliers due to all the piles in the group.

The p-multipliers reported in the literature were developed from the analysis of static or cyclic load tests on single piles and pile groups. These tests, however, do not represent the dynamic loading conditions during an earthquake event. Therefore, it is necessary to check the validity of the p-multiplier concept under dynamic loading conditions and develop, if possible, p-multipliers from dynamic loading events. This was a major objective of the overall project. The following section describes the results of an exploratory investigation into dynamic p-multipliers, independent of the analysis of the load tests conducted explicitly for this project (Appendix D).

The approach suggested by El Naggar and Novak [23] to account for the group effect, along with the analytical model described above for the analysis of a single pile's response, were used to analyze the response of a single pile and groups of two piles to a prescribed harmonic displacement at the pile heads. Thus, dynamic p-multipliers could be established by comparing the soil resistance for a pile in a group of two piles to that of a single pile. At this point, a limited parametric study was considered for piles in cohesionless soil with different densities (e.g. loose, medium and dense sand profiles). The parameters whose influence on p-multipliers is investigated in this study for a given pile and soil profile include:

- The ratio of the spacing between the two piles to the diameter of the piles, S/d.

- The pile head displacement ratio, y/d.

- The dimensionless frequency, a_0.

- The angle between the line connecting the two piles and the load direction, θ.

To establish the p-multiplier, two loading cases were considered separately: a pile loaded individually and a group of two identical piles. In both loading cases, a prescribed harmonic

B-42

displacement with specified peak amplitude was applied at the pile head, the response was analyzed and the force at the pile head was calculated. The p-multiplier was approximated by the peak pile head force at one pile in the two-pile group divided by the peak force for the single pile. The loading starts from zero and the forces are established after five loading cycles. The response was found to stabilize almost completely after this number of cycles.

The p-multiplier was plotted versus the peak of the applied harmonic displacement, as a ratio of the pile diameter. Figure B-41 shows the p-multipliers for piles installed in loose sand (S4 in Table B-1), and $\theta = 0°$. It can be noted from Figure B-41 that the main factors that affect the p-multipliers in this case are the spacing ratio, S/d, and the pile head displacement ratio, y/d. The p-multiplier increased as S/d increased, meaning that the group effect decreased. The p-multipliers also increased as the y/d increased. This means that during a dynamic loading event, which is characterised by large pile head displacement, the pile-soil-pile interaction decreases and the piles, tend to behave as individual piles. This may be attributed to the concentration of soil deformations in the vicinity of the pile at higher displacements. Comparing the p-multipliers in Figure B-41 obtained for different loading frequencies, it can be noted that the effect of the frequency on the p-multipliers is small and that there is no clear trend for it.

Figures B-42 and B-43 show the p-multipliers for piles installed in medium dense and dense sand, respectively. Similar observations can be made for both cases. The p-multipliers increased as both S/d and y/d increased, and the effect of the frequency is negligible. However, it must be emphasised that these observations are based on limited results. Further investigations should be done before these observations can be asserted. Also, the behavior of piles in clay is different and is currently under investigation.

The p-multipliers shown in Figures B-42 and B-43 (and similar ones for other soil profiles) could be curve fitted. The best curve-fit function would be in the form:

$$\text{p-multiplier} = f\left(S/d, \; y/d, \; a_0, \; \theta \right) \tag{B-35}$$

This function can then be evaluated to yield the p-multiplier according to S/d, θ values for each two piles in the group, and the expected y/d and a_0 for a specific event.

SUMMARY, CONCLUSIONS AND RECOMMENDATIONS FOR IMPROVEMENTS

Summary and Conclusions

A simple, two-dimensional analysis method was developed to model the response of piles to dynamic loads. The model was formulated in the time domain and developed to model transient nonlinear response of the pile-soil system efficiently. Static p-y curves were used to generate the nonlinear soil stiffness in the context of a Winkler model. The piles were assumed to be vertical and circular, although piles with other cross sections can be modelled by simply computing an equivalent radius r_0 for the non-circular pile. The piles were modelled using standard beam elements. A practically accurate and computationally efficient model was developed to represent the soil reactions. This model accounted for soil nonlinearity, slippage and gapping at the pile-soil interface, and viscous and material damping.

Dynamic soil reactions (dynamic p-y curves) were generated for a range of soil types and harmonic loading with varying frequencies applied at the pile head. Closed-form solutions were derived from regression analysis relating the static p-y curve, dimensionless frequency, and apparent velocity of the soil particles. That model is summarized in Eq. B-27, which converts a static p-y model into an approximate dynamic model by multiplying p values on the static p-y curve (such as the API sand curve) by a factor that is dependent upon both frequency and lateral

pile displacement relative to the pile diameter. Several curve-fitting parameters that were necessary to write Eq. B-27 in closed form from the results of numerous numerical solutions are given in Table B-2. Although the dynamic p-y curves are frequency dependent, they are approximately frequency independent for frequencies above about 10 Hz (ω = 62.8 radians). This model is included in FLPIER (Appendix C), although verification against full-scale or centrifuge tests on piles using this relationship was not accomplished with FLPIER within the time frame limitations of this project.

A simple spring and dashpot model was also proposed whose constants were established by splitting the dynamic p-y curves into real (stiffness) and imaginary (damping) components. The model is summarized in Eq. B-29, in which a displacement-dependant soil stiffness k is determined from Eq. B-31 and displacement and frequency dependent damping is determined from Eq. B-32. This model appears to be most accurate for dimensionless frequencies (a_o = $\omega r_o / V_s$) > 0.02. This model is intended to be used in programs that employ equivalent linear analyses for harmonic loading at the pile head.

The proposed dynamic p-y curves and the spring and dashpot model were incorporated into a commercial finite element program (ANSYS) that was used to compute the response of a laterally loaded pile. The computed responses compared well with the predictions of the two-dimensional analysis.

The group effect (lateral pile-soil-pile interaction through the soil) was considered in the analysis, and a procedure for the development of dynamic p-multipliers for sand profiles was proposed. Like the p-y curves, the p-multipliers are frequency dependent, although, based on limited evidence given here (Figures B-41 through B-43), the p-multipliers for loose through dense sand can be treated in design practice as frequency independent in the frequency range a_o =

$\omega r_o/V_s = 0.02$ to 0.12, especially for pile-head displacements, y, equal to or greater than 0.2 d, where d is the pile diameter (or equivalent diameter for non-circular piles). Such displacements are typical of those for which solutions are needed for extreme event loading.

For relatively low frequencies, the predominant frequency of the earthquake motion being modelled can be used to compute the values on the *p-y* curves. However, for cases where inertial behavior is stronger than kinematic behavior (the piles are driven by inertial superstructure feedback rather than the kinematic motion of the surrounding soil), the natural frequency of the structure being modelled may be the controlling predominant frequency ω to be used in evaluating the dynamic p-y curves and p-multipliers. Selection of a value for ω must therefore be done carefully by the user of the model (Eqs. B-27, B-29, B-30 and B-32). If the user decides that the primary frequency at the pile head will be 10 Hz or greater, the *p-y* model can be evaluated by setting $\omega = 62.8$ radians per second in the expression for a_o and the curve can be treated as frequency independent.

The dynamic *p-y* curves and the dynamic p-multipliers can then be used to model the dynamic lateral behavior of pile groups approximately, either in FLPIER or other software that uses *p-y* models for the soil.

Recommendations for Further Development

The dynamic p-multipliers have been developed exclusively for sand profiles (in which strength and stiffness increase with depth). Time and resources did not permit a corresponding development for clay profiles. Further development of the model should include the development of p-multipliers for clay profiles (uniform strength stiffness with depth) and for mixed soil profiles. The models should also be used directly in FLPIER (Appendix C) to ensure that it is performing properly in the context of that computer code.

REFERENCES — APPENDIX B

1.   *ANSYS* , "General Finite Element Analysis Program," Version 5.4, ANSYS, Inc. Houston, PA (1996).

2.   Wu, G., and Finn, W. D. L., (1996). "Dynamic Nonlinear Analysis of Pile Foundations Using Finite Element Method in the Time Domain," *Canadian Geotechnical Journal*, Vol. 34 (1996) pp. 44-52.

3.   Trochanis, A. M., Bielak J., and Christiano, P., "A Three-Dimensional Nonlinear Study of Piles Leading to the Development of a Simplified Model," *Technical Report*, Carnegie Mellon University , Research Sponsored by NSF, (1988) Grant No. ECE-86/1060.

4.   American Petroleum Institute, "Recommended Practice for Planning, Designing and Constructing Fixed Offshore Platforms," API Recommended Practice 2A (RP 2A), 19th Ed., Washington, D.C., (1991) pp.47-55.

5.   Novak, M., and Mitwally, H., "Transmitting Boundary for Axisymmetrical Dilation Problems." *Journal of Engineering Mechanics*, ASCE, Vol.114, No.1, (1988) pp. 181-187.

6.   National Center for Earthquake Engineering Research (NCEER) Information Service, State University of New York at Buffalo, web site: http://nceer.eng.buffalo.edu (1998).

7.   Kramer, S. L., *Geotechnical Earthquake Engineering*, Prentice-Hall, Englewood Cliffs, New Jersey (1996).

8.   El Sharnouby, B. and Novak, M., "Static and Low Frequency Response of Pile Groups," *Canadian Geotechnical Journal*, Vol. 22, No. 2, (1985) pp.79-84.

9.   Poulos, H. G., and Davis, E. H., *Pile Foundation Analysis and Design*, John Wiley and Sons (1980).

10. Idriss, I. .M. and Sun, J. I., "Modifications to SHAKE Program published in Dec. 1972 by Schnabel, Lysmer & Seed," USER'S MANUAL FOR SHAKE91 (with Accompanying Program), Center for Geotechnical Modeling, University of California at Berkeley, (1992).

11. Takemiya, H., and Yamada, Y., "Layered Soil-Pile-Structure Interaction," *Earthquake Engineering and Structural Dynamics*, Vol. 9 (1981), pp. 437 - 357.

12. Flores-Berrones, R., and Whitman, R. V. "Seismic Responses of End-Bearing Piles," *Journal of Geotechnical Engineering*, ASCE, Vol. 108 (1982), pp. 555 - 569.

13. Gazetas, G., "Seismic Response of End-Bearing Piles," *International Journal of Soil dynamics and Earthquake Engineering*, Vol. 3, No. 2 (1984), pp. 82 - 93. 14.

14. Tazoh, T., Wakahara, T., and Shimizu, K., "Effective Motion of Group Pile Foundation," 9th World Conference on Earthquake Engineering, Proceedings Vol. III (1988).

15. Ahmad, S., and Mamoon, S. M., "Seismic Response of Floating Piles to Obliquely Incident Waves," 2nd International Conference on Recent Advances in Geotechnical Earthquake Engineering and Soil Dynamics, St. Louis, MO, Proceedings Vol. 1 (1991), pp. 805 - 813.

16. Fan, K., Gazetas, G., Kaynia, A., Kausel, E., and Ahmad, S., "Kinematic Seismic Response of Single Piles and Pile Groups," *Journal of Geotechnical Engineering*, ASCE, Vol. 117, No. 12, (1991) pp.1860-1879.

17. Kaynia, A. M. and Kausel, E., "Dynamic Stiffnesses and Seismic Response of Pile Groups" *Research Report*, Dept. of Civil Engineering, MIT, Cambridge, Mass (1982).

18. Makris, N. and Gazetas, G., "Dynamic Pile-Soil-Pile Interaction. Part II: Lateral and Seismic Response," *Earthquake Engineering and Structural Dynamics*, Vol. 21, (1992) pp. 145-162.

19. Novak, M., Nogami, T., and Aboul-Ella, F., "Dynamic Soil Reactions for Plane Strain Case," *Journal of the Engineering Mechanics Division*, ASCE, Vol. 104, (1978) pp. 953-959.

20. Gazetas, G., and Dobry, R., " Horizontal Response of Piles in Layered Soils" *Journal of Geotechnical Engineering*, ASCE, Vol. 110, No.1, (1984) pp.20-40.

21. Nogami, T., Konagai, K., Otani, J., and Chen H.L., "Nonlinear Soil-Pile Interaction Model for Dynamic Lateral Motion," *Journal of Geotechnical Engineering*, ASCE, Vol. 118, No.1, (1992) pp. 106-116.

22. El Naggar, M. H., and Novak, M., "Nonlinear Lateral Interaction in Pile Dynamics," *Journal of Soil Dynamics and Earthquake Engineering*, Vol. 14, No. 3, (1995) pp. 141-157.

23. El Naggar, M. H., and Novak, M., " Nonlinear Analysis for Dynamic Lateral Pile Response," *Journal of Soil Dynamics and Earthquake Engineering*, Vol. 15, No. 4, (1996) 233-244.

24. Novak, M., and Sheta, M., (1982). "Dynamic Response of Piles and Pile Groups," 2nd International Conference on Numerical Methods in Offshore Piling, Proceedings, Austin, Texas, (1982) pp. 489-507.

25. Hardin, B. O., and Black, W. L., "Vibration Modulus of Normally Consolidated Clay," *Journal of the Soil Mechanics and Foundations Division*, ASCE, Vol. 94, No. SM2, (1968) pp. 353-369.

26. Matlock, H., "Correlations for Design of Laterally Loaded Piles in Soft Clay," 2nd Offshore Technology Conference, Houston, Texas, Proceedings Vol. 1, (1970) pp. 577-588.

27. Bhushan, K., Haley, S. C., and Fong, P. T., (1979). "Lateral Load Tests on Drilled Piers in Stiff Clays," *Journal of the Geotechnical Engineering Division*, ASCE, Vol. 105, No. GT8, Proc. Paper 14789, (1979) pp. 969-985.

28. Reese, L. C., and Welch, R. C., (1975). "Lateral Loading of Deep Foundations in Stiff Clay," *Journal of the Geotechnical Engineering Division*, ASCE, Vol. 101, No. GT7 (1975), pp. 633-649.

29. Reese, L. C., Cox, W. R., and Koop, F. D., "Field Testing and Analysis of Laterally Loaded Piles in Stiff Clay," 7th Annual Offshore Technology Conference, Houston, Texas, Proceedings Vol. 2 (1975), pp. 671-690.

30. Desai, C. S., and Wu, T. H., "A General Function for Stress-Strain Curves," 2nd Int. Conference on Numerical Methods in Geomechanics, ASCE, Vol. 1 (1976), pp. 306-318.

31. Abendroth, R. E., and Greimann, L. F., "Pile Behavior Established from Model Tests" Journal of Geotechnical Engineering, ASCE vol. 116, No. 4, (1990) pp. 571-588.

32. Reese, L. C., Cox, W. R., and Koop, F. D., "Analysis of Laterally Loaded Piles in Sand," Paper No. OTC 2080, 6th Annual Offshore Technology Conference, Houston, Texas, Proceedings Vol. 2 (1974), pp.473-483.

33. Bhushan, K., Lee, L. J., and Grime, D. B., "Lateral Load Tests on Drilled Piers in Sand," *Drilled Piers and Caissons*, Ed. by M. W. O'Neill, ASCE (1981) pp. 131-143.

34. Bhushan, K., and Askari, S., "Lateral Load Tests on Drilled Pier Foundations for Solar Plant Heliostats" Laterally Loaded Piles, *ASTM STP 835*, James A. Langer, Ed., American Society for Testing and Materials, (1984) pp. 141-155.

35. Bhushan K., and Haley, S. C., "Development of Computer Program Using P-Y Data from Load Test Results for Lateral Load Design of Drilled Piers," a research report prepared for Woodward-Clyde Consultants Professional Development Committee, San Francisco, California (1980).

36. Meyer, B. J., and Reese, L. C., "Analysis of Single Piles Under Lateral Loading" *Research Report* 244-1, Center for Highway Research, The University of Texas at Austin, Austin, Texas, (1979) pp.1-145.

37. Idriss, I. M., Dobry, R., and Singh, R. D., "Nonlinear Behavior of Soft Clays During Cyclic Loading," *Journal of the Geotechnical Engineering Division*, ASCE, Vol. 104, No. GT12 (1978), pp.1427-1447.

38. El Naggar, M. H., "Interpretation of Lateral Statnamic Load Test Results" *Geotechnical Testing Journal*, ASTM, Vol. 21, No. 3 (1998) pp. 169-179.

39. Focht, J. A., Jr. and Koch, K.J., "Rational Analysis of the Lateral Performance of Offshore Pile Groups", Offshore Technology Conference, Paper No. OTC. 1896, Proceedings (1973) Dallas.

40. Cox, W. R., Dixon, D. A., and Murphy, B. S., "Lateral Load Tests on 25.4-mm (1-in.) Diameter Piles in Very Soft Clay in Side-by-Side and In-Line Groups," *STP 835*, American Society for Testing and Materials (1984), pp. 122 - 139.

41.   Brown, D. A., Morrison, C., and Reese, L.C., (1988). "Lateral Load Behaviour of Pile Group in Sand", Journal of Geotechnical Engineering, ASCE, Vol. 114, No. 11 (1988) pp. 1326-1343.

42.   Brown, D.A. and Bollman, H., "Pile Group Design for Lateral Loading Using COM 624, "Conference on The Design of Bridges for Extreme Events, U.S. Department of Transportation, Federal Highway Administration, Proceedings (1996).

Table B-1. Description of parameters used for each test case.

CASE I	SOIL TYPE	C_u (kPa)	ν	d (m)	L/d	E_p/E_s	G_{max} (kPa)	V_s (m/s)
(clays)								
C1	SOFT CLAY	< 50	0.45	0.25	40	10000	6.6e6	70
C2	MEDIUM CLAY	80	0.45	0.25	40	4500	1.6e7	150
C3	STIFF CLAY	>100	0.45	0.25	40	1600	8.3e7	200

CASE II (sands)	SOIL TYPE	D_r (%)	ϕ	ν	d (m)	L/d	E_p/E_s	G_{max} (kPa)	V_s (m/s)
S4	LOOSE SAND (saturated)	35	32	0.3	0.25	40	6300	1.2e7	70
S5	MEDIUM SAND (saturated)	50	34	0.3	0.25	40	3800	2.0e7	100
S6	MEDIUM SAND (saturated)	50	34	0.3	0.50	20	3800	2.0e7	100
S8	DENSE SAND (saturated)	90	38	0.3	0.25	40	1580	4.7e7	150
S9	DENSE SAND (unsaturated)	90	38	0.3	0.25	40	790	9.7e7	220

**Note: all values represent those calculated at a depth of 1.5m.

Table B-2. Dynamic p-y curve parameter constants for a range of soil types
($d = 0.25$, $L/d = 40$, $0.015 < a_o = \omega r_o/V_s < 0.225$).

$$P_d = P_s\left[\alpha + \beta a_o{}^2 + \kappa a_o\left(\frac{\omega y}{d}\right)^n\right]$$

SOIL TYPE	DESCRIPTION	α	β		κ	n
			$a_o < 0.025$	$a_o > 0.025$		
SOFT CLAY	$C_u < 50$ kPa $V_s < 125$ m/s	1	-180	-200	80	0.18
MEDIUM CLAY	$50 < C_u < 100$ kPa $125 < V_s < 175$ m/s	1	-120	-360	84	0.19
STIFF CLAY	$C_u > 100$ kPa $V_s > 175$ m/s	1	-2900	-828	100	0.19
MEDIUM DENSE SAND (saturated)	$50 < D_r < 85$ % $125 < V_s < 175$ m/s	1	3320	1640	-100	0.1
MEDIUM DENSE SAND (unsaturated)	$50 < D_r < 85$ % $125 < V_s < 175$ m/s	1	1960	960	-20	0.1
DENSE SAND (saturated)	$D_r > 85$ % $V_s > 175$ m/s	1	6000	1876	-100	0.15
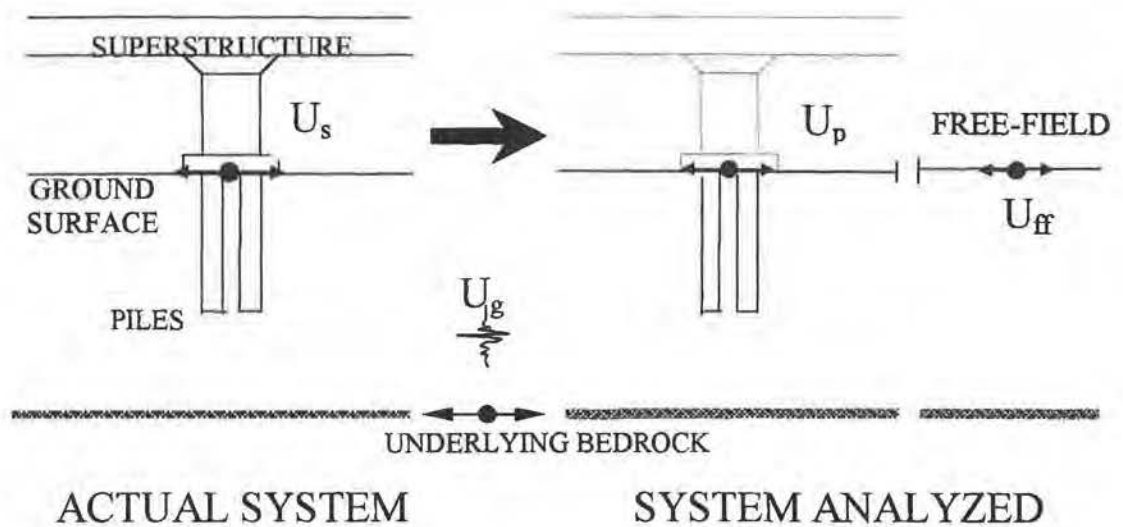
Figure B-1. Definition of the problem and terminology (actual acceleration, U_s, acceleration due to kinematic interaction only, U_p, bedrock acceleration, U_g, and free-field acceleration, U_{ff})

(a)

(b)
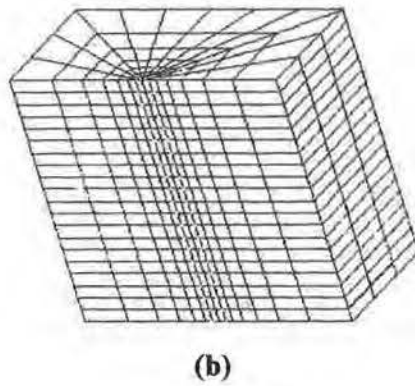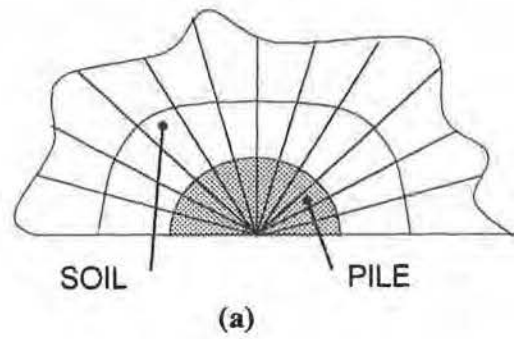
Figure B-2.   (a) Detail of wedge shaped pile elements surrounded by soil elements (plan view), (b) Isometric view of soil and pile mesh model
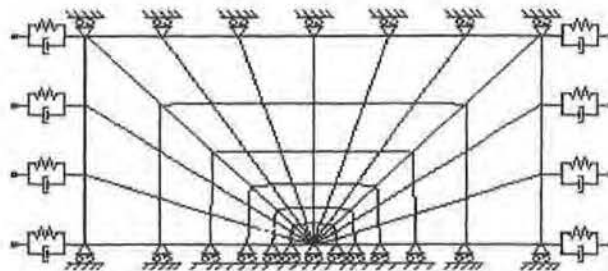
(a)
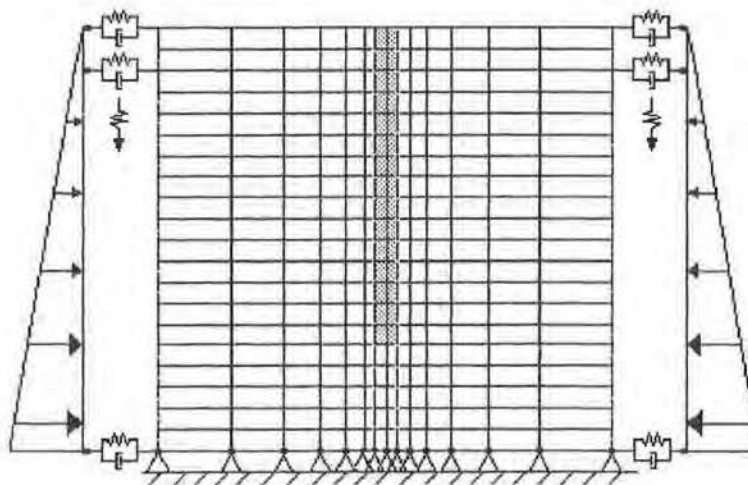
(b)

Figure B-3. Finite element mesh (Mesh No.3) showing boundary conditions: (a) plan view, (b) front cross section view with geostatic pressure distribution.

B-57

(a) - 8 noded Block element, DOF: X, Y, Z

(b) - 5 noded Contact element, DOF: X, Y, Z

(c) - 2 noded Boundary element, DOF: X, Y, Z
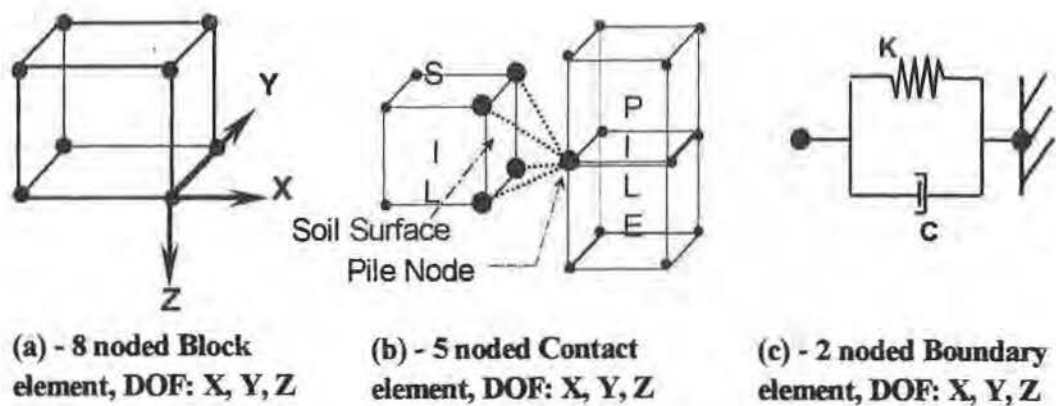
Figure B-4. (a) Block element used for soil and pile, (b) Surface Contact element used between pile and soil to allow for slippage and separation, (c) Transmitting Boundary element consisting of "spring(K)" and "dashpot(C)" to allow for radiating boundaries.

PILE CONFIGURATIONS

SOIL PROFILES
(E_s X 1000 kN/m²)

FLOATING PILE
$L_f = 7.5$ m

SOCKETED PILE
$L_s = 10$ m

HOMOGENEOUS

LAYERED

$D = 5$ m
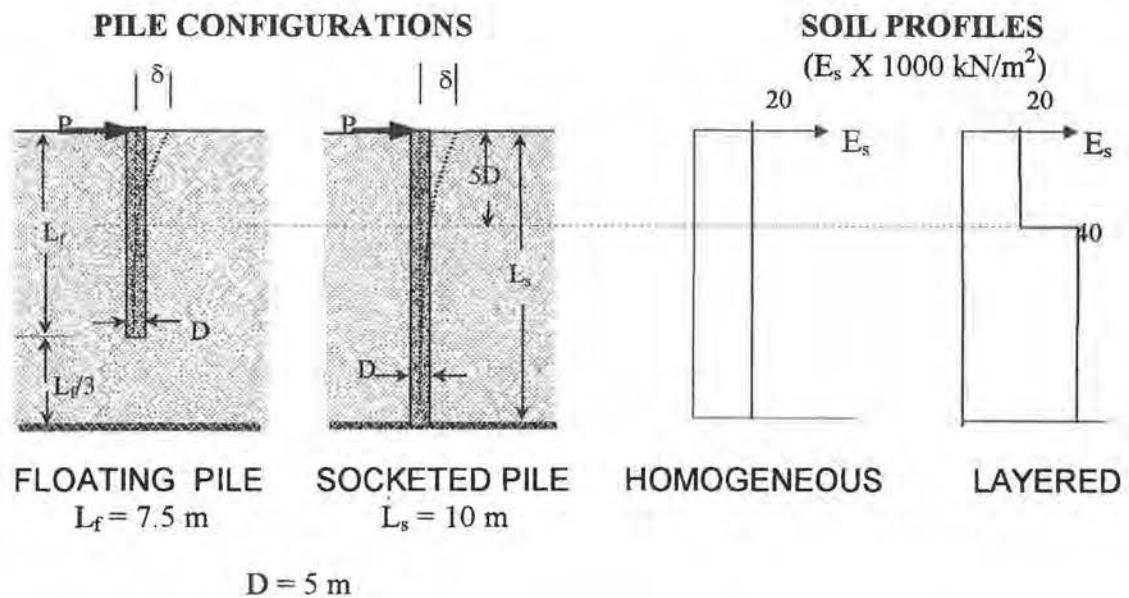
E_s= Soil Young's Modulus
δ = Horizontal deflection
P = Horizontal load
V_s = shear wave velocity = 60-120 m/s
c' = 34 kPa, $\phi = \Psi = 16.5°$ (Plasticity)

E_p= Pile Young's Modulus = $2*10^7$kPa
ρ_s = Soil submerged unit weight = 11.8 kN/m³
ρ_p = Pile mass density = 2.3 Mg/m³
ν_s= Soil Poisson's ratio = 0.45
ν_p= Pile Poisson's ratio = 0.30

Figure B-5. Two-dimensional representation of floating and socketed pile in either homogeneous (used for verification) or layered soil profile
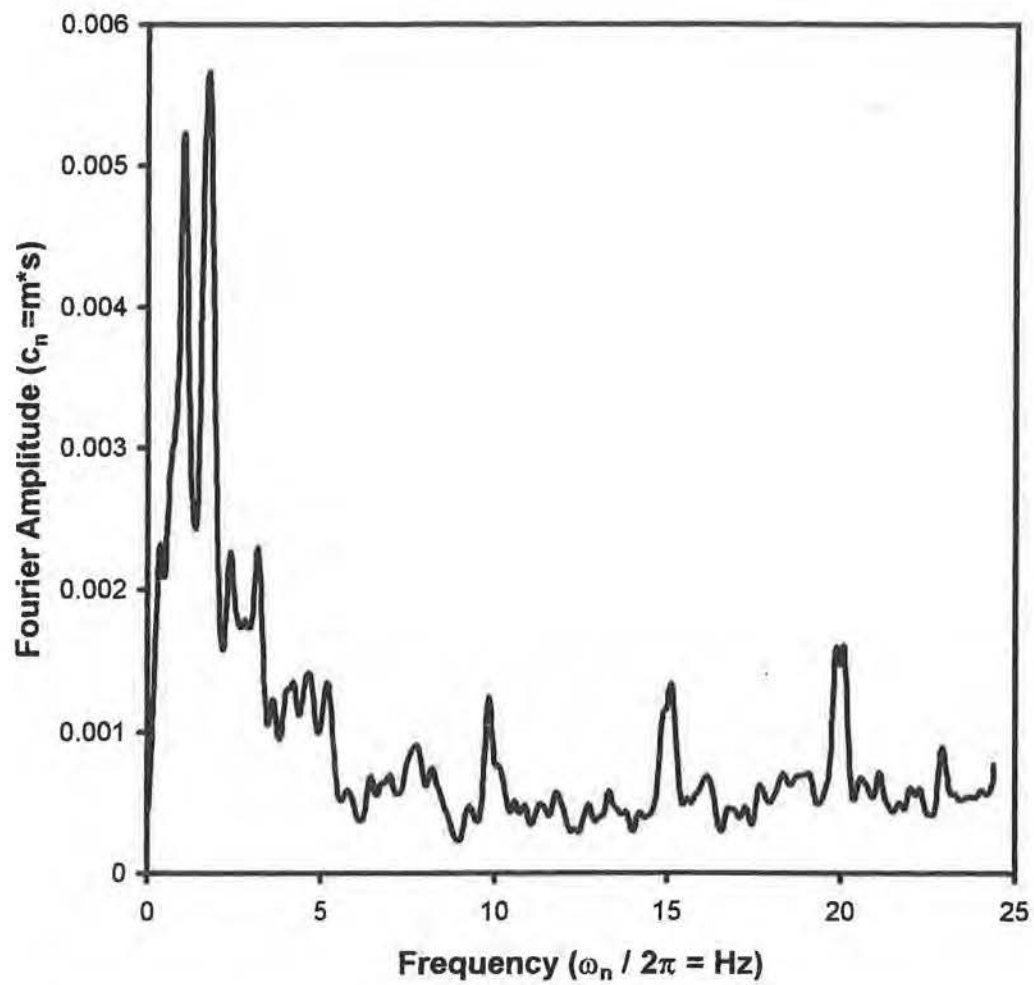
Figure B-6. Fourier amplitude spectrum for earthquake loading at the bedrock level
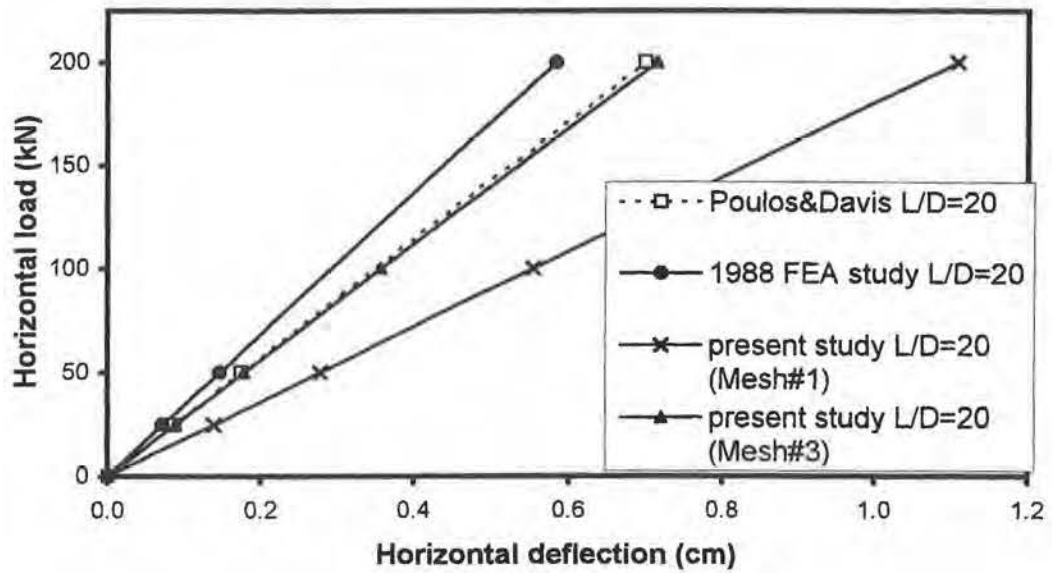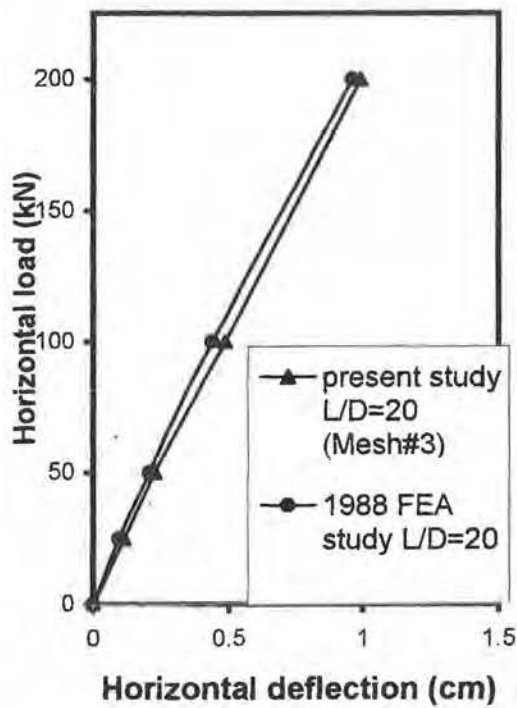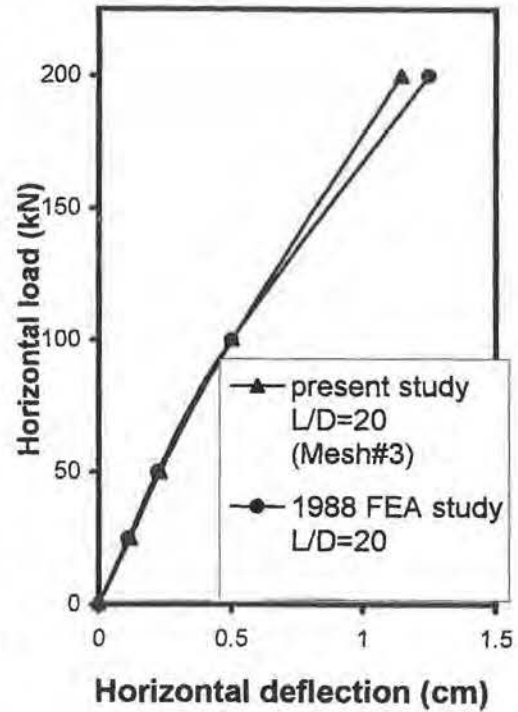
Figure B-7. Response of single socketed pile for: (a) elastic, (b) elastic-gapping, (c) plastic-gapping
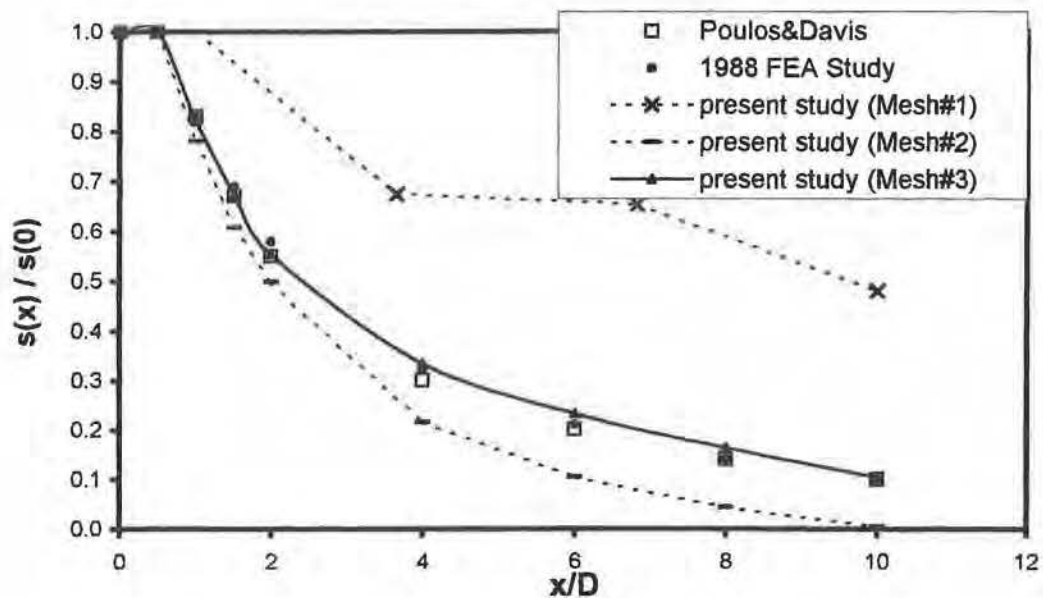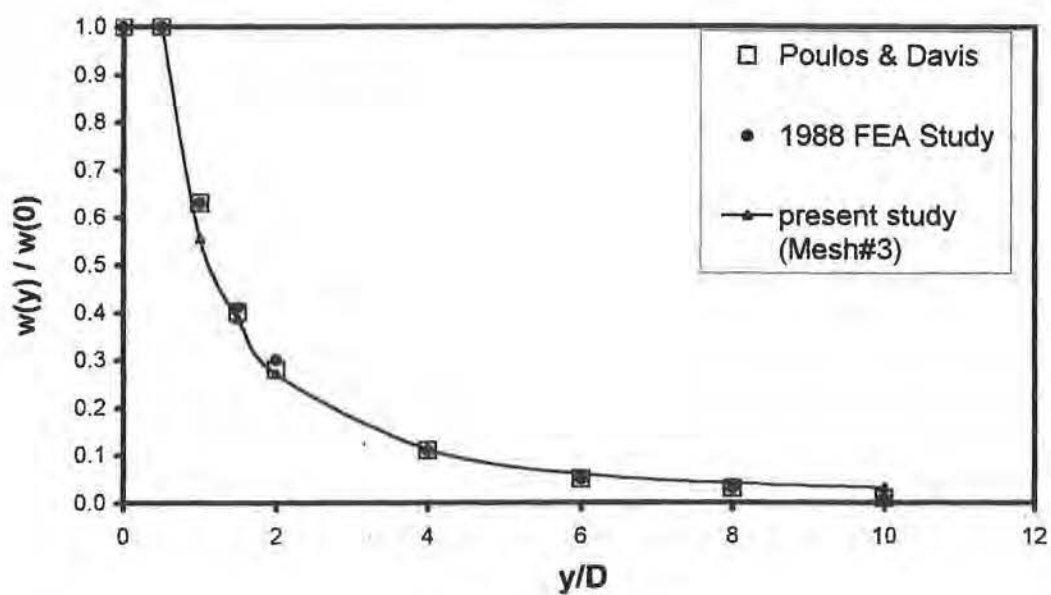
Figure B-8.(a) Comparison of soil displacements along line of loading, s(x), relative to pile head displacement, s(0),(b) Comparison of soil displacements normal to direction of loading, w(y), relative to pile head displacement, w(0)
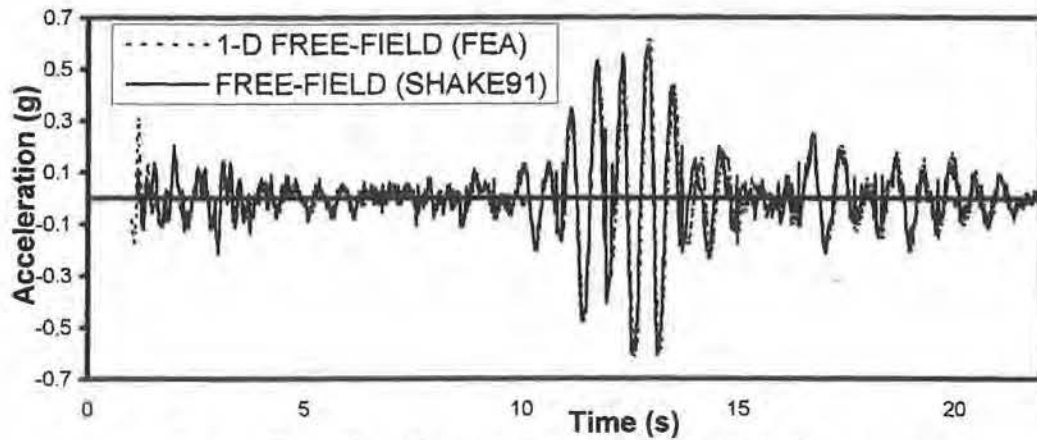
Figure B-9. One dimensional verification of finite element analysis (FEA using ANSYS) with SHAKE91
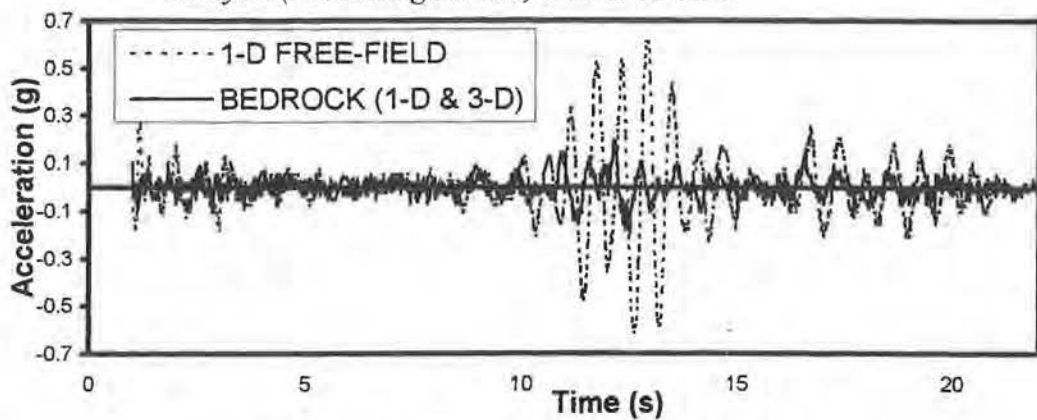
Figure B-10. Response of underlying bedrock and free-field for homogeneous soil (using one-dimensional FEA)
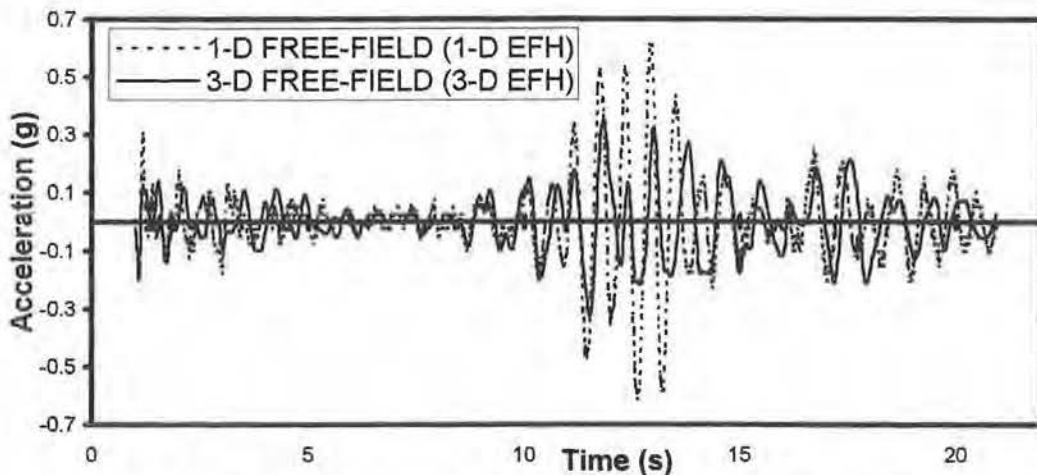
Figure B-11. Elastic free-field response for homogeneous soil (EFH) for one and three dimensional analysis

B-63
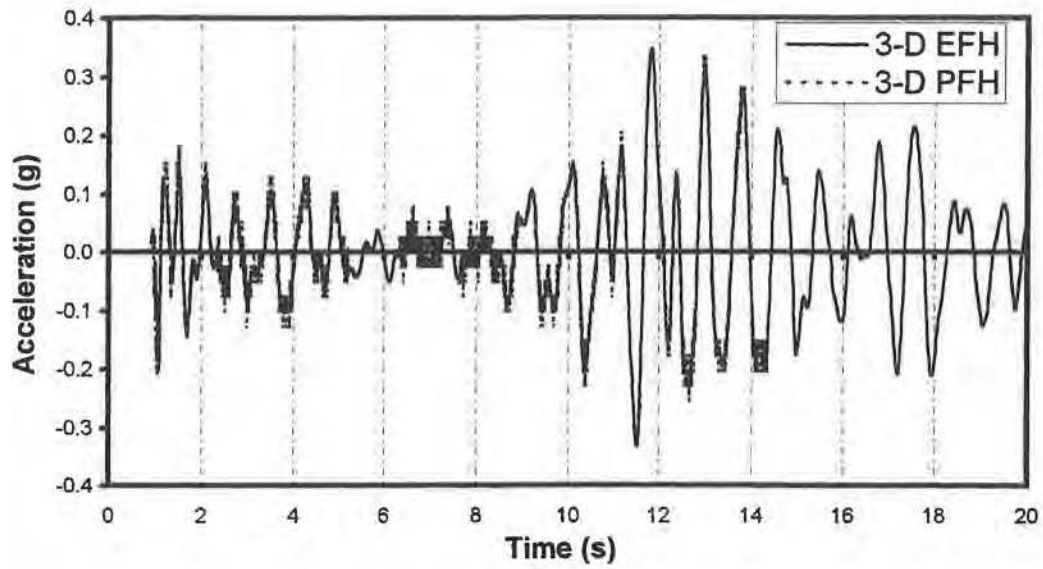
(a)
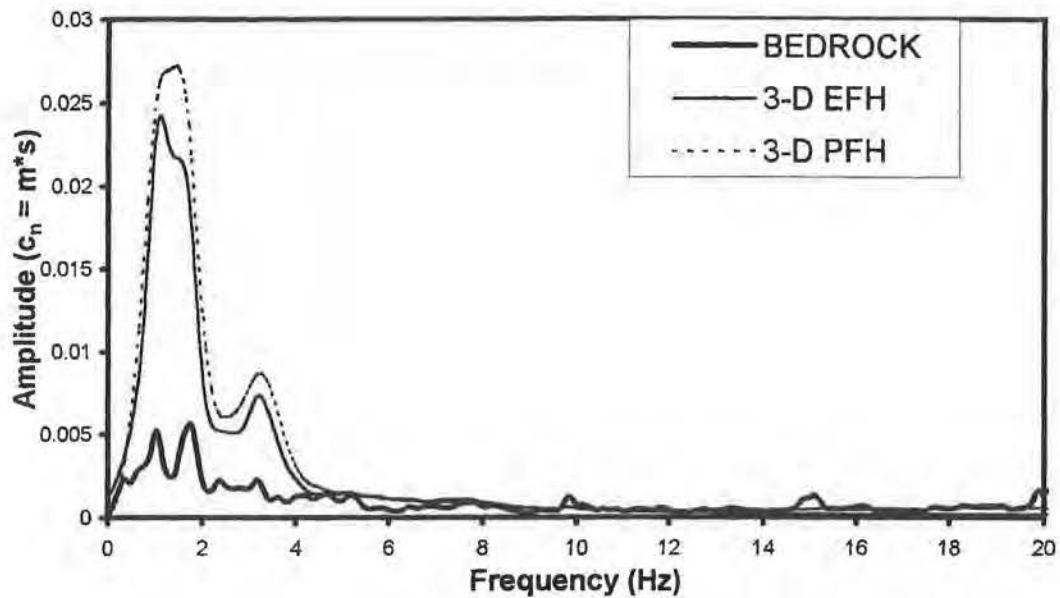
(b)

Figure B-12. (a) Comparison between calculated accelerations for elastic free-field (EFH) and plastic free-field (PFH) using the Druker-Prager criteria for a homogeneous soil profile. (b) Fourier spectrum for the response at the bedrock level, elastic soil free-field, and plastic soil free-field

B-64
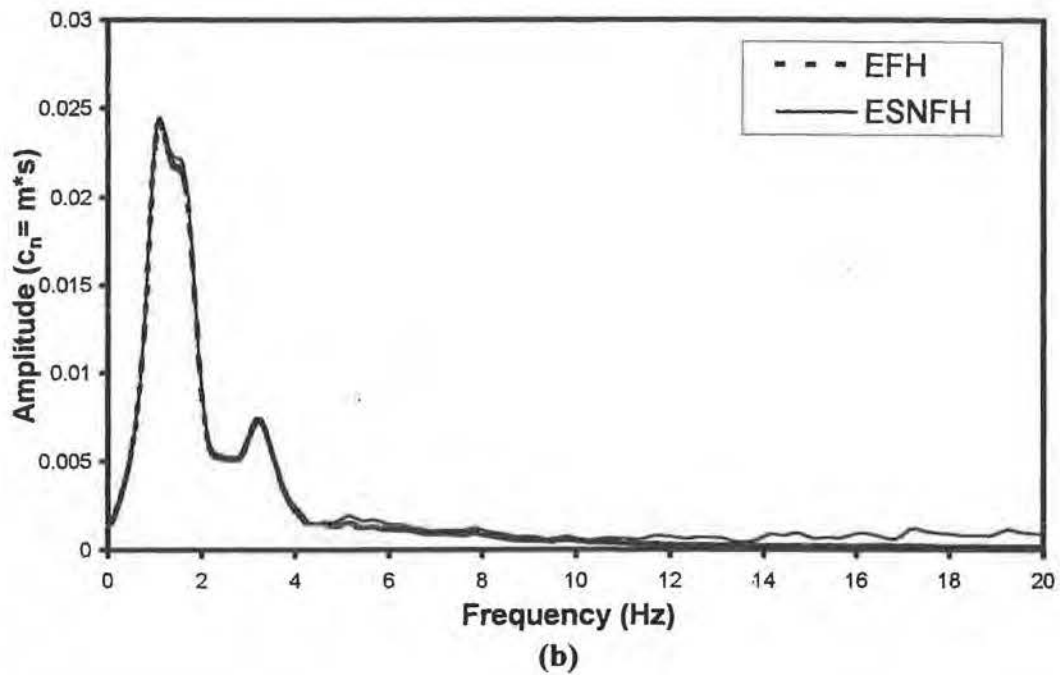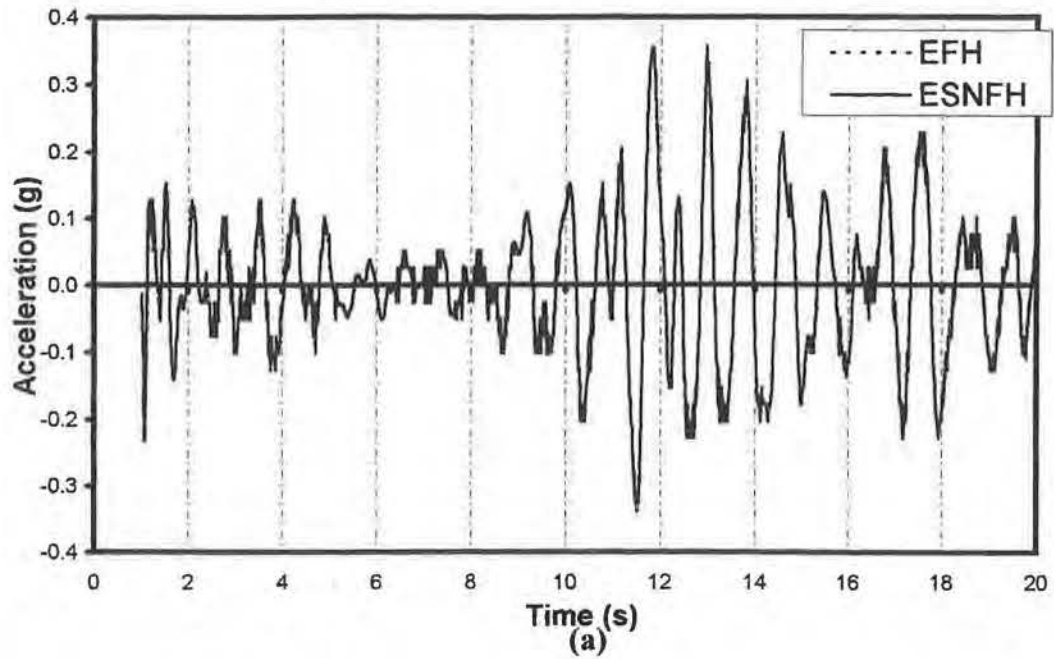
Figure B-13. (a) Comparison between calculated accelerations for elastic free-field (EFH) and floating pile head (ESNFH) for a homogeneous elastic soil profile. (b) Fourier spectrum for the response of the elastic soil free-field and floating pile head
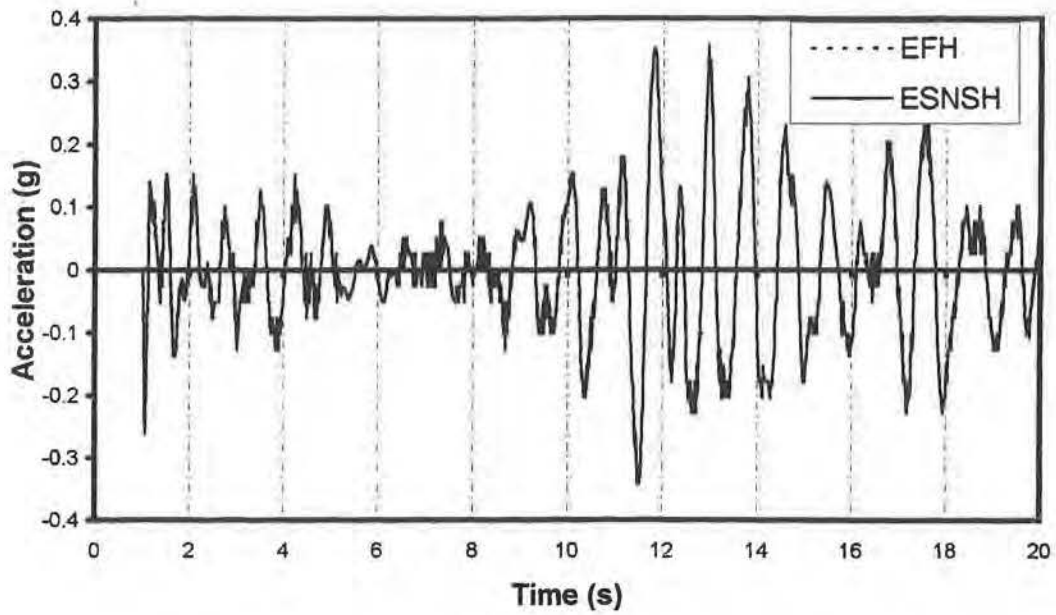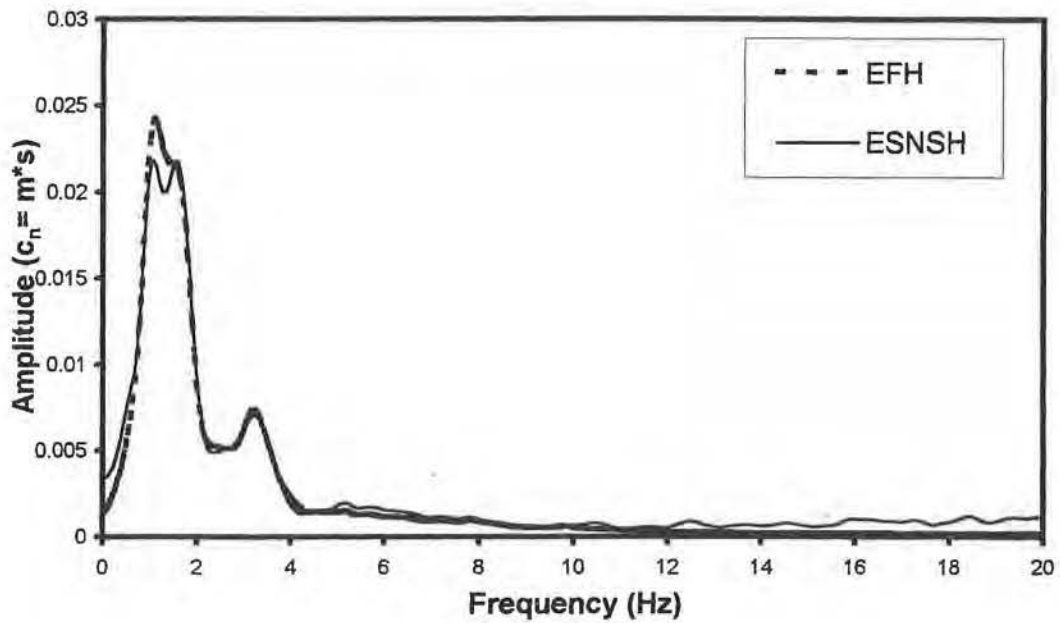
Figure B-14. (a) Comparison between calculated accelerations for elastic free-field (EFH) and socketed pile head (ESNSH) for a homogeneous soil profile. (b) Fourier spectrum for the response at the plastic soil free-field and socketed pile head

B-66
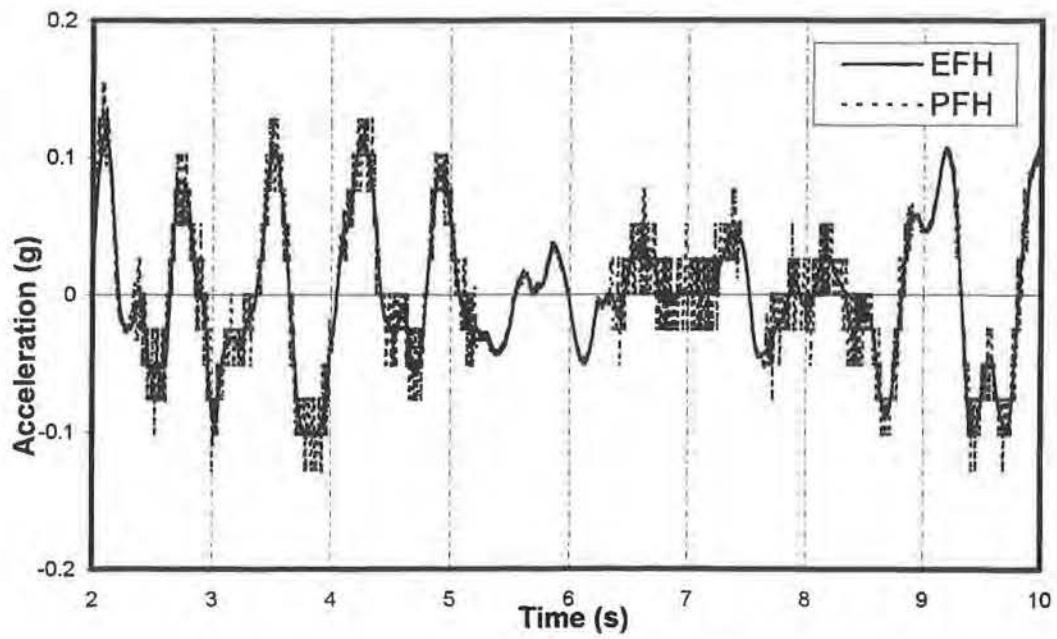
*Figure B-15. EFH and PFH response (Elastic and Plastic free-field,
$E_s = 20000$ kPa)*
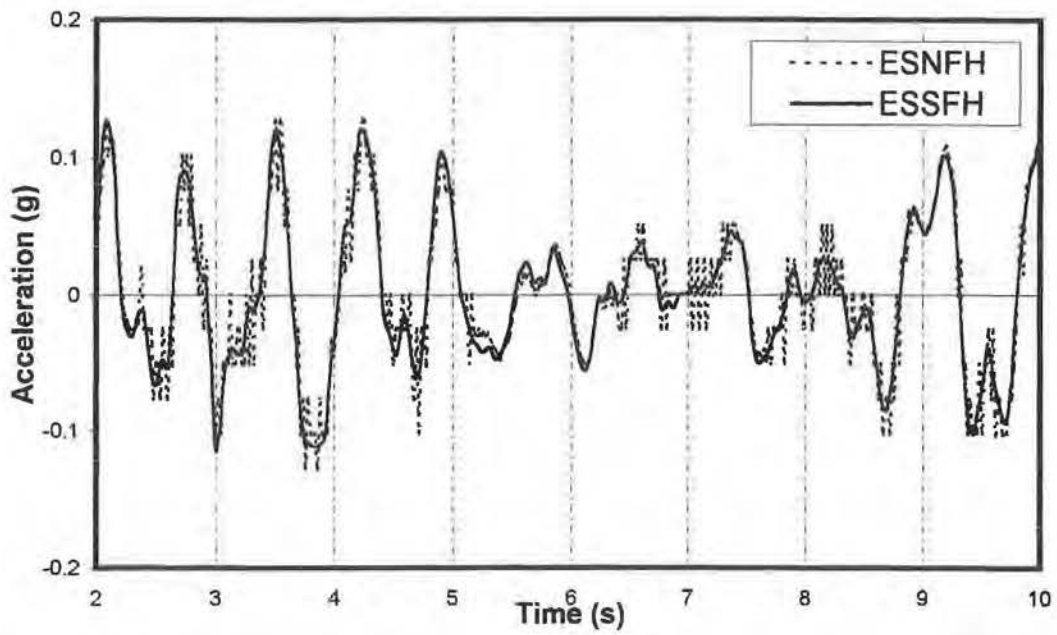
*Figure B-16. Pile head response for floating pile (Elastic, Elastic with
Gapping)*
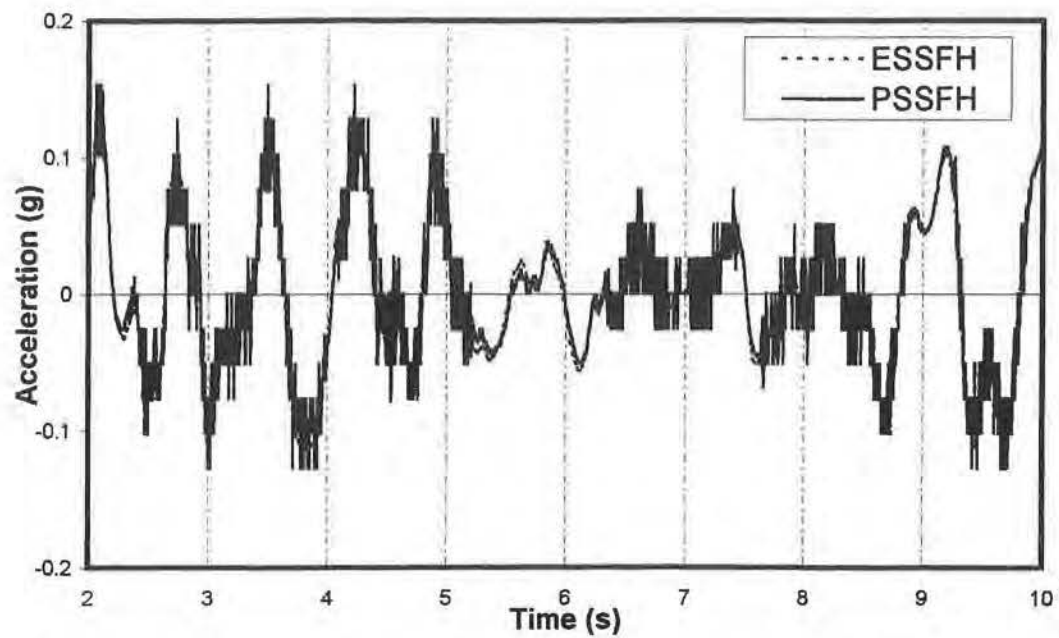
Figure B-17. Pile head response for floating pile (Elastic gapping, Plastic gapping)
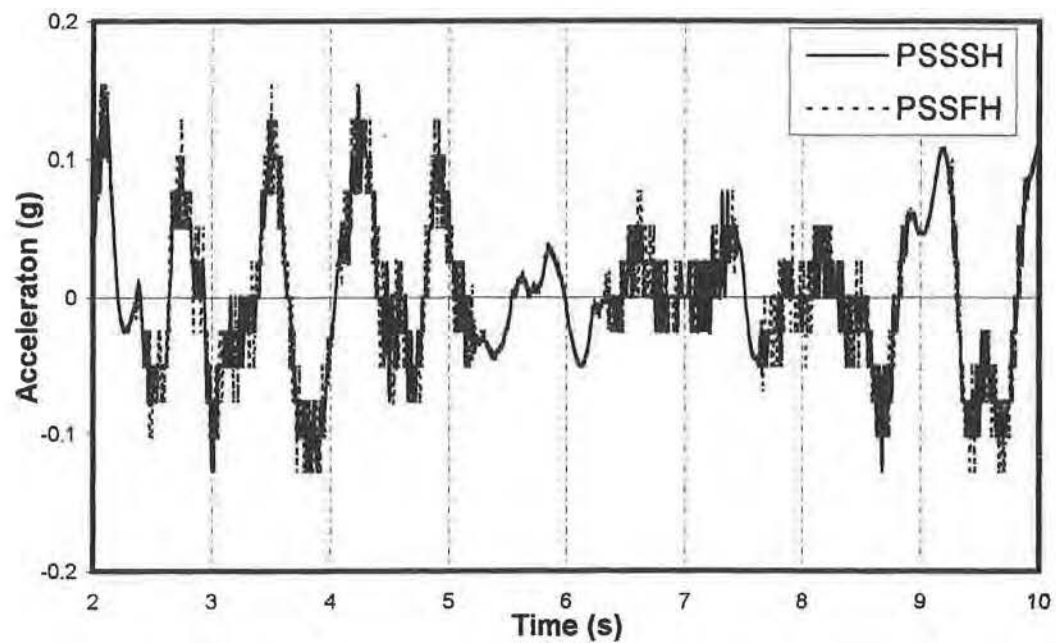
Figure B-18. Pile head response for floating and socketed pile (Plastic Gapping)
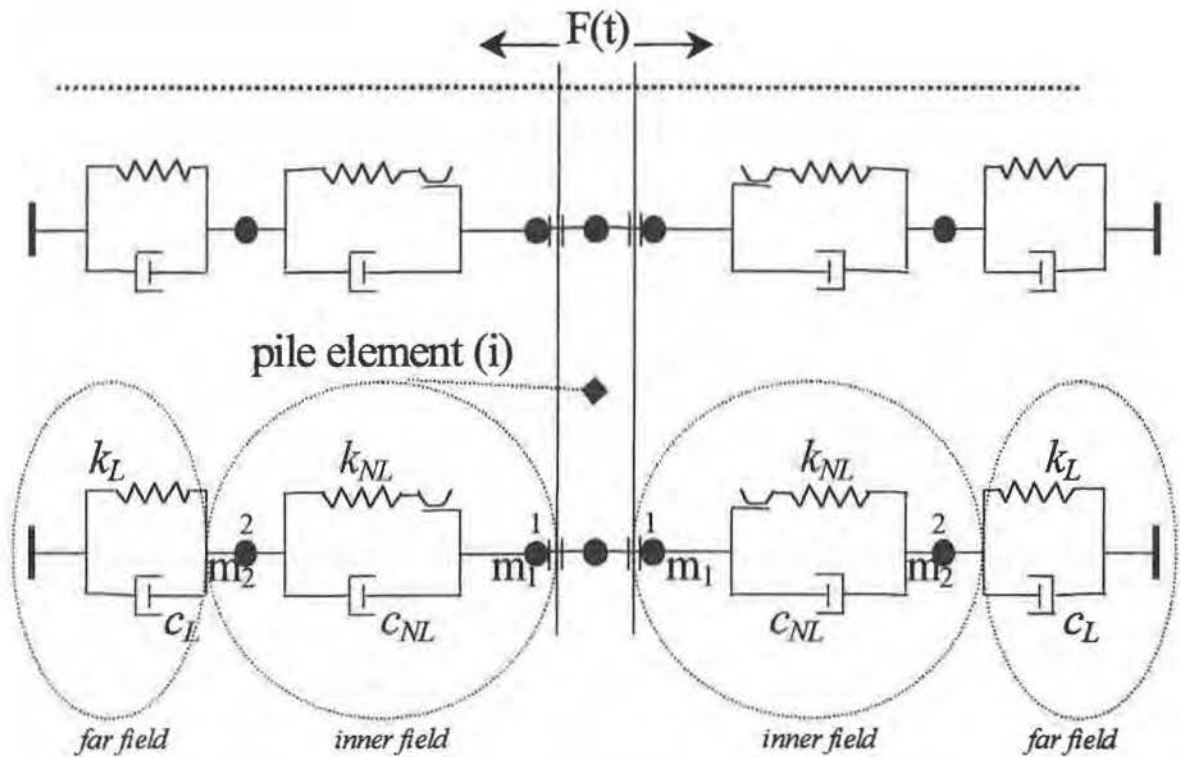
Figure B-19. Element representation of proposed model
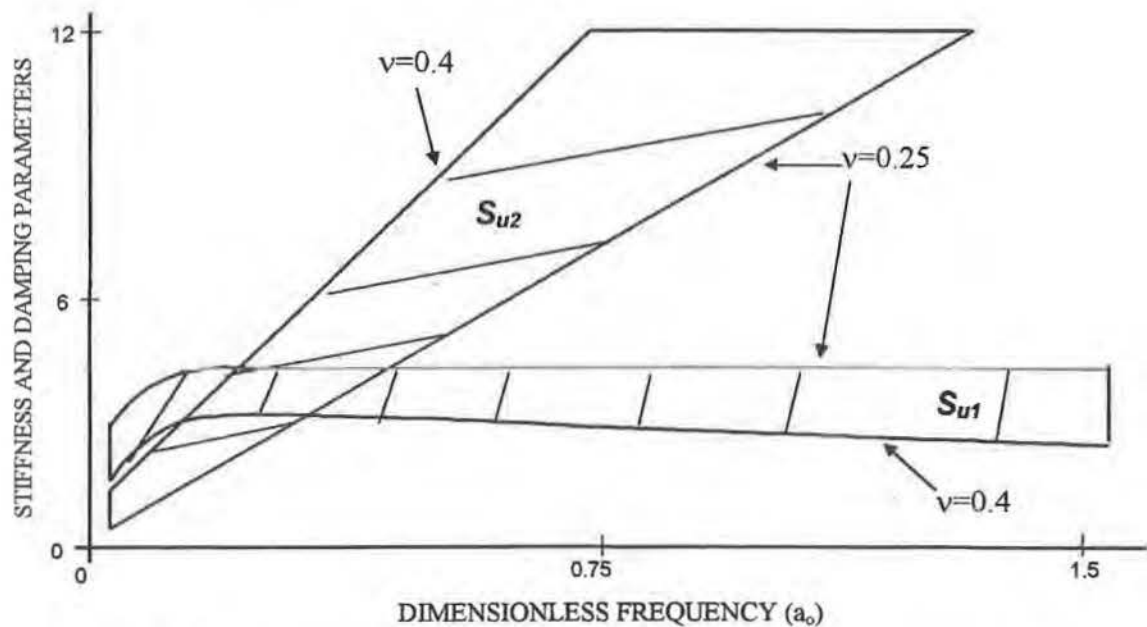
Figure B-20. Envelope of variations of horizontal stiffness and damping stiffness parameters for ν=0.25 - 0.40. (after Novak et al., 1978)

Composite Medium Model (Inner zone-Outer zone)   ***p-y* Curve Model**

NEAR ZONE   FAR ZONE   UNIFIED ZONE

a)
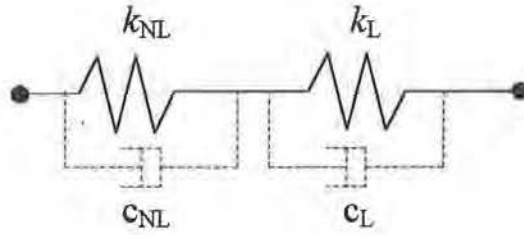
b)

Figure B-21. Soil model: a) Composite medium and p-y curve, b)inclusion of damping
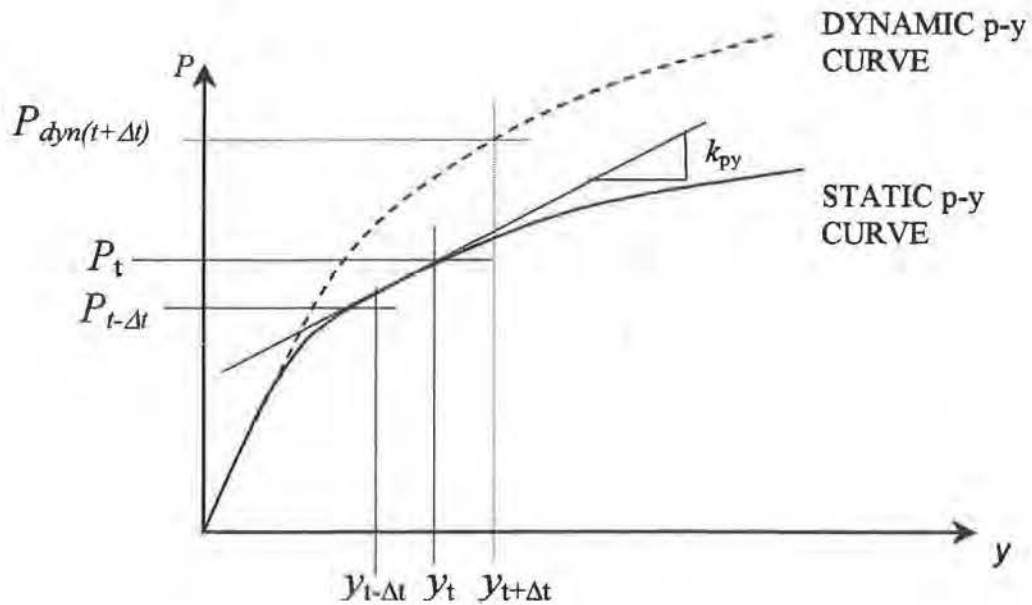
Figure B-22. Determination of stiffness (k_{py}) from an internally generated static p-y curve to produce a dynamic p-y curve (including damping)

PILE-SOIL SYSTEM   **LINEAR**   **PARABOLIC**
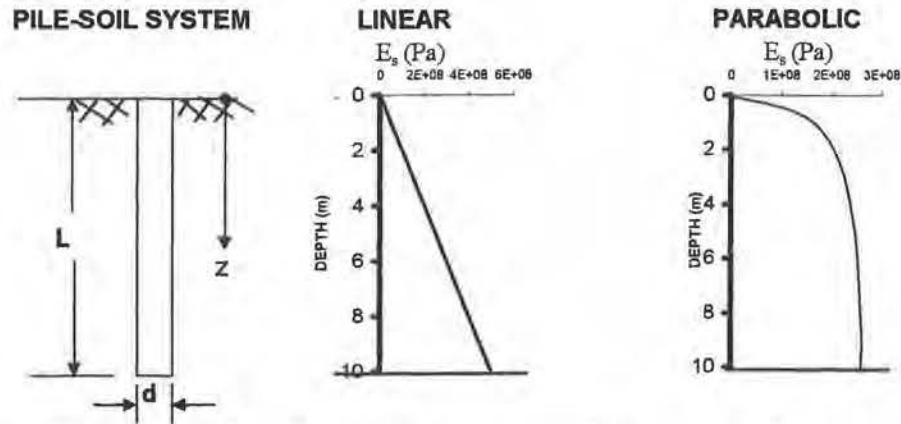
Figure B-23. Soil modulus variation for profiles considered in the analysis
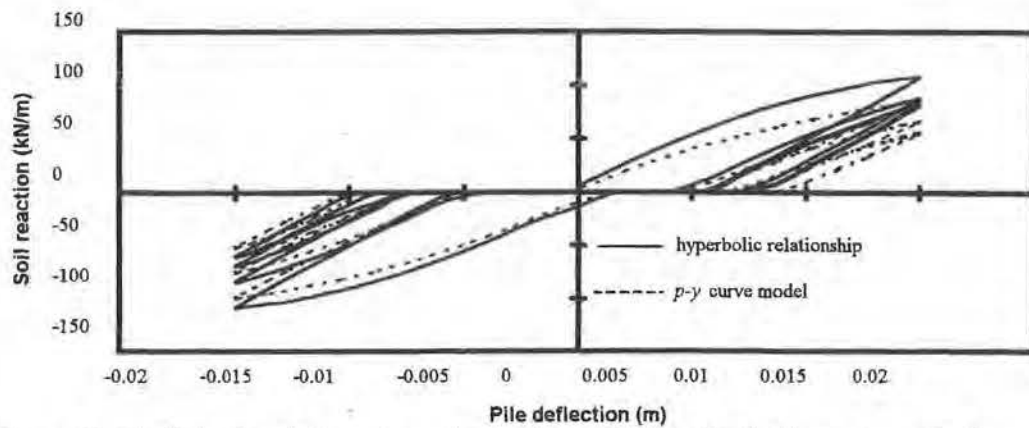
Figure B-24. Calculated dynamic soil reactions at 1.0 m depth (for a prescribed harmonic displacement at pile head with amplitude = 0.015m, L/d=30)
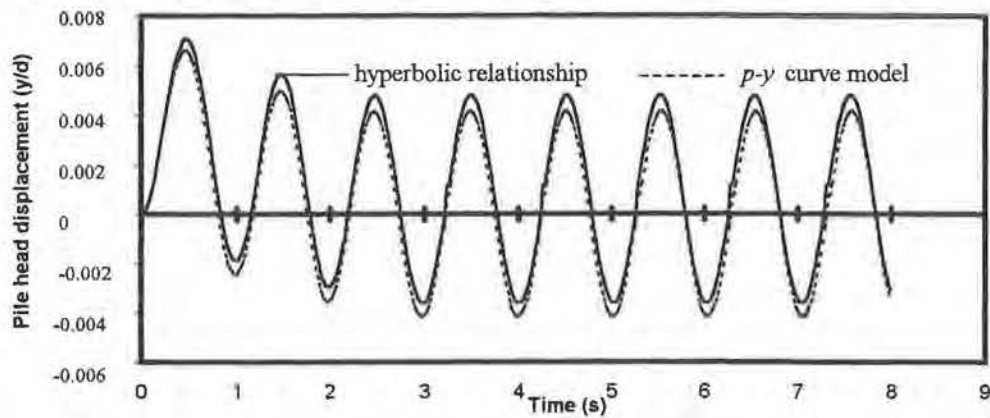
Figure B-25. Pile head response under applied harmonic load with amplitude equal to 10% of the ultimate load (L/d=30, $E_p/E_s(L)=1000$, linear profile)

B-71

Parabolic Halfspace $E_p/E_s(L)=1000$ L/d=25   d=0.5m $\rho_p/\rho_s=1.25$

(a)

(b)
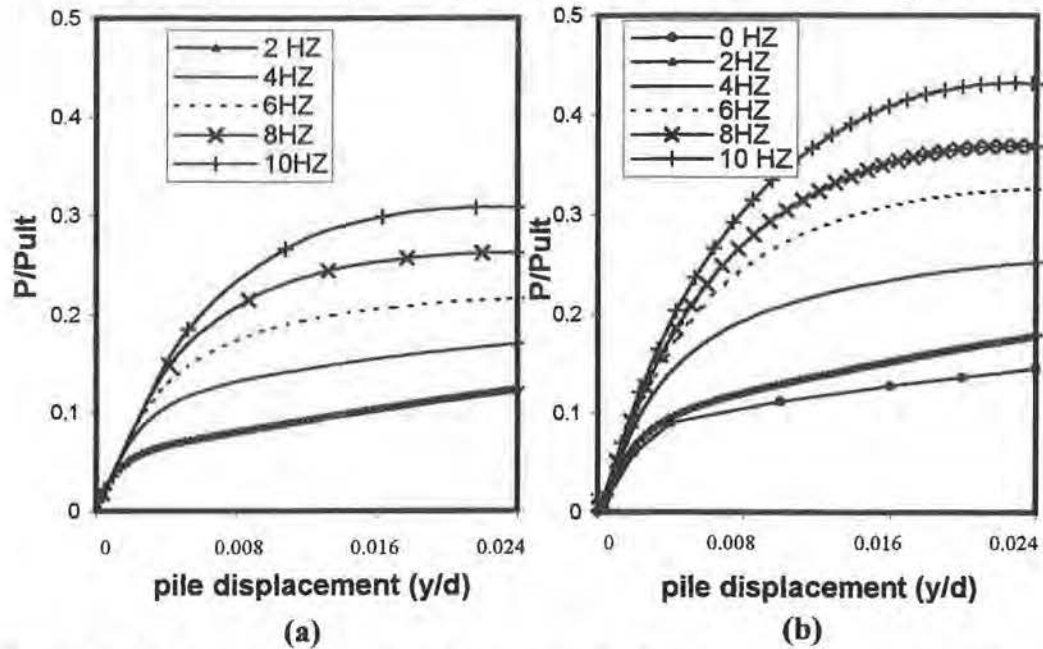
Figure B-26. Calculated dynamic p-y curves at 1.5 m depth (for a prescribed harmonic displacement at pile head with amplitude equal to 0.05d) using: (a) hyperbolic model, (b) p-y curve model

(a)

(b)
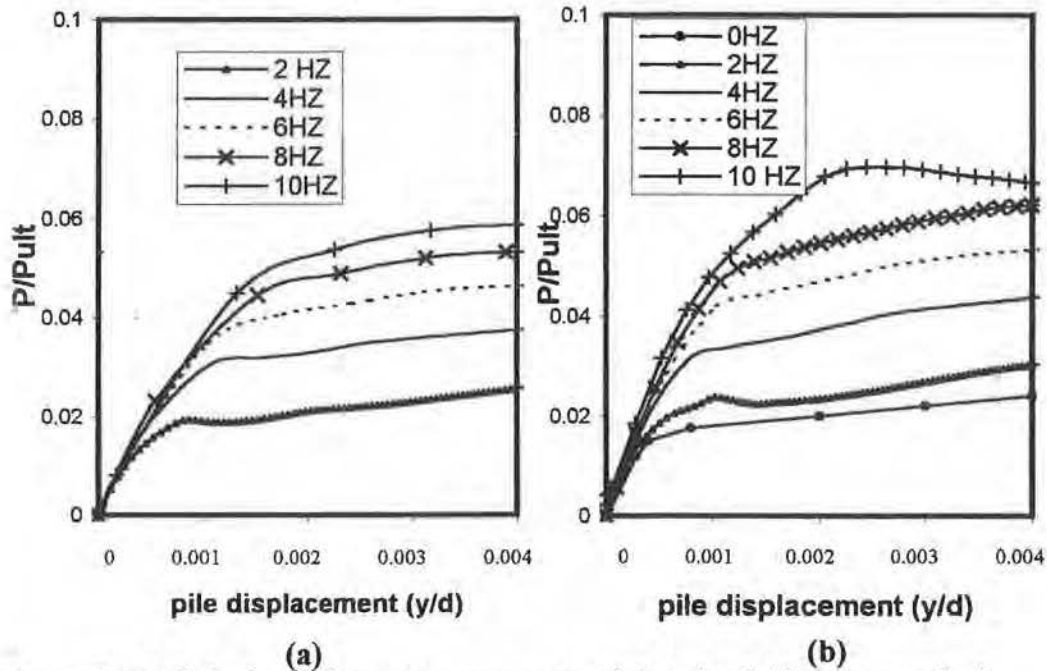
Figure B-27. Calculated dynamic p-y curves at 3.0 m depth (for a prescribed harmonic displacement at pile head with amplitude equal to 0.05d) using: (a) hyperbolic model, (b) p-y curve model

B-72
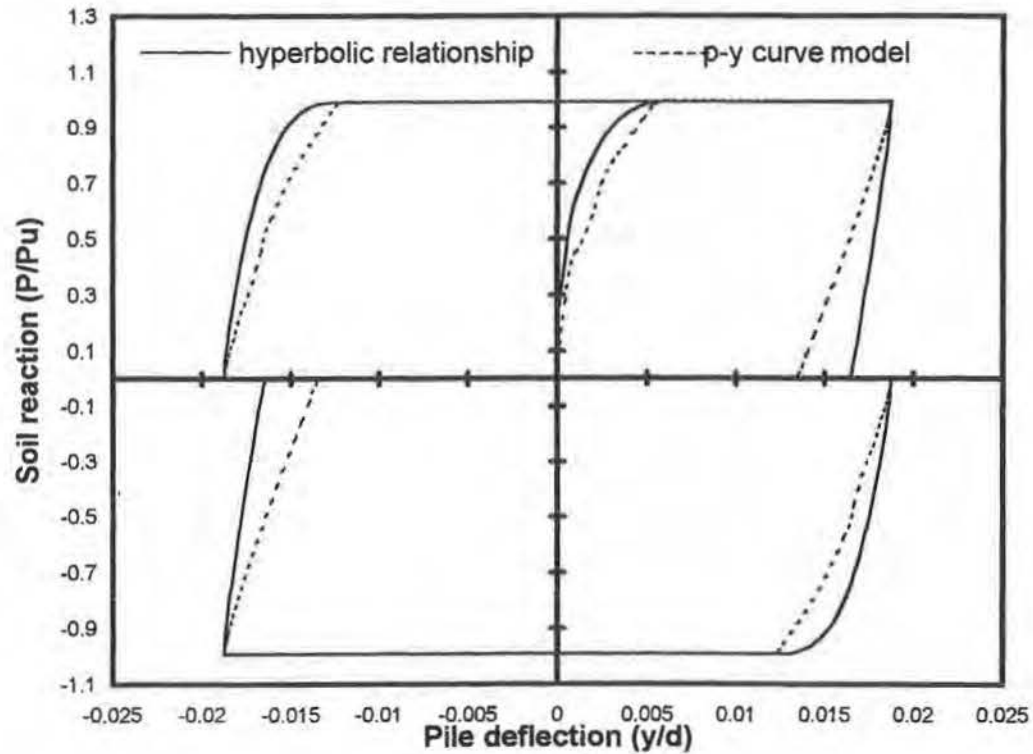
Figure B-28. Calculated dynamic soil reactions at 1.0 m depth (for a prescribed harmonic displacement at pile head with amplitude equal to 0.0375d, L/d = 25, $E_p/E_s(L) = 1000$)
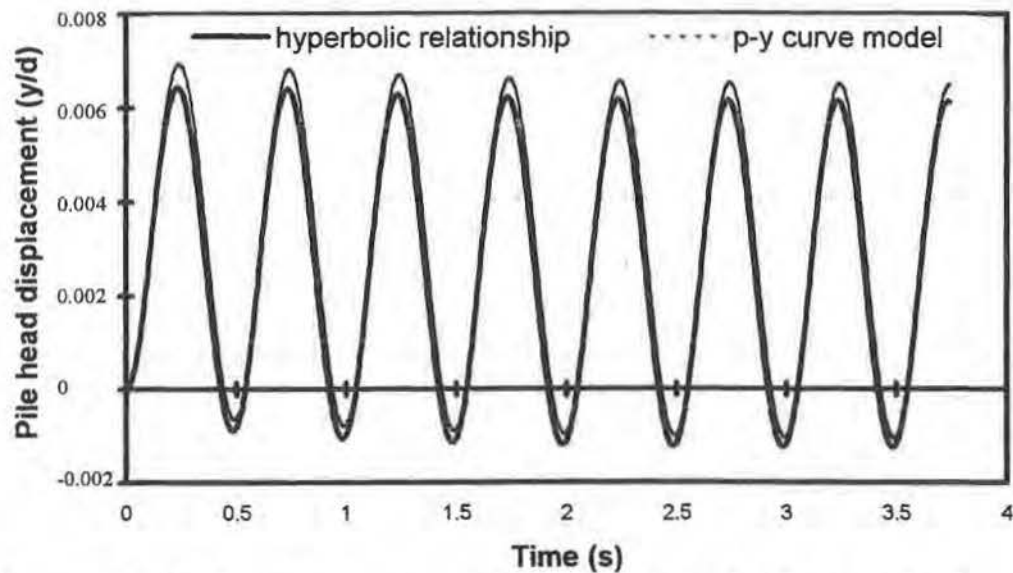
Figure B-29. Pile head response to applied harmonic load with an amplitude equal to 8% of the ultimate load (L/d =25, $E_p/E_s(L) = 1000$, linear profile)

B-73

Loose Sand - Linear Halfspace - $E_p/E_s(L)=1000$ $L/d=25$ $\rho_p/\rho_s=1.25$

(a)   (b)
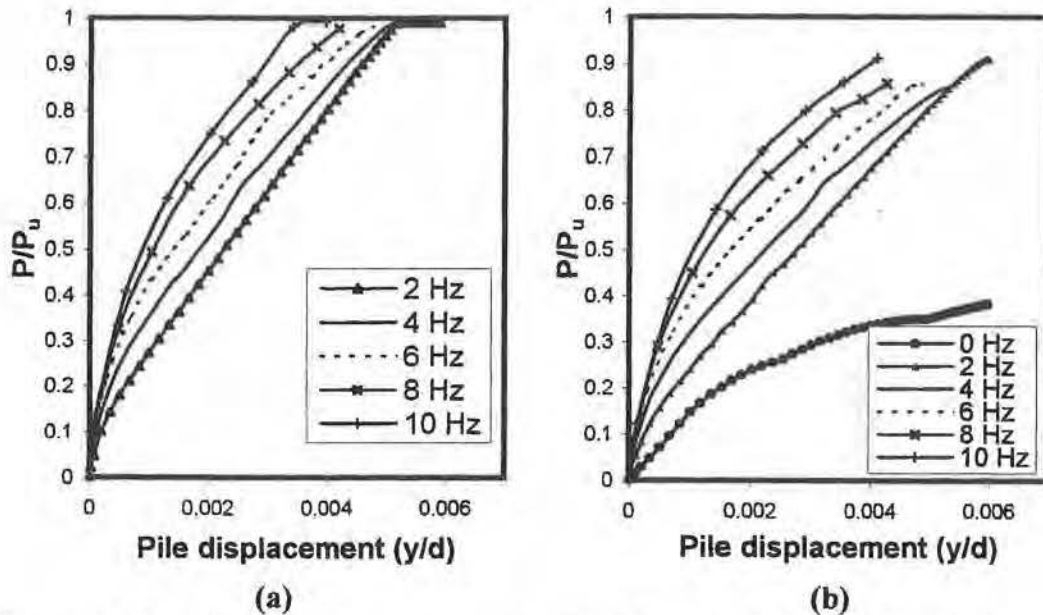
Figure B-30. Calculated dynamic p-y curves at 3.0 m depth (for a prescribed harmonic displacement at pile head with amplitude equal to 0.05d) using: (a) hyperbolic model, (b) p-y curve model

(a)   (b)
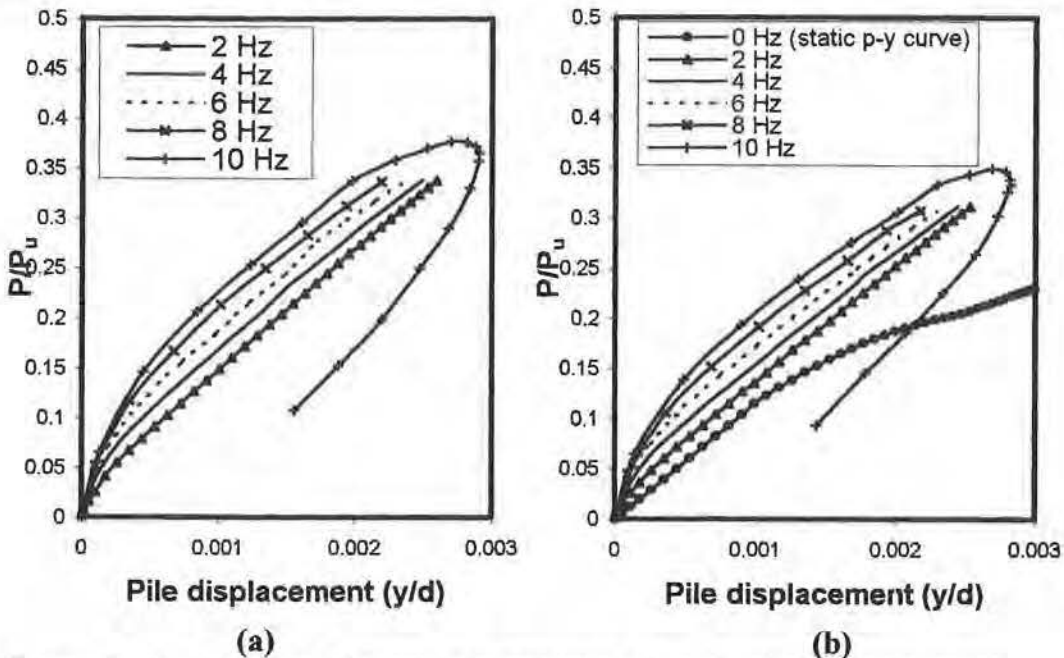
Figure B-31. Calculated dynamic p-y curves at 4.0 m depth (for a prescribed harmonic displacement at pile head with amplitude equal to 0.05d) using: (a) hyperbolic model, (b) p-y curve model

B-74

STATNAMIC DEVICE

1.30m

Tan brown fine sand
SPT = 10

4.00m

Gray silty clay
C_u = 20 kPa

3.00m

Gray green fine sand
SPT = 16

2.50m

0.61m

13.70m

Gray calcareous coarse sand
SPT = 35

7.00m

Gray fine sand
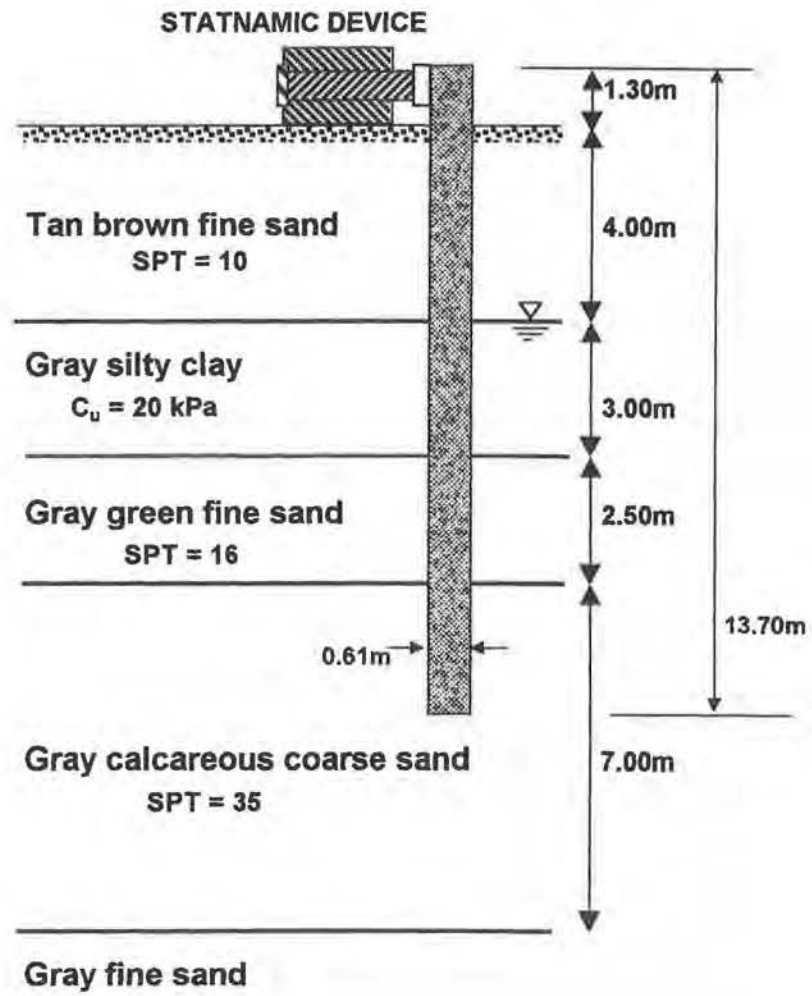
Figure B-32. Soil profile and Statnamic pile test set-up at Camp Johnson, Jacksonville
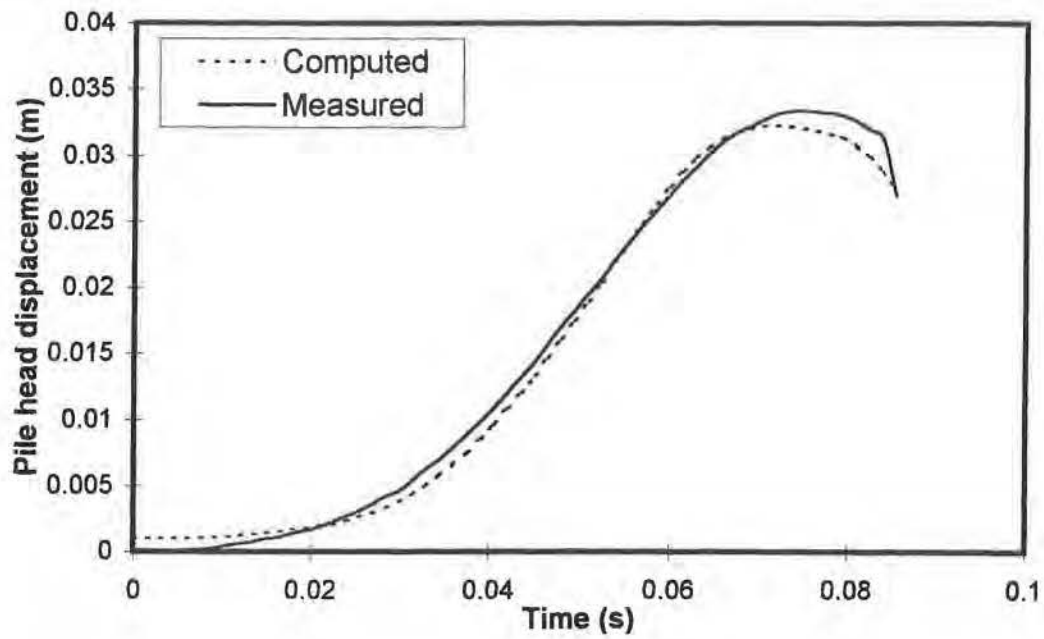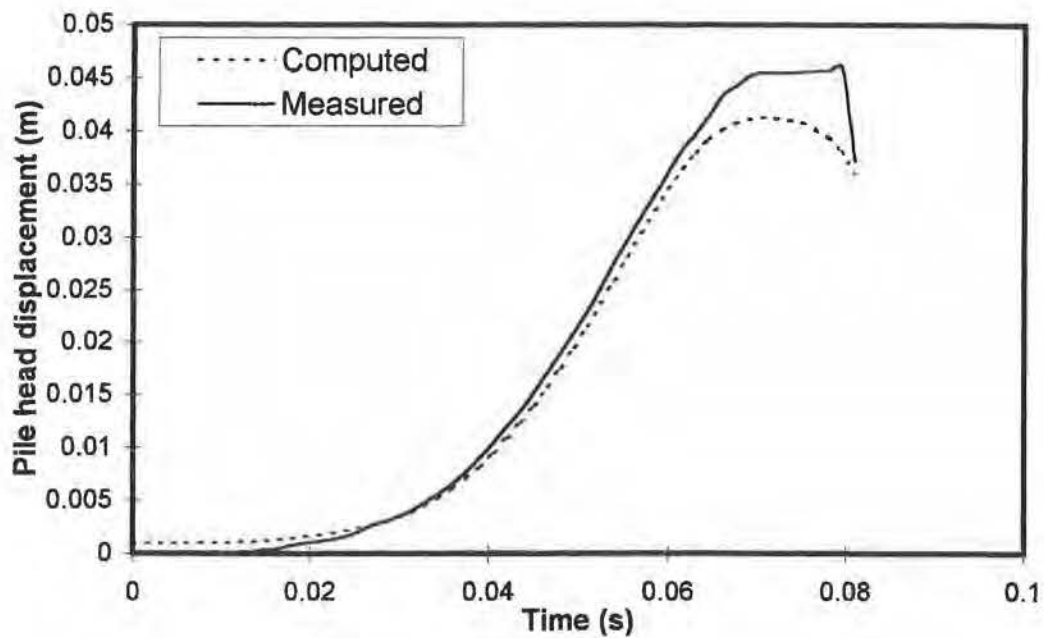
Figure B-33. Pile head displacement for Statnamic test with peak load equal to:
(a) 350 kN, (b) 470 kN

B-76

Case I (Parabolic)

L

V_s

d
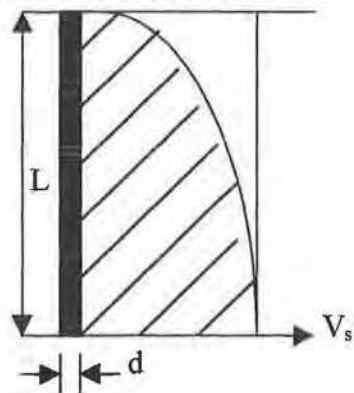
ρ_s = 2000 kg/m³
ρ_p/ρ_s = 3.75
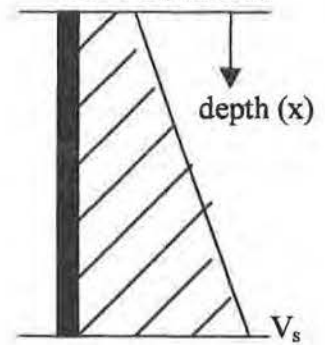
PILE (steel pipe)

E_p = 200 GPa
ρ_p = 7500 kg/m³
L = 10 m
t = 9 mm

t

d

Case II (Linear)

depth (x)

V_s
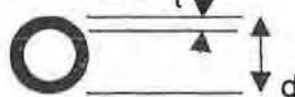
Figure B-34. Description of soil and pile properties for Case I and Case II
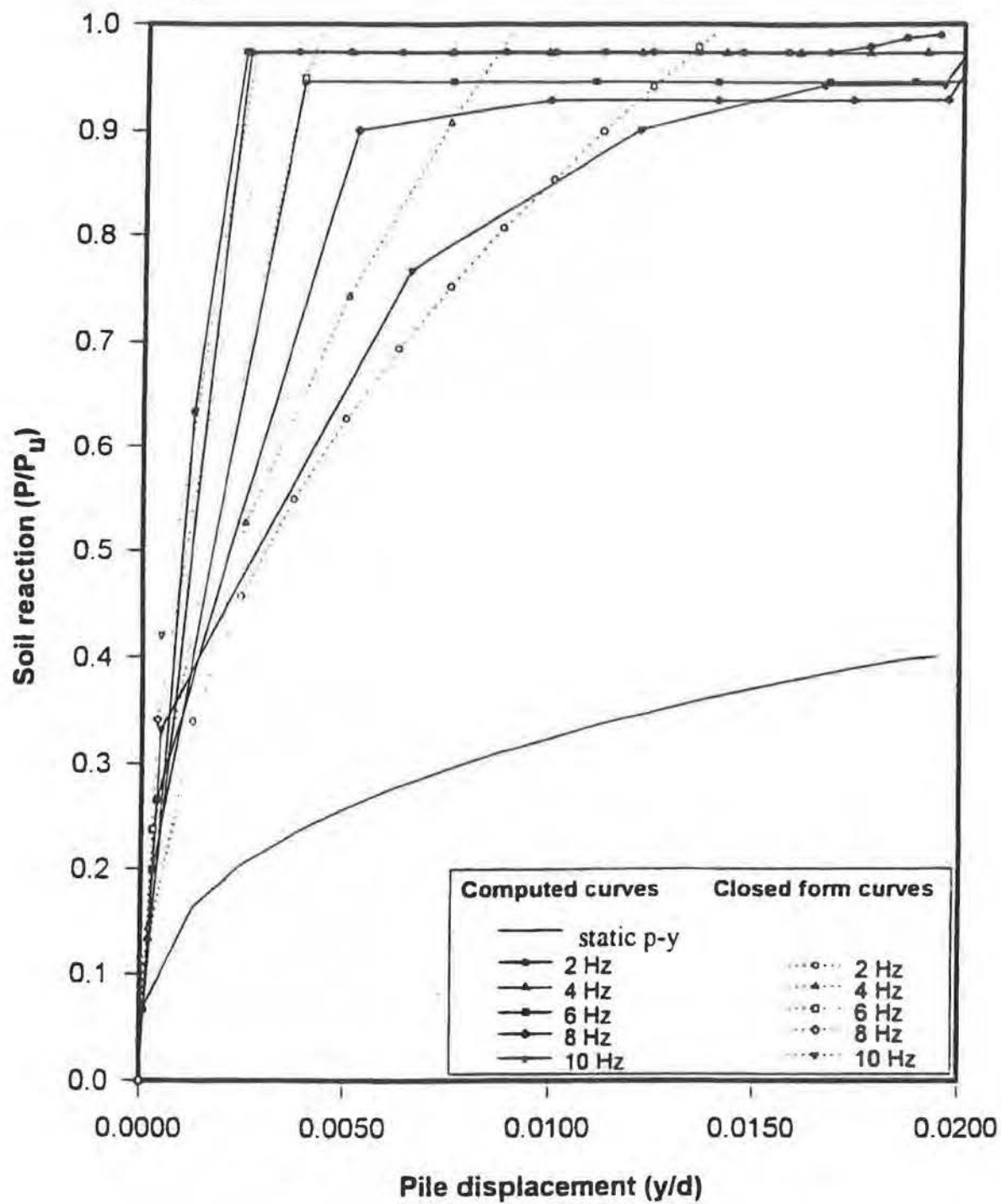
Figure B-35. Dynamic p-y curves and static p-y curve for case C1 (depth = 1.0 m)

B-78
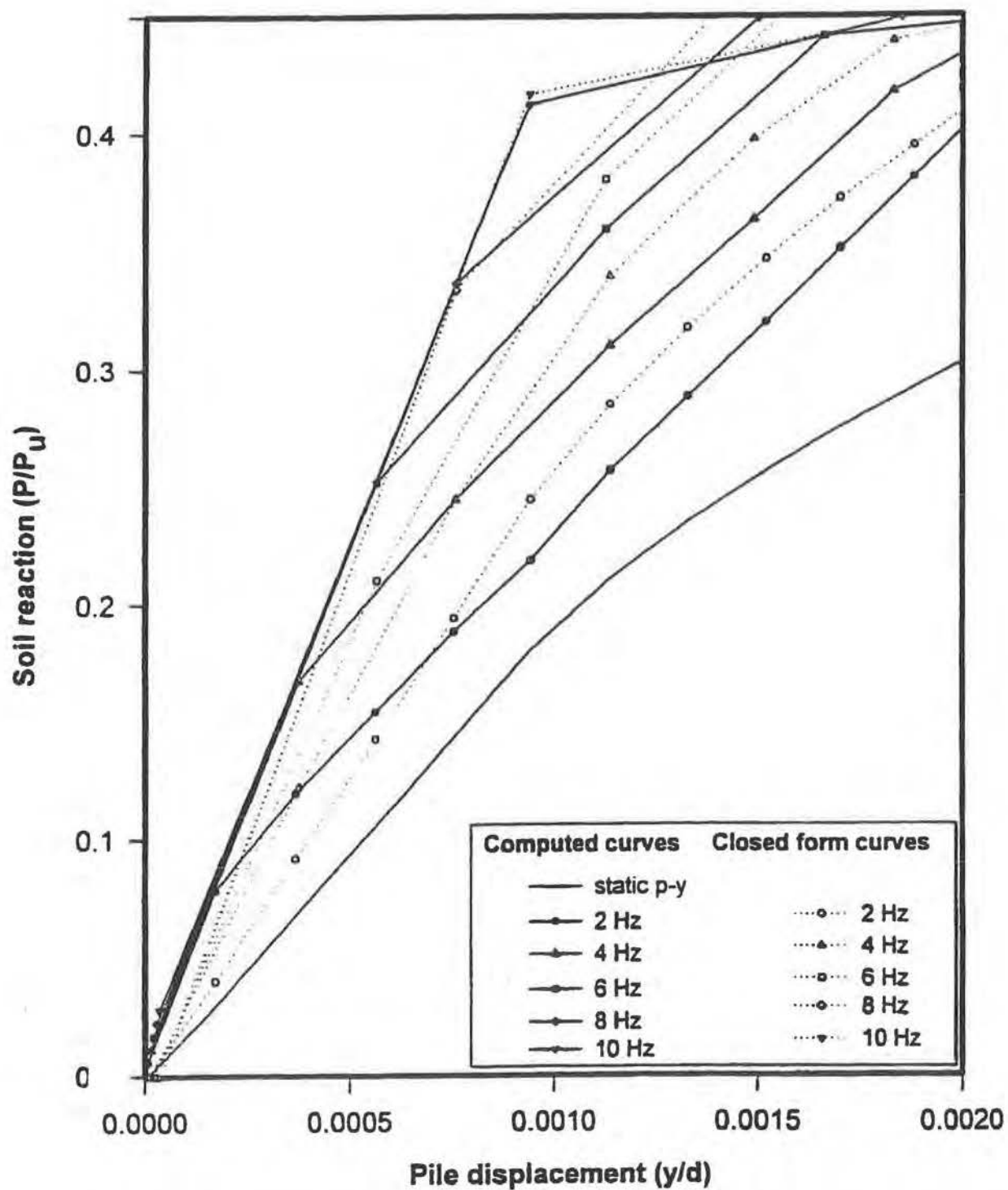
Figure B-36. Dynamic p-y curves and static p-y curve for case S5 (depth = 1.5 m)
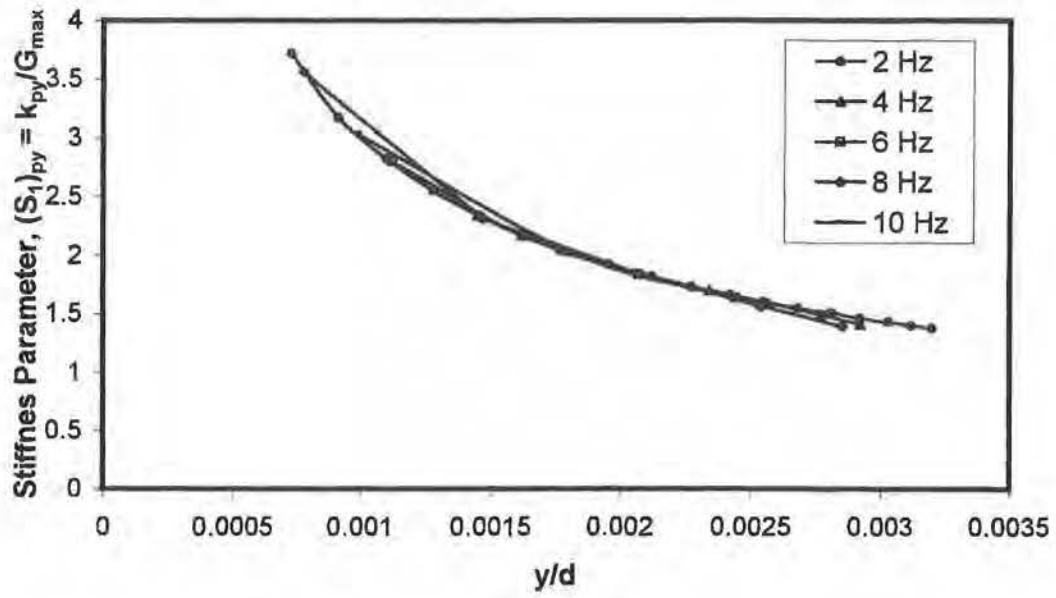
Figure B-37. True stiffness parameter for Test C1 (Soft Clay)
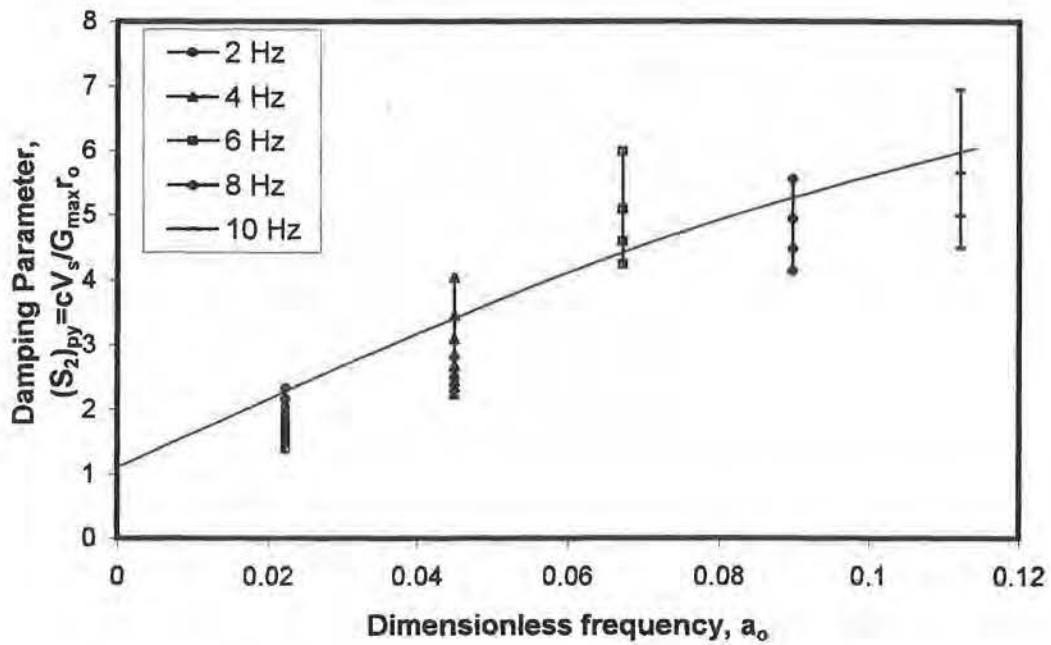
Figure B-38. Equivalent damping parameter for Test C1 (Soft Clay) with dimensionless frequency
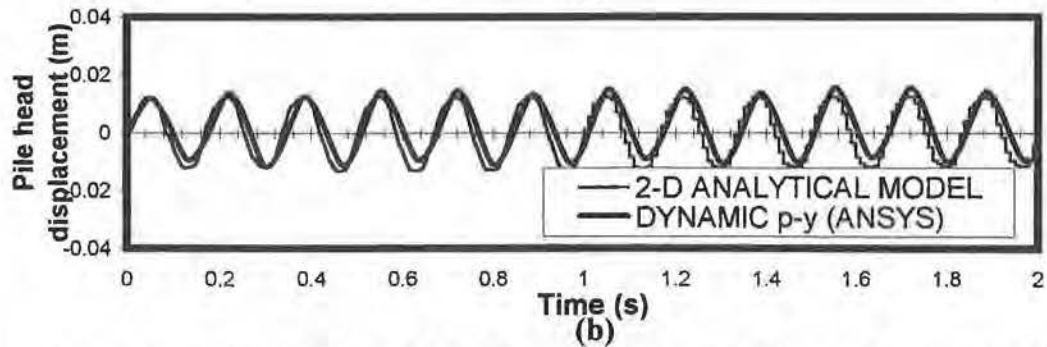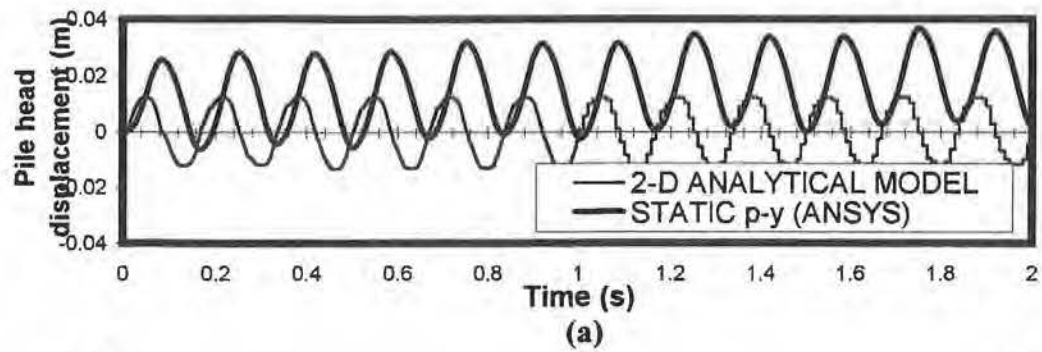
Figure B-39. Calculated pile head response using 2-D analytical model compared with ANSYS using: (a) static p-y curves, (b) dynamic p-y curves
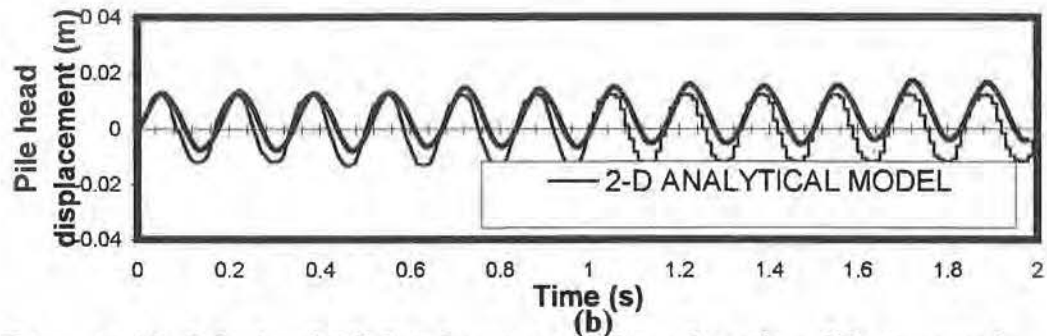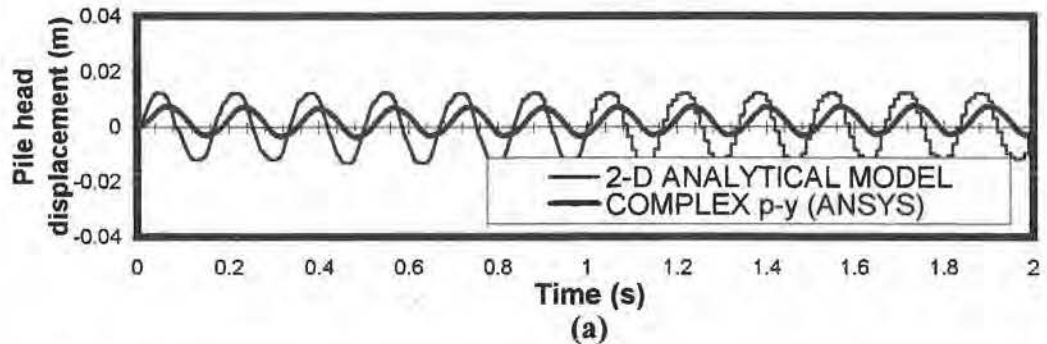
Figure B-40. Calculated pile head response, 2-D analytical model, compared with ANSYS using: (a) complex stiffness, (b) modified complex stiffness
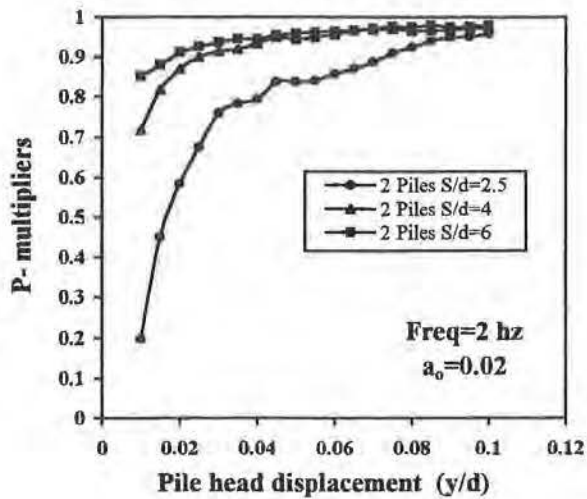
B-81
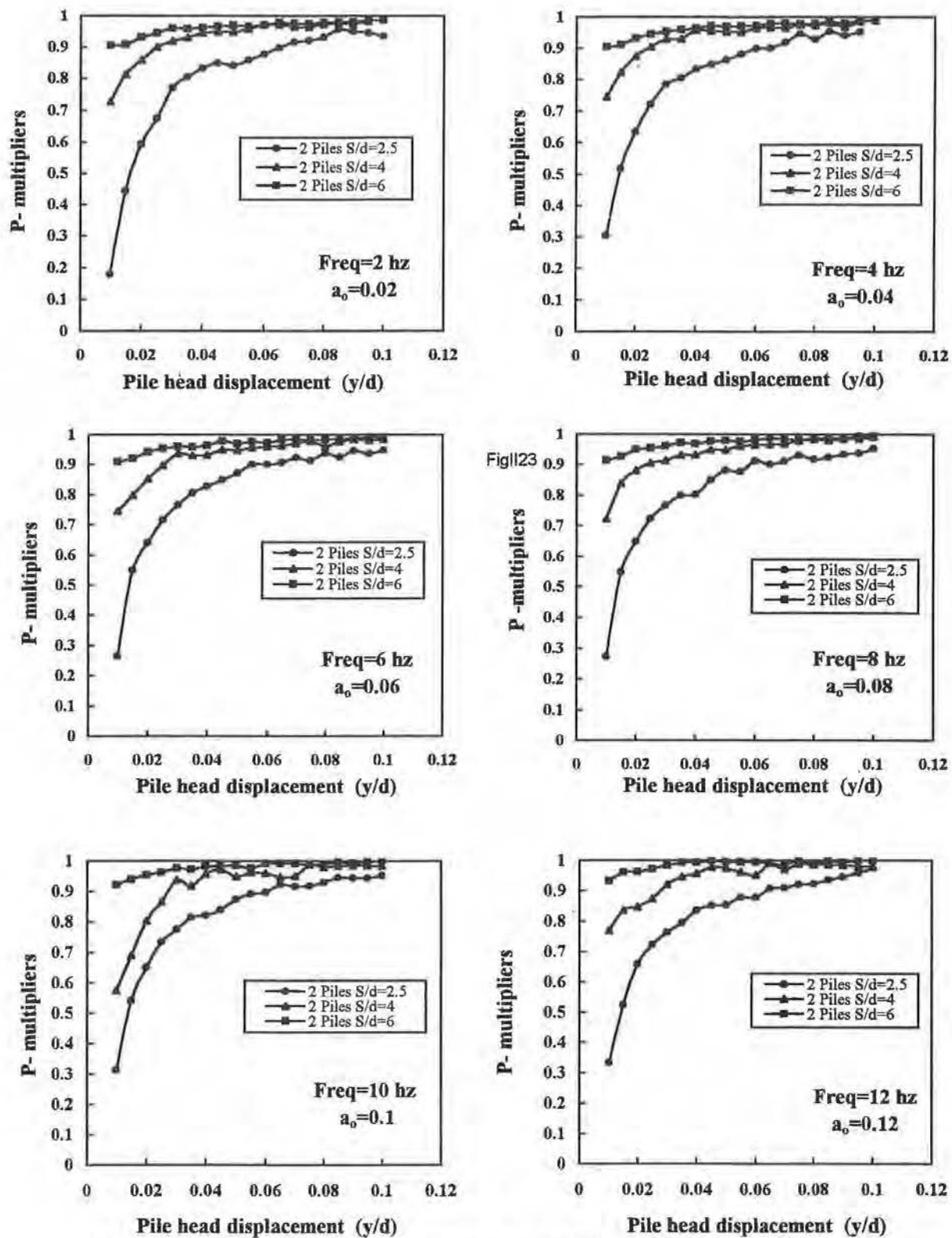
Figure B-41. P-multipliers versus pile head displacement for loose sand
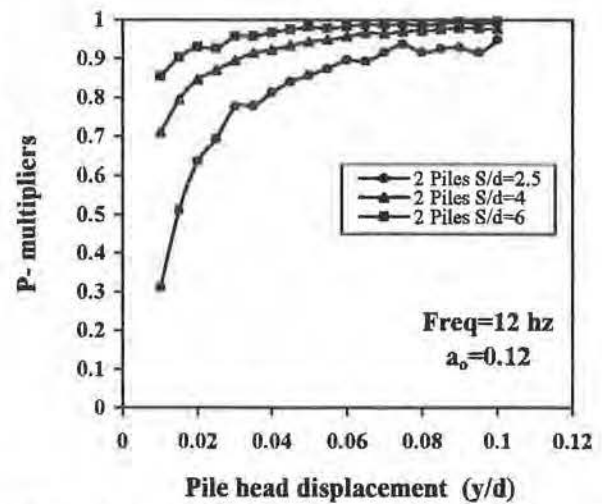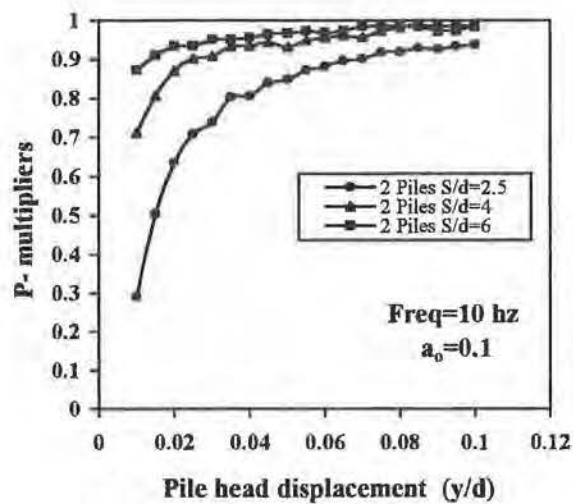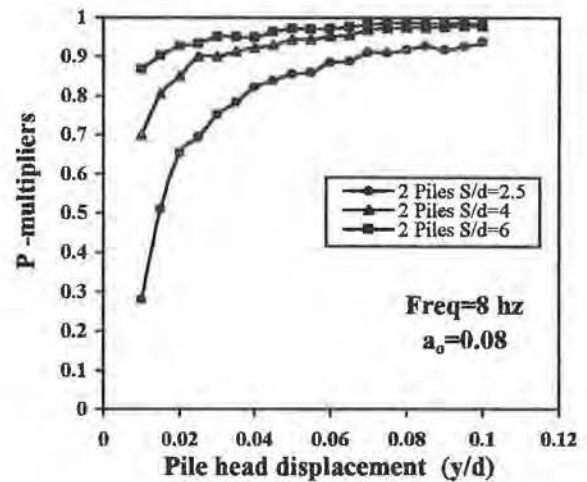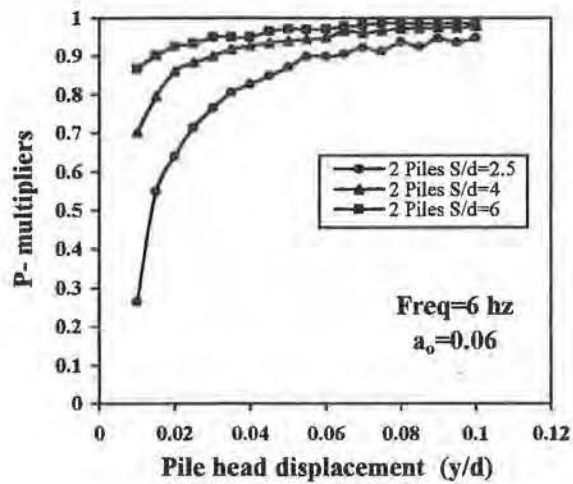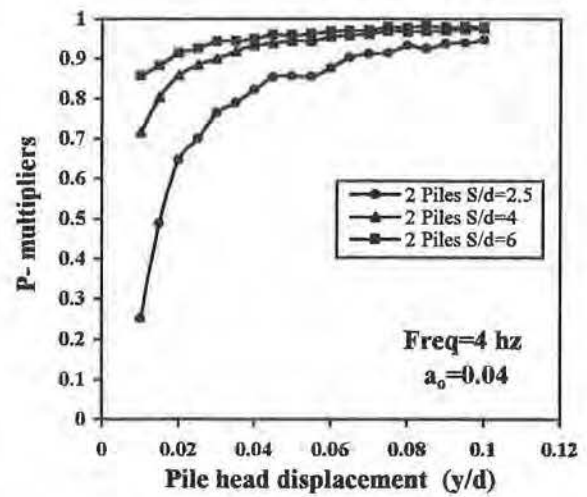
Figure B-42. P-multipliers versus pile head displacement for medium dense sand

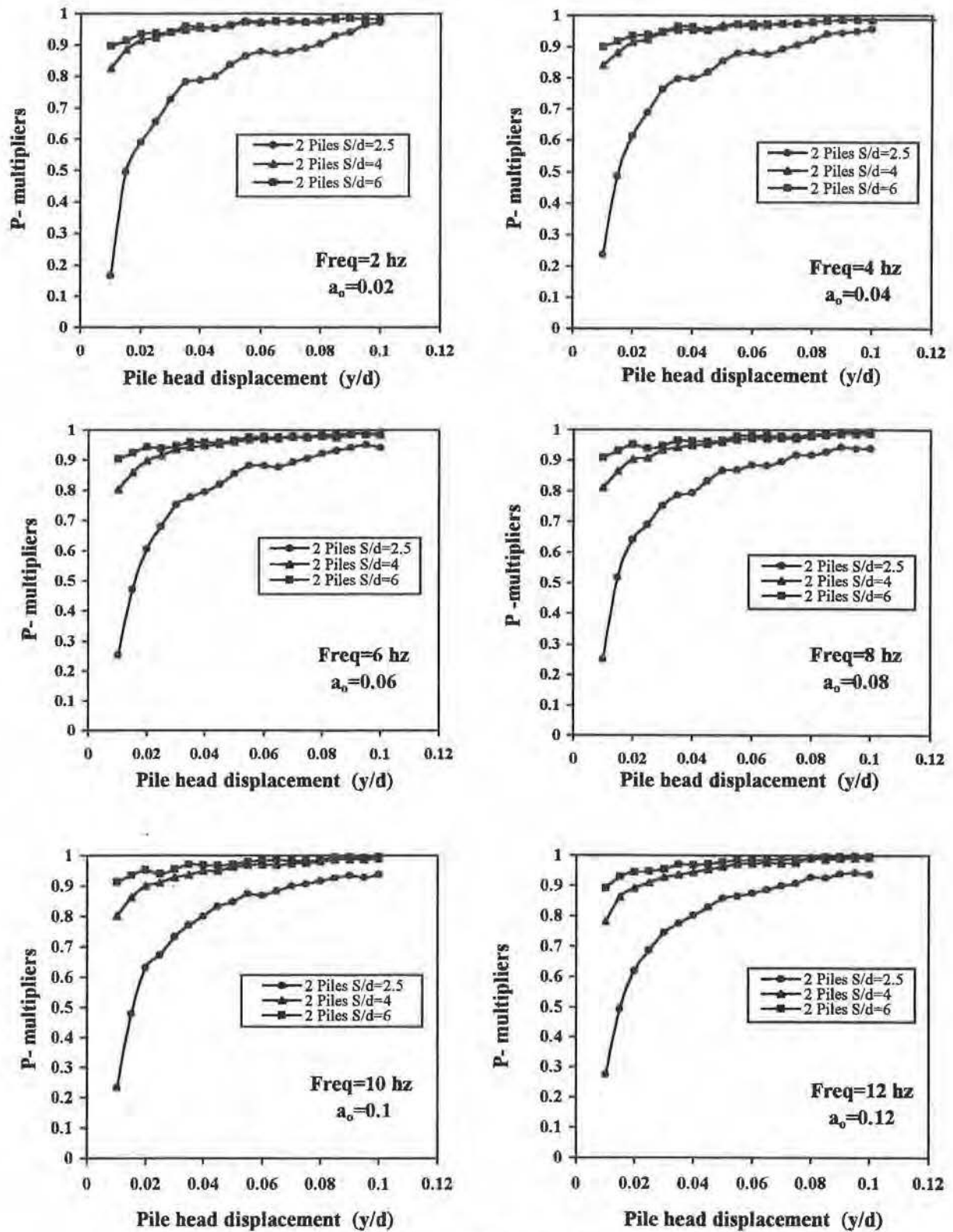*Figure B-43. P-multipliers versus pile head displacement for dense sand*

APPENDIX C

DYNAMIC MODEL FOR LATERALLY LOADED PILE GROUPS --

COMPUTATIONAL MODEL (FLPIER)

INTRODUCTION

Appendix C provides a comprehensive explanation of the material models and computational procedures used in the "Florida Pier" (FLPIER) computer program, as modified to consider dynamic loading. Considerable attention is given to modelling pile, pile cap and structural elements, especially their nonlinear behavior, in addition to modelling of the soil. A thorough knowledge of the models and computational procedures used in FLPIER is desirable for those who will apply FLPIER to design laterally loaded pile groups subjected to extreme event loading.

Background

Extensive research efforts have been directed to the nonlinear response of structures subjected to extreme load events. These extreme load events could be an earthquake or hurricane for a building, a ship impact for a bridge, or the effects of waves and wind action for offshore oil platforms. Traditionally, large factors of safety have been used in such cases, resulting in over-conservative design and cost ineffectiveness. On the other hand, an unsafe design could result in catastrophic human and economic losses. Because a more sophisticated nonlinear dynamic analysis is computationally expensive, these structures are designed using factored static loads to account for the dynamic effects. This procedure is acceptable for very low frequency vibrations, however the introduction of non-linearity, damping, and pile-soil interaction during transient loading may significantly alter the response (e. g., Appendix B).

Because in recent years computers have become much faster and cheaper, it has become possible to consider, and consequently to study, the dynamic nonlinear behavior of structures considering many factors neglected in the past. In this report, the computer program Florida Pier [1], which will be referred to simply as FLPIER from now on, has been modified to allow the nonlinear dynamic analysis of bridge piers. FLPIER is a computer program based on the Finite Element Method developed by Hoit, McVay, and Hays at the University of Florida for the nonlinear static analysis of bridge piers. Nonlinear aspects of structural analysis, such as material and geometric non-linearity, as well as structure-soil interaction can be incorporated into the analysis leading to more accurate results. It can model all the components of a bridge pier and its foundation, such as pier, pier cap, piles cap, piles, and soil, as shown in Figure C-1. The pier, pier cap, and piles can be represented using discrete elements that can incorporate the effects of material and geometric nonlinear behavior. More details about the discrete element are found in later in this appendix. The pile cap is modeled as linear 9-node shell elements. The lateral soil resistance is modeled with nonlinear p-y springs, while the axial resistance is modeled with nonlinear t-z springs.

FLPIER is now used by many DOTs throughout the United States because of its reliability and ease of use. Unlike general-purpose finite element programs, like ADINA and SAP, where modelling and analyzing can be time consuming, in FLPIER it is easy and fast for the user to perform these tasks thanks to a user-friendly interface for model generation. The modification of soil or structure parameters in the model is not difficult. The results can also be seen through a graphic interface that is currently being updated. In the modified dynamics version, resulting from this NCHRP research, speed and ease were maintained, allowing the user to easily perform the nonlinear dynamic analysis and modify parameters in the soil or structure if necessary. Although

the program is more suitable for the analysis of bridge piers, other types of structures can also be modeled.

The new additions to FLPIER are a new concrete model and dynamic solution techniques.

Literature Review and Adaptation of Material Models to FLPIER

Modelling of Structural Materials

Over the last years different analytical models have been proposed for the analysis of reinforced concrete structures. Models for these types of structures, which are under primarily flexural and axial loads, can be classified as:

(i)   Simple or lumped models.

(ii)   Discrete models.

(iii)   Fiber models.

(iv)   Finite element models.

Single-degree-of-freedom (SDOF) models belong to the first class of analytical models. In this class of models it is assumed that the structure's response to an extreme event such as an earthquake is dominated by its first natural frequency, allowing the system to be represented as a SDOF system with lumped mass and stiffness [2, 3, 4, 5]. A more general representation for multi-degree-of freedom systems (MDOF) is derived using the concept of shear building. In this model the stiffness of each story is represented by nonlinear springs, and the beams are considered to be infinitely rigid. Despite its simplicity and satisfactory performance in predicting the maximum response, this class of models does not provide enough data for more detailed seismic analysis. Furthermore for more complicated frames the assumption that the beams are infinitely rigid may not be correct.

In the second class of analytical models, the discrete models, there is a correspondence between the analytical model and the actual structure. In such models, a linear elastic element and a nonlinear spring represent the structural elements. The most common case is that of a nonlinear spring attached to both ends of a linear beam element. Atalay [6], Clough [7], Nakata et al. [8], Park et al. [9], and Takeda et al. [10], among others, have extensively used this class of models to analyze the behavior of reinforced concrete structures. In these models a set of predefined rules defines the hysteretic behavior of the nonlinear springs. These rules are usually obtained from laboratory experiments with real scale specimens. It is mainly the difference between these rules that distinguishes the models. Although these models give satisfactory results, its main disadvantage is the fact that the nonlinear spring's rules are based on experiments that may not correspond to the actual structural member, or type of loading, that they are representing.

The fiber models have been used in the study of reinforced concrete [11, 12, 13, 14, 15] and steel members [16, 17]. These models are based on the finite element approach, and are better suited for members and structures under complex loading histories. In these models the cross-section is divided into segments. Each segment can then be divided in one or more fibers. Each fiber is assumed to obey a uniaxial stress-strain relationship. From the integration of the stresses of each fiber over the cross section, the element forces can be calculated, and from the evaluation of the stiffness of each fiber the overall element stiffness can be obtained. Once the element forces and stiffness are obtained the analysis is carried out using standard finite element method procedures. Therefore, only the stress-strain relationships for concrete and reinforcing steel in the case of reinforced concrete sections, or steel, in the case of steel sections, are necessary to describe the properties of each section of the element. This makes these models very effective under complex loads (e. g., axial load plus bending). The main difference among all the

fiber models are the rules adopted for the uniaxial behavior of the different materials that make the cross-section. In the case of most civil engineering structures, these are steel and concrete, but other materials can also be used if the stress-strain relationships are known.

In the specific case of concrete the model's backbone is the envelope curve obtained from a monotonic test. This curve limits the concrete stresses in any loading phase. In some models the compression envelope curve for concrete is represented by the well-known Hognestad parabola [11, 13]. Another approach is to use multilinear curves to define concrete behavior in compression [14, 15]. In the case of dynamic analysis, the unloading and reloading rules are particular for each author. Ala Saadeghvaziri [11] and Zeris and Mahin [14, 15], unloading under compressive stress has a slope equal to the initial Young's modulus of the material. However, Hajjar et al. [12] and Park et al. [13] have more complicated expressions for the unloading curve. The reloading curves are very specific for each model, and the reader is referred to the preceding references for more information. The tension strength of concrete can be neglected [14, 15] or assumed to be equal to the measured concrete tensile strength [11, 13], in which case the slope of the reloading curve is assumed to be equal to the initial slope of the compression side. The unloading and reloading criteria are again specific for each model, and the reader is referred to the above references for more information. Confinement, strain-rate, and stiffness degradation effects are also particular for each model.

In the case of steel, no distinction is made between steel sections and reinforcement steel. The rules are valid for both cases. For the stress-strain curves, the Baushinger's effect can be considered [13, 16], or ignored, in which case a bilinear or tri-linear relationship (elastoplastic with kinematic or isotropic hardening) is used [11, 14, 15, 17].

The major disadvantage of these models is that they are computationally very expensive, but with the recent advances in computer technology, this class of models has become more popular because of its versatility. This is the analytical model for structural materials used in this work. FLPIER already incorporates a nonlinear discrete element, which uses fiber modeling at two points along the element's length to characterize its nonlinear behavior. New stress-strain curves were introduced to allow the nonlinear discrete element to perform dynamic analysis.

The last class of analytical methods is the finite element method. In this class of methods different elements are used to represent the structural members, such as truss members to represent the reinforcing steel, and plane stress elements to represent the concrete. The cracking typical of concrete represents a computational difficulty for these models, requiring the development of more sophisticated elements. The development of such elements is a challenge based on complex elasticity and plasticity theories. Like fiber modeling, this class of methods is computationally expensive and time consuming.

Limitations

It is very difficult for a model to incorporate all the aspects inherent to nonlinear dynamic analysis, and the model presented here is no exception. The first limitation is the fact that all the theory developed for nonlinear dynamic analysis is based on small displacement theory. The second limitation comes from the fact that the effect of shear deformation is not included in the constitutive models. It was also not included in the original derivation (Hoit et al., 1996). Problems of local buckling are also outside the scope of this work.

Hysteresis Models

A static analysis considers only the case in which the element is subjected to monotonic loading. For dynamic analysis a structural element will usually be subjected to two additional phases: unloading and reloading. It is important to notice that even for nonlinear static analysis these two new phases could be present due to a nonlinear redistribution of forces on the structure that could cause some elements to be over-loaded and others to be under-loaded. The relationship that is used to describe this behavior is called hysteresis. For any inelastic analysis, the proper selection of hysteretic models for the materials is one of the critical factors in successfully predicting the dynamic response under strong motion. Several models have been proposed in the past for reproducing various aspects of reinforced concrete behavior under inelastic loading reversals (Figure C-2). In order to closely reproduce the hysteretic behavior of various components, a highly versatile model is required in which several significant aspects of hysteretic loops can be included, i. e., stiffness degradation, strength deterioration, pinching behavior and the variability of hysteresis loop areas at different deformation levels under repeated loading reversals. However, the model should also be as simple as possible since a large number of inelastic springs are necessary in modeling the entire structure, and additional parameters to describe a complicated hysteresis loop shape may sometimes require an excessive amount of information.

Some of the existing popular models [6, 7, 8, 9, 10, 19, 20, 21, 22, 23, 24, 25, 26, 27] are shown in Figure C-2. It appears that most of the available models are aimed at a particular type of structural component, such as beams, columns or shear walls only, and therefore, fall short of the versatility required for modeling structures having a large number of different components. Most of these models were obtained by performing curve fits to experimental data. This approach

results in really good approximations for the behavior of the specific member being studied, but lacks versatility when applied to a real structure.

The advantage of using the discrete element with fiber modeling is that the element's general behavior will be governed by its material properties, instead of experimental observations, making this procedure useful for representing multiple cross-section configurations under more general load histories.

Material Models

Rather than trying to develop a new element that would model hysteretic behavior using elasticity and plasticity theories, the discrete element used in FLPIER was modified to develop such behavior. Based on various studies and experiments [13, 18, 28, 29, 31, 32, 33, 34, 35, 36, 37, 38, 39, 40] relating to the uniaxial cyclic behavior of concrete and steel, and the behavior of R/C members, the stress-strain curves of these materials were modified for dynamic analysis. Shear deformations were not included because they were not included in the references cited. Moreover, they were also not included in the formulation of the discrete element model in order to overcome numerical difficulties found in the various hysteresis models. Although computationally more expensive, the fiber modeling approach with uniaxial hysteresis gave the modified discrete element the versatility not found in many models. A description of these modified uniaxial curves follows next.

Uniaxial Mild Steel Model. Because the cyclic behavior of steel is very dependent on the process which it was produced, it was decided that rather than trying to predict steel behavior based on exponential curves [31, 41], a bilinear representation would be specified for the steel behavior. This represents a safe lower bound solution that is adequate for most construction steel.

C-8

Mild steel reinforcement is assumed to be perfectly elastic-plastic (no hardening) and similar in both tension and compression, as shown in Figure C-3. The parameters needed for the mild steel bilinear model are the modulus of elasticity E_s and yield stress f_y. The rules for this model are as follows (Figure C-3):

Loading is represented by segment a-b, the tangent stiffness is the initial modulus of elasticity for steel E_s and the stress is given by $\sigma = E_s . \varepsilon$.

Yielding: If $\varepsilon > \varepsilon_y$ yielding occurs and is represented by segment b-c. The tangent stiffness E_s is equal to 0 and the stress $\sigma = f_y$, the yield stress for steel. The residual strain ε_r is given by $\varepsilon_r = \varepsilon - \varepsilon_y$.

Unloading is represented by segment c-d, the tangent stiffness is E_s and the stress is given by $\sigma = (\varepsilon - \varepsilon_r).E_s$.

Reloading is represented by segment e-f, the tangent stiffness is E_s and the stress is given by $\sigma = (\varepsilon - \varepsilon_r).E_s$.

For any of these phases the secant stiffness E_{ss} is given by

$$E_{ss} = \frac{\sigma}{\varepsilon} \qquad \text{(C-1)}$$

Uniaxial Monotonic Concrete Model Used in FLPIER. . The concrete model used in FLPIER is generated from the values of the concrete strength f_c'' and modulus of elasticity of concrete E_c, input by the user. The compression portion of the curve, which is is based on the work of Wang and Reese [42], is highly non-linear and has a maximum compressive stress f_c'', which is related to but not always equal to the compressive strength of a standard test cylinder, f_c'.

Based on experimental research, f_c'' is taken to be 85% of f_c', the maximum cylinder compression stress.

The tension side of the curve is based on the tension-stiffening model proposed by Mitchell [43]. This procedure assumes an average tensile stress-strain curve for concrete. The stress strain relation of concrete in tension is very nearly linear, with cracking occurring at a small rupture stress f_r. The high local stresses actually experienced at tensile cracks in the concrete are not reproduced by the model. However the average response over a finite length of beam will be adequately represented.

Based on user input the program will generate the concrete curve as a series of points connected by straight lines as shown in Figure C-4. Values between the points are obtained by linear interpolation of the extreme points in the interval. For values of $f'_c = 6$ ksi and $E_c = 4615$ ksi, the strain and stress values for the concrete stress-strain curve generated by the program can be seen in Figures C-5 and C-6, respectively.

Models for the Uniaxial Inelastic Cyclic Behavior of Concrete. Two concrete models are implemented in FLPIER. One, called the rational model, is based on the work of Sinha et al. [32], the other is a bilinear model, similar to the mild steel model presented earlier. These two models are discussed in more details next.

Rational Model. Figure C-4 shows the default envelope of the stress-strain curve supplied by the program, which is a function of f'_c and E_c input by the user. This curve is the backbone of the model, because it limits the value of the stress in concrete during all phases in the analysis. The compression portion of the concrete curve is highly nonlinear and is defined by the Hognstead parabola up to a stress equal to $0.85f'_c$. Beyond this point, a straight line is adopted,

connecting this maximum to another point with residual stress of $0.20f'_c$ and strain equal to $4\,\varepsilon_u$, as shown in the Figure C-7. For strains greater than $4\,\varepsilon_u$, the stress is kept at a constant value of $0.20f'_c$ (residual stress), as suggested by Chen [28]. For the tension portion, the curve is assumed to be linear up to a stress of f_r and then has a tension-softening branch as shown in Figure C-7. The tension-softening branch attempts to account for the uncracked sections between cracks where the concrete still carries some stress. The value of f_r is based on the fixed value of ε_r shown in the figure, and the modulus of elasticity E_{ci} input by the user. For English units (psi), this will give a value of $f_r = 7.5\sqrt{f'_c}$. The rules for the rational model are described next.

A. Loading in Compression

Compression follows the curve described above. The equations that define this phase are:

When $\varepsilon < \varepsilon_o$ concrete follows the Hongnestead parabola defined by

$$f = 2f''_c\left(\frac{\varepsilon}{\varepsilon_o}\right) - f''_c\left(\frac{\varepsilon}{\varepsilon_o}\right)^2 \qquad \text{(C-2)}$$

The tangent modulus of elasticity is defined as follows:

If $\varepsilon < \varepsilon_e$ then

$$E_c = E_{ci} \qquad \text{(C-3)}$$

If $\varepsilon > \varepsilon_e$ then

$$E_c = \frac{2f''_c}{\varepsilon_o}\left(1 - \frac{\varepsilon}{_o}\right) \qquad \text{(C-4)}$$

This correction was necessary because the derivative of the Hongnestead parabola gives very high values of the tangent modulus for low values of the compressive strain ε, which caused instabilities in the model. Based on research [28, 29] it was found that at about 30% of $f''c$ it is reasonable to assume that concrete still have the initial tangent modulus, E_{ci}.

When the strain $\varepsilon > \varepsilon_o$, the concrete enters a phase called softening. In this research this phase is defined as follows:

If $\varepsilon_o < \varepsilon < 4\,\varepsilon_u$ then

$$f = f''_c - \left(\frac{0.8f''_c}{4\varepsilon_u - \varepsilon_o}\right)(\varepsilon - \varepsilon_o) \qquad \text{and} \qquad \text{(C-5)}$$

$$E_c = \frac{-0.8f''_c}{(4\varepsilon_u - \varepsilon_o)} \qquad \text{(C-6)}$$

If $\varepsilon > 4\,\varepsilon_u$

$$f = 0.20f''_c \quad \text{and} \qquad \text{(C-7)}$$

$$E_c = 0 \qquad \text{(C-8)}$$

B. Loading in Tension

Tension is also represented by the envelope curve described earlier. The following equations define loading in tension:

If $\varepsilon < \varepsilon_r$

$$f = E\varepsilon \qquad \text{and} \qquad \text{(C-9)}$$

$$E_c = E_{ci} \qquad \text{(C-10)}$$

If $\varepsilon_r < \varepsilon < \varepsilon_{stf}$ then

C-12

$$f = f_r + \left(\frac{0.5f_r}{\varepsilon_r - \varepsilon_{stf}}\right)(\varepsilon - \varepsilon_r) \qquad \text{and} \qquad \text{(C-11)}$$

$$E_c = \frac{0.5f_r}{\varepsilon_r - \varepsilon_{stf}} \qquad \text{(C-12)}$$

If $\varepsilon_{stf} < \varepsilon < e_{ut}$ then

$$f = \left(\frac{0.5f_r}{\varepsilon_{stf} - \varepsilon_{ut}}\right)(\varepsilon - \varepsilon_{ut}) \qquad \text{and} \qquad \text{(C-13)}$$

$$E_c = \left(\frac{0.5f_r}{\varepsilon_{stf} - \varepsilon_{ut}}\right) \qquad \text{(C-14)}$$

Finally if $\varepsilon > \varepsilon_{ut}$ then

$$f = 0 \qquad \text{and} \qquad \text{(C-15)}$$

$$E_c = 0 \qquad \text{(C-16)}$$

C. Unloading

The expressions for unloading in compression and tension are based on the work of Sinha et al. [32] defined for different concrete mixes. Due to the lack of exhaustive experimental data, it is assumed that for stronger concrete ($f'_c > 4$ ksi), the response will be that of 4 ksi concrete. If new experiments are performed for stronger concrete these changes can be easily incorporated into the program. The family of unloading curves is represented by second order curves. From experiments for various concrete strengths a good fit was obtained with the formula:

$$\sigma + H = \frac{J}{X}(\varepsilon - X)^2 \qquad , \qquad \text{(C-17)}$$

where H and J are experimental constants whose values for the three mixes used [32] are given in Table C-1. For stress in units of ksi and strains in units of in./in., X is a particular parameter, different values of which represent different members of the family. To determine the value of the parameter X, for a curve passing though a certain point in the stress-strain plane σ_1, ε_1 :

$$X = \varepsilon_1 + \frac{\sigma_1 + H}{2J} - \sqrt{\left(\left(\varepsilon_1 + \frac{\sigma_1 + H}{2J}\right)^2 - \varepsilon_1^2\right)} \qquad \text{(C-18)}$$

The tangent modulus E_c for unloading is taken as the slope for two consecutive points in the unloading curve:

$$E_c = \frac{f_n - f}{\varepsilon_n - \varepsilon} \qquad \text{(C-19)}$$

There are two choices for the case in which unloading in compression crosses the strain axis. The first option assumes that a gap is formed in compression, and concrete will totally unload until reloaded in tension. The second option assumes that no gap is formed, and concrete will go straight into the tension reloading phase from compression. When unloading from tension a gap is always formed, and concrete will not go into compression until the gap is closed.

D. Reloading

The reloading curves in either compression or tension are represented by a family of converging straight lines; accordingly, Eq. C-20 was chosen.

$$\sigma + K = Y(\varepsilon + L) \qquad \text{(C-20)}$$

in which K and L are experimental constants, and Y, is a parameter. The value of Y can be found, in a manner similar to the way in which the value of X was obtained in the previous section. By

C-14

substituting the coordinates σ_1, ε_1 of a known point on the reloading curve, and solving for Y, which is also taken as the tangent modulus, E_c, one obtains:

$$Y = \frac{\sigma_1 + K}{\varepsilon_1 + L} \qquad\qquad \text{(C-21)}$$

When concrete goes into tension, if it goes back to compression it will reload only when the gap resulting form the previous cycle is closed. The process can be visualized in Figure C-8.

Bilinear Model. In another study, Agrawal et al. [31] claimed that the response of under-reinforced concrete beams is governed by the steel. It was therefore proposed to use a simplification of the concrete model to simplify the analysis of doubly reinforced concrete beams. Idealized elastic plastic curves were drawn with a yield stress equal to the nominal strength $f'c$ value for concrete, and an elastic modulus equal to the average stiffness of the initial portion of the actual stress-strain curve as shown in Figure C-9. Also, the tensile strength of concrete is neglected in this model. In FLPIER the stress-strain curve for concrete is based on 13 points as shown in Figure C-4. Referring to Figure C-4, the value of the average elastic modulus is taken as

$$E_c = \frac{\sigma(5)}{\varepsilon(5)} \qquad\qquad \text{(C-22)}$$

and the value of the yielding strain ε_y is taken as

$$\varepsilon_y = \frac{\sigma(2)}{E_c} \qquad\qquad \text{(C-23)}$$

Strain Rate Effect. The strength of reinforced concrete sections is very dependent on the strain rate [44], and degree of confinement of the section [36, 45]. At a high strain rate, both the modulus of elasticity and the strength of concrete increase. The increase in strength can be as much as 17 % for a strain rate of 0.01/sec [29]. It is very difficult to test structural members under such conditions. So before using the results from static tests, it is important to consider the effect of strain rate in dynamic analysis. Important findings about the strain rate effects on reinfoced concrete members are summarized below [46]:

1) High strain rates increased the initial yield resistance, but caused small differences in either stiffness or resistance in subsequent cycles at the same displacement amplitude.

2) Strain rate effect on the resistance diminished with increased deformation in a strain-hardening range.

3) Non substantial changes were observed in ductility and overall energy absorption capacity.

Otani [46] also suggests that the strain rate during an oscillation is highest at low stress levels, and gradually decreases toward a peak strain. Cracking, crushing and yielding will contribute to a reduction in the system's stiffness, elongating the period of oscillation. Such damage is caused by the lower modes of vibration having long periods. Therefore, the strain rate e is small in earthquake analysis, and it has a small effect on the concrete response. FLPIER uses the confinement model described below to include the effects of strain rate.

Confinement Effect. The confinement of reinforced concrete columns is an effective way to increase its strength and ductility, as shown in Figure C-10.

Confinement basically decreases the slope of the descending branch of the loading curve of concrete, making the confined concrete member more ductile and less brittle. The reader is referred to References 36 and 45 for further discussion of the subject.

Soroushian et al. [36] proposed a very simplified model, that incorporates both strain-rate and confinement effects in the compression envelope curve for concrete. The following constitutive model, based on that model, was implemented in FLPIER:

$$
f = \begin{cases} K_1 K_2 f_c'' \left[\dfrac{2\varepsilon}{0.002 K_1 K_3} - \left(\dfrac{\varepsilon}{0.002 K_1 K_3} \right)^2 \right] \\ \qquad \varepsilon \le 0.002 K_1 K_3 \\ K_1 K_2 f_c'' \left[1 - z(\varepsilon - 0.002 K_1 K_3) \right] \\ \qquad \ge 0.2 K_1 K_2 f_c'' \\ \qquad \varepsilon \ge 0.002 K_1 K_3 \end{cases} \tag{C-24}
$$

where

f = concrete compressive stress,

ε = concrete compressive strain,

$K_1 = 1 + \dfrac{\rho_s f_{yh}}{f_c''}$,

ρ_s = volumetric ratio of the hoop reinforcement to concrete core = $\dfrac{V_{spiral}}{V_{core}} = \dfrac{4 A_{sp}}{sh'}$,

f''_c = 28-day compressive strength of concrete, adopted as $0.85 f'c$,

f_{sh} = yield strength of transverse reinforcement,

$$z = \begin{cases} \dfrac{0.5}{\dfrac{3 + 0.002f_c''}{f_c'' - 1000} + \dfrac{3}{4}\rho_s\sqrt{\dfrac{h'}{s}} - 0.002K_1K_3} & (psi) \\[20pt] \dfrac{0.5}{\dfrac{3 + 0.29f_c''}{145f_c'' - 1000} + \dfrac{3}{4}\rho_s\sqrt{\dfrac{h'}{s}} - 0.002K_1K_3} & (MPa) \end{cases} \qquad (C\text{-}25)$$

h' = width of concrete core measured to outside of the transverse reinforcement, as shown

in Figure C-11 for square, rectangular, and circular sections,

s = center-to center spacing of transverse reinforcement

$$K_2 = 1.48 + 0.160\log_{10}\dot{\varepsilon} + 0.0127(\log_{10}\dot{\varepsilon})^2 \ , \qquad \text{and} \qquad (C\text{-}26)$$

$$K_3 = 1.08 + 0.160\log_{10}\dot{\varepsilon} + 0.0193(\log_{10}\dot{\varepsilon})^2 \qquad (C\text{-}27)$$

Note: For $\dot{\varepsilon} < 10^{-05}$ / sec, $K_2 = K_3 = 1.0$.

In this model, K_2 represents the strain rate effect on the compressive strength of the concrete, and K_3 takes care of the strain rate effect on the strain at maximum stress. It is assumed that the strain rate effect on the slope of the descending branch of the stress-strain diagram is similar to the strain rate effect on the compressive strength of concrete. This is supported by test results. The model representation can be seen in Figure C-12. There is no change in the unloading or reloading curves.

The following modifications were also proposed by Soroushian et al. [36] for the secant and tangent stiffness of concrete when subjected to dynamic loading:

$$\frac{E_{cd}}{E_{cs}} = 1.241 + 0.111\log_{10}\dot{\varepsilon} + 0.127(\log_{10}\dot{\varepsilon})^2 \qquad \text{and} \qquad (C\text{-}28)$$

$$\frac{E_{cd}}{E_{ts}} = 1.061 + 0.464 \, log_{10} \, \dot{\varepsilon} + 0.00683 \left(log_{10} \, \dot{\varepsilon} \right)^2 \qquad \text{(C-29)}$$

In the preceding equations E_{cd} = dynamic secant modulus of elasticity, E_{cs} = static secant modulus of elasticity, E_{td} = dynamic tangent modulus of elasticity, and E_{ts} = static tangent modulus of elasticity. Note that when compared to the secant modulus, the tangent modulus seems to be less influenced by the rate of straining. These changes were also implemented in FLPIER.

Modal Analysis in FLPIER

The computer program FLPIER has been implemented with both time domain and modal analysis capabilities. Figure C-13 illustrates the iterative procedure that was adopted.

In the first cycle the earthquake motion is applied to the structure and the initial forces at the base of the piers are computed. Initially, the springs that represent the foundation are considered very stiff, to simulate fixed supports. Then for each column, a vector of six forces is generated, the three forces Fx, Fy, and Fz in the x, y, and z directions, and the three Mx, My, and Mz respective moments.

Each of these forces is then applied to the foundation, one at a time, as in a standard static analysis. This will produce three displacements, dx, dy, and dz, in the x, y, and z directions, and three respective rotations θy, θy, and θz, at the base of each column. These define the first column of the flexibility matrix for the foundation. After all six forces are applied, one for each column in the matrix, the six-by-six flexibility matrix for the foundation is obtained. By inverting this matrix the new stiffness for the foundation is obtained, which becomes the foundation springs for the base of each pier for the next cycle.

The analysis is carried out until two consecutive base forces for one pier are the same, within a tolerance. To compare vectors norms are used, also called absolute values. The 2-norm of two consecutive base force vectors is computed, and if within a stipulated tolerance, the analysis is terminated and the final forces are printed. The 2-norm of a vector is defined as follows: If $\vec{u} = \left(u_1 ... u_n \right)^T$ then the 2-norm of u is $\|\vec{u}\|_2 = \sqrt{u^t u}$.

It is important to note that in this analysis the structure is always considered to be linear, the main pre-requisite for modal analysis of any type. However, the springs generated for each cycle will reflect the characteristic nonlinear behavior of the foundation. This is an approximate method used for bridge pier analysis.

Multiple Support Excitation

It is usually assumed that all supports, where the structure is connected to the ground, undergo identical prescribed motion. In this section the previous formulation of the equation of motion is generalized to allow different — possibly even multi-component — prescribed motions at the various supports. Such multiple-support excitation may arise in several situations. First, consider the earthquake analysis of extended structures such as the Golden Gate Bridge, in San Francisco, California. The ground motion generated by an earthquake on the nearby San Andreas Fault is expected to vary significantly over the 6450-ft length of the structure. Therefore different motions should be prescribed at the four supports: the bases of the two towers, and two ends of the bridge. Second, consider the dynamic analysis of bridge foundations. The earthquake occurs deep in the soil, at the rock level. As the seismic waves move up in the soil the acceleration records at different soil depths are expected to vary. Therefore, the piles will be subjected to different accelerations along their depth during the earthquake.

In order to analyze multiple support excitation systems, the effects of the support motions must be included in the equations of motion (Figure C-14). The displacement vector is first divided into two parts D^t and D_g; D^t includes the NDOF of the superstructure, where the superscript t denotes that these are total displacements; and D_g contains the N_g components of support displacements.

The equation of dynamic equilibrium for all the degrees of freedom (DOF) can then be rewritten in partitioned matrix form:

$$\begin{bmatrix} m & m_g \\ m_g^T & m_{gg} \end{bmatrix} \begin{Bmatrix} \ddot{D}^t \\ \ddot{D}_g \end{Bmatrix} + \begin{bmatrix} c & c_g \\ c_g^T & c_{gg} \end{bmatrix} \begin{Bmatrix} \dot{D}^t \\ \dot{D}_g \end{Bmatrix} + \begin{bmatrix} k & k_g \\ k_g^T & k_{gg} \end{bmatrix} \begin{Bmatrix} D^t \\ D_g \end{Bmatrix} = \begin{Bmatrix} 0 \\ p_g(t) \end{Bmatrix} \qquad \text{(C-30)}$$

Observe that no external forces are applied along the superstructure DOF. In Eq. C-30 the mass (m), damping (c), and stiffness (k) matrices can be determined from the properties of the structure using traditional methods of matrix analysis, while the support motions $D_g(t)$, $\dot{D}_g(t)$ and $\ddot{D}_g(t)$ must be specified. Because the data that are usually available for an earthquake consists of the acceleration record at some depth, $\ddot{D}_g(t)$, the quantities $D_g(t)$ and $\dot{D}_g(t)$ can be obtained by numerical integration of $\ddot{D}_g(t)$, by using, for example, the Trapezoidal rule. The objective is to determine the displacements D^t in the superstructure DOF and the support forces $p_g(t)$.

The displacements are first separated into two parts:

$$\begin{Bmatrix} D^t \\ D_g \end{Bmatrix} = \begin{Bmatrix} D^s \\ D_g \end{Bmatrix} + \begin{Bmatrix} D \\ 0 \end{Bmatrix} \qquad \text{(C-31)}$$

In this equation D^s is the vector of structural displacements due to static application of the prescribed support displacements D_g at each time instant. The two are related through

$$\begin{bmatrix} k & k_g \\ k_g^T & k_{gg} \end{bmatrix} \begin{Bmatrix} D^s \\ D_g \end{Bmatrix} = \begin{Bmatrix} 0 \\ p_g^s \end{Bmatrix} \qquad , \tag{C-32}$$

where p_g^s are the support forces necessary to statically impose displacements D_g that vary with time; obviously, D^s varies with time and therefore is known as the vector of quasi-static displacements. Observe that $p_g^s = 0$ if the structure is statically determinate or if the support system undergoes rigid-body motion; for the latter condition an obvious example is identical horizontal motion of all supports. The remainder D of the structural displacements are known as dynamic displacements because a dynamic analysis is necessary to evaluate them.

With the total structural displacements split into quasi-static and dynamic displacements, Eq. C-31, the following equation can be written from Eq. C-30,

$$m\ddot{D}^t + m_g\ddot{D}_g + c\dot{D}^t + c_g\dot{D}_g + kD^t + k_gD_g = 0 \tag{C-33}$$

Substituting Eq. C-31 and transferring all terms involving D_g and D^s to the right side leads to

$$m\ddot{D} + c\dot{D} + kD = p_{eff}(t) \qquad , \tag{C-34}$$

where the vector of effective earthquake forces is

$$p_{eff}(t) = -\left(m\ddot{D}^s + m_g\ddot{D}_g\right) - \left(c\dot{D}^s + c_g\dot{D}_g\right) - \left(kD^s + k_gD_g\right) \qquad . \tag{C-35}$$

This effective force vector can be rewritten in a more useful form. The last term drops out because of Eq. C-32 resulting in

$$kD^s + k_gD_g = 0 \tag{C-36}$$

This relation also allows the quasi-static displacements D^s to be written in terms of the specified support motions D_g:

$$D^s = \ell D_g \qquad , \qquad \text{(C-37)}$$

and

$$\ell = -k^{-1} k_g \qquad \text{(C-38)}$$

ℓ is called the influence matrix because it describes the influence of support displacements on the structural displacements. If all the supports undergo the same motion, the influence matrix ℓ is unitary. It is clear from Eq. C-38 that ℓ is obtained by solving the linear system of equations:

$$k\ell = -k_g \qquad \text{(C-39)}$$

Substituting Eqs. C-37 and C-36 into Eq. C-35 gives

$$p_{\mathit{eff}}(t) = -(m\ell + m_g)\ddot{D}_g(t) - (c\ell + c_g)\dot{D}_g(t) \qquad \text{(C-40)}$$

If the ground (or supports) accelerations $\ddot{D}_g(t)$ are prescribed, the velocities $\dot{D}_g(t)$ can be obtained by numerical integration of the accelerations $\ddot{D}_g(t)$. With $p_{\mathit{eff}}(t)$ known from Eq. C-40, this completes the formulation of the governing equation (Eq. 34).

However, Eq. C-40 can be simplfied on two counts. First, if the damping matrices are proportional to the stiffness matrices (i.e. $c = a_1 k$ and $c_g = a_1 k_g$), the damping term is zero. Second, if the mass is idealized as lumped at the DOF, the mass matrix is diagonal, implying that m_g is a null matrix and m is diagonal. With these simplifications Eq. C-40 can reduces to

$$p_{\mathit{eff}}(t) = -m\ell\ddot{D}_g(t) \qquad \text{(C-41)}$$

For a better understanding of how the influence ℓ matrix is formed, consider the 2D frame with the DOF illustrated in Figure C-15.

Note that the support DOF, 4 and 5, are numbered last, according to Eqs. C-30. By applying unit displacements to DOF 4 and 5 the 4th and 5th columns of k, shown below, are obtained.

$$ k = \frac{EI}{L^3} \begin{bmatrix} 24 & 6L & 6L & 12 & 12 \\ 6L & 8L^2 & 2L^2 & 6L & 0 \\ 6L & 2L^2 & 8L^2 & 0 & 6L \\ 12 & 6L & 0 & 12 & 0 \\ 12 & 0 & 6L & 0 & 12 \end{bmatrix} \qquad (C-42) $$

If $k_g = \left[k_{g,1}, k_{g,2} \right]$, where $k_{g,1}$ and $k_{g,2}$ are respectively the 4th and 5th columns of k, and the influence matrix $\ell = \left[\ell_1, \ell_2 \right]$ (note that ℓ is $N \times N_g$), by solving $k\ell_n = k_{g,n}$ the *nth* column of ℓ is obtained. This procedure can be extended to 3-D analysis as well. In this case there are six possible directions for the motion of each support; however, in most cases the horizontal movement controls the analysis. In FLPIER the support motions are applied to the soil springs that connect with the footing or the piles. In the case of the simplified pile shown in Figure C-16, considering the DOF illustrated, the support stiffness k_g (8 x 4) is then given by Eq. C-43.

$$k_g = \begin{bmatrix} -k_1 & 0 & 0 & 0 \\ 0 & 0 & 0 & 0 \\ 0 & -k_2 & 0 & 0 \\ 0 & 0 & 0 & 0 \\ 0 & 0 & -k_3 & 0 \\ 0 & 0 & 0 & 0 \\ 0 & 0 & 0 & -k_4 \\ 0 & 0 & 0 & 0 \end{bmatrix}$$

(C-43)

Modal analysis has also been developed by others for multi-support excitation. The reader should refer to References 5, 47, 48 and 49 for more details.

Soil-Structure Interaction

The earthquake response of bridge structures depends on the soil-pile-structure interaction during the earthquake loading. The subject has been extensively studied by many researchers [50,, 51, 52, 53, 54, 55, 56, 57, 58]. There are two basic limitations to these studies. The first is that most of them apply to single-pile structures, making it impossible to account for multiple pile interaction effects, characteristic of a real structure. The second is that because of obvious cost problems, large-scale tests are rarely done. Another limitation is that the original data for most of these studies are not available.

In FLPIER soil-structure interaction is accounted for by the use of equivalent nonlinear soil springs. In particular, the complicated soil-pile-superstructure interaction is captured by determining the primary structural earthquake response, and then driving this response into the foundation system. In terms of the discussion in Appendix B, this allows for the simultaneous consideration of kinematic and inertial effects in the substructure system, especially in the pile groups. The coupled problem of soil-structure interaction is solved in terms of the structure first and the foundation system second. This procedure is considerably simpler than performing a

completely coupled solution; however, there are some approximations and uncertainties in the simplified procedure.

Abghari and Chai [59] suggest that the main source of uncertainty in the present approach can be illustrated by a simple modal response argument. The primary response of the structure is often a purely structural "fundamental" mode that does not capture the accurate response of the foundation (the "inertial" effect in Appendix B). The primary soil response mode approximates a free-field shear deformation (the "kinematic" effect in Appendix B) in which the superstructure is displaced in a near-rigid-body manner. As can be deduced from Appendix B, the two modes may not be closely coupled at certain frequencies of ground excitation; therefore, driving the design of the piles with the response of the superstructure may not accurately estimate the actual response of the entire system. In the absence of more rational analysis data, the uncertainties present in the simplified analysis make it difficult to predict whether the resulting pile foundations are over- or under-designed. It is therefore necessary to develop models that can account for the coupling between foundation and structure.

A simplified coupled solution would be to select a single pile from the pile group, with the superstructure being modeled as a single-degree-of-freedom system having the same period as the fundamental period of the structure, and a mass equal to the contribution of the superstructure to each pile. The pile is then subjected to displacement time histories previously calculated from a dynamic site response analysis, and forces and defections are calculated. There are basically two methods for applying the displacement histories to the piles: the Uncoupled Method and the Coupled Method. Both methods are described next.

Uncoupled Method

This method is illustrated in Fig. 18 (a). The analysis is done in two steps:

1) The computation of the free field motions;

2) The prediction of the pile-superstructure response.

The free-field motions are computed independently through a one-dimensional site response analysis using widely available computer codes {SHAKE [60]}. These computed ground motions are then used as boundary conditions applied at nodal locations, corresponding to the supports for nonlinear "p-y springs," (Appendix B) in the foundation system. It should be clear that what is done is a multiple support excitation analysis, with the support motions given by step (1). In this method the soil mass is lumped at the pile nodes. This method is the state-of-practice in dynamic analysis of foundations. This method is used in FLPIER

Coupled Method

This method is illustrated in Figure C-17b. The analysis could be performed by applying the free-field motion to the base of a soil column, modeled with "soil elements". The idea is that the earthquake occurs at the rock level, so applying the free-field motion to the bottom of the soil column makes sense. The "soil elements" are connected to the pile nodes through "p-y springs" and dashpots. Note that in this method only one free field motion is applied to the structure-foundation system, so there is no necessity for multiple support excitation. One advantage of this method would be that the soil mass can be obtained from the "soil elements" using the finite

element method procedure (e. g., a consistent mass formulation). The disadvantage is that the "soil element" must be a good representation of the soil, because all the interaction behavior between the support motion and the structure-foundation system is dependent on this element.

Although this simplified procedure may be efficient for a first estimate of the behavior of the structure when subjected to earthquake loading, it is somewhat impractical for design. Note that the pile cap, pier cap, and pile group effects are not present in this type of analysis, making it difficult to estimate the forces to design for. Therefore the computer program FLPIER was modified to perform a time-step analysis of the structure using the uncoupled method. It is now possible to input, for each pile node, the ground acceleration record at the elevation of the node, and the program will run the time-step analysis considering a multiple support excitation. All piles in the group are considered to be submitted to the same acceleration record. This results in the maximum forces that each element are subjected to during the dynamic analysis.

Cyclic Behavior of Soil

The cyclic behavior for soil presented here is based on the recommendations of O'Neill et al. [61] and is a simplified approach to the complex dynamic behavior of soil. Although the changes in FLPIER were limited to the lateral resistance springs (p-y), the extension to the axial pile-soil resistance springs (t-z) is obvious. It is also important to note that the dynamic factor usually incorporated in the p-y curves for soil under dynamic loading has not been incorporated in this model. The static p-y curves are used for the dynamic analysis. A typical static p-y curve is illustrated in Figure C-18.

The p-y behavior for cyclic loading is illustrated in Figure C-19. Loading is described by the original p-y curve. As the pile load is reversed at a given level, the soil reaction unloads along a path parallel to the loading path, not along the initial loading path, which produces hysteretic damping. When the soil reaction reaches zero, no further reaction is generated until the displacement of the pile at the location of concern reverses, at which time it follows the loading path in the opposite direction. Then, upon load reversal in the opposite direction, a mirror image effect is generated, except that no further soil reaction will be generated until the defection reaches the value of deflection corresponding to the width of the gap in the previous cycle. Then, loading occurs along the previous unloading path. Once the gap develops at a particular level due to lateral loading, the axial performance of the pile is affected because the development of shearing resistance is no longer permitted at that location, however this effect is not taken into account in the actual dynamic version of FLPIER at this time.

The dynamic p-y curve formulation described in Appendix B has also been programmed for FLPIER   However, that formulation has not been extensively checked either against load tests or against the standard, static p-y curve model described herein, so the user should proceed carefully with that formulation until sufficient experience has been gained with its use.   The descriptions below proceed with p-y curves that are based on static or quasi-static behavior.

Cyclic Degradation

Cyclic p-y degradation is specified through the use of Eq. C-44 [61]:

$$p_c = (1 - \lambda)(p_p - p_d) + p_d \tag{C-44}$$

In this equation λ is a soil degradation parameter specified by the user, p_c is the soil resistance (e. g., p for p-y curve corresponding to a given value of deflection y) for the current

cycle of loading, p_p is the value of resistance corresponding to the present value of y on the previous cycle of loading, and p_d is the fully degraded value of p at the present value of y. The analysts inputs the back bone, or first cycle, p-y curve and also a fully degraded p-y curve. In FLPIER the initial p-y curve can be automatically generated by the program based on the soil properties. The fully degraded p-y curve is given by a degradation factor, given by the user, multiplied by the initial p-y curve. At this time the user can not supply the fully degraded p-y curve. In a seismic event or for an extreme event that involves impact loading, some cyclic degradation may occur, but the fully degraded value may never be reached. A typical value for the soil degradation parameter, λ, is given in Eq. C-45.

$$\lambda = 1 - 10^{\left(\frac{log\,2}{1-N_{50}}\right)} \tag{C-45}$$

In Eq. C-45 N_{50} is the number of cycles that would be necessary to degrade the soil by 50 percent. This would be a site-specific parameter that wold have to be obtained by appropriate laboratory tests or from cyclic lateral pile testing.

The dynamic p-y curve formulation described in Appendix B has also been programmed for FLPIER However, that formulation has not been extensively checked either against load tests or against the standard, static p-y curve model described herein, so the user should proceed carefully with that formulation until sufficient experience has been gained with its use.

Strain Rate Effect

Usually, when soil is subjected to dynamic loading, cyclic degradation occurs simultaneously with an increase in the apparent soil (axial or lateral) resistance caused by rapid

rates of loading that occur in the most extreme events. Once the cyclic degradation has been accounted for, the rate effect is computed from [61]:

$$\frac{p_i}{p_c} = 1 + F_2 \, log\left(\frac{t_r}{t_s}\right) \qquad\qquad (\text{C-46})$$

where p_i is the instantaneous soil resistance considering both cyclic and loading rate effects, p_c is the resistance considering only cyclic loading, t_r is the actual rate of loading in Hz or unit of distance per second, t_s is the corresponding rate of loading appropriate for standard slow cyclic loading (typically 0.01 to 0.1 Hz) and F_2 is a soil factor, which can be taken as 0.01 - 0.03 for sand, 0.02 - 0.07 for silts, 0.02 - 0.12 for clays, and 0.01 - 0.03 for calcareous soils. Both the rate effect and cyclic degradation models are built into FLPIER.

Radiation Damping

Radiation damping is modeled through the use of dashpots having constants C that are attached to the pile nodes [61], where

$$C_h = 2D\frac{\gamma}{g}(v_s + v) \qquad\qquad (\text{C-47})$$

and where C_h is for horizontal (p-y) resistance in units of FT/L^2, D is the pile diameter, γ is the unit weight of the soil, g is the acceleration of gravity, v_s is the shear wave velocity of the soil, which would need to be estimated at a given site, and v is a velocity in between the shear and compression wave velocities of the soil. A lower bound solution for C_h, which is used in FLPIER, is given by taking $v = v_s$:

$$C_h = 4D\frac{\gamma}{g}v_s \qquad\qquad (C\text{-}48)$$

A similar expression can be developed at a later time for axial loading, although the current version of FLPIER does not have this capability.

PREDICTIONS OF RESPONSE USING FLPIER

This section provides a comparison between the experimental response of test columns reported in the literature [16, 17, 62, 63, 64, 65] and the theoretical predictions of FLPIER. The tests include different cross sections, such as steel sections, and circular and square reinforced concrete sections. When the data were available, the monotonic and the cyclic tests were compared. Three examples considering soil are also presented, but the structure is considered to remain linear during the analysis. The results for the various tests are presented in the following.

Example 1 - Steel Section 1

Although this report mainly addresses the behavior of reinforced concrete structures, it is opportune to verify the behavior of a steel section to validate the adopted bilinear steel model. A W 14 x 176 steel section that was first studied by Baron and Venkatesan [16] and later used by Chen and Atsuta [17] in similar studies, is used for comparison. The steel is ASTM-A36, with yielding stress f_y = 36 ksi, and Young's Modulus E_s = 29000 ksi. The history of deformations is given. No axial load is applied. The W section is modeled as a single steel H-pile, composed of 16 nonlinear discrete elements, the default in FLPIER, and is fixed at the base. A mass, a damper, and a spring were attached to the top of the pile to minimize the dynamic effects, resulting in a 'pseudo-dynamic' model with imposed displacements. The FLPIER model and the dynamic

parameters are shown in Figure C-20. A comparison between the actual test and the FLPIER model is shown in Figure C-21. Based on the fact that just a few points are reported in the original work, the comparison is very good.

Example 2 - Steel Section 2

In Example 2 the geometric nonlinearities already incorporated in FLPIER are included in the analysis, with the presence of an axial load. In this test the tangent stiffness approach added to the code is compared to the current approach, the secant stiffness, considering the p-Δ effects. The computer model and the dimensions for the cross section are illustrated in Figure C-22. The FLPIER results are compared to the results that were obtained using a computer program that also considers material and geometric nonlinearities [62]. A summary of the results for this test is contained in Table C-2. The comparison between FLPIER and Hays [62] is shown in Figures C-23 and C-24.

The following observations can be made from this example:

a) As expected, the tangent and the secant approaches give the same response until a point where the secant approach does not converge (between 1.5 and 2.0 in). Beyond this point FLPIER is in good agreement with the results given by Hays [62]. This indicates that the new tangent approach introduced in the FLPIER model appears to work well, and in this particular example is more stable than the secant approach.

b) Second, the p-Δ (or second order) moment effect is also modeled and is clear in Figure C-24. Note that the shear force starts to decrease as the second order moment dominates the response. Although this is not a dynamic test, its importance relies on the fact that it tests the tangent stiffness approach used in the dynamic analysis.

Example 3 - Circular Reinforced Concrete Column 1

The third example analyzed by FLPIER was the full-scale flexure column presented in Chai et al. [63]. This reference mentions that this column represented the then-current (1991) ductile design for bridge columns. Table C-3 summarizes the parameters for the test column, which was subjected to a constant axial compression force of 1000 kips and a lateral cyclic displacement of increasing amplitudes until failure of the column. Unfortunately, the data for the cyclic test were not available for comparison. The computer model is identical to the one shown in Figure C-22, except for the cross section and length L, now 30 ft. The different parameters for the tests are shown in Table C-4. All tests have the same material properties.

The first step was to perform an incremental static analysis using both the secant and the tangent methods. The static test uses a uniaxial material model and the proposed concrete model. The comparison between FLPIER and the test is shown in Figures C-25 and C-26 for the shears and moments, respectively. From Figures C-25 and C-26 note is taken that although the column strength values are very close, the slopes of the curves are slightly different. Three factors may have contributed to that phenomenon:

a) Because the original publication did not provide the values for the modulus of elasticity for steel and concrete, they had to be adopted. For the concrete, the empirical value given by the formula [66]

$$E_c = 57000\sqrt{f'_c} \tag{C-49}$$

was adopted. For the steel 29,000 ksi was adopted as the modulus of elasticity, which is typical for steel.

b) The use of a discrete curve, defined by straight lines segments, instead of a continuous curve (parabola) for the concrete model may also have introduced some error.

c) A phenomenon called anchorage-slip, which is explained in more detail later, may be present. Basically, this phenomenon causes additional displacements usually not accounted for by the analysis, making the column behave 'softer' than predicted.

All of these factors have direct influence on the column stiffness, explaining the difference between the FLPIER model and the test results.

A 'pseudo-dynamic' computational analysis, following the concept presented in Example 1, but with an adjustment in the mass and damper because of the change in stiffness, was then run to compare the effects of including confinement in the analysis. A plot comparing the FLPIER unconfined and confined dynamic models to the reference test is shown in Figure C-27. Note that there is still some discrepancy in the predicted and test stiffness of the column, which may have been be caused by the facts mentioned earlier. Although all the approaches could predict very well the ultimate moment, only the confined model could predict the more ductile behavior shown in Figure C-27 for the original physical test.

This computational test is important because it shows clearly the effects of confinement. Note that for the static analysis the theoretical column strength is just slightly over the actual test value, however the maximum displacement achieved was much less than the one in the test. This is because no confinement was considered in the analysis. This illustrates the main characteristic of confinement, that although there is no great increase in the column strength (Figure C-27), the column's ductility is reasonably increased, an important characteristic that should be present in columns in seismic regions. Although the confined model gives a response much closer to the original test, failure of the column at about 23 in. of displacement could not be predicted.

Example 4 - Circular Reinforced Concrete Column 2

Another monotonic test for a circular column was presented in Chai et al. [63]. The column test data are summarized in Table C-5.

Following the same procedure used in Example 3, an incremental load static computaional test was first performed using the secant and tangent approaches. No confinement was considered. The comparison of the shear forces is shown in Figure C-28. Note the effect of the second order moment as the shear force decreases after 2 in of lateral displacement. Then, a pseudo-dynamic test was run to verify the FLPIER predictions for the confined and unconfined options. The comparison can be seen in Figures C-29 and C-30. Note that this produces a much closer agreement in the stiffness. This agreement can be explained by the fact that this is a much smaller column, so the factors that contributed to the discrepancy in the previous test have a much smaller influence.

It is noteworthy that, based on the FLPIER confinement model, the column is not adequately confined. Note that in Figure C-29 the confined response is even worse than the unconfined response. The conclusion is that if the column is not adequately confined the confinement model is going to give the worse results than the unconfined model, and therefore should not be used. However, when the hoop spacing was changed to 2 in., a much closer agreement is observed between the confined model and the physical test (Figure C-31). The adopted confined concrete model makes no distinction between hoop and spiral confinement.

Example 5 - Rectangular Reinforced Concrete Column

In order to verify the concrete model under cyclic loading a series of tests performed by Bousias et al. [64] was used for comparison with FLPIER. This physical test program consisted of a series of 11 separate physical tests performed to study the behavior of reinforced concrete columns subjected to various types of cyclic loading. The tests referred as S0, S1, S2, S3, S4 and S10 in the original work were used for comparison because they reflect closely the type of cyclic loading common in dynamic analysis. Tests S0 to S4 consist of a cantilever column subjected to imposed displacements or forces in the X and Y direction with a constant axial load. Test S10 is also a cantilever column, but the axial force (Z direction) is not constant during the test. These directions are indicated in Figure C-31. Table C-6 summarizes the loading parameters and concrete strength for each test .

The details about the specimens used in the test can be found in Gutierrez et al. [67]. The specimens had a 0.25-m-square cross section and a free length of 1.50m, and were built in as a cantilever into a 1-m-square, 0.5 m thick, heavily reinforced foundation base. Longitudinal reinforcement consisted of eight 16-mm-diameter bars, uniformly distributed around the perimeter. A double hoop pattern of 8-mm-diameter stirrups at a 70 mm spacing was used as transversal reinforcement. The steel yielding stress is 460 MPa. No reference is made in the original work about the values of the modulus of elasticity for steel or concrete.

For the FLPIER model, nonlinear discrete elements were first used to model the column, but this number of elements proved to be very time consuming for these cyclic tests. The number of discrete elements was then reduced to four, and good agreement was obtained. All the moments from FLPIER were computed at the internal node of element four, indicated in Figure C-31, to avoid the addition of the second-order moments and allow the results to be compared to

the original test. The original tests were also set up in a way that the second-order moments were avoided. All the moments reported are about the Y axis (Figure C-31). These are basically cyclic tests with loading modelled as imposed pile tip displacements, so a lumped mass m, a damper c, and a spring k were added to the top of the pile to minimize the dynamic effects. The computer model and the values for the dynamic parameters can be seen in Figure C-31.

Monotonic Tests

The first step in the computer analsyis was to verify the concrete model under monotonic load. Using the actual static version of the computer program FLPIER, the column capacity was found. This was done by applying incremental increasing forces until no convergence was achieved. Then, with the dynamics option on, the same type of analysis was performed. The plot of moment at the base of the pile versus tip displacements for both analyses is illustrated in Figure C-32. Note that the static version of FLPIER cannot predict the softening behavior of the column beyond failure because the secant stiffness approach is used. In the dynamics version the tangent stiffness approach is used, so the softening behavior can be modeled. The moment capacity for this column, from the static analsyis, was found to be approximately 100,000 KN-mm, at a correponding tip displacement of 15.4 mm. Note from Figure C-32 that both models are in very good agreement.

A parametric study on the influence of changing the parameters of steel and concrete was also performed for the monotonic case. Each of the parameters, modulus of elasticity of concrete E_c, compressive strength of concrete $f'c$, modulus of elasticity of steel E_s, and yield stress of steel fy, was changed by a factor of 0.5 for comparison. Table C-7 helps to identify the tests and the changed parameters. The input files are identified by the .in extension. The extension .DAT identifies the output data file for the plots. Confinement was not considered in these

computational tests. The comparison between the various parametric tests and the model with the original parameters is shown in Figures C-33 to C-36.

The following comments can be made about these monotonic computational tests:

a) When the modulus of elasticity is changed there is no significant decrease in the column strength; however, reducing the modulus of elasticity of steel has a more significant influence than reducing the modulus of elasticity of concrete (Figure C- 33).

b) From Figure C-34, reducing the concrete strength by one-half decreases the column capacity but not by the same proportion. Reducing the steel strength by half decreases the column strength by a larger amount than when the concrete strength is reduced by one-half.

c) From Figure C-35, reducing both values of the modulus of elasticity by one-half makes the model unstable, which is expected. However, decreasing the strengths by one-half decreases the column capacity by approximately the same proportion, as expected, but the model did not become unstable.

d) Finally, by decreasing all of the parameters by by one-half, the column strength and stiffness is decreased by one-half, as expected (Figure C-36).

The file bm1_5.in did not converge. This is the test in which the elastic modulus of steel and concrete were decreased by half, but the original values for stresses were maintained. Note that decreasing drastically one of the parameters, while keeping the other constant, may cause instabilities to occur the model (FLPIER).

In order to illustrate the strain-rate effect, another set of computational tests was performed considering confinement at different strain rates. The strain rates were changed from 10^{-5}/s (very slow) to 1/s (very fast). The concrete and steel properties were not changed and are

those of file bm1.in, as described in Table C-7. Table C-8 helps to identify the strain rate tests. The comparison between the unconfined and confined models, as well as the effect of different strain rates, can be seen in Figure C-37.

In Figure C-37, there is a difference between the unconfined and confined models and in the increase in moment capacity as the strain rate is increased. The additional strength provided by the increase in the strain rate should be used with caution. In the case of an earthquake, for example, it is very probable that the structure will experience some cracking and yielding, what will make it less stiff, increasing the period and leading to lower strain rates. Therefore, the use of small strain rates is usually a safer lower bound approach to the problem.

Cyclic Test S0

In order to verify the behavior of the concrete model under cyclic loading, which is typical of dynamic analysis, a cyclic numerical test was performed for the first 90 seconds of the original physical test. The maximum imposed displacement was slightly over 15 mm, which characterizes failure from the static tests. The tip displacement time history for the first 90 seconds of the physical test can be seen in Figure C-38, which also shows the FLPIER time history. Note that the physical and numerical results are in perfect agreement. The first run was performed with the original data for steel and concrete. The comparison is shown in Figure C-39. Note that the FLPIER model is stiffer than the physical test specimen. It was then necessary to adjust the values of the elastic modulus of steel and concrete to calibrate the model. In lieu of information from the original work, the initial adopted values for steel and concrete were respectively, $E_s = 199.96$ KN/mm^2, and $E_c = 26.25$ KN/mm^2, which are reasonable values for steel and concrete [66]. However, the best agreement between the physical test and FLPIER was obtained with $E_s = 90$

KN/mm^2, and $E_c = 20$ KN/mm^2, asa depicted in Figure C-40. Three factors may have contributed to the disagreement using standard steel and concrete moduli:

a) The value of the modulus of elasticity for concrete was computed using the empirical formula given by Meyer [66], which could introduce some error.

b) The modulus of elasticity for the steel was adopted considering a typical value for construction steel. This could also introduce some error.

c) The third, and perhaps most important, component for the error could be anchorage slip. Alsiwat and Saatcioglu [68] and Saatcioglu et al.[69] reported that anchorage slip is one of the major components of inelastic deformation in reinforced concrete. Alsiwat and Saatcioglu [68] define anchorage slip by the following statement:

"Anchorage slips occurs when the critical section of a member for flexure is located near the adjoining member. Formation of a flexural crack at the interface of two members strains the reinforcement crossing the crack. Widening of the crack may produce inelastic strains in the reinforcement. This results in penetration of yielding into the adjoining member, giving rise to significant extension of reinforcement. Additional rigid body deformation may occur due to slippage of reinforcement. The combined effect of reinforcement extension and slip in the adjoining member may be referred to as anchorage slip."

Anchorage slip will result in member end rotations that are not accounted for in flexural analysis, resulting in a member that is 'softer' than initially predicted. In the new concrete model in FLPIER this effect is not considered, but it seems, based on the results presented in Reference 68, that this effect may be considered by decreasing the modulus of elasticity of the materials, making

the member 'softer'. Alsiwat and Saatcioglu [68] and Saatcioglu et al. [69] developed models for anchorage slip, and the reader is referred to their work for more information on this topic. The strain rate adopted for all the confined tests was 10^{-05} 1/sec (very slow).

The next step was to model the complete test, changing the modulus of elasticity for steel and concrete. The total duration of the test was 700 seconds. The complete imposed tip displacement time history is shown in Figure C-41. It is important to note that failure for the column was characterized by a displacement of about 15 mm. Note that in the test the column is subjected to tip displacements of about 90 mm, what is very extreme. The analysis was performed with a time step equal to 0.01s. Table C-9 helps to identify the modulus of elasticity of the materials for each run. Concrete confinement was also added to the analysis. Figures C-42 through C-45 show the comparison of each model to the physical test results. Note that the response given by FLPIER using the original material properties is always stiffer than the physical response, although the column strength is very close for all cases. However, when the moduli of elasticity for steel and concrete were decreased, there is a much better agreement, but the FLPIER model is still stiffer. It seems that there is an additional stiffness degradation factor, caused by the large amplitude of the cyclic loading, not accounted for by the FLPIER concrete model. Note that cyclic degradation is usually related to a large number of low intensity loading cycles, but in this example, after a relatively small number of cycles, the stiffness degradation is considerable. This phenomenon can be introduced into the FLPIER concrete model in the future.

These are mixed-mode control tests: displacement-controlled in the X-direction and force-controlled in the Y-direction. The imposed displacement in the X-direction and force in the Y-direction for Test S3 are shown in Figure C-46 and Figure C-47. The comparison between the physical test results and the FLPIER output is shown in Figures C-48 and C-49. Test S4 differed from Test S3 in that each constant level of the Y-force was applied first in the +Y direction and then in the -Y direction, with the repetition of three cycles of X-displacement. The imposed displacement in the X-direction and force in the Y-direction for test S4 are shown in Figures C-50 and C-51, respectively. The comparisons are shown in Figures C-52 through C-54. The test parameters are given in Table C-10.

Note again that changing the values of the modulus of the elasticity of concrete and steel improves the FLPIER predictions; however, FLPIER again over-predicted the column capacity, which also indicates the necessity of a strength degradation factor for the FLPIER model. In ts43 the steel strength was reduced to illustrate the effect of changing one of material parameters in the cyclic analysis.

Example 6 - Piles in Sand

In this example the response given by FLPIER considering the soil effects is compared to tests conducted by Wilson et al. [65]. This was a series of dynamic centrifuge tests to investigate soil-pile-structure interaction in liquefiable sand. The models consisted of structures supported on single piles and 2 x 2 and 3 x 3 pile groups. Although in the original work a variety of tests were performed, three tests were chosen for comparison. From the series of tests referred as CSP2, a single pile with a single column called SP, a 2 x 2 pile group with single a column called PG2, and a 3 x 3 pile group with single column called PG3, were selected for comparison. In the

physical tests the centrifuge models were subjected to a series of shaking events, with liquefaction occurring during the stronger events. In the current study of FLPIER, to avoid the effects of liquefaction not yet included in the FLPIER model, the structure was subjected only to the first event in the series numerically, and the results were then compared. The structure was assumed to behave linearly in all the tests. The three tests are described next.

Test SP

System SP simulated a superstructure with a mass of 50 tonnes (1 tonne = 1000 kg) supported by a single steel pipe pile 0.67 m in diameter, 16.8 m long, and with a 19 mm wall thickness. The column height is 5.4 m. Figure C-55 shows the model used in FLPIER. The soil data for all the tests are described in Table C-11. A set of five tests were run, where only the shear wave velocity for the soil layers was changed. Because the values for the shear wave velocity for the soil were not given in the original work, reasonable values obtained from Richart et al. [70] were adopted. The values $v_1 = 68$ m/s and $v_2 = 78$ m/s were adopted for the upper and lower layers respectively, because they gave the best response. No damping was added to the structure. The acceleration record for the top ring of the centrifuge was taken as input for FLPIER; it can be seen in Figure C-56. The comparison between the FLPIER output and the test, for displacements and moments, can be seen in Figures C-57 and C-58, respectively. Note that the comparison is very good for a single pile.

Tests PG2 and PG3

Tests PG2 and PG3 consisted of a single column supported by a 2 x 2 (PG2) and a 3 x 3 (PG3) pile group, respectively. The pile and soil properties are identical to those in the single pile test described previously. The prototype-scaled structure dimensions (in meters) and test setup

are shown in Figures C-59 and C-60. The masses for the cap, column and top mass are given in Table C-12. The period of the superstructure, considering it to be fixed at the base of the column, is 0.5 s. The model of the prototype in FLPIER had its pier stiffness adjusted to give this same period. Because the structure is considered to be linear, this was done simply by changing the values of the modulus of elasticity, E, and moment of inertia, I, for the linear 3-D beam elements that model the pier. The soil was modelled with O'Neill's p-y criterion for sand, p-multipliers of 1.0 and radiation damping was simulated by specifying values of soil shear wave velocity.

The comparison between FLPIER and the tests are shown in Figures C-61 and C-62 for the 2 x 2 group and in Figure C-63 for the 3 x 3 group (the displacement data were not available for the 3 x 3 configuration). For the 2 x 2 group FLPIER under-predicted the displacements, as can be seen in Figure C-61. However, when the magnitude of these displacements is compared to the structure dimensions, they are very small. Considering that the investigators were trying to predict a maximum displacement of about 0.002 m for a structure that is about 30 m tall (from the bottom of the piles to the top of the piers), the approximations are very good. Some error could also have been contained in the physical measurements.

On the other hand, a very good approximation for the moment was obtained for the 2 x 2 group from FLPIER, as can be seen in Figure C-62. For the 3 x 3 group, such a good approximation was not obtained. FLPIER over-estimated the pile-head moments by about 50 percent. Note that as the number of piles increased the predicted results for the pile-head moments got worse. This is expected, since the group influence, as represented, for example by the p-multiplier (Appendix B), was not included in the FLPIER analysis. Softening the p-y curves using the p-multiplier would have resulted in lower pile-head moments, especially for the larger group. It is clear that more study is necessary in this area, but note that values obtained for

the FLPIER approximation are reasonable for a pre-design analysis. The advantage of using FLPIER is that the pile and structure configurations can be easily changed, and once the displacements are in the desirable range, a more sophisticated analysis can be done. In the future, with a larger database, the FLPIER soil code can be calibrated to give even closer approximations for earthquake analysis.

Example 7 - Mississippi Dynamic Test

The last physical test that was modelled is one of the few full-scale tests performed to analyze the dynamic response of a pile group. The actual data for the test were obtained from the East Pascagoula River test program report. The tests details can be found in Reference 71. Basically, the test structure consisted of six prestressed rectangular concrete piles subjected to a pulse load. Four of the piles were battered. A schematic of the structure is shown in Figure C-64. The load history, applied to the pile cap, illustrated in Figure C-64, is shown in Figure C-65. Loading was applied by a Statnamic device driving the pile cap horizontally. The displacement time history for the pile cap is shown in Figure C-66. The test results were then compared to the FLPIER program using different sets of soil properties. The first and second comparisons were based on the p-y criteria shown in Figure C-64 using estimates of soil properties from the CPT and SPT, respectively. FLPIER has the capability of generating p-y and t-z curves directly from the CPT and SPT data. In the third comparison the proposed idealized soil properties proposed in Reference 71 were used.

From the comparisons for Example 7 the FLPIER models are in good agreement with the physical test data, especially using the p-y curves that were generated from the SPT data. The computed initial period for the system was very close to the measured period in all the cases, which shows that the estimate for the initial stiffness of the system is very good. However, the

same agreement is not observed in later cycles in this under-damped system. The FLPIER model exhibits stiffer behavior than the physical system. This is expected, since the FLPIER soil (p-y) model does not yet include soil degradation. Also note that there is a small residual displacement at the end of the analysis, which shows that there was some damage to the piles, or to the soil. This is also found in the FLPIER model, which suggests that the concrete model is adequate even for prestressed piles. It is expected that once soil degradation is added to the analysis, an almost perfect match will be obtained. It is interesting to note that FLPIER gave good approximations for this rather complicated nonlinear dynamic analysis, which included the presence of prestressed battered piles and four soil layers. However, modeling was easy and straightforward using the FLPIER program.

VALIDATION OF FLPIER RESULTS

The results from the dynamic formulation of FLPIER were compared to results from an existing, well-used finite element program in order to validate the results of the dynamic analysis procedures. The program chosen for validation was ADINA, a reliable FEM program developed at the MIT, that performs linear and nonlinear dynamic analysis [72]. A finite element model was constructed with ADINA for comparison. A detailed description of the model and test results follows.

System Modelling

A 2 x 2 pile group was adopted for this numerical test, as shown in Figure C-70. The structure consisted of one concrete pile cap and four concrete piles, with no pier connected to the cap. The cap and piles had similar masses in both the FLPIER and ADINA analyses. In both cases the masses were distributed. The focus of this test problem was on modelling soil behavior,

so the structure was assumed to behave elastically. The geotechnical model has only one soil layer above the water level, and the dynamic loading is a pulse load, as shown in Figure C-71. No additional damping was added to the structure or soil. The only damping source in the analysis is hysteretic damping due to the nonlinear soil behavior. The piles were modeled as linear 3-D frame elements, and the cap was modelled with 9-node linear shell elements.

To verify that the foundation modeling was correct, the system was first tested without soil. A harmonic load of 20 kips was applied to the system (the point of application is shown in Figure C-70) and the response was computed using both programs. From basic dynamics principles the system would oscillate with maximum displacement equal to two times the displacement caused by the 20 kip load applied statically. The cap displacements given by FLPIER and ADINA are shown in Figure C-72. They should and do match exactly because this is a linear analysis.

The next step was to add soil, but to apply such a small load (10 kips) that the system should behave linearly. Figure C-73 shows the comparison between both programs for 500 time steps and time step size equal to 0.001s. Note that there is no numerical damping in either.

FLPIER Soil Modelling

First, the structure was modeled using the FLPIER generator. This took about 15 minutes of the analyst's time with all data in hand. The summary soil data are shown in Figure C-70. The sand was modeled as O'Neill sand. (Various internal p-y criteria are documented in FLPIER help files.) The O'Neill sand criterion does not consider hysteresis; therefore, the p-y curves for the soil were modified in FLPIER to behave as illustrated in Figure C-74. This is the behavior of a nonlinear plastic material, with a gap in unloading. This nonlinear material is represented by a nonlinear spring, with a gap, that is connected to each pile node. FLPIER generates the p- curves

for all of the soil nodes automatically. The p-y curve generator generator is very helpful and speeds up the input process considerably, especially as compared to the effort required in inputing information in a more generic FEM program, such as ADINA.

ADINA Soil Modeling

ADINA is a generic FEM program, so the elements have to be created and then generated with a mesh. For modeling the cap, two 9-node shell elements were used; for the piles, each pile segment (a total of 16 segments for each pile) was modeled using 3D-beam elements. Both elements were assigned elastic material properties, defined by modulus of elasticity E and Poisson's ratio v.

The soil is more complicated. As mentioned previously soil is modeled as a nonlinear plastic material, and each node in a pile has a different soil material relationship because the p-y curves change with depth. The nonlinear spring element in ADINA, which can be attached to the pile at selected nodes, is elastic, i. e., it unloads along the same path along which it loads, so, unmodified, it is not a very good representation of lateral soil behavior. An improved option was to use truss elements with nonlinear properties based on the soil p-y curve for each soil node. So the soil reactions were defined using nonlinear truss elements with the material option "multilinear with isotropic hardening." This material behavior is illustrated in Figure C-75 Although using this behavior is more realistic than using a nonlinear, elastic spring, modelling the soil with this behavior is not equivalent to using FLPIER's nonlinear spring because there is no gap model. This will cause the responses computed by ADINA and FLPIER to be somewhat different. Because this soil model in ADINA is defined by stress and strain values, the p-y curve that it represents had to be transformed to an equivalent stress-strain curve, which may also introduce some error. This procedure was used for each node in the soil, a total of 16, which resulted in 16

nonlinear material truss element curves. It took about 2 days the model the soil using ADINA, which is quite a long time for such a simple problem. Figure C-75 shows a representation of the ADINA nonlinear material model.

Nonlinear Results – Test 1

The first nonlinear numerical test was to apply a harmonic load to the structure such that would it would behave nonlinearly. The load applied was 100 kips; the analysis was performed for 500 time steps, and the time step size was equal to 0.001s. A comparison of output from both programs is shown in Figure C-76. Figure C-77 shows a plot of the p-y behavior for the first soil spring in FLPIER and the stress-strain curve for the first nonlinear truss element in ADINA. Note that these plots explain the difference in period after the first cycle in Figure C-76, since the soil stiffness is unavoidably different in both models.

Nonlinear Results – Test 2

A second nonlinear numerical test was performed. First to make sure that the soil models were in agreement for both programs for static loading, a static load that would produce a nonlinear behavior was applied. It was applied as a 200 kip load in the direction shown in Figure C-70. This is the same location at which the harmonic load was applied before. A cap displacement of 0.646 inches was obtained after 6 iterations using FLPIER. Using ADINA, a cap displacement of 0.666 inches was obtained. These are close enough to conclude that ADINA validated the stiffness of the system computed by FLPIER. Next, the dynamic load was applied, and the results for the cap displacements are illustrated in Figure C-78. In the early part of the time history both computed relations intercepted the time axis at the same time, which validates correct modeling of the mass of the system by FLPIER, as well as the numerical integration procedure used in FLPIER. The discrepancy observed later in the time history is explained by the

differences between the nonlinear models adopted by the two programs, which have already been described.

Figure C-79 depicts the p-y behavior for the first (topmost) nonlinear soil spring in FLPIER and the stress-strain curve for the first (topmost) nonlinear truss element in ADINA. Note that while the FLPIER model absorbs energy in the unloading, ADINA absorbs very little energy because of its unloading path. This explains why the FLPIER response is different from the response from ADINA in Figure C-78.

Validation Conclusions

Although this test was simple and did not address complications such as multiple soil layers, soil cyclic degradation or earthquake loading, the results that were obtained show that for this very simplified test the FLPIER dynamic formulation gives reasonable answers compared to those given by ADINA. This is a first step in understanding the nonlinear dynamic behavior of soil. The results, combined with actual test results modelled in the previous section, confirm the validity of the FLPIER program.

SUMMARY, CONCLUSIONS AND RECOMMENDATIONS FOR FURTHER STUDY

Summary and Conclusions

A model for the nonlinear dynamic analysis of pile groups, group caps and supported superstructures has been presented. Special attention was given to proper modelling of reinforced concrete members of the system. The version of FLPIER that has been developed for this project contains the following improvements relative to older versions of FLPIER.

1) A fiber model for modelling nonlinear bending of reinforced concrete cross sections, including hysteresis with gapping in cracked regions.

2) Distributed mass models for the piles, cap and superstructure for modelling dynamic loads.

3) The facility to impose dynamic loads at the level of the pile cap or motion time histories at some prescribed elevation in the soil, usually the top-of-rock elevation, for which the acceleration time history is either known or can be estimated for a given design seismic event.

4) The capability to input estimated ground acceleration time histories into the piles within the pile group at the support points of all p-y curves (equally in all piles).

5) Extension of the existing p-y models for the soil to consider unloading and gapping, to include effects of radiation damping through user-prescribed values of a dashpot constant attached to each p-y curve, and to include forced movement of the reference points (supports) for the family of p-y curves needed to implement the algorithm for 4).

6) The specific formulation for p-y curves under dynamic loading given in Appendix B.

None of the p-y models currently implemented in FLPIER explicitly considers soil liquefaction.

FLPIER was validated against a sophisticated finite element code, ADINA, for the case of linear piles and nonlinear soil.

Application of the new version of FLPIER indicates that the proposed model for concrete is in reasonable agreement with a number of reported test results. The comparisons of predicted and measured behavior is thoroughly documented in this appendix. The fiber model adopted by FLPIER to consider nonlinear bending and hysteresis in reinforced concrete seems to be effective in modeling steel as well as circular and square reinforced concrete sections. It is clear from the test results that anchorage slip is an important concern when analyzing reinforced concrete members under cyclic loading, typical during earthquakes. Anchorage slip is not explicitly

included in the concrete model for FLPIER; however, it was shown that it is possible to model anchorage slip effects by decreasing the value of the modulus of elasticity for both concrete and steel. The model can be calibrated by performing physical tests for different cross sections and adopting the corrected value for the moduli of elasticity in the analytical model. Note that for all types of tests performed for the rectangular cross-section that was modelled numerically, the same values of the corrected moduli of elasticity for steel and concrete gave the best results, showing that anchorage slip is a function of the cross-section details rather than the type of loading.

It is important to point out that the in concrete gap that was introduced into the fiber model seems to replicate the stiffness degradation of the section very well. However, it is clear from the hysteresis diagrams for all the tests that the bilinear steel model is not adequate for larger lateral displacements. In such cases a steel model that includes strain hardening, and possibly cyclic degradation, should be used. Anchorage slip should also be included in this model.

In the case of the structures where soil was present (piled structures) it is clear that more studies will need to be performed when multiple piles are used, because the dynamic group effect is not yet well understood. Appendices D and E provide more insight into the dynamic group effect based on new dynamic lateral load tests that were performed simultaneously with the development of the new version of FLPIER. Use of the dynamic p-multipliers described in Appendix B may also be of use in obtaining improved solutions for groups of laterally loaded vertical piles. Although the p-multiplier model in Appendix B has not been incorporated into the new version of FLPIER, user-input "static" p-multipliers can be specified for each pile or each row of piles. Since the dynamic p-multipliers are shown in Appendix B to be frequency

dependent, the user must first estimate the predominant frequency of the free-field ground motion and then select an approximate value of the p-multiplier from Appendix B based on that frequency. It is pointed out that dynamic p-multipliers have only been developed in Appendix B for sands (soils whose stiffness increases in proportion to depth).

The approximations for p-y curves that were made in the analysis of centrifuge tests and full-scale tests using FLPIER (Examples 6 and 7) gave reasonable estimates for the displacements and forces acting in the structures from very simple soil parameters.

The FLPIER model presented here will require more study to be accurate for more complicated cases, but it is important to point out that in all examples the program gave credible predictions of the magnitude of the forces and displacements observed in physical experiments under a variety of extreme loads. An example is the case of the pile groups in sand (Example 6). FLPIER gave good approximations for the single pile and 2 x 2 pile group. For the 3 x 3 group, its prediction was off by about 50% in relative terms but close in absolute value terms. In the case of the Mississippi example (Example 7) FLPIER gave an excellent prediction for the pile cap response, even with complications such as nonlinear prestressed battered piles. In this field test system behavior was dominated more by the freestanding piles than by the soil that supported the piles, so this example was a good test of the concrete model and program mechanics

The nonlinear dynamic analysis of pile-supported structures is a very complex subject, and this appendix describes a fairly simple approximation to the problem that produced good results for the types of structures studied. As a result, FLPIER can be used as-is by design engineers who wish to develop a general understanding of what to expect from a structure under lateral earthquake or impact loading with minimal effort in preparing input files.

Copies of the version of FLPIER described here can be obtained from the Bridge Software Institute at the University of Florida (http://www.ce.ufl.edu/~bsi/).

Recommendations for Further Development of FLPIER

The steps that should next be taken in the development of FLPIER for dynamic loading are as follows:

1) Introduce a new steel constitutive model that includes strain hardening.

2) Study the behavior of full structures modelled with the nonlinear discrete element model, compare the results to test results reported in the literature, and improve those parts of FLPIER that warrant improvement.

3) Study, then model explicitly if warranted, the behavior of other cross sections, such as prestressed concrete sections, sections with voids and sections with steel shapes or pipes encased.

4) Analyze structures modelled with nonlinear discrete elements, including the new p-y model for the soil, and compare the results, if possible, to measurements reported in the literature.

5) Perform additional field tests with pile groups to calibrate the FLPIER model for the pile group effects, add the dynamic p-multiplier model described in Appendix B, and verify the dynamic p-multiplier model.

6) Extend the hysteretic model developed herein for p-y curves to unit axial soil resistance-displacement relations ("t-z" curves). Add a dynamic "t-multiplier" to the soil model if warranted based on analysis of field tests on laterally loaded pile groups.

REFERENCES — APPENDIX C

1. Hoit, M. I., McVay, M., Hays, C., and Andrade, P. W., " Nonlinear Pile Foundation Analysis using Florida-Pier," *Journal of Bridge Engineering*, ASCE, Vol.1, No. 4 (1966), pp.135-142.

2. Crandall, S. H., *Engineering Analysis* (1956), McGraw-Hill, New York.

3. Craig, Jr., R. R., *Structural Dynamics* (1981), John Wiley and Sons, New York.

4. Paz, M., *Structural Dynamics — Theory and Computation* (1985), Van Nostrand Reinhold Company, Inc., New York.

5. Chopra, A. K., *Dynamics of Structures — Theory and Applications to Earthquake Engineering* (1995), Prentice-Hall, Englewood Cliffs, NJ.

6. Atalay, M. B., and Penzien, J., "The Seismic Behavior of Critical Regions of Reinforced Concrete Components Influenced by Moment, Shear and Axial Force," *UCB/EERC Report 75-19* (1975), University of California, Berkeley.

7. Clough, R. W., "Effect of Stiffness Degradation on Earthquake Ductility Requirement," *Report No. 6614, Structural and Material Research* (1966), University of California, Berkeley.

8. Nakata, S., Sproul, T., and Penzien, J., "Mathematical Modeling of Hysteretical Behavior of Concrete Columns," *Report No. UCB/EERC-78/11* (1978), Earthquake and Engineering Center, College of Engineering, University of California, Berkeley, CA.

9. Park, Y. J., Ang, A.H-S., and Wen, Y. K. (1984), "Seismic Damage Analysis and Damage-limiting Design of R/C Buildings," *Civil Engineering Studies, SRS No.516* (1984), University of Illinois, Urbana, IL.

10. Takeda, T., Sozen, M. A., and Nielsen, N. N., "Reinforced Concrete Responses to Simulated Earthquakes," *Journal of the Structural Division*, ASCE, Vol. 96, No.ST12 (1970).

11. Ala Saadeghvarizi, M., "Nonlinear Response and Modeling of RC Columns Subjected to Varying Axial Load," *Engineering Structures*, Vol. 19, No. 6 (1997), pp. 417-424, Elsevier, Great Britain.

12. Hajjar, J. F., Schiller P. H., and Molodan A., "A Distributed Plasticity Model for Concrete-filled Steel Tube Beam-columns with Interlayer Slip." *Engineering Structures*, Vol. 20, No. 8 (1998), pp. 663 - 676, Elsevier, Amsterdam.

13. Park, R., Kent, D. C., and Sampson, R. A., "Reinforced Concrete Members under Cyclic Loading," *Journal of the Structural Division*, ASCE, Vol. 98, No.7 (1972), pp.1341 - 1360.

14. Zeris, C. A., Mahin, S. A., "Behavior of Reinforced Concrete Structures Subjected to Uniaxial Excitation," *Journal of Structural Engineering*, ASCE, Vol. 117, No. 9 (1991), pp. 2640 - 2656.

15. Zeris, C. A., Mahin, S. A., "Behavior of Reinforced Concrete Structures Subjected to Biaxial Excitation," *Journal of Structural Engineering*, ASCE, Vol. 117, No. 9 (1991), pp. 2657 - 2672.

16. Baron, F., and Venkatesan, M. S., "Inelastic Response for Arbitrary Histories of Loads," *Journal of the Engineering Mechanics Division*, ASCE, Vol. 95, No. EM3 (1969), pp. 763 - 786.

17. Chen, W. F., and Atsuta, T. (1973). "Inelastic Response of Columns Segments under Biaxial Loads," *Journal of the Engineering Mechanics Division*, ASCE, Vol. 99, No. EM4, pp. 685 - 701.

18. Mo, Y. L., *Dynamic Behavior of Concrete Structures* (1994), Elsevier, Amsterdam.

19. Fukada, Y., "A Study of the Restoring Characteristics of Reinforced Concrete Buildings," Kanto District Symposium of AIJ, Proceedings (1969), Tokyo Japan.

20. Ayoama, H. (1971). "Analysis of a School Building Damaged During the Tockachi-Oki Earthquake," Kanto District Symposium of AIJ, Proceedings (1971), Tokyo Japan.

21. Kustu, O., and Bouwkamp, J. G., "Behavior of Reinforced Concrete Deep Beam-columns Subassembleges under Cyclic Loads," *UCB/EERC Report 73-8* (1975), University of California, Berkeley.

22. Tani, S., and Nomura, S., "Response of Reinforced Concrete Structures Characterized by Skeleton Curve and Normalized Characteristic Loops to Ground Motion." 5th World Conference on Earthquake Engineering, Rome, Proceedings (1973).

23. Iwan, W. D., "A model for the dynamic analysis of deteriorating structures," 5th World Conference on Earthquake Engineering, Rome, Proceedings (1973).

24. Takayanagi, T., and Schnobrich, W. C., "Computed Behavior of Coupled Shear Walls," 6th World Conference on Earthquake Engineering, New Delhi, Proceedings (1977).

25. Muto, K., Hisada, T., Tsugawa, T., and Bessho, S., "Earthquake Resistant Design of a 20-story Reinforced Concrete Building." 5th World Conference on Earthquake Engineering, Proceedings, Rome (1973).

26. Blakeley, R. W. G., "Prestressed Concrete Seismic Design." *Bull., New Zealand Nat. Soc. for Earthq. Eng.*, Vol. 6, No. 1 (1973), pp. 2 - 21.

27. Mo, Y. L., "Analysis and Design of Low-rise Structural Walls Under Dynamically Applied Shear Forces," *ACI Structural Journal*, American Concrete Institute, Vol. 83, No.2 (1988), pp. 180 - 189.

28. Chen, W. F., *Plasticity in Reinforced Concrete* (1982), McGraw-Hill, New York.

29. Park, R., and Paulay T., *Reinfoced Concrete Structures* (1975), John Wiley and Sons, New York.

30. Roufaiel, M. S. L., and Meyer, C., "Analytical Modeling of Hysteretic Behavior of R/C Frames," *Journal of Structural Engineering*, ASCE, Vol.113, No.3 (1987), pp. 429 - 443.

31. Agrawal, G. L., Tulin, L. G., and Gerstle, K. H., "Response of Doubly Reinforced Concrete Beams to Cyclic Loading," *Journal of the American Concrete Institute*, Vol. 62, No. 7 ((1965), pp. 823-835.

32. Sinha, B. P., Gerstle, K. H., and Tulin, L. G., "Stress-strain Relations for Concrete under Cyclic Loading," *Journal of the American Concrete Institute*, Vol. 61, No. 2 (1964), pp. 195 - 211.

33. Sinha, B. P., Gerstle, K. H., and Tulin, L. G., "Response of Singly Reinforced Beams to Cyclic Loading." *Journal of the American Concrete Institute*, Vol. 61, No. 8 (1964), pp. 1021 - 1037.

34. Kwak, H. G., "Nonlinear Response and Modeling of RC Columns Subjected to Varying Axial Load," *Engineering Structures*, Vol. 19, No. 6 (1997), pp.417 - 424.

35. Magdy, S. L., and Meyer, C., "Analytical Modeling of Hysteretic Behavior of R/C Frames." Journal of Structural Engineering, ASCE, Vol. 113, No. 3 (1987), pp. 429 - 444.

36. Soroushian, P., Choi, K. B., Alhamad, A., "Dynamic Constitutive Behavior of Concrete," *Journal of the American Concrete Institute*, Vol. 83, No. 2 (1986), pp. 251 - 259.

37. Nilsson, L. G., *Impact Loading on Concrete Structures* (1979), Department of Structure Mechanics, Chalmers University of Technology, Goteborg, Sweden.

38. Ozcebe, G., and Saatcioglu, M., "Hysteretic Shear Model for Reinforced Concrete Members," *Journal of Structural Engineering*, ASCE, Vol. 115, No. 1 (1989).

39. Penzien, J., "Dynamic Response of Elasto-plastic Frames," *Journal of the Engineering Mechanics Division*, ASCE, Vol. 86, No. ST7 (1960), pp. 81 - 94.

40. Tseng, G., Stea, W, Weissman, S., Dobbs, N., and Price, P., "Elastic and Elasto-plastic Computerized Dynamic Analysis of Frame Structures Subjected to Blast Overpressure." National Structural Engineering Conference, Proceedings (1976), ASCE, pp. 977 - 987.

41. Shen, Z., and Dong, B., "An Experimental-based Cumulative Damage Mechanics Model of Steel under Cyclic Loading," *Advances in Structural Engineering - An International Journal*, Vol. 1, No. 1 (1997), Multi-Science Publishing Co. Ltd., London, UK.

42. Wang, S., and Reese, L. C., "COM624 Version 2.0 by Ensoft," *Publication No. FHWA-SA-91-048* (1993), Federal Highway Administration, Washington, D. C.

43. Mitchell, J, S., "A Nonlinear Analysis of Biaxially Loaded Beam-columns Using a Discrete Element Model." PhD Dissertation (1973), University of Texas at Austin, TX.

44. Shkolnik, I. E., "Evaluation of Dynamic Strength of Concrete from Results of Static Tests," *Journal of Engineering Mechanics*, ASCE, Vol. 122, No. 12 (1996), pp. 1133 - 1138.

45. Saatcioglu, M., and Razvi, S. R., "Strength and Ductility of Confined Concrete," *Journal of Structural Engineering*, ASCE, Vol. 118, No. 6 (1992), pp. 1590 -1 607.

46.   Otani, S., "Nonlinear Dynamic Analysis of Reinforced Concrete Building Structures," *Canadian Journal of Civil Engineering,* Vol. 7 (1980), pp. 333 - 344.

47.   Monti, G., Nuti, C., and Pinto, P. E., Nonlinear Response of Bridges under Multisupport Excitation," *Journal of Structural Engineering,* Vol. 122, No. 10 (1996), ASCE, pp. 1147 - 1159.

48.   Der Kiurieghian, A., and Neuenhofer, A., "Response Spectrum Method for Multiple Support Seismic Motion,*" International Journal of Earthquake Engineering and Structural Dynamics,* Vol. 21, No. 8 (1992), pp. 713 - 740.

49.   Der Kiurieghian, A., "A Coherency Model for Spatially Varying Ground Motion," *International Journal of Earthquake Engineering and Structural Dynamics,* Vol. 25 (1995), pp. 99 - 111.

50.   Nogami, T. (Editor), *Observation and Modeling in Numerical Analysis and Model Tests in Dynamic Soil-structure Interaction Problems,* Geotechnical Special Publication No. 64 (1997), ASCE, New York.

51.   Prakash, S. (1997). "Seismic Analysis and Design for Soil-Pile-Structure Interactions," *Geotechnical Special Publication No. 70* (1997), ASCE, New York.

52.   Turner, J. P., "Performance of Deep Foundations under Seismic Loading,*" Geotechnical Special Publication No. 51* (1995), ASCE.

53.   Bandoni, D., and Makris, N., "Nonlinear Response of Single Piles under Lateral Inertial and Seismic Load," *Soil Dynamics and Earthquake Engineering,* Vol. 15 (1996), pp. 29 - 43.

54.   Reese, L. C., Cox, W. R., and Koop, F. D., "Analysis of Laterally Loaded Piles in Sand." Offshore Technology Conference, Proceedings (1974), Houston, TX.

55. Matlock, H., Foo, S. H., and Bryant, L. L., "Simulation of lateral pile behavior," *Earthquake Engineering and Soil Dynamics* (1978), ASCE, New York, pp. 600 - 619.

56. Anderson, J. M. (1972). " Seismic Response Effects on Embedded Structures," *Bulletin of the Seismological Society of America*, Vol. 62, No. 1 (1972), pp. 177-194.

57. Ting, J. M., "Full-scale Cyclic Dynamic Lateral Pile Responses," *Journal of Geotechnical Engineering*, ASCE, Vol. 113, No. 1 (1987), New York.

58. McVay, M. C., Shang, T., and Casper, R., "Centrifuge Testing of Fixed-head Laterally Loaded Battered and Plumb Pile Groups in Sand," *Geotechnical Testing Journal*, ASTM (1996), pp. 41 - 50.

59. Aghari, A., and Chai, J. (1995). "Modeling of Soil-Pile Superstructure Interaction in the Design of Bridge Foundations," *Geotechnical Special Publication No. 51, Performance of Deep Foundations under Seismic Loading*, ASCE, Ed. by John Turner (1995), pp. 45-59.

60. Schnabel, P. B., Lysmer, J., and Seed, H. B., "SHAKE: A Computer Program for Earthquake Response Analysis of Horizontally Layered Site." *Report No. USB/EERC 72/12* (1972), University of California, Berkeley, 102 pp.

61. O'Neill, M. W., Brown, D. A., Anderson, D. G., El Naggar, M. H., Townsend, F. C., and McVay, M. C. (1997), "Static and Dynamic Lateral Loading of Pile Groups," *Interim Report, NCHRP 24-9* (1997), Highway Research Center, Harbert Engineering Center, Auburn University, Auburn, AL.

62. Hays, C. O., "Nonlinear Dynamic Analysis of Framed Structures with Pile Foundations." Preprint, National Structural Engineering Convention, ASCE (1975), New Orleans, LA.

63. Chai, Y. H., Priestley, M. J. N., and Seible, F., "Flexural Retrofit of Circular Reinforced Bridge Columns by Steel Jacketing," *Report No. SSRP - 91/05* (1991), Department of Applied Mechanics and Engineering Sciences, University of California, San Diego, La Jolla, CA.

64. Bousias, S. N., Verzeletti, G., Fardis, M. N., and Gutierrez, E., "Load-path Effects in Column Biaxial Bending with Axial Force," *Journal of Engineering Mechanics*, Vol. 121, No. 5 (1995), pp. 596 - 605, ASCE.

65. Wilson, D. W., Boulanger, R. W., and Kutter, B. L., "Soil-Pile-Superstructure Interaction at Soft or Liquefiable Soil Sites — Centrifuge Data Report for CSP2," *Report No. USD/CGMDR-97/03* (1997), Department of Civil and Environmental Engineering, College of Engineering, University of California at Davis, Davis, CA.

66. Meyer, C., *Design of Concrete Structures* (1996), Prentice-Hall, Inc., Upper Saddle River, NJ.

67. Gutierrez, E., Magonette, G., and Verzeletti, G., "Experimental Studies of Loading Rate Effects on Reinforced Concrete Columns," *Journal of Engineering Mechanics*, ASCE, Vol. 119, No. 5 (1993), pp. 887 - 904.

68. Alsiwat, M., Saatcioglu, M., "Reinforcement Anchorage Slip under Monotonic Loading," *Journal of Structural Engineering*, ASCE, Vol. 118, No. 9 (1992), pp. 2421-2438.

69. Saatcioglu, M., Alsiwat J. M., and Ozcebe, G., "Hysteretic Behavior of Anchorage Slip in R/C Members," *Journal of Structural Engineering*, ASCE, Vol. 118, No. 9 (1992), pp. 2439 - 2458.

70. Richart, F. E., Hall, J.R., and Woods, R. D., *Vibrations of Soils and Foundations* (1970), Prentice-Hall, Inc., Englewood Cliffs, NJ.

71. Brown, D. A., "Report of Statnamic Load Testing, US90 over the Pascagoula River," Special Report to the Mississippi Department of Transportation, Jackson MS (1998).

72. Bathe, K. J., *ADINA*, Adina R and D, Inc., Watertown, MA.

Table C-1. Curve Coefficients

f'ᴄ (psi)	H	J	K	L
3000	0.07	0.95	3.42	1.26
3750	0.09	0.52	2.52	1.03
4000	0.10	0.61	4.61	1.01

Table C-2. Results for Example 2

Δx(in)	FLPIER				Hays (tangent)	
	Secant		Tangent			
	S(kips)	M(kip.in)	S(kips)	M(kip.in)	S(kips)	M(kip.in)
0.5	3.5	906.4	3.5	906.4	3.5	907
1.0	7.1	1812.7	7.1	1812.7	7.1	1810
1.5	11.0	2721.6	10.8	2717.8	10.6	2720
2.0	NC	NC	11.4	3145.5	11.5	3140
2.5			10.9	3297.8	10.9	3290
3.0			9.7	3363.2	9.7	3360
3.5			8.4	3393.6	8.4	3390
4.0			7.0	3407.3	7.0	3400

NC = No convergence achieved for the analysis.

Table C-3. Design Details for Example 3

Diameter	60"
Height	30'
Cover to main bar	4"
Concrete strength $f'c$ Modulus of elasticity E_c	5.2 ksi 4110 ksi
Longitudinal steel Yield strength fy Modulus of elasticity E_s (adopted)	25#14 68.9 ksi 29000 ksi
Transverse steel Yield strength fy	#5 spiral at 3.5" 71.5 ksi
Axial force	1000 kips

Table C-4. Model Parameters for Example 3

File	Stiffness	Analysis type	Confinement	Convergence
circ2.in	Secant	Static	No	OK
circ21.in	Tangent	Static	No	OK
circ22.in	Tangent	Dynamic	No	NO
circ23.in	Tangent	Dynamic	Yes	OK

Table C-5. Design Details for Example 4

Diameter	24"
Height	12'
Cover to main bar	0.8"
Concrete strength f'_c Modulus of elasticity E_c	4.725 ksi 3918 ksi
Longitudinal steel Yield strength fy Modulus of elasticity E_s (adopted)	26#6 45.7 ksi 29000 ksi
Transverse steel Yield strength fy	#2 hoop at 5" 51 ksi
Axial force	400 kips

Table C-6. Loading for Each Test for Example 5

Test	$f'c$ (MPa)	Axial (kN)	Loading path
S0	30.75	300	Imposed X displacement
S1	29.0	212	Imposed X displacement Imposed Y displacement
S2	31.1	284	Imposed X displacement Imposed Y displacement
S3	29.9	310	Imposed X displacement Imposed Y force
S4	27.7	253	Imposed X displacement Imposed Y force
S10	28.5	Variable	Imposed X force Imposed Z force

Table C-7. Example 5: Parametric Computational Tests (Units are kN/mm^2)

File	E_c	$f'c$	E_s	fy	Confinement
bm1.in	26.25	0.031	200	0.46	No
bm1_1.in	13	0.031	200	0.46	No
bm1_2.in	26.25	0.031	100	0.46	No
bm1_3.in	26.25	0.015	200	0.46	No
bm1_4.in	26.25	0.031	200	0.23	No
bm1_5.in	13	0.031	100	0.46	No
bm1_6.in	26.25	0.015	200	0.23	No
bm1_7.in	13	0.015	100	0.23	No

Table C-8. Example 5: Parametric Computational
Tests for Concrete Confinement under Different Strain Rates

File	Strain rate (1/s)	Confinement
bm1.in	0	No
bm1_sr1.in	1×10^{-5}	Yes
bm1_sr2.in	1×10^{-4}	Yes
bm1_sr3.in	1×10^{-3}	Yes
bm1_sr4.in	1×10^{-2}	Yes
bm1_sr5.in	1×10^{-1}	Yes
bm1_sr6.in	1	Yes

Table C-9. Example 5: Parameters for Test S0 (Units are kN/mm^2)

File	ts01	ts02	ts03	ts04
Ec	26.25	26.25	20	20
Es	200	200	90	90
Confinement	No	Yes	No	Yes

Table C-10 . Parameters Used in Tests S3 and S4

File	Test	f'c	Ec	fy	Es	Confinement	Time step
ts31.in	S3	0.029	26.25	0.46	200	No	0.35
ts32.in	S3	0.029	20	0.46	90	No	0.35
ts41.in	S4	0.027	26.25	0.46	200	No	0.41
ts42.in	S4	0.027	20	0.46	90	No	0.41
ts43.in	S4	0.027	20	0.25	90	No	0.41

Table C-11 . Example 6: Some Soil Properties for CSP1

Soil Type	Nevada Sand	
ρmax	1.76	
ρmin	1.41	
Unit Weight (g/cm^3)	1.52 Upper layer	1.66 Lower layer
Relative Density	35-45 % Upper layer	75-80% Lower layer

After Wilson et al. [65]

Table C-12. Example 6: Masses (tons) for pile group tests

PG	Cap mass	Column mass	Top mass
2 x 2	132	174	233
3 x 3	329	193	468
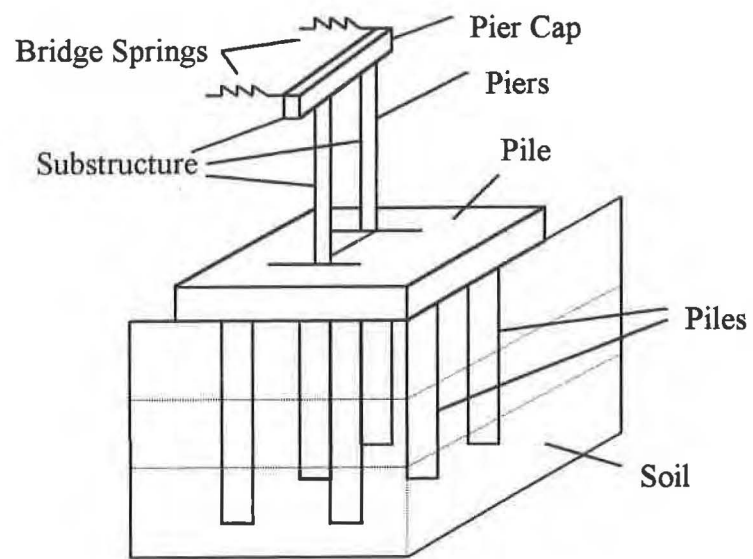
Figure C-1. Bridge pier components

(a) Clough   (b) Fukada   (c) Aoyama

(d) Kustu   (e) Tani   (f) Takeda

(g) Park   (h) Iwan   (i) Takayanagi

(j) Muto   (k) Atalay   (l) Nakata

(m) Blakeley   (n) Mo
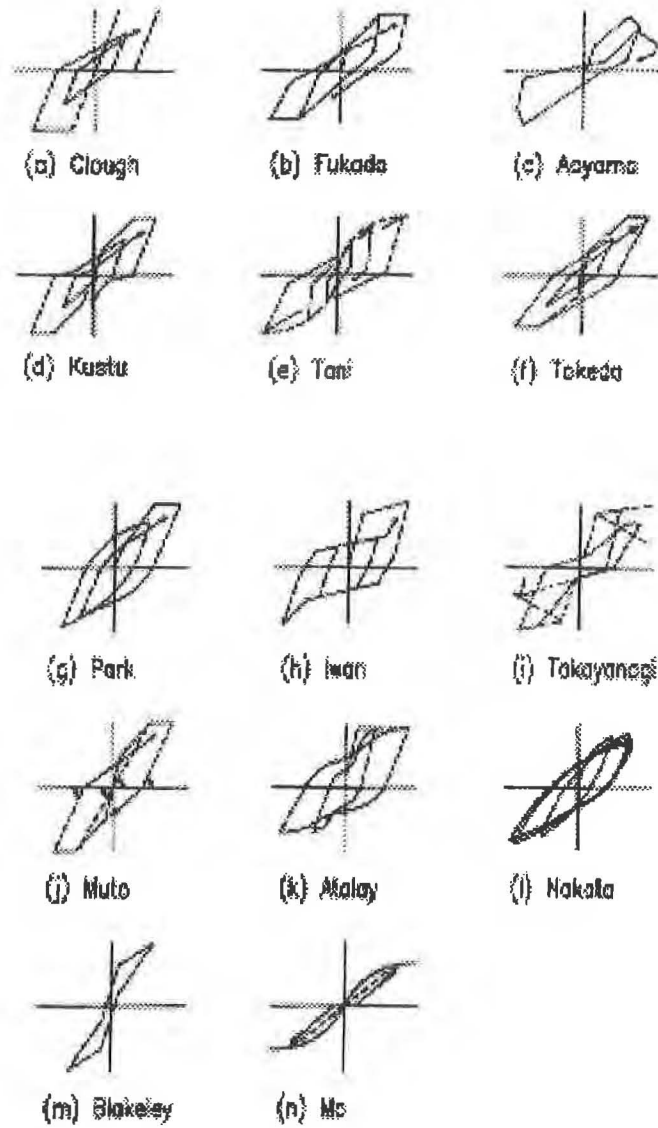
Figure C-2. Models for hysteresis loops proposed by some authors [18]
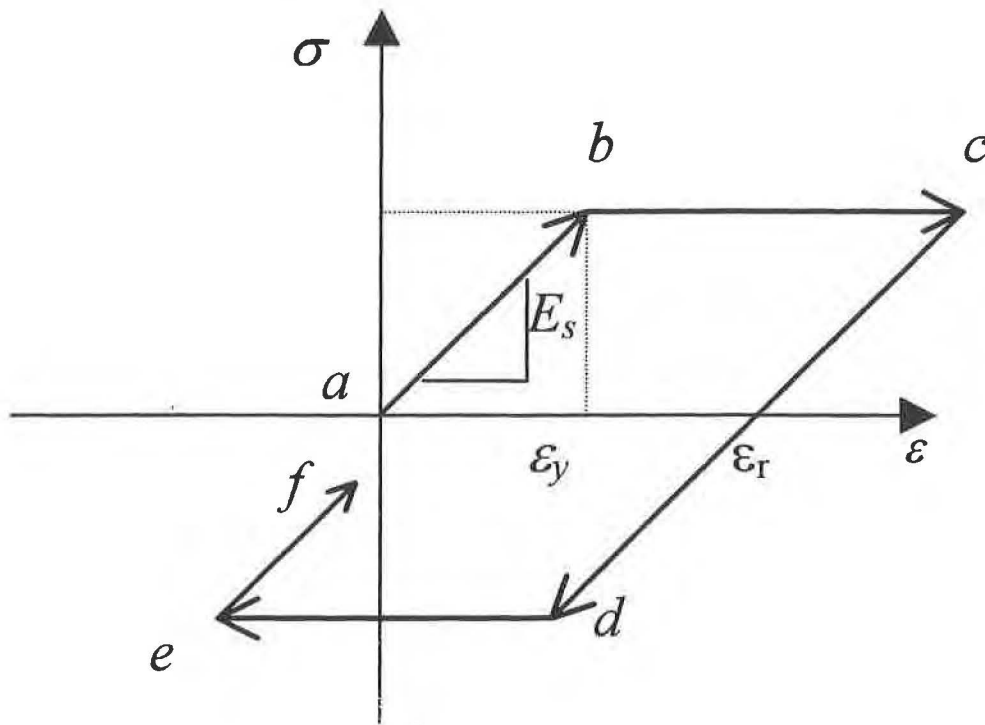
Figure C-3. Elastic-perfectly plastic model for mild steel
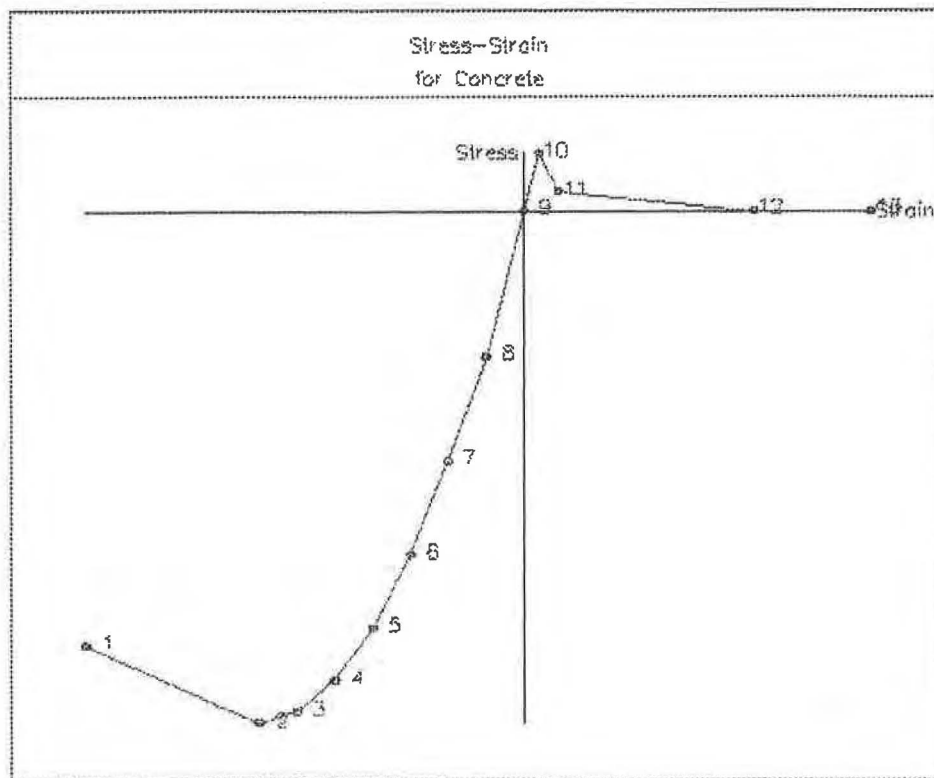
Figure C-4. Points on Concrete Stress-Strain Curve Used in FLPIER
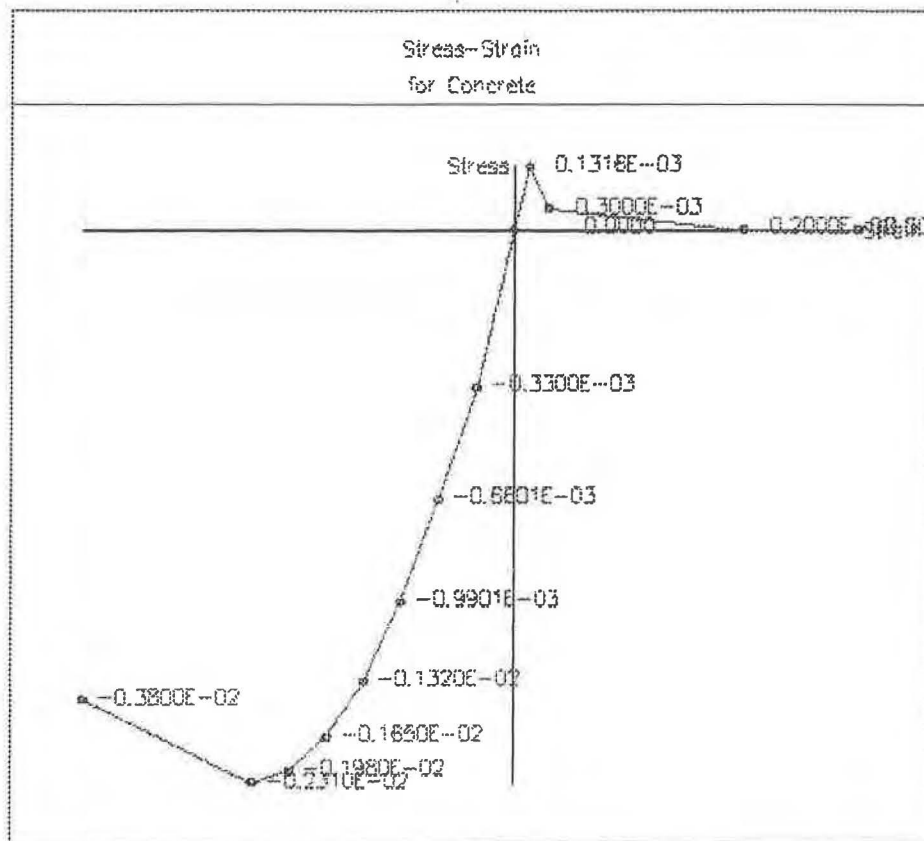
Figure C-5. Strain Values on Concrete Stress-Strain Curve Used in FLPIER
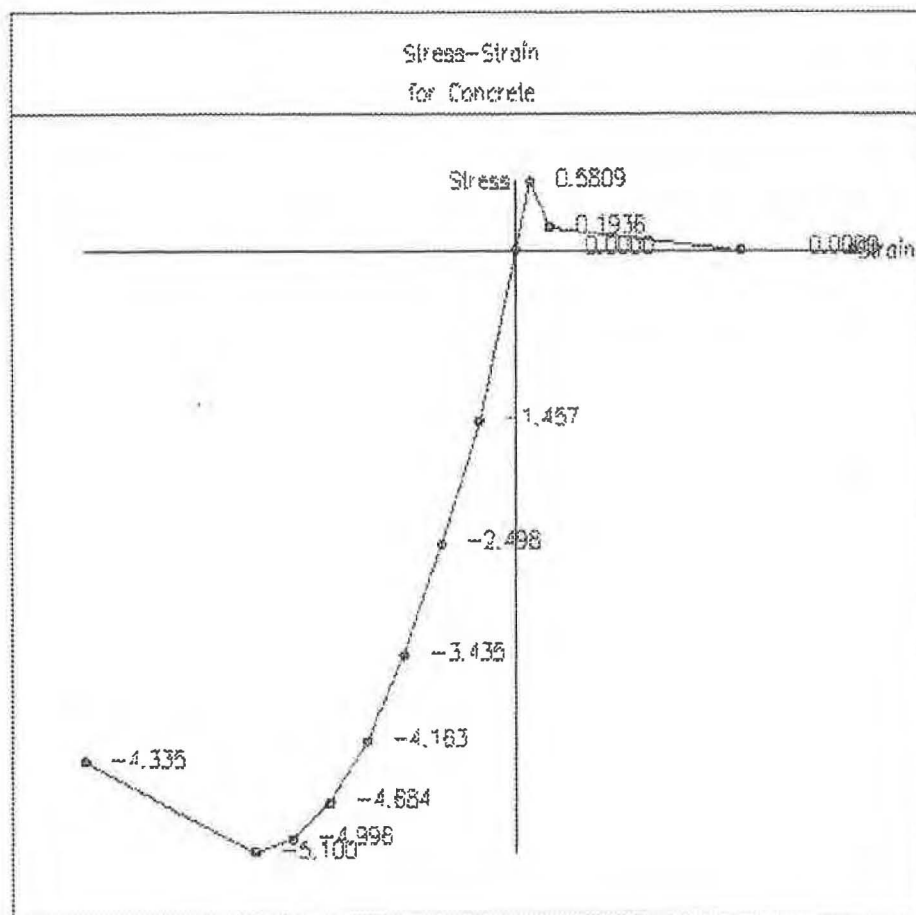
Figure C-6. Stress Values on Concrete Stress-Strain Curve Used in FLPIER
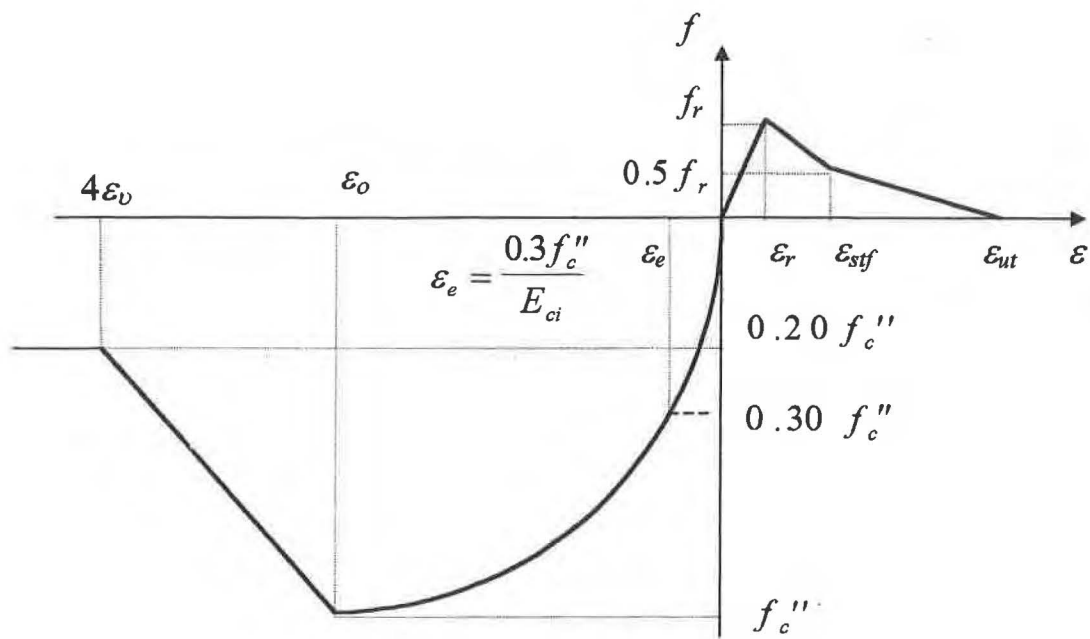
Figure C-7. Envelope Curve for Concrete
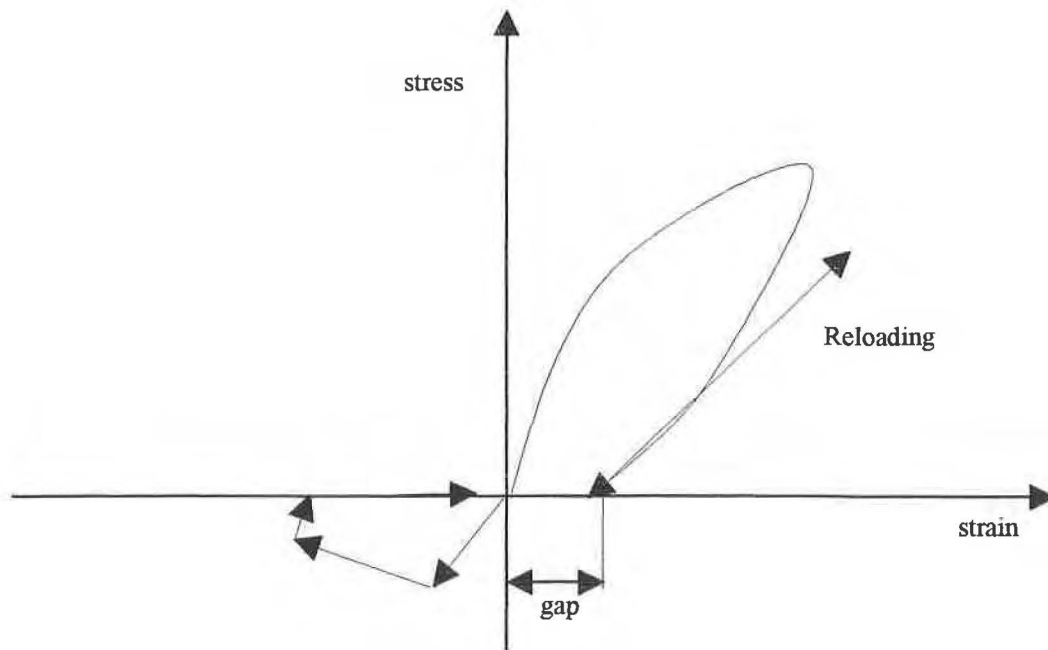
Figure C-8. Concrete Behavior with Gap
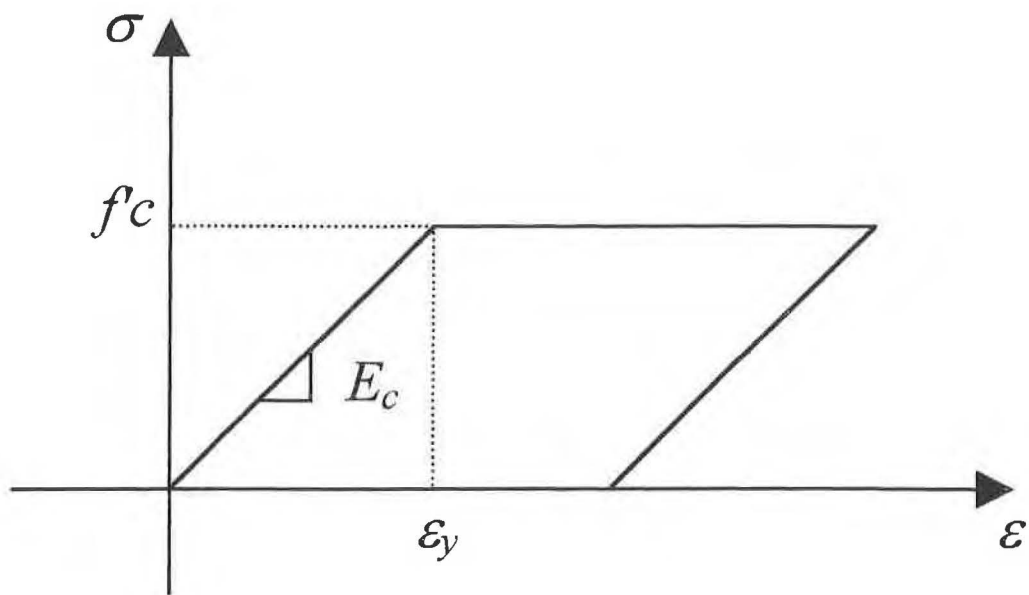
Figure C-9. Bilinear Model for Concrete
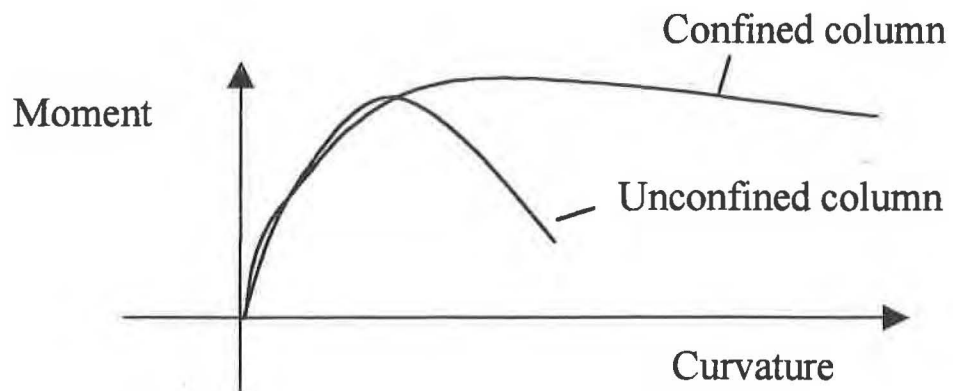
Figure C-10.   Confined and Unconfined Concrete Models Response
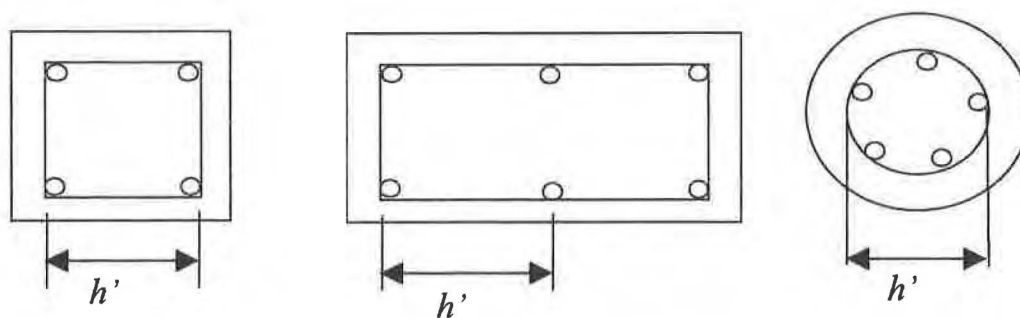
Figure C-11.   Core Width (h') for Various Cross Sections

Concrete Compressive Stress (f)

$K_1K_2f''c$

$K_1K_2f''_cz$

1

$0.2K_1K_2f''_c$

$0.002K_1K_2$

Concrete Compressive Strain (ε)
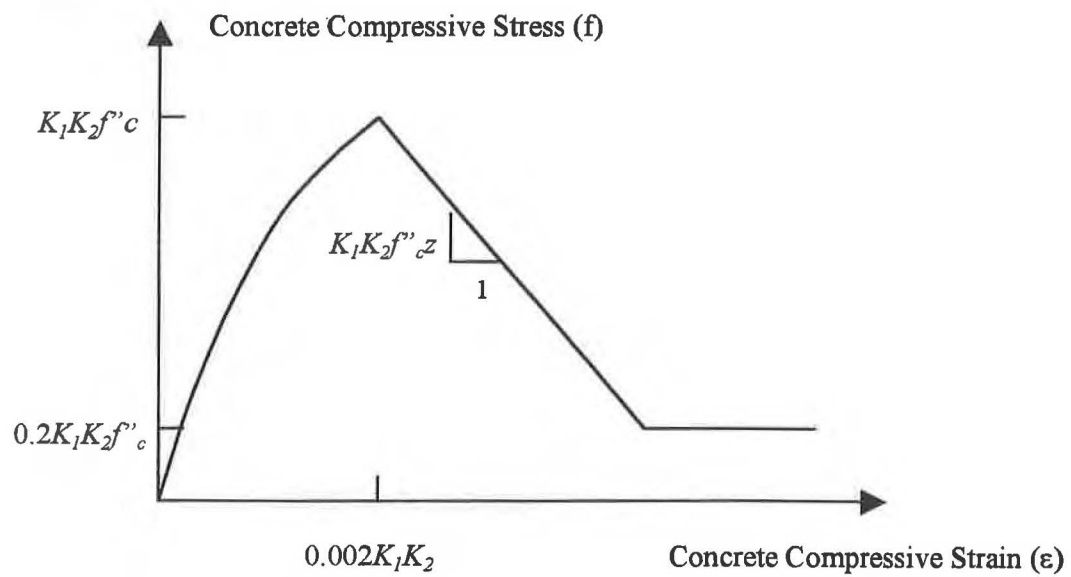
Figure C-12. Confined Concrete Model
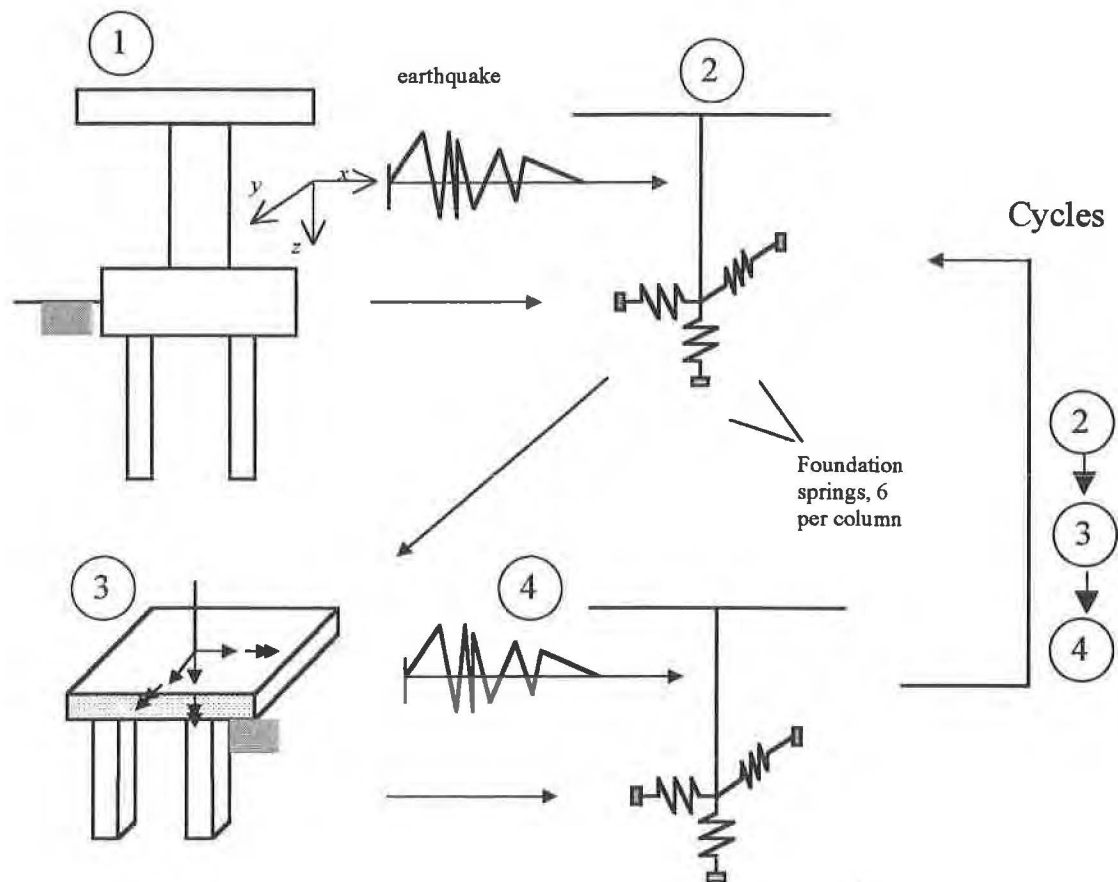
Figure C-13. Modal Analysis of a Pier in FLPIER
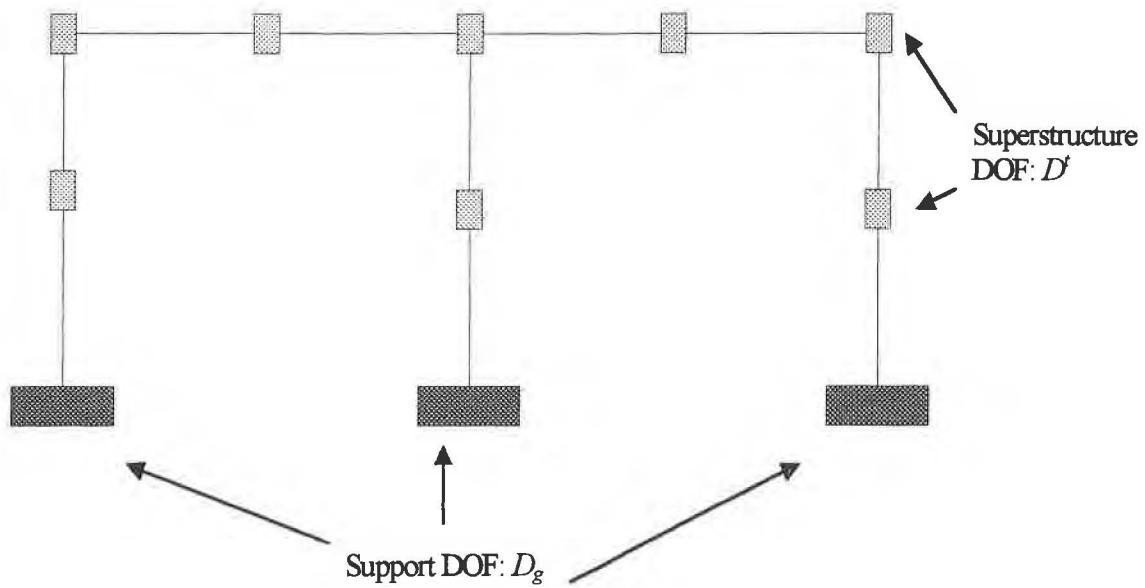
Figure C-14. Multiple Support Motion
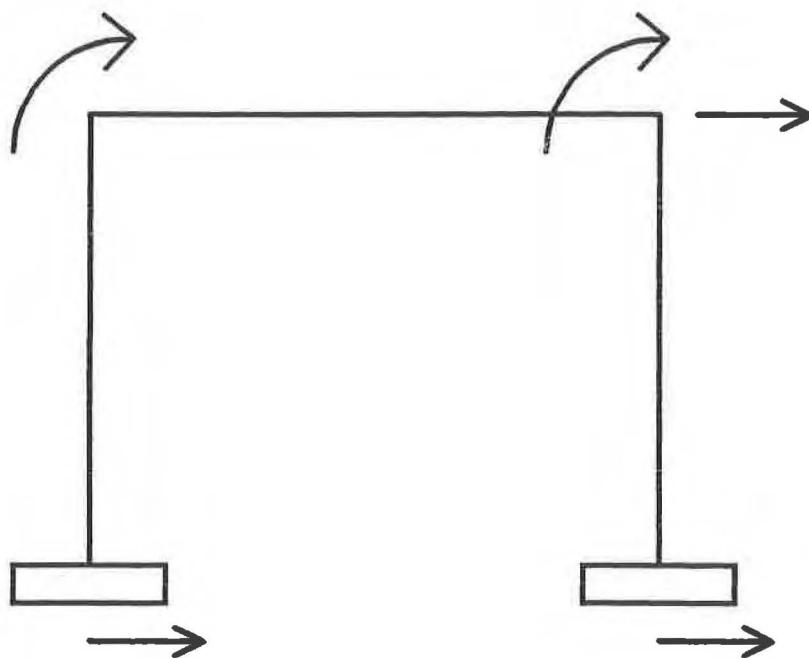
Figure C-15. 2-D Frame Subjected to Multiple Support Motion
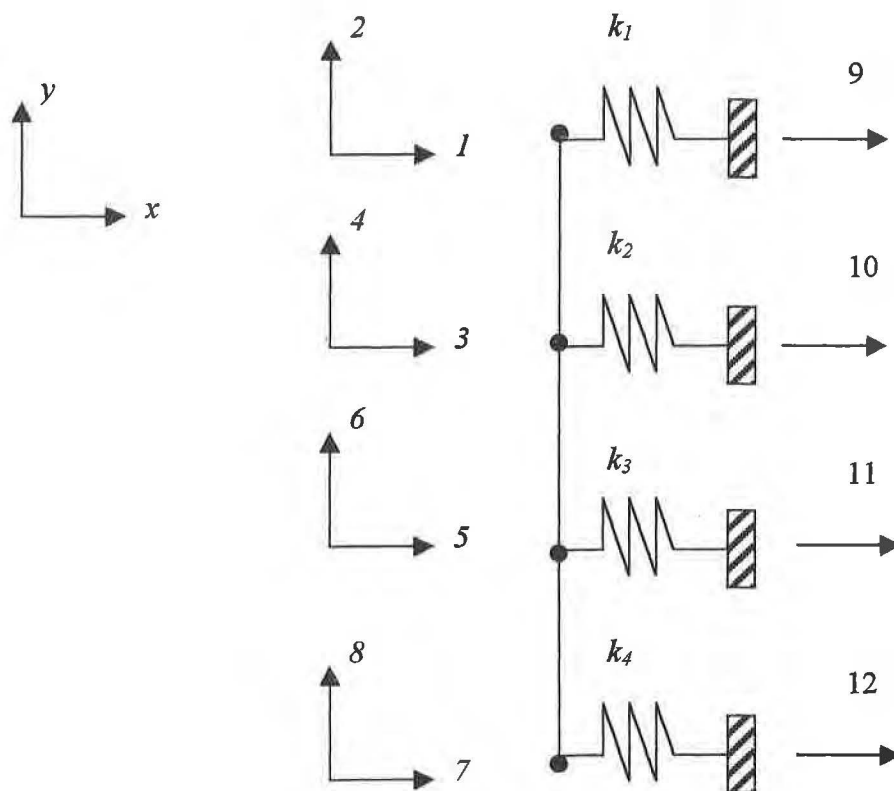
Figure C-16. Pile Subjected to Multiple Support Excitation
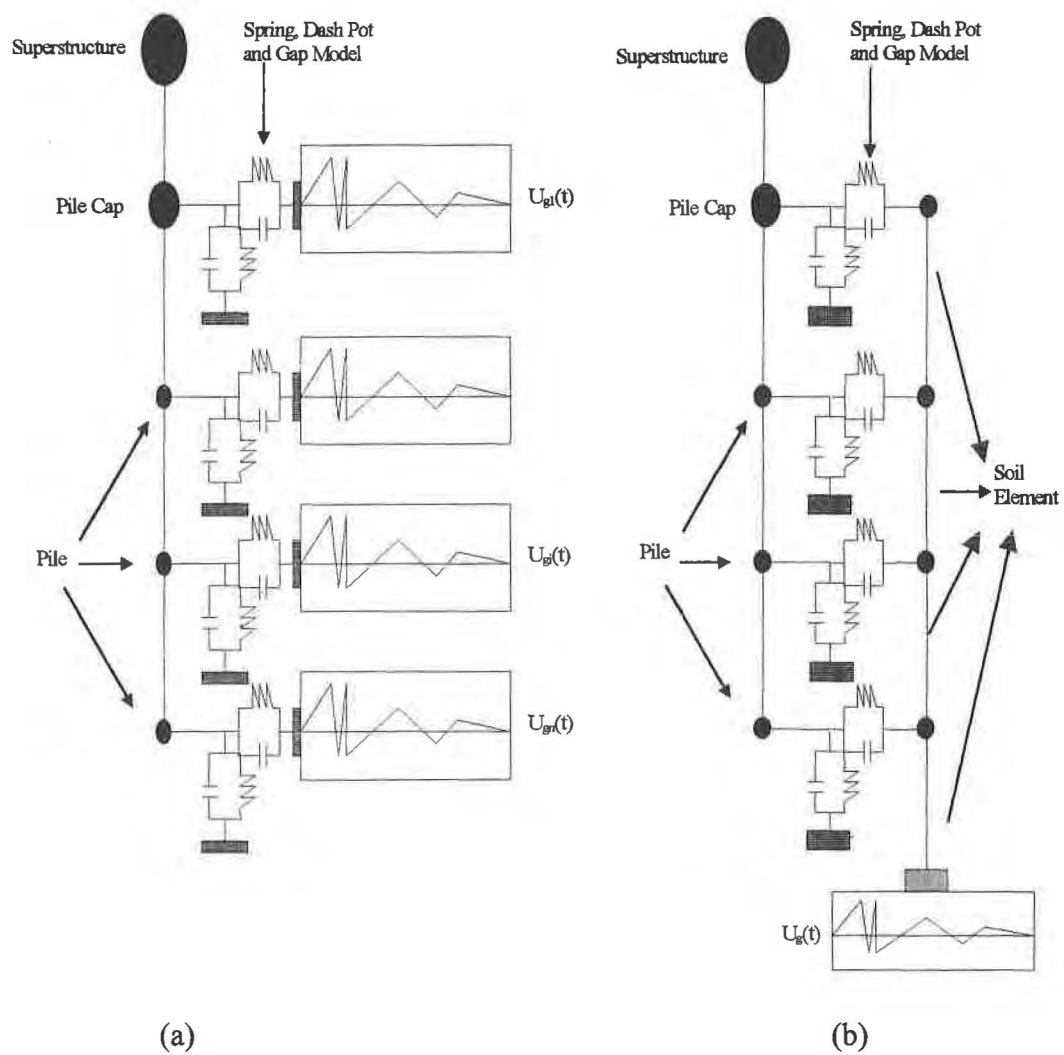
Figure C-17. (a) Coupled Model; (b) Uncoupled Model
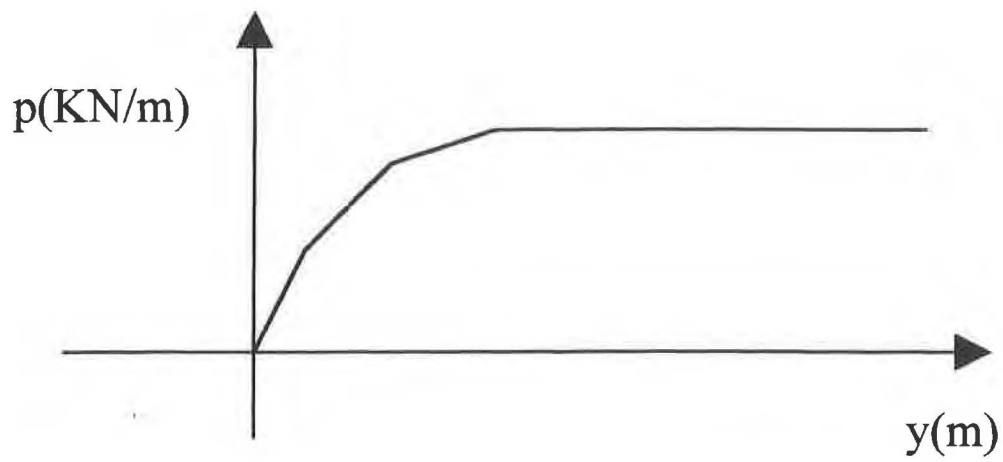
Figure C-18. Form of a Typical Static p-y Curve
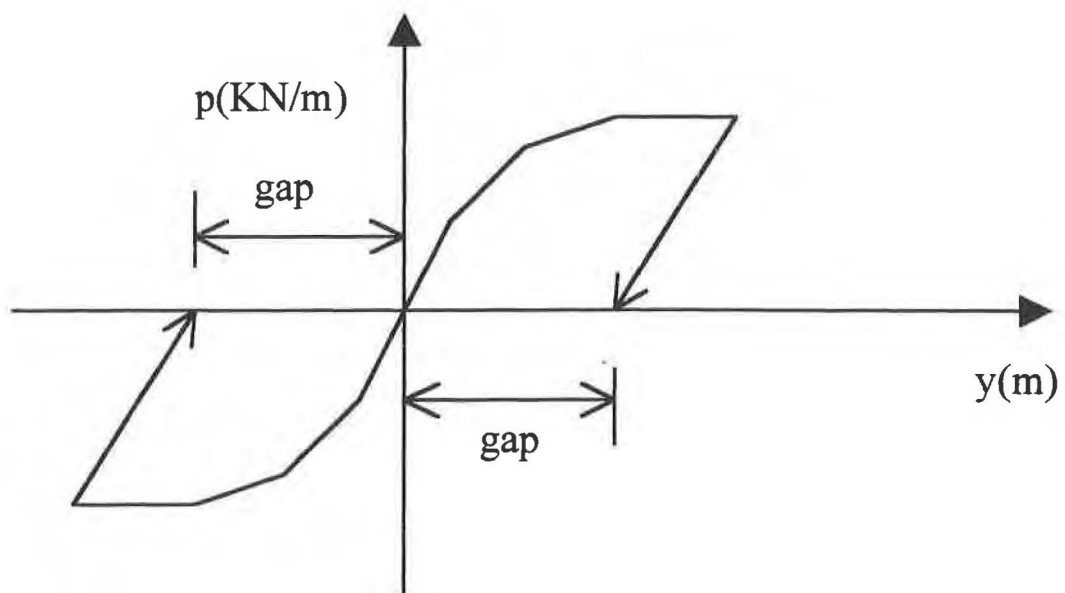
Figure C-19. Cyclic p-y Model

$m = 1 \ kip \ s^2/in$

$k = 10000 \ kip/in$

$c = 200 \ kip \ s/in$

L
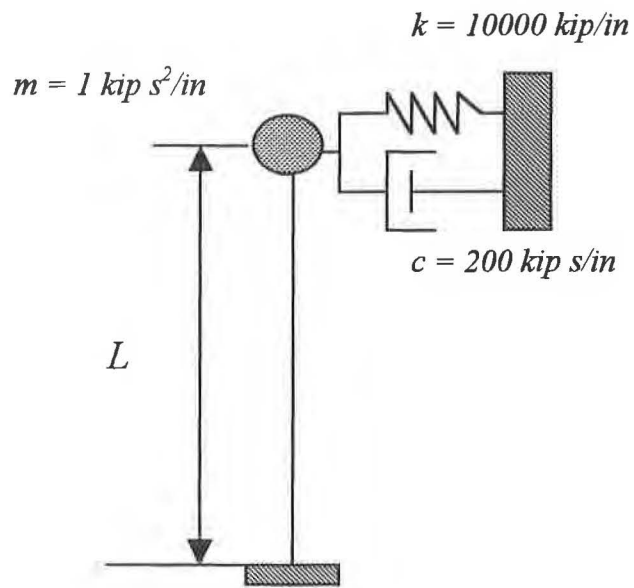
Figure C-20. Example 1: Computer (Rheological) Model
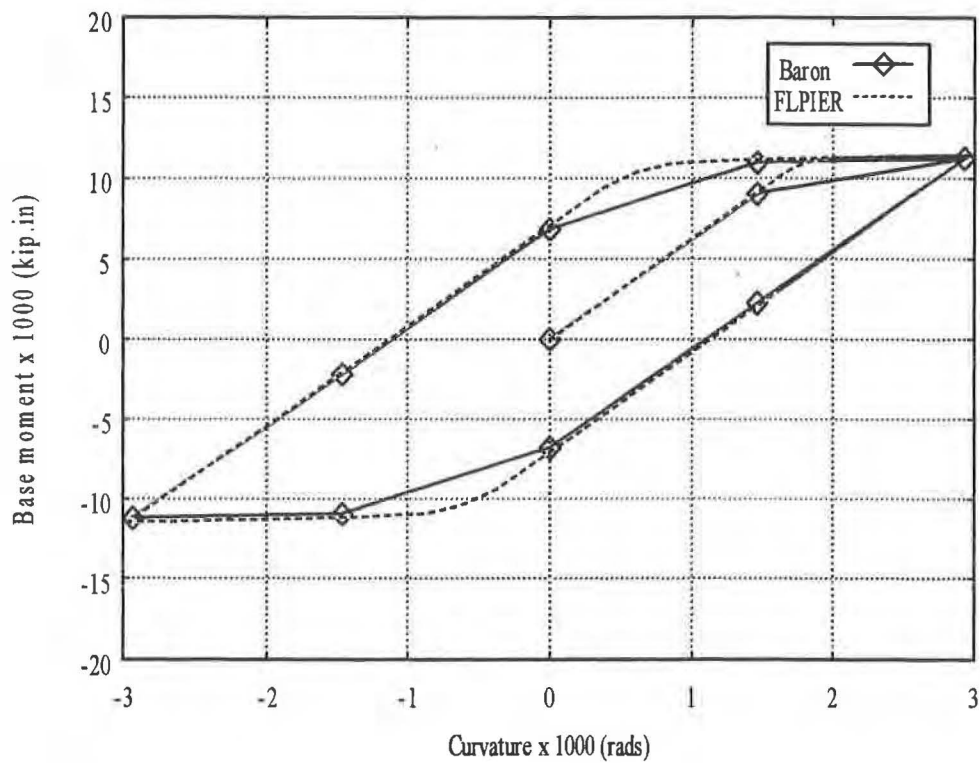
*Figure C-21. Example 1: Comparison FLPIER and Measured Results —Reference for
Cyclic Loading*

14.585

0.505

0.505

13.61

12.60

0.505

$P=537.5\,kips$

$k=1\times10^{10}\,kip/in$

Δc

$L=15'=180''$
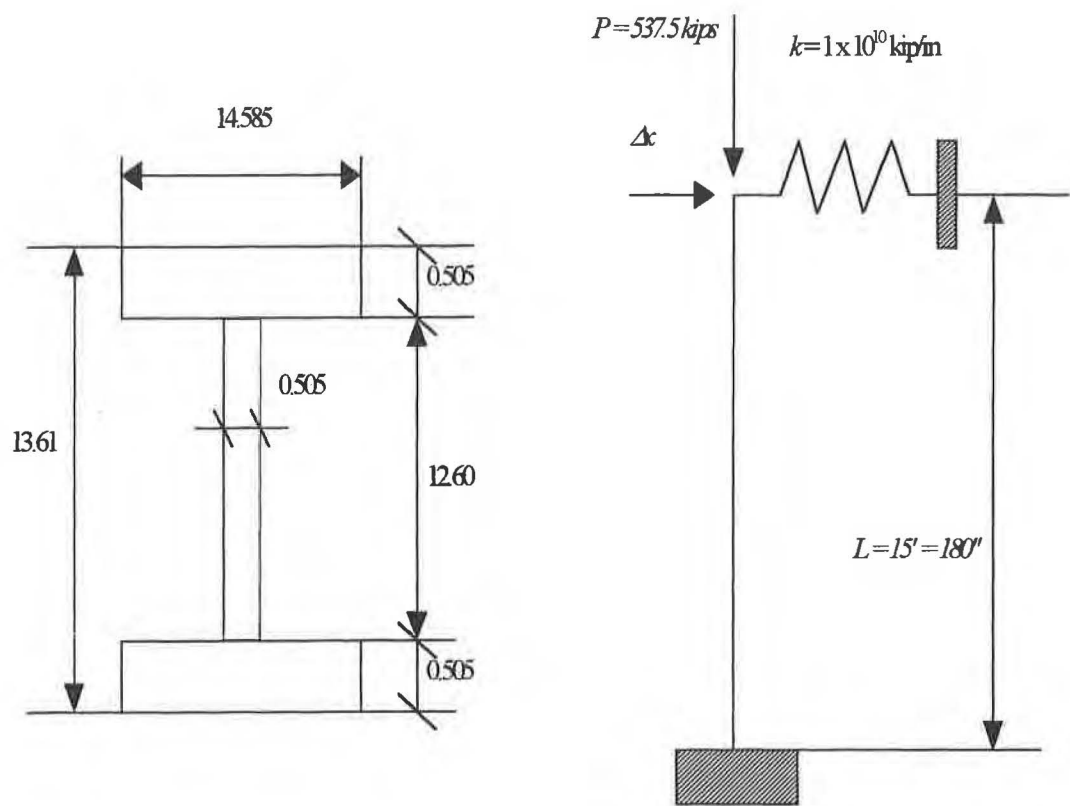
Units are inches.
$fy=50\,ksi,\ E_s=29000\,ksi$

Figure C-22. Example 2: Computer (Rheological) Model
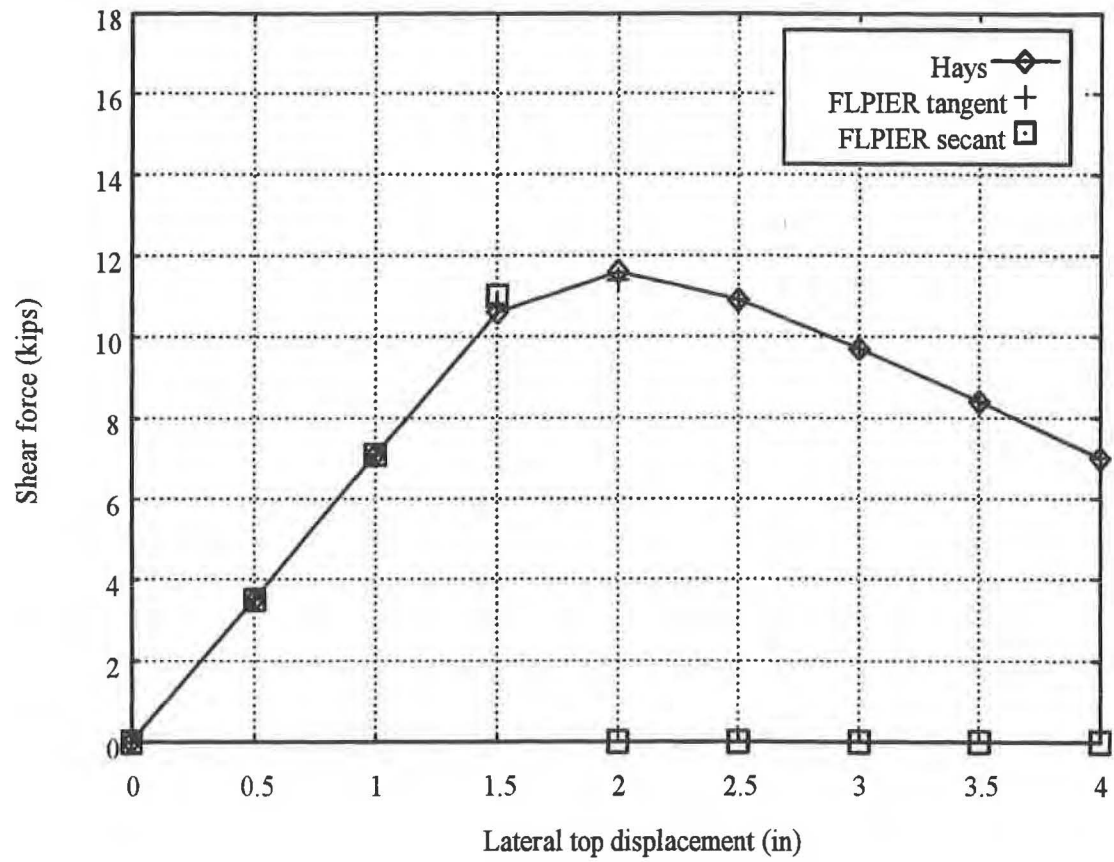
Figure C-23. Example 2: Comparison of FLPIER and Hays —Shear Forces
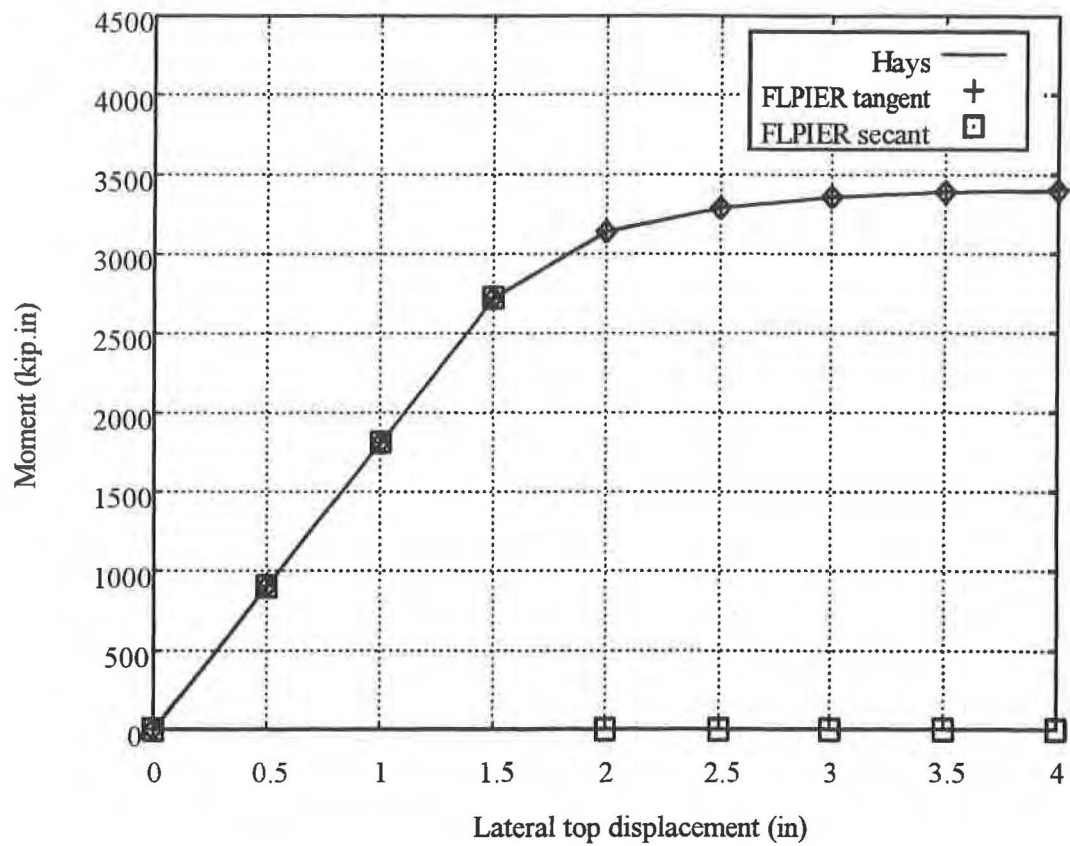
Figure. C-24. Example 2: Comparison of FLPIER and Hays — Bending Moments
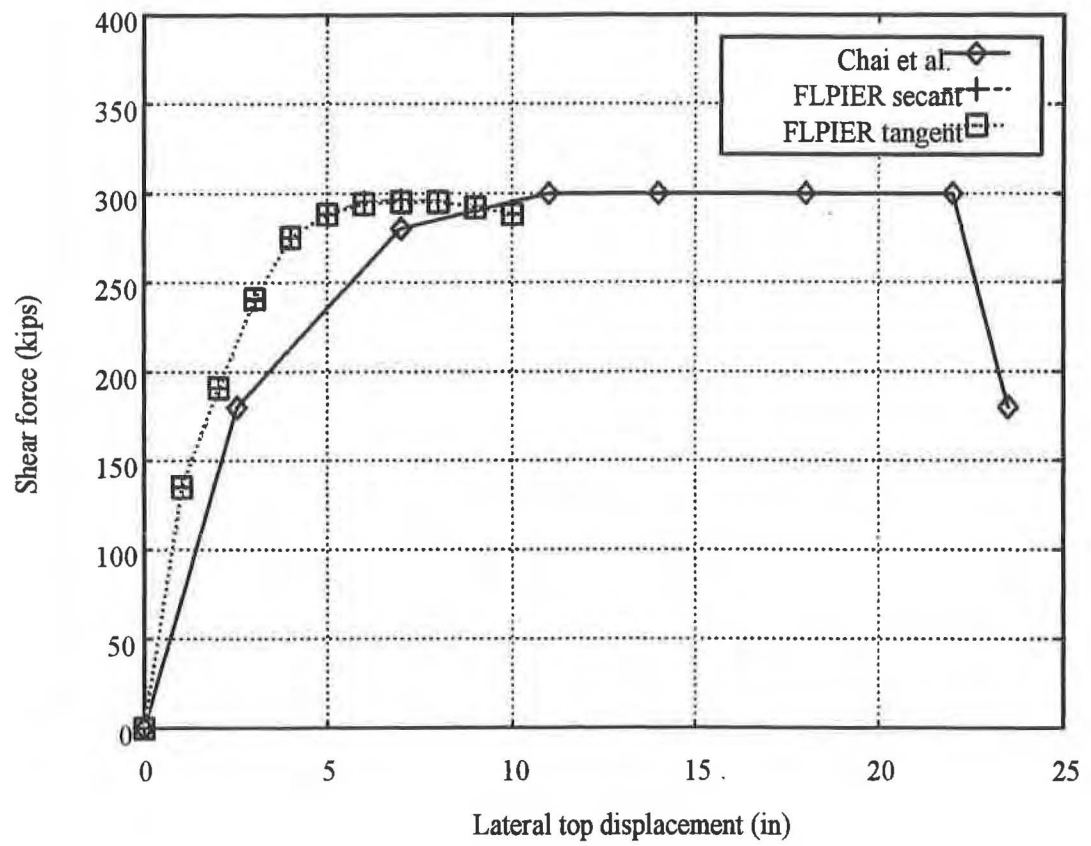
Figure C-25. Example 3:   Comparison of FLPIER and Test Results — Shear
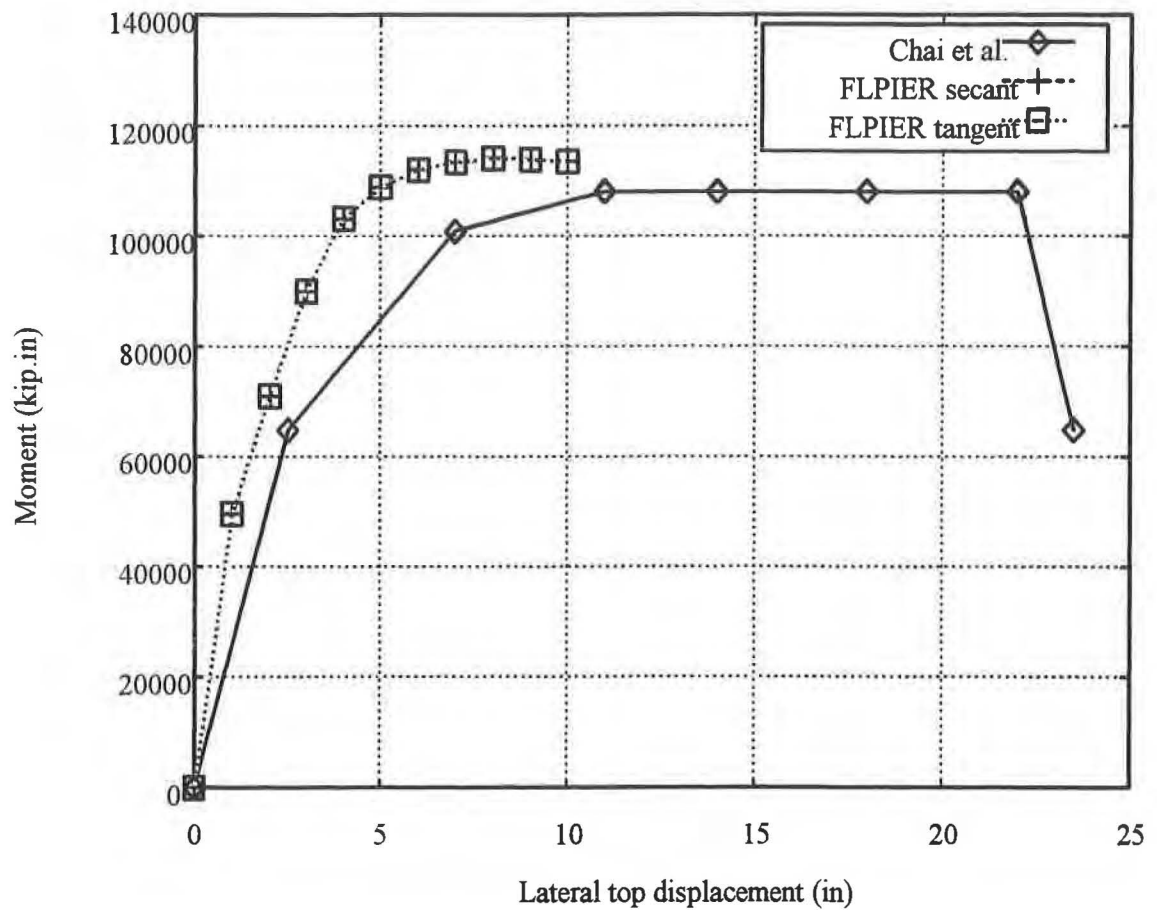
Figure C-26. Example 3: Comparison of FLPIER and Test Results —Moment
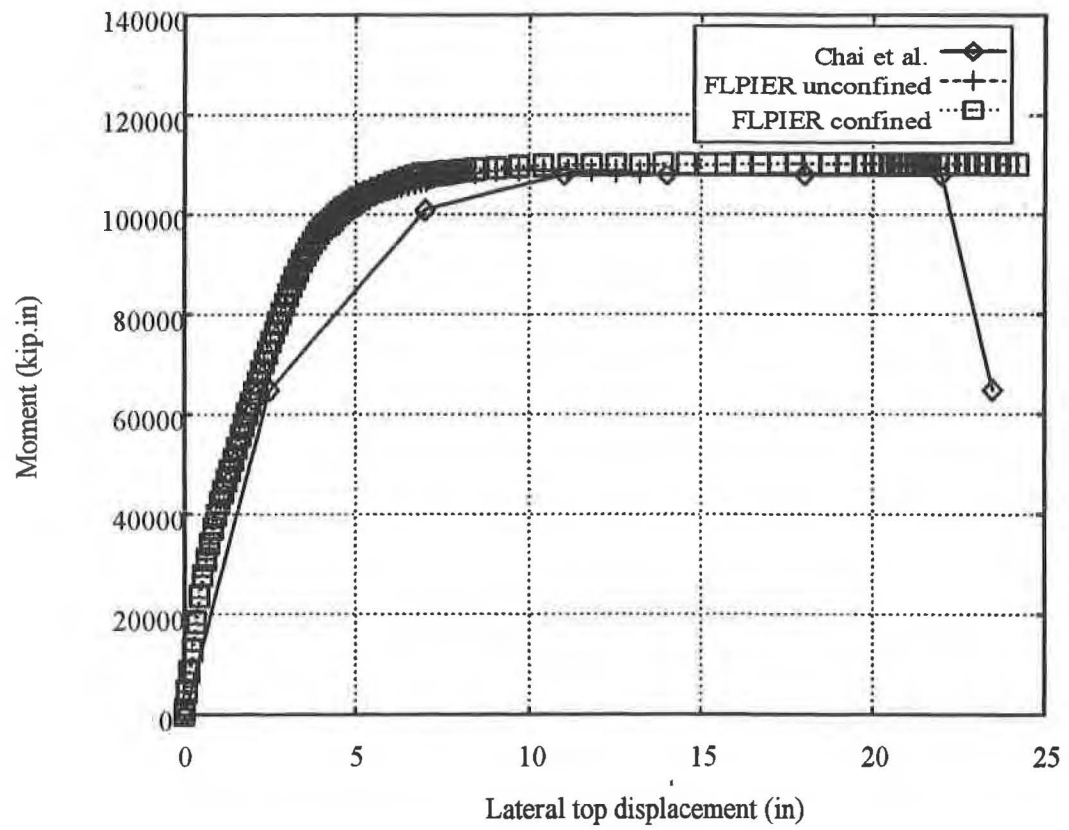
Figure C-27. Example 3: Comparison of FLPIER and Test Results Using Quasi-Dynamic Model —Effect of Concrete Confinement
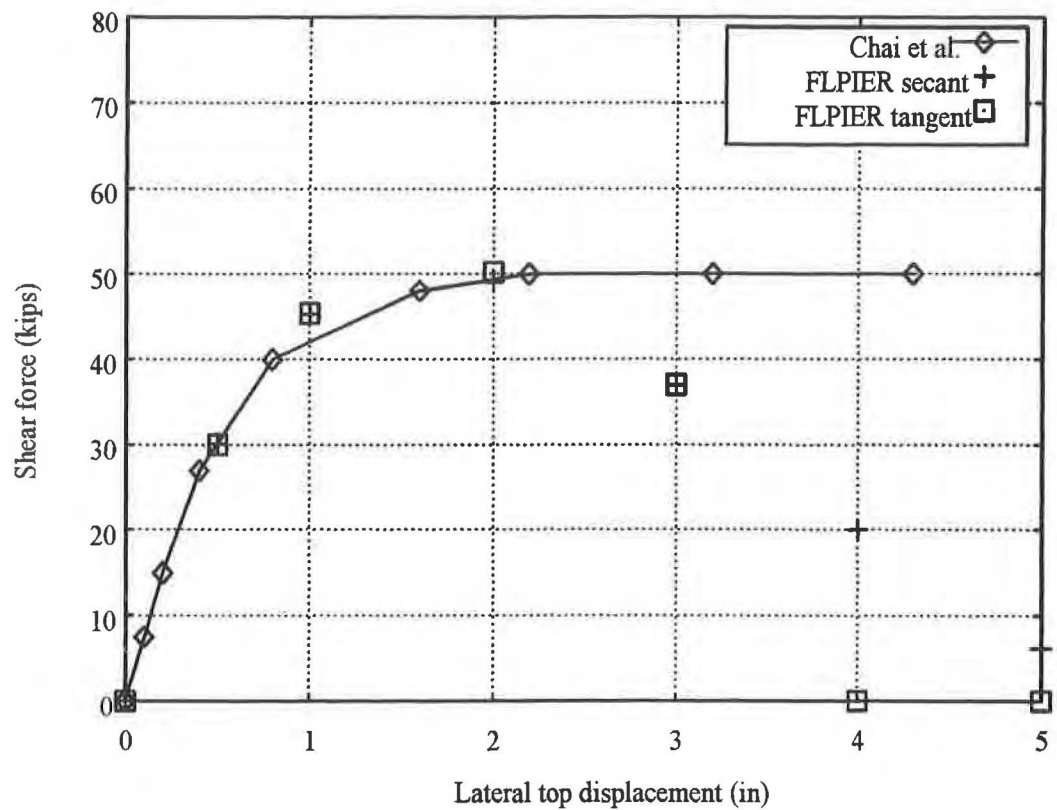
Figure C-28. Example 4: Comparison of FLPIER with Test — Static Shear
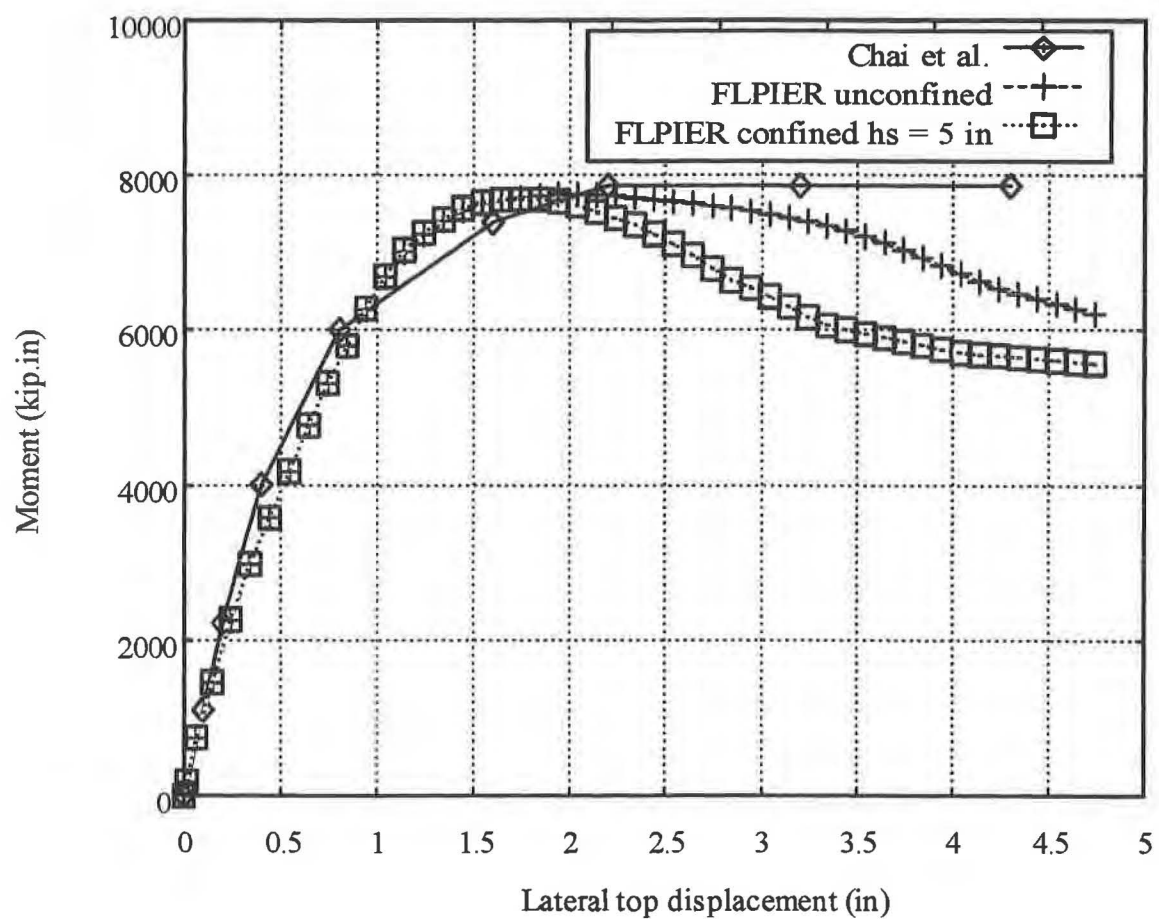
Figure C-29.   Example 4: Comparison of FLPIER and Test — Dynamic Moment with.
Hoop Spacing = 5 in.
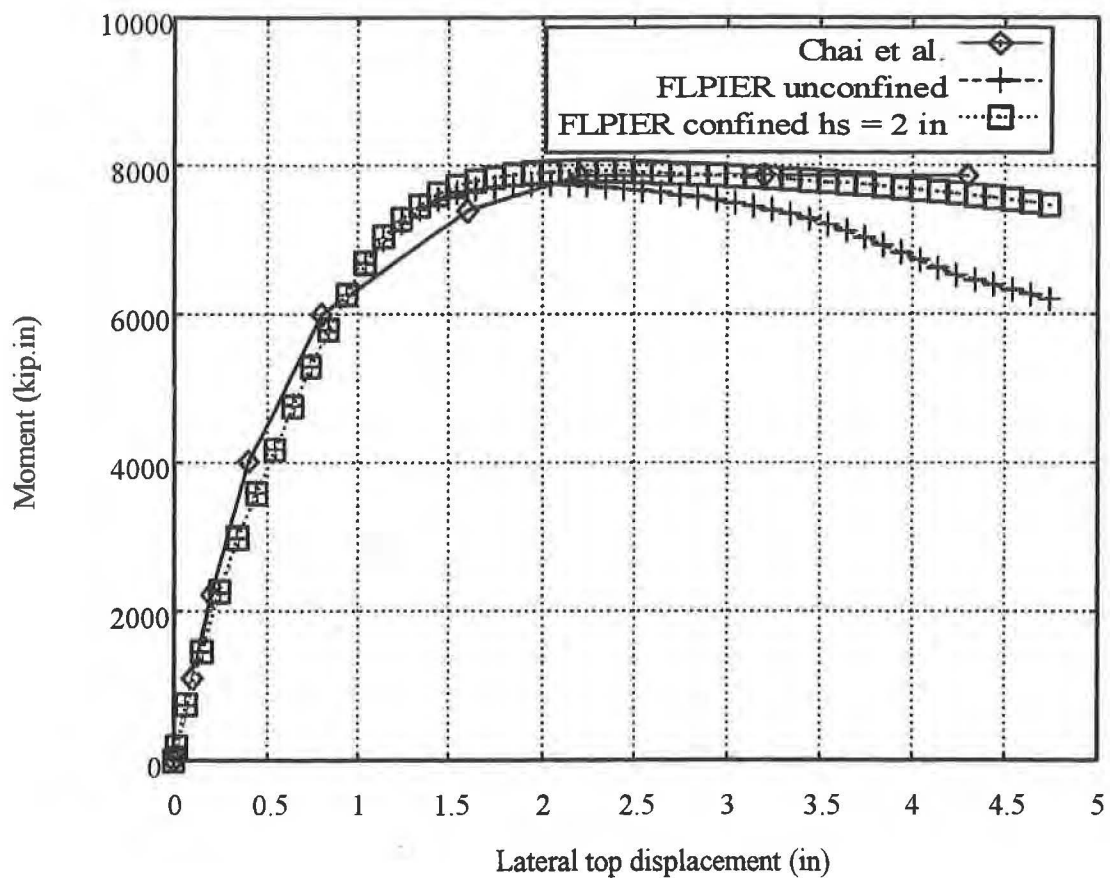
Figure C-30. Example 4: Comparison of FLPIER and Test —Dynamic Moment with Hoop Spacing = 2 in.
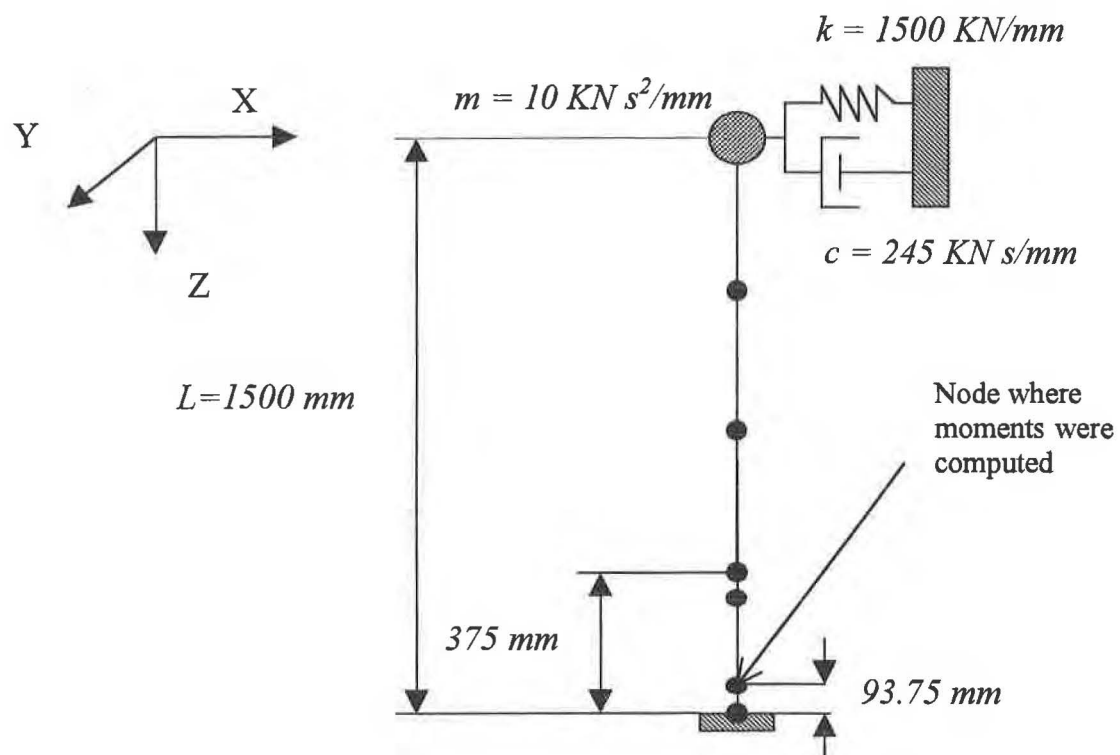
Figure C-31. Example 5: Computer (Rheological) Model for Test S03
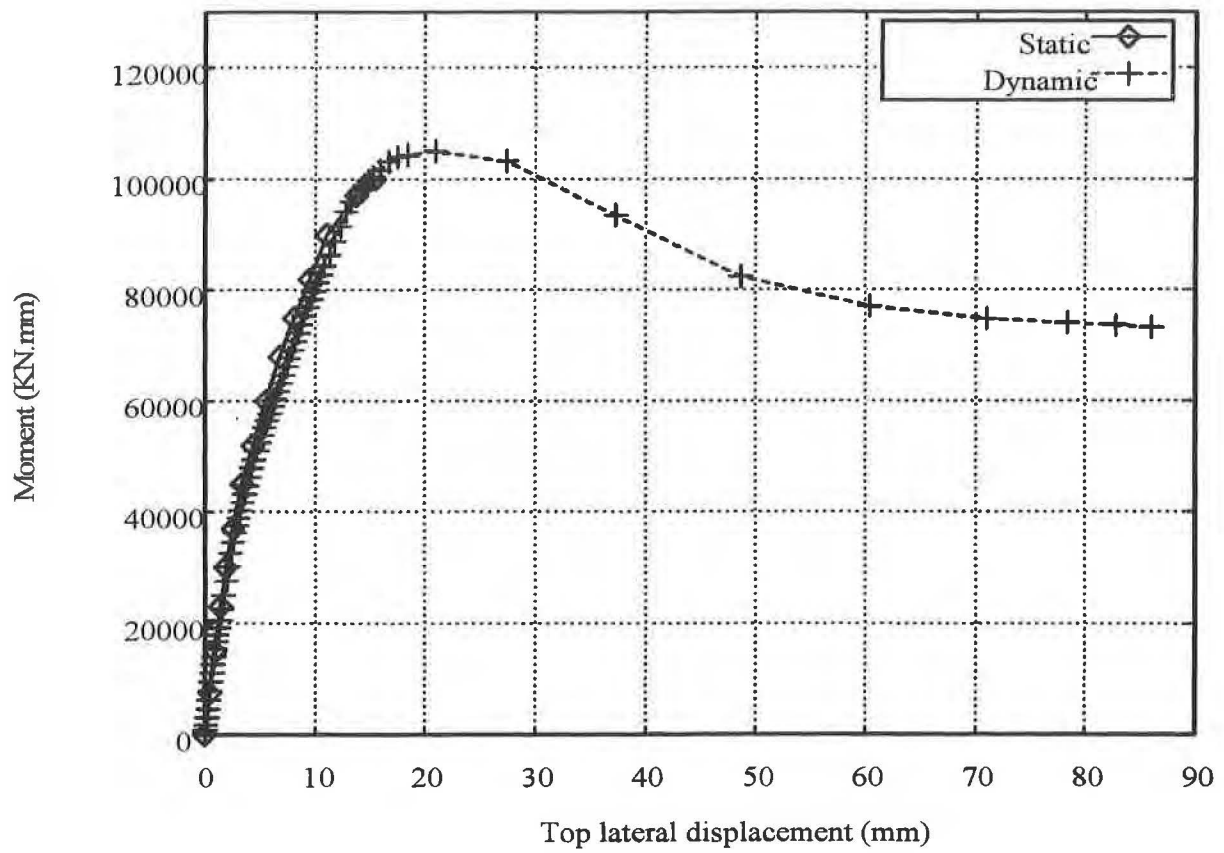
Figure C-32. Example 5: Column Capacity from FLPIER with Static and Dynamic Concrete Models
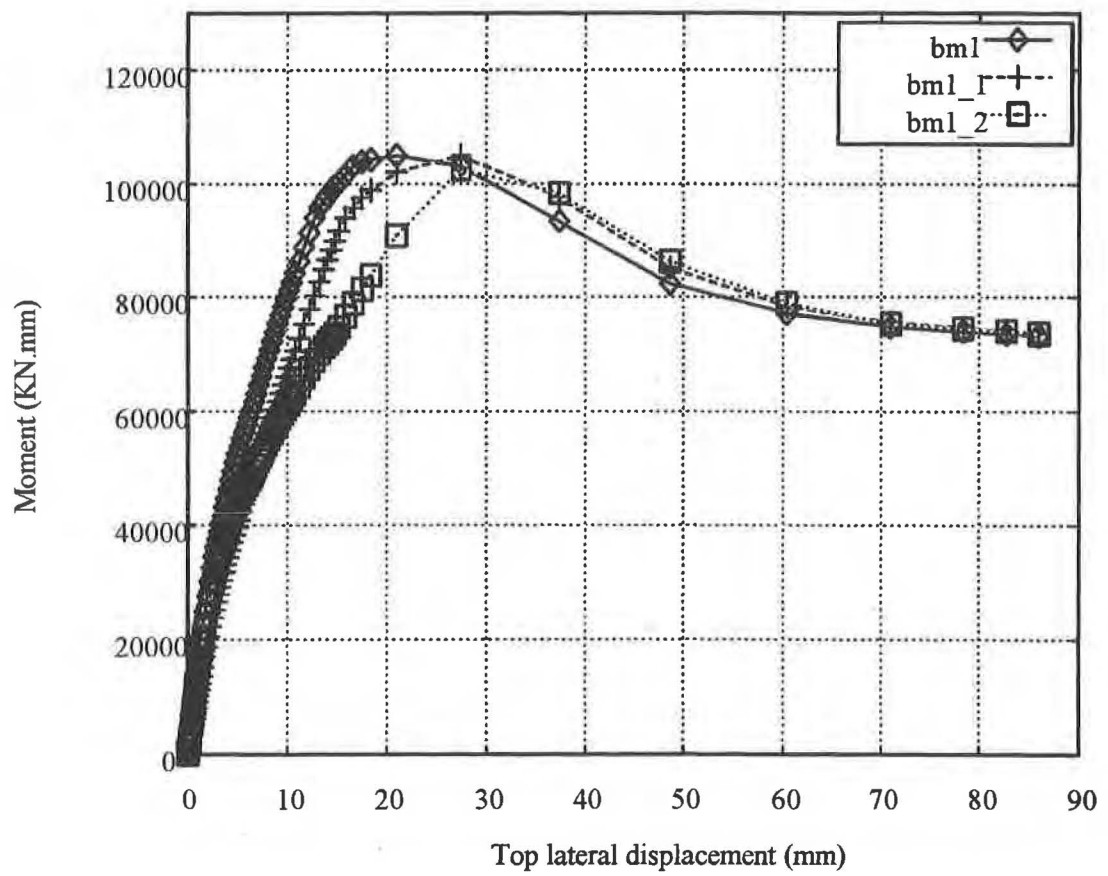
Figure C- 33. Example 5: Parametric Study — E_c and E_s Changed
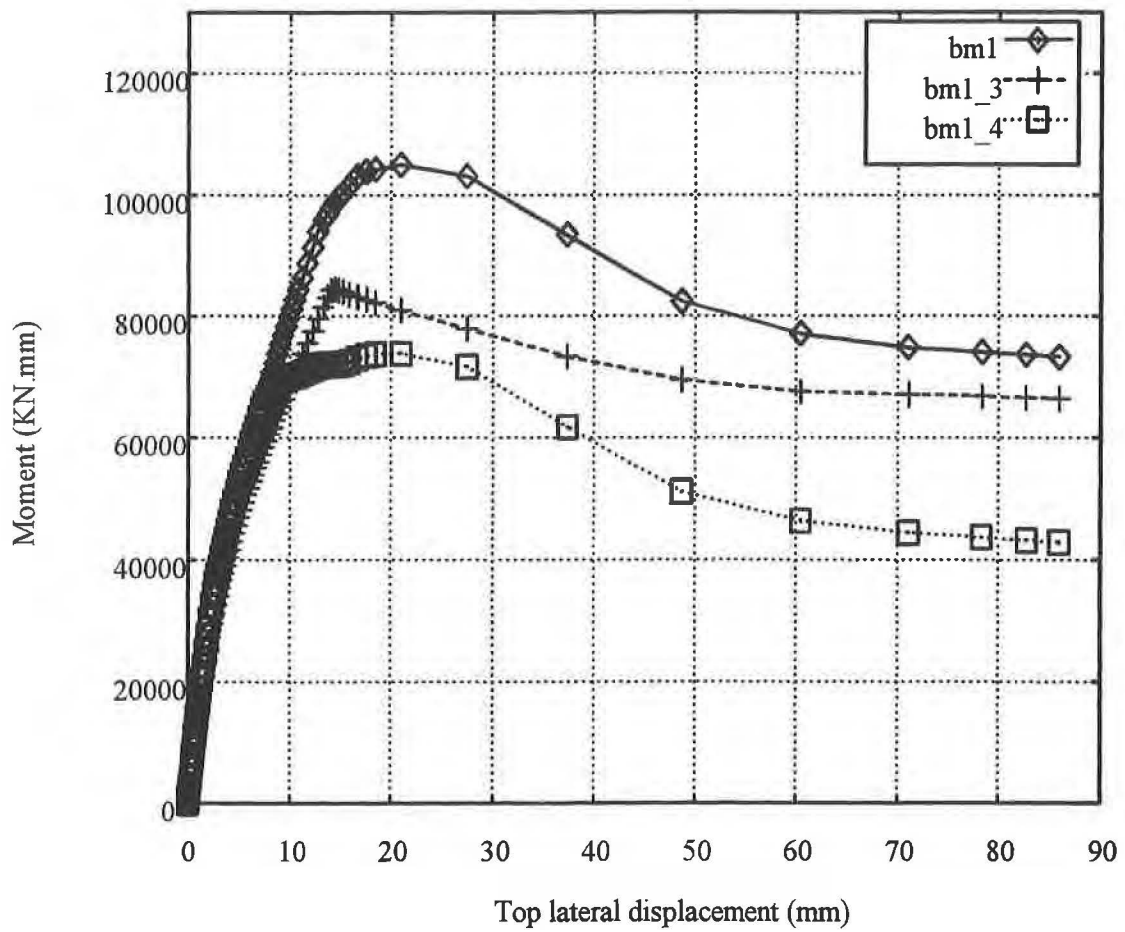
Figure C- 34. Example 5: Parametric Study — f'c and fy Changed
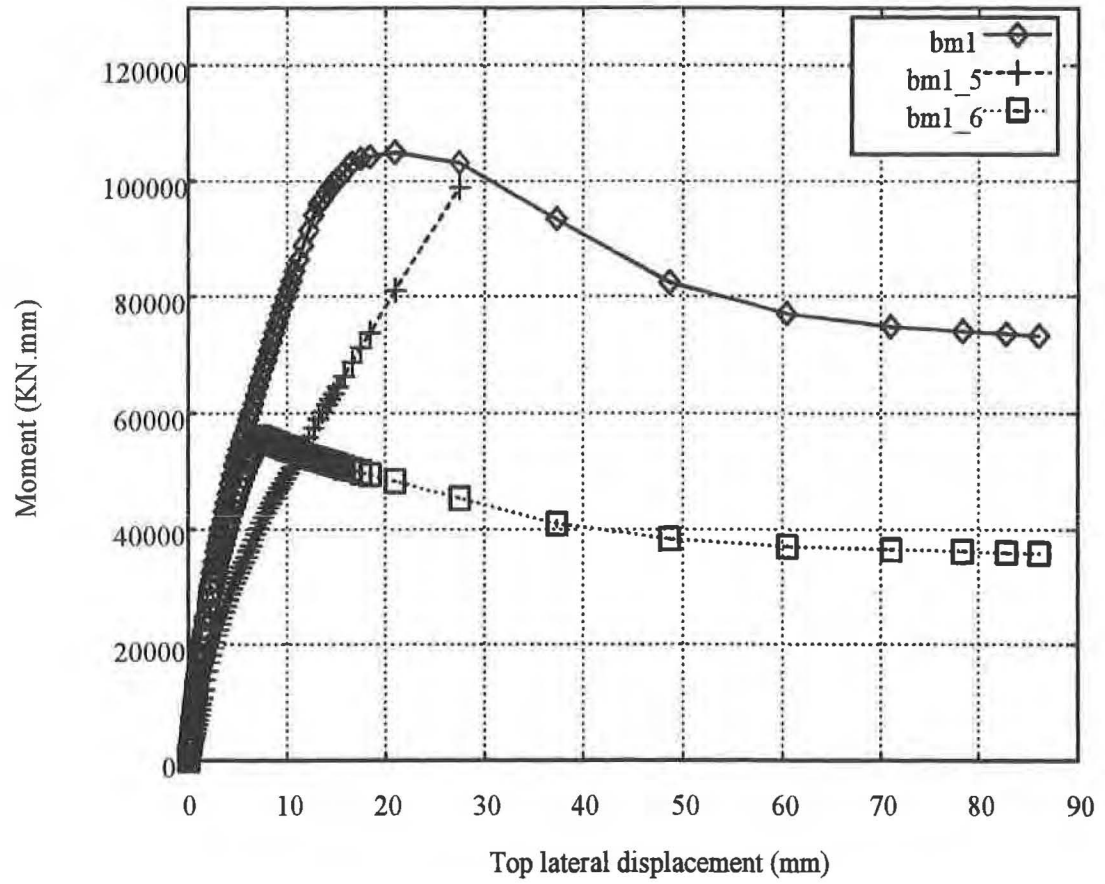
Figure C- 35. Example 5: Parametric Study — E and f Changed
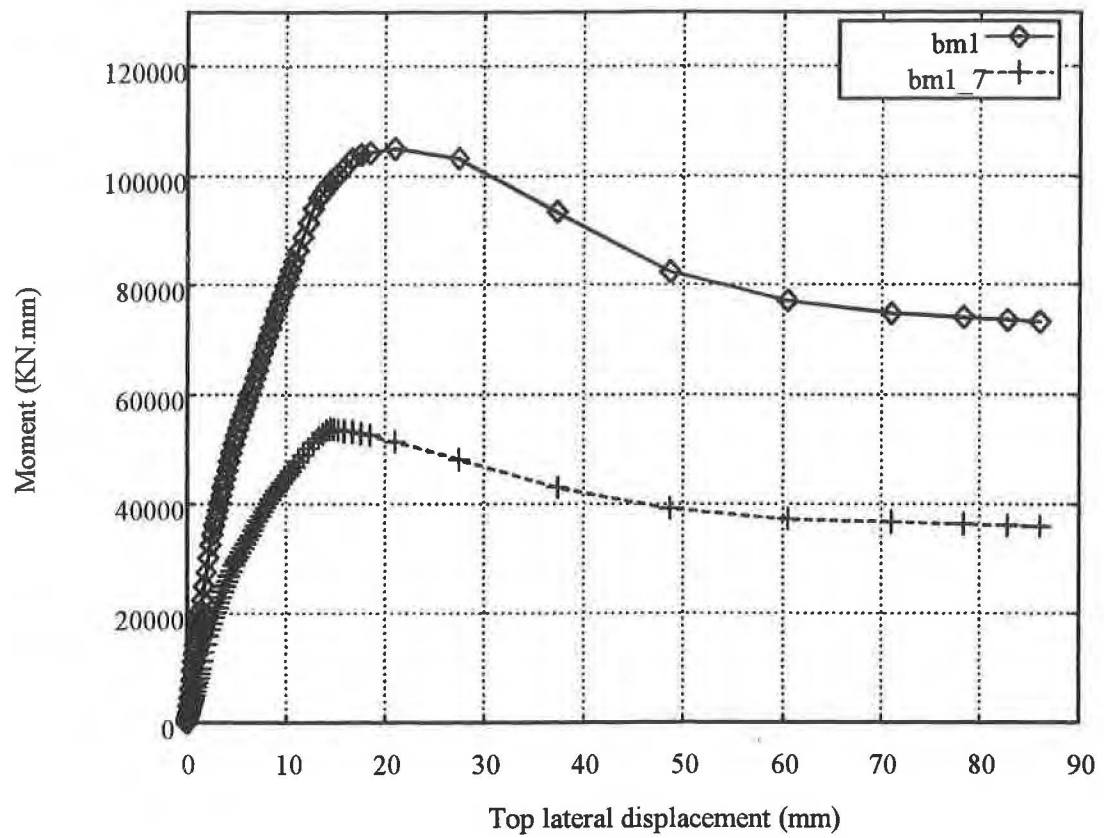
Figure C- 36. Example 5: Parametric Study — All Parameters Changed
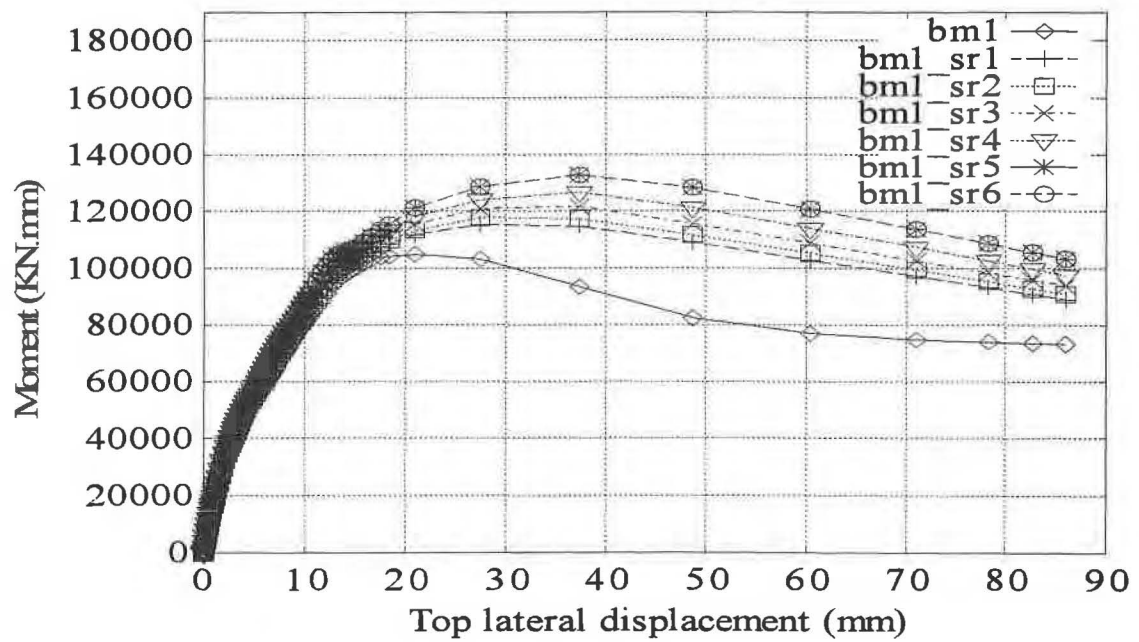
Figure C- 37. Example 5: Parametric Study — Confinement and Strain Rate Effects
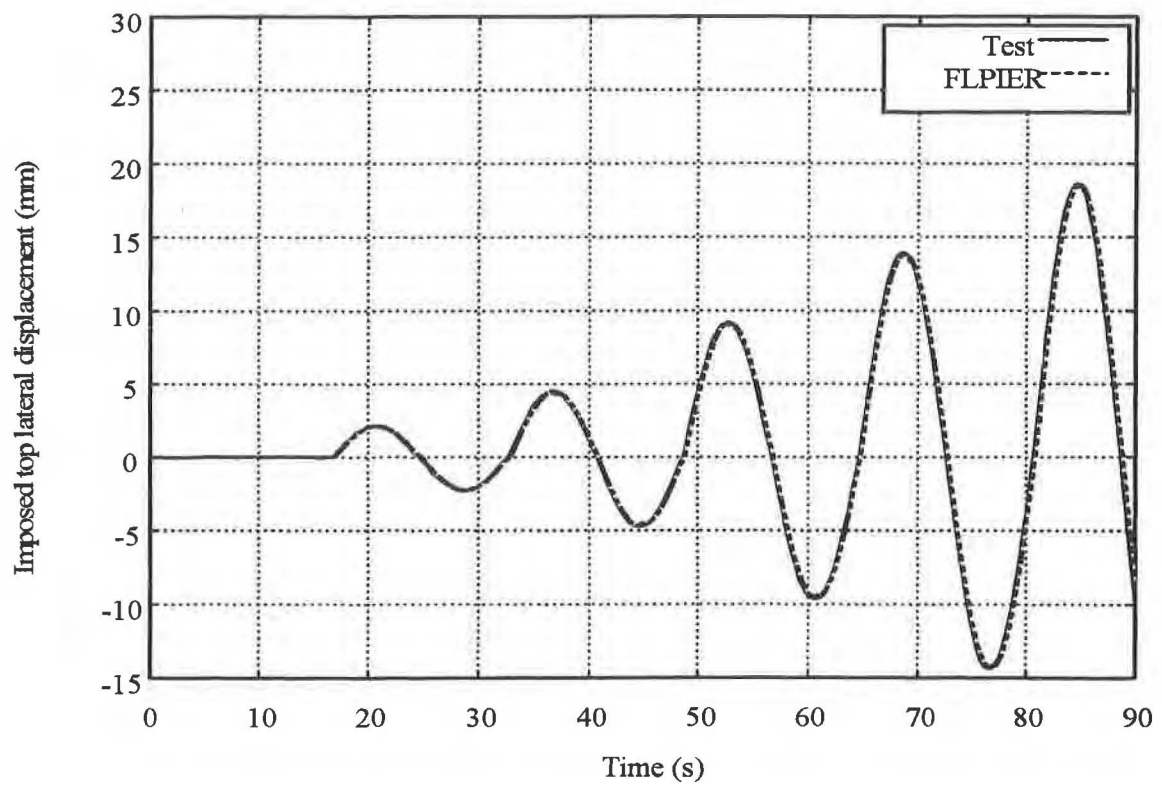
Figure C-38. Example 5: Imposed Displacement History for the First 90 Seconds for Physical Test and FLPIER
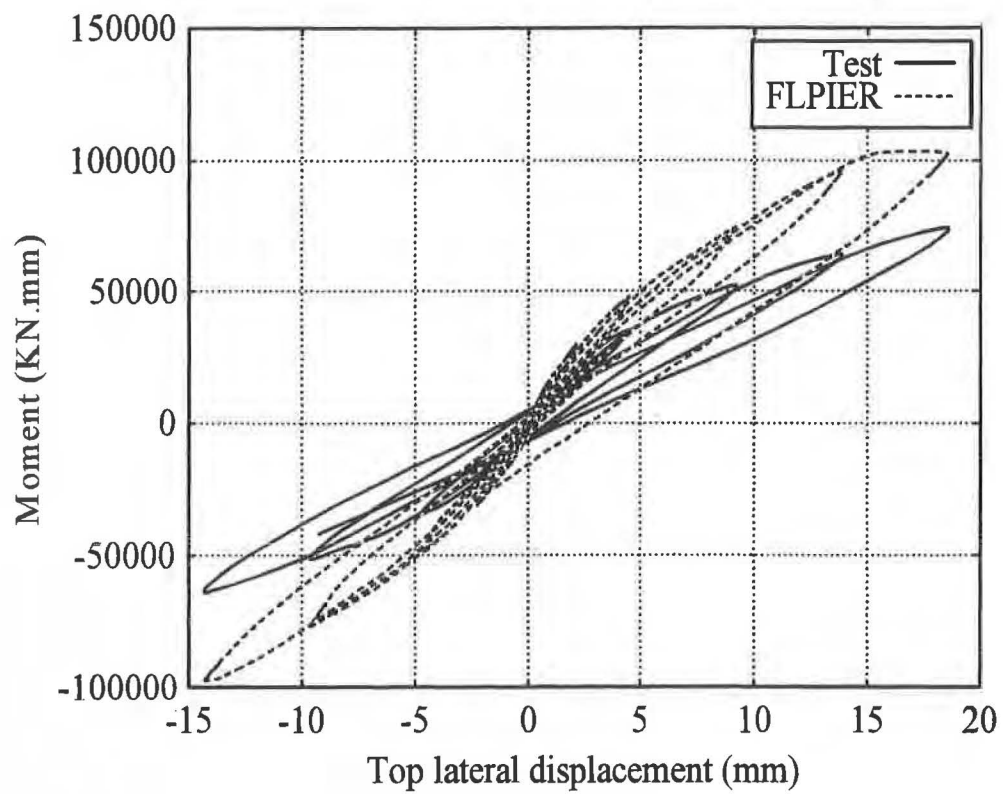
Figure C-39. Example 5: Comparison FLPIER with Physical Test, Original Properties
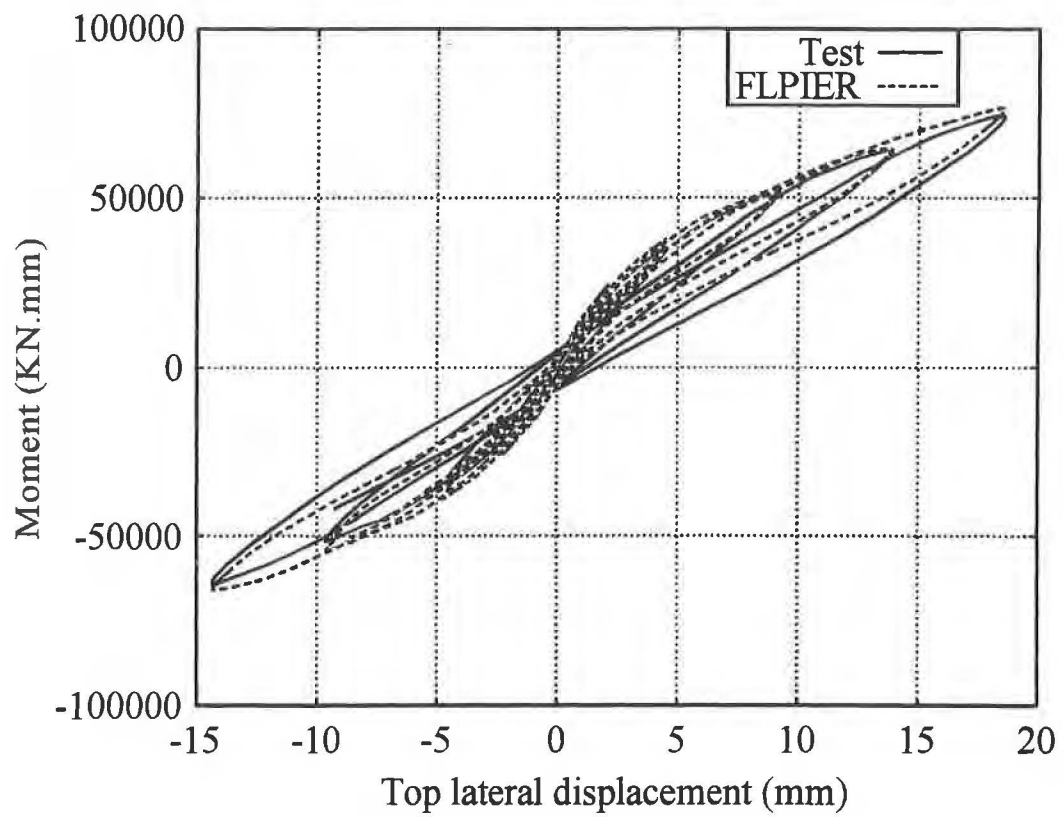
Figure C-40. Example 5: Comparison FLPIER with Physical Test, Modified Properties
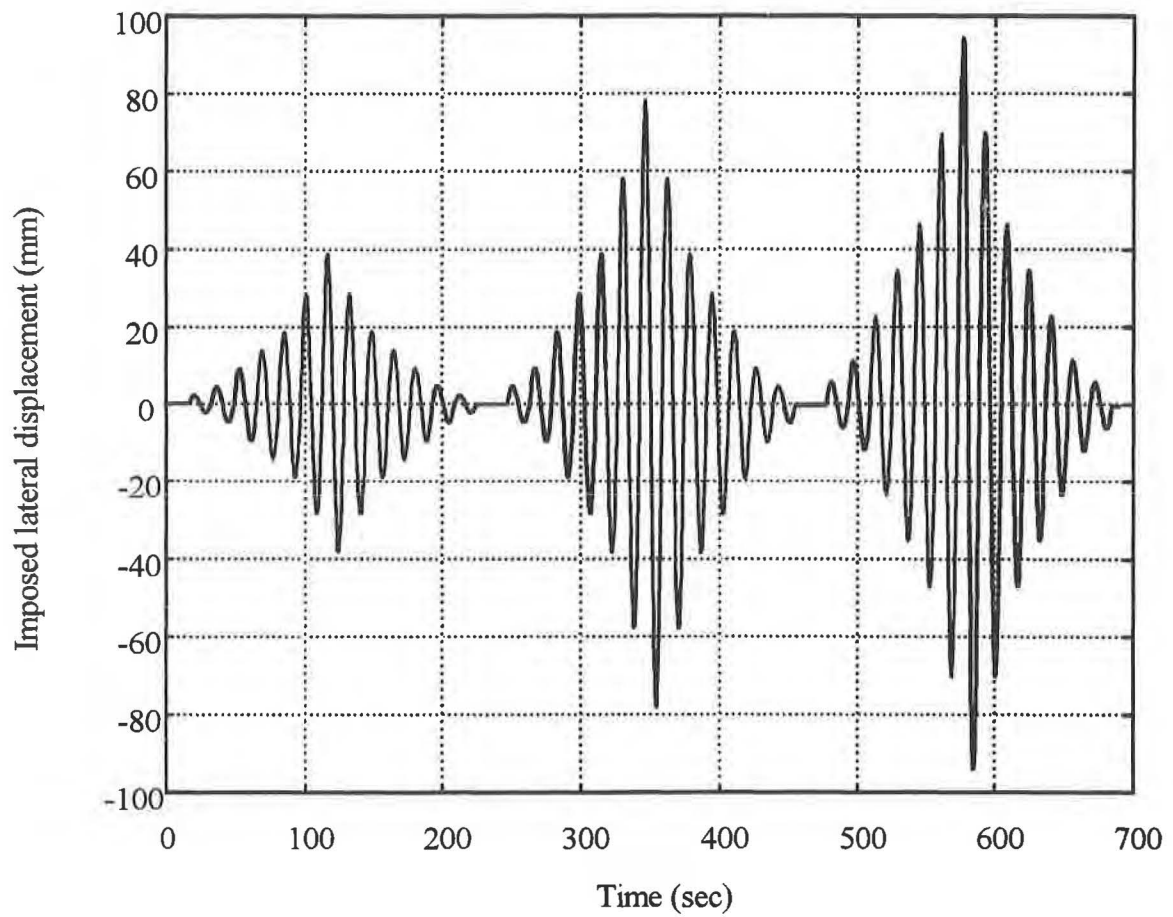
Figure C-41. Example 5: Imposed Tip Displacement Time History
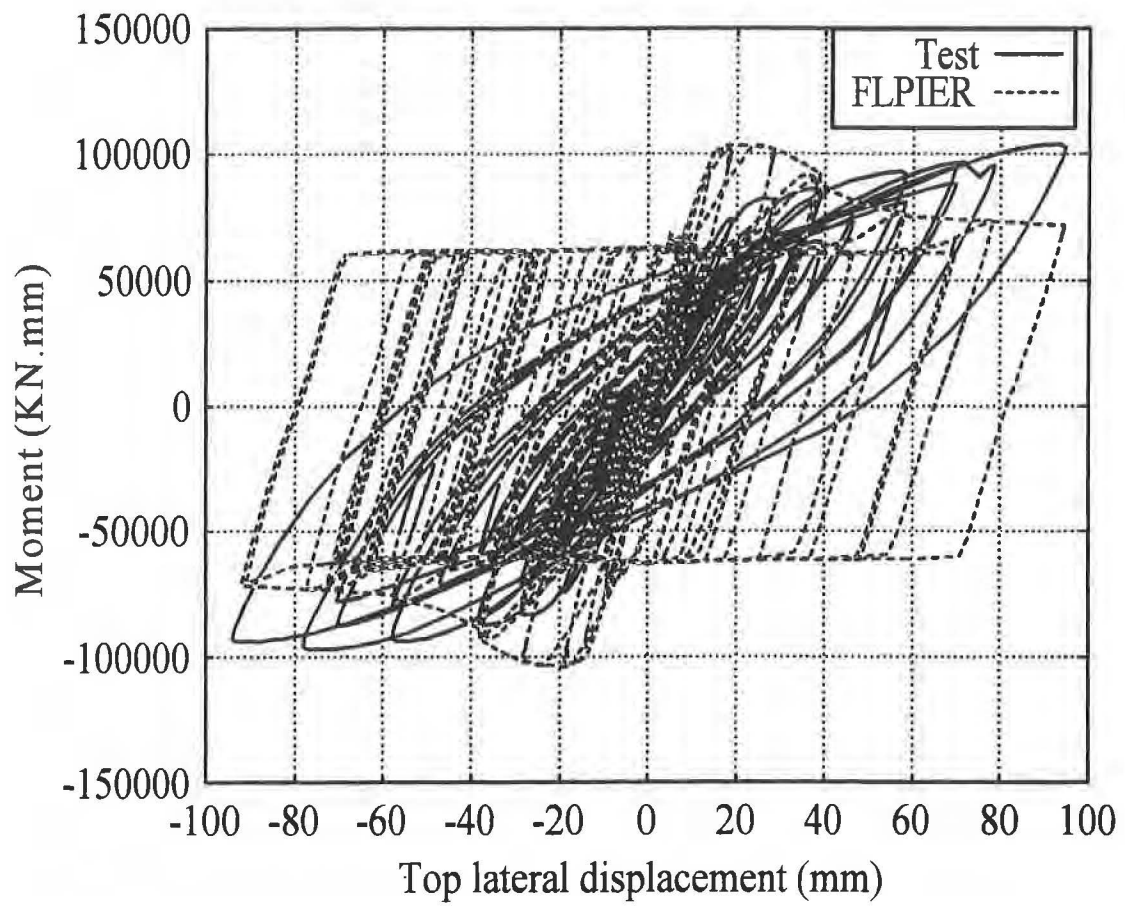
Figure C-42. Example 5: Comparison of FLPIER with Physical Test, ts01
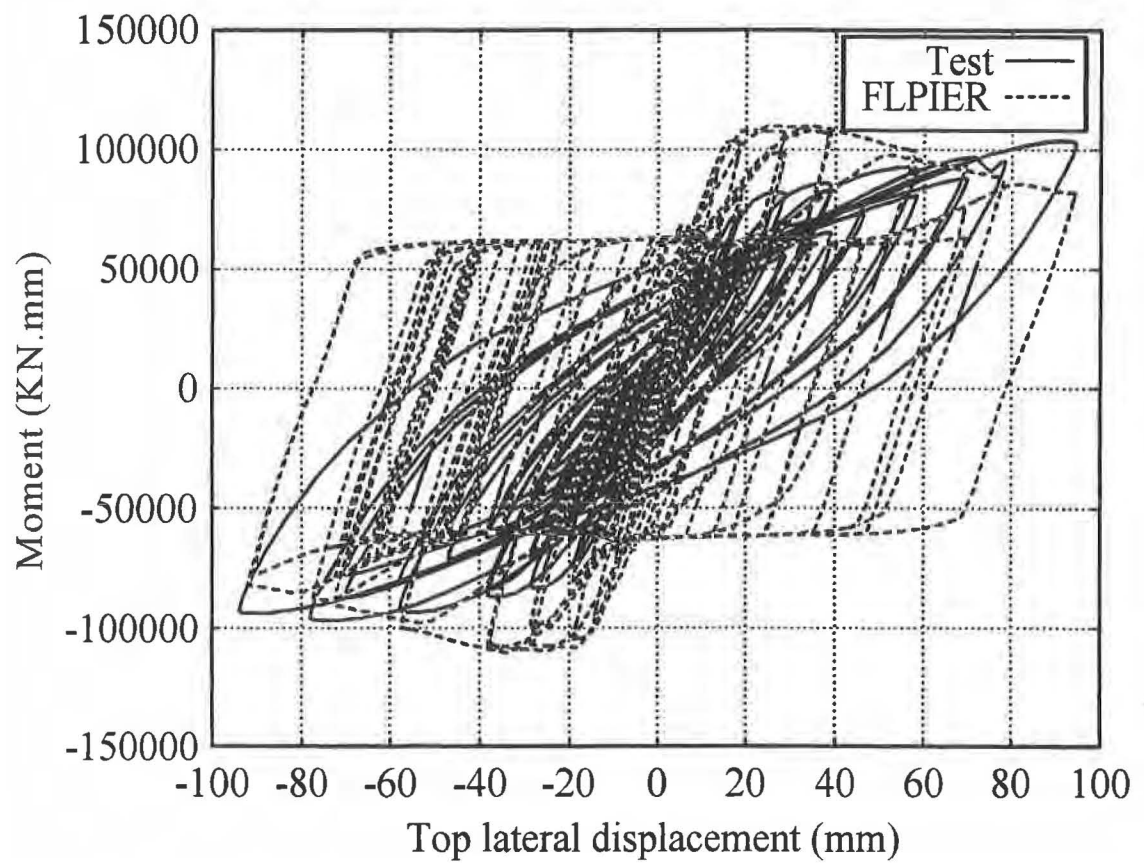
Figure C-43. Example 5: Comparison of FLPIER with Physical Test, ts02
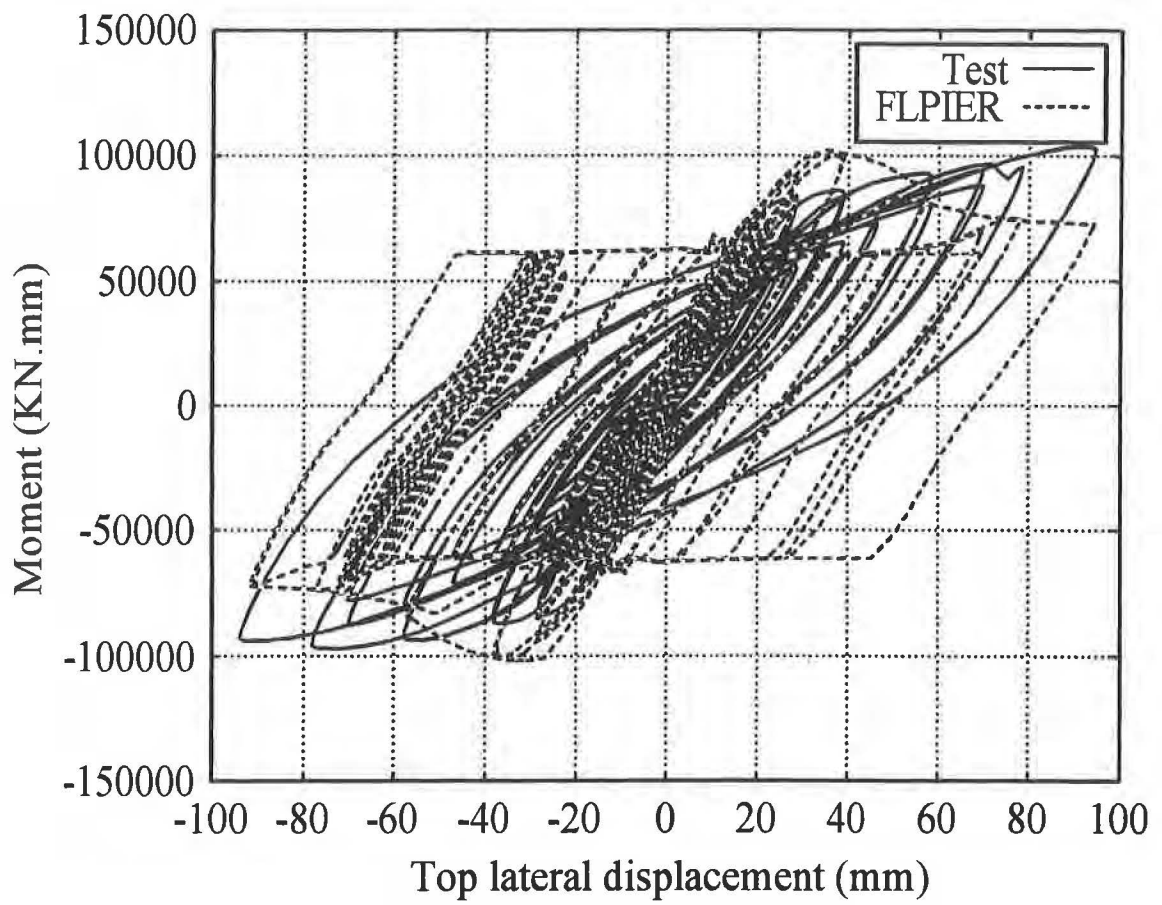
Figure C-44. Example 5: Comparison of FLPIER with Physical Test, ts03
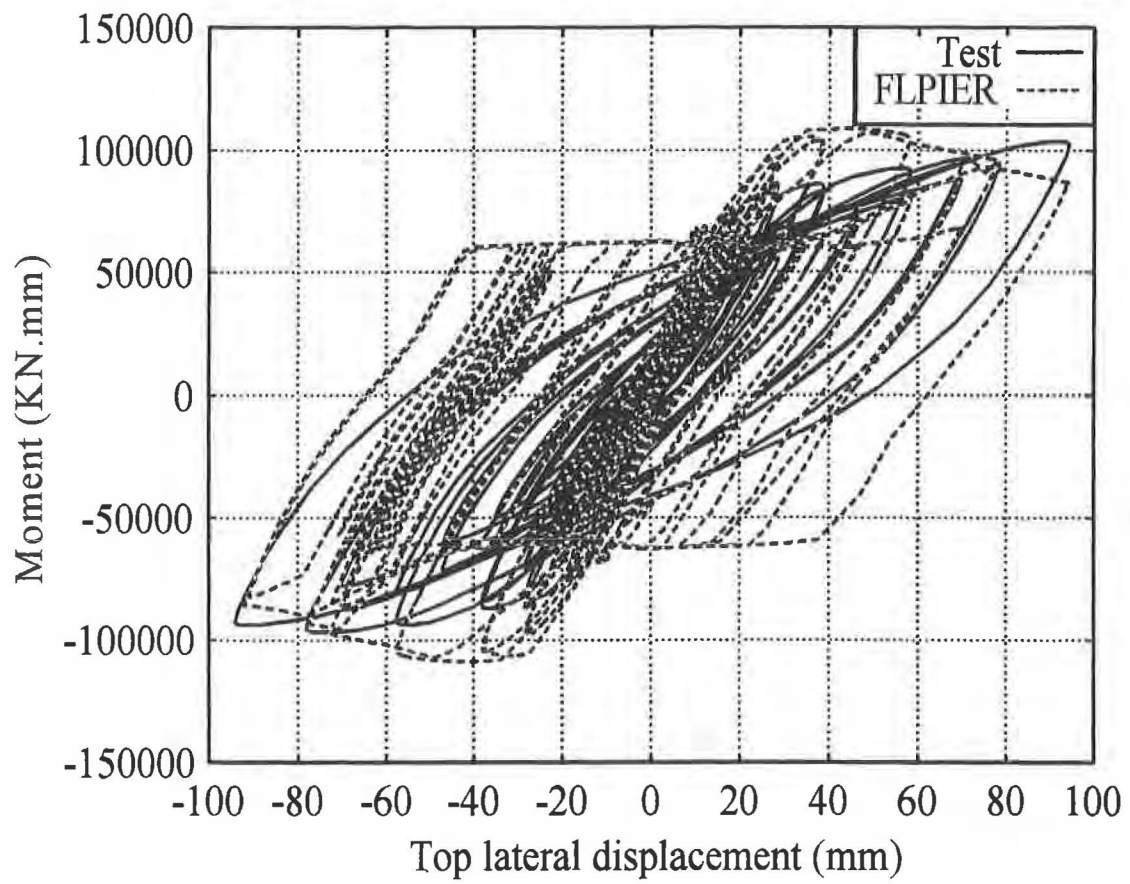
Figure C-45. Example 5: Comparison of FLPIER with Physical Test, ts04
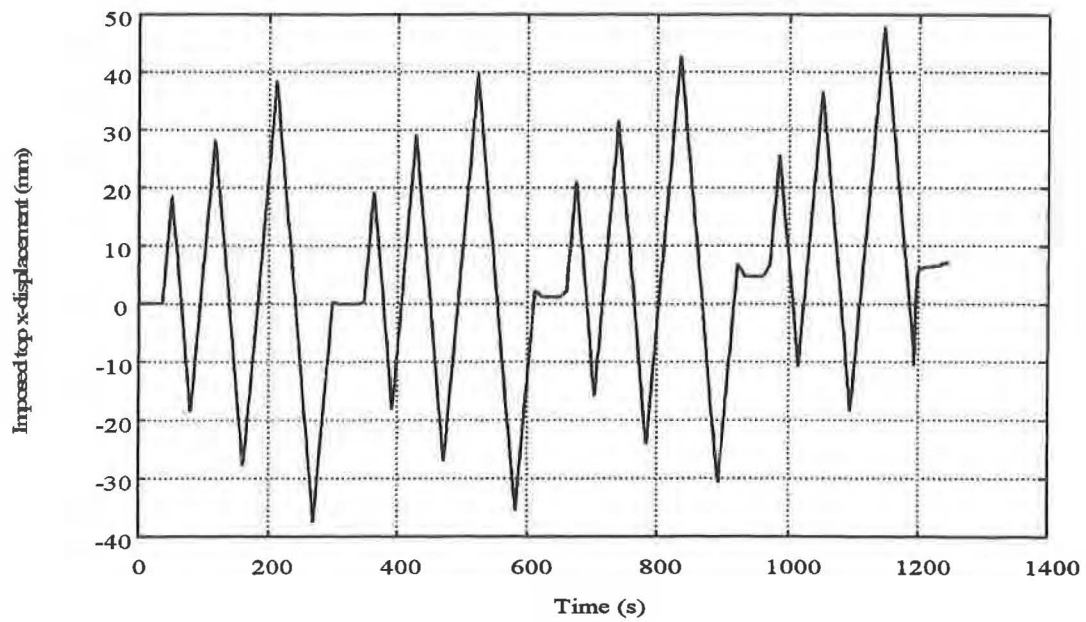
Figure C-46. Example 5: Imposed X Displacement for Test S3
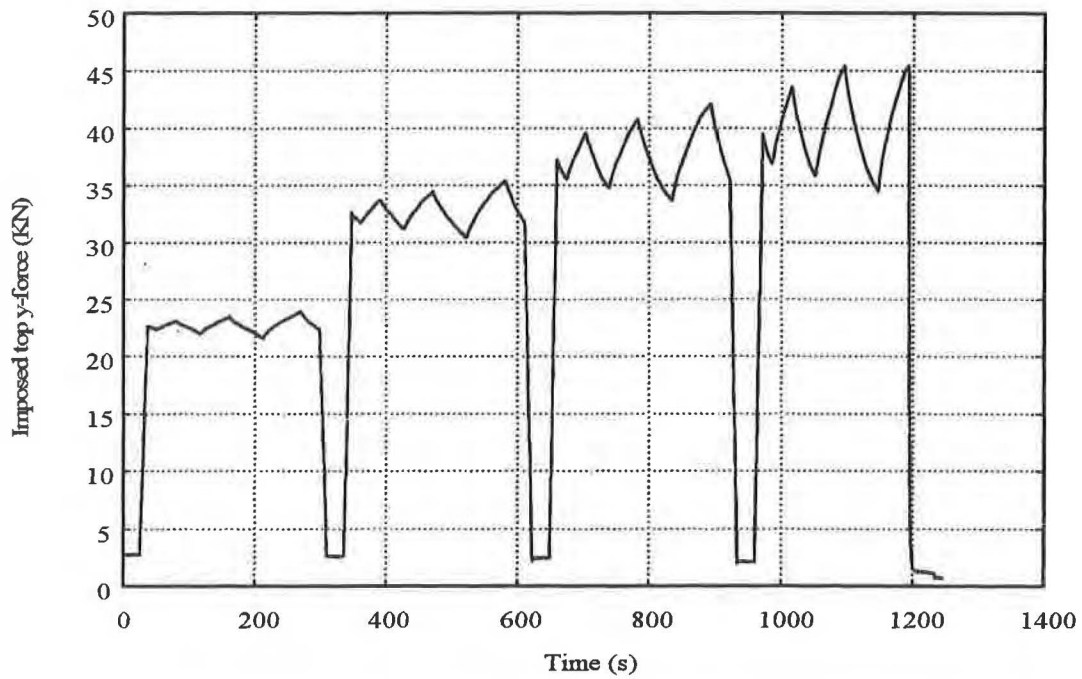
Figure C-47. Example 5: Imposed Y forces for Test S3

C-112
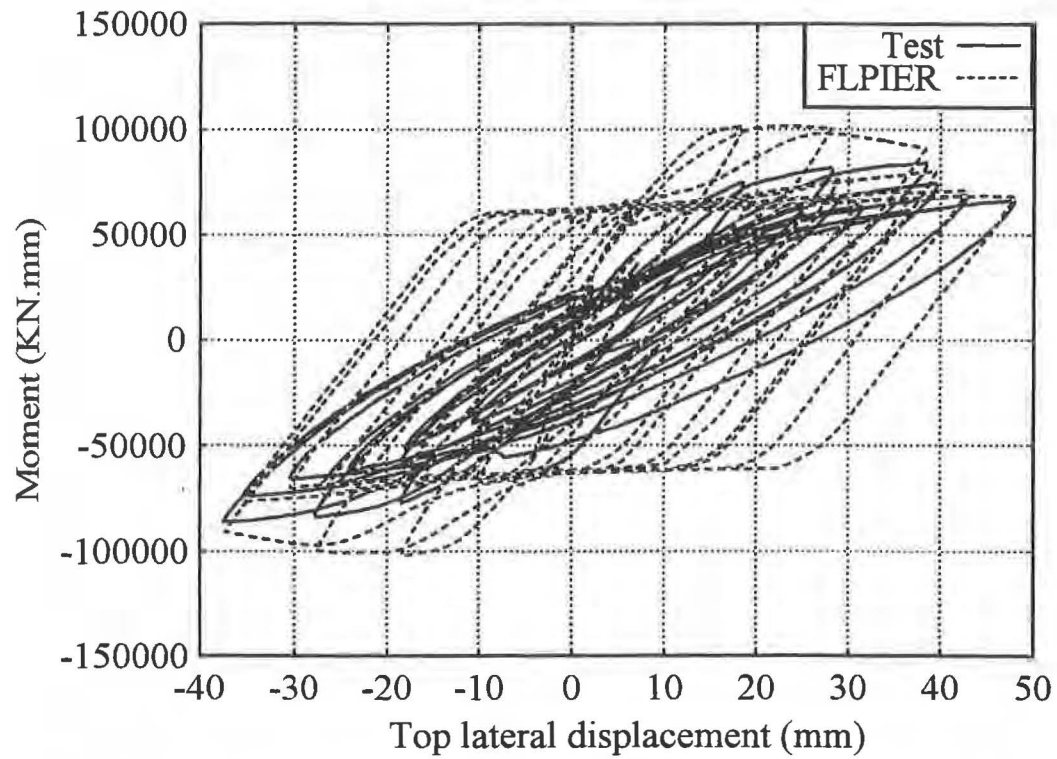
Figure C-48. Example 5: Comparison of FLPIER with Test S3, ts31
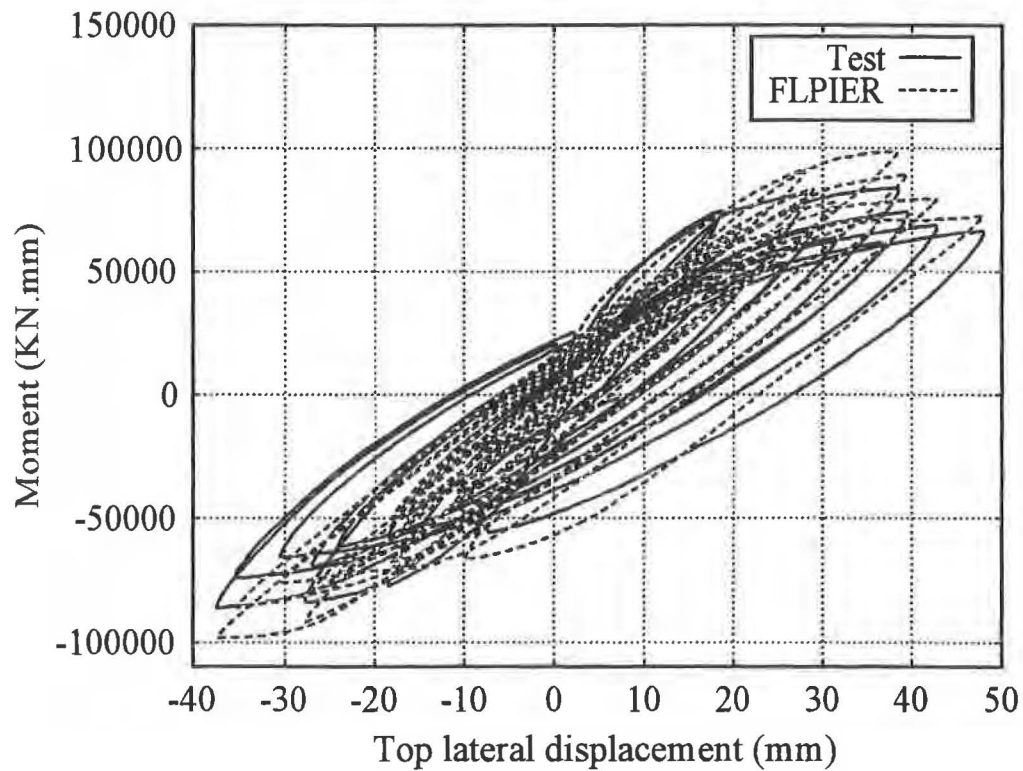
Figure C-49. *Figure C-48. Example 5: Comparison of FLPIER with Test S3, ts32*
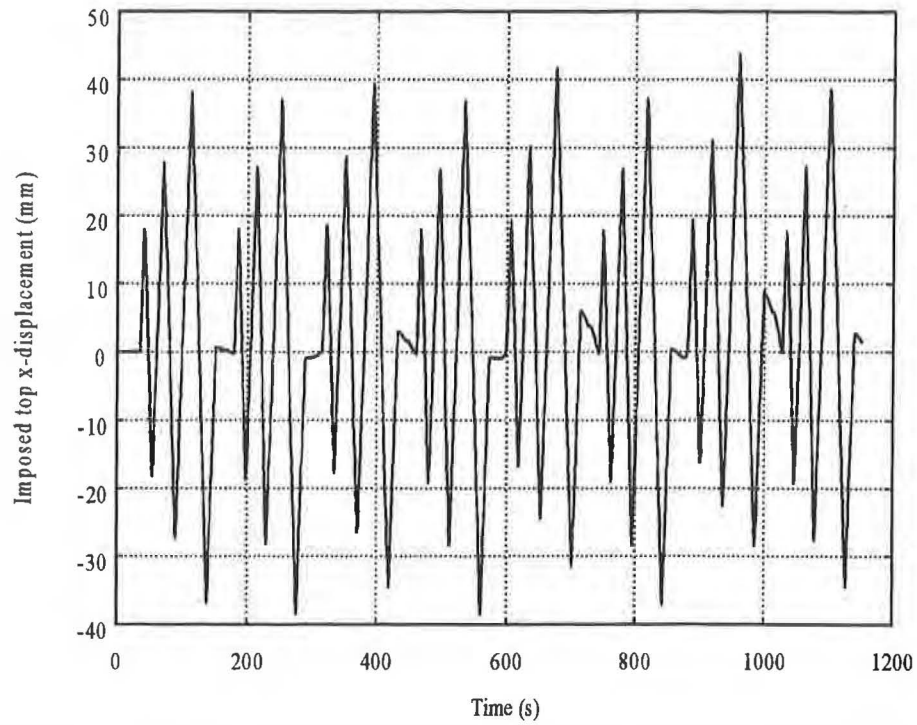
Figure C-50. Example 5: Imposed Displacement in X Direction for Test S4
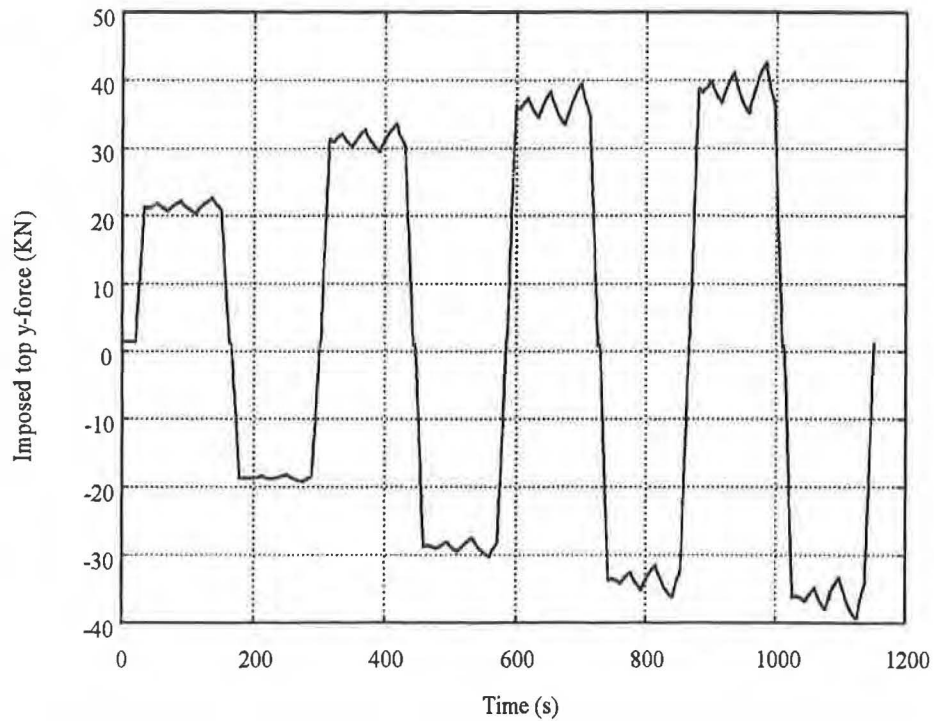
Figure C-51. Example 5: Imposed Load in Y direction for Test S4
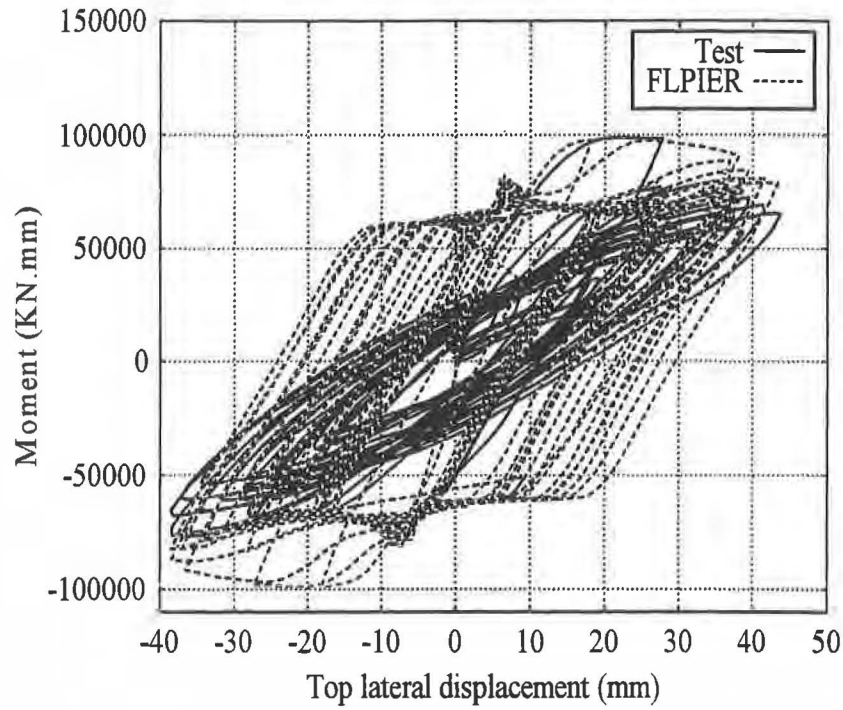
Figure C-52. Example 5: Comparison of FLPIER and Physical Test, ts41
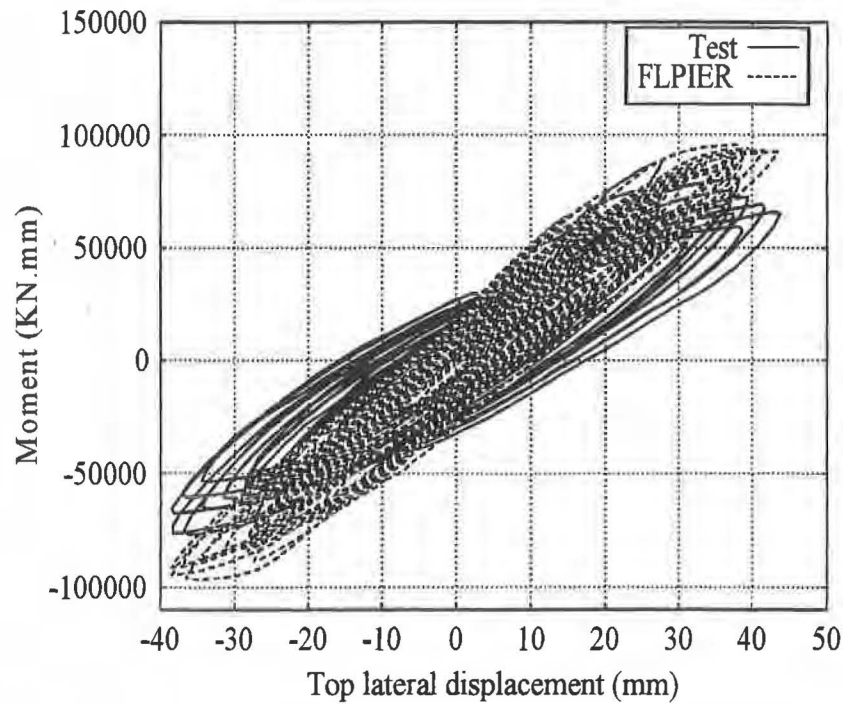
Figure C-53. Example 5: Comparison of FLPIER and Physical Test, ts42
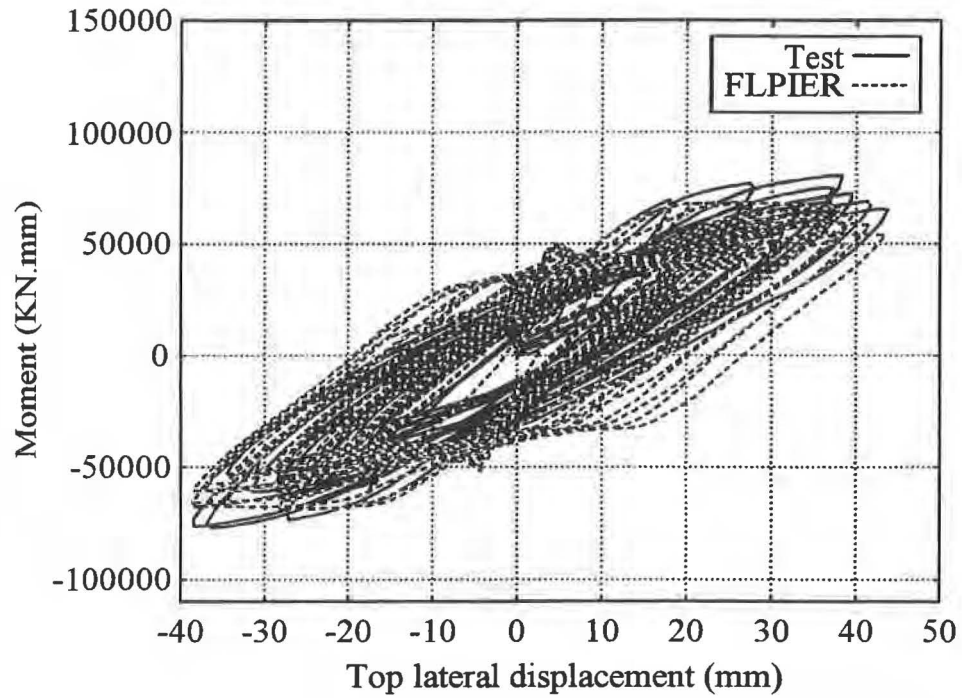
Figure C-54. Example 5: Comparison of FLPIER and Physical Test, ts42
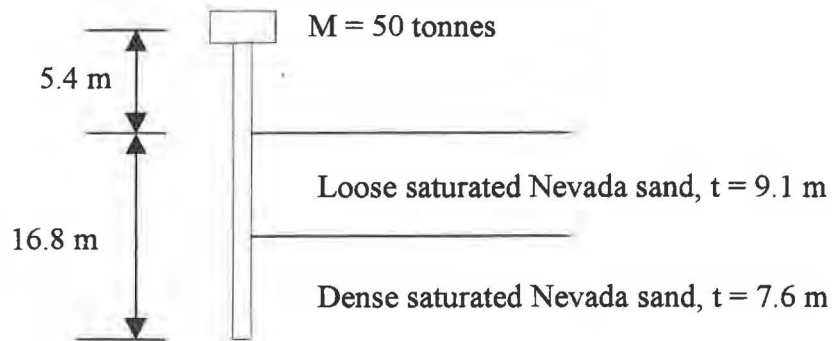
Figure C-55. Example 6: Single Pile in Sand (Scaled Dimensions)
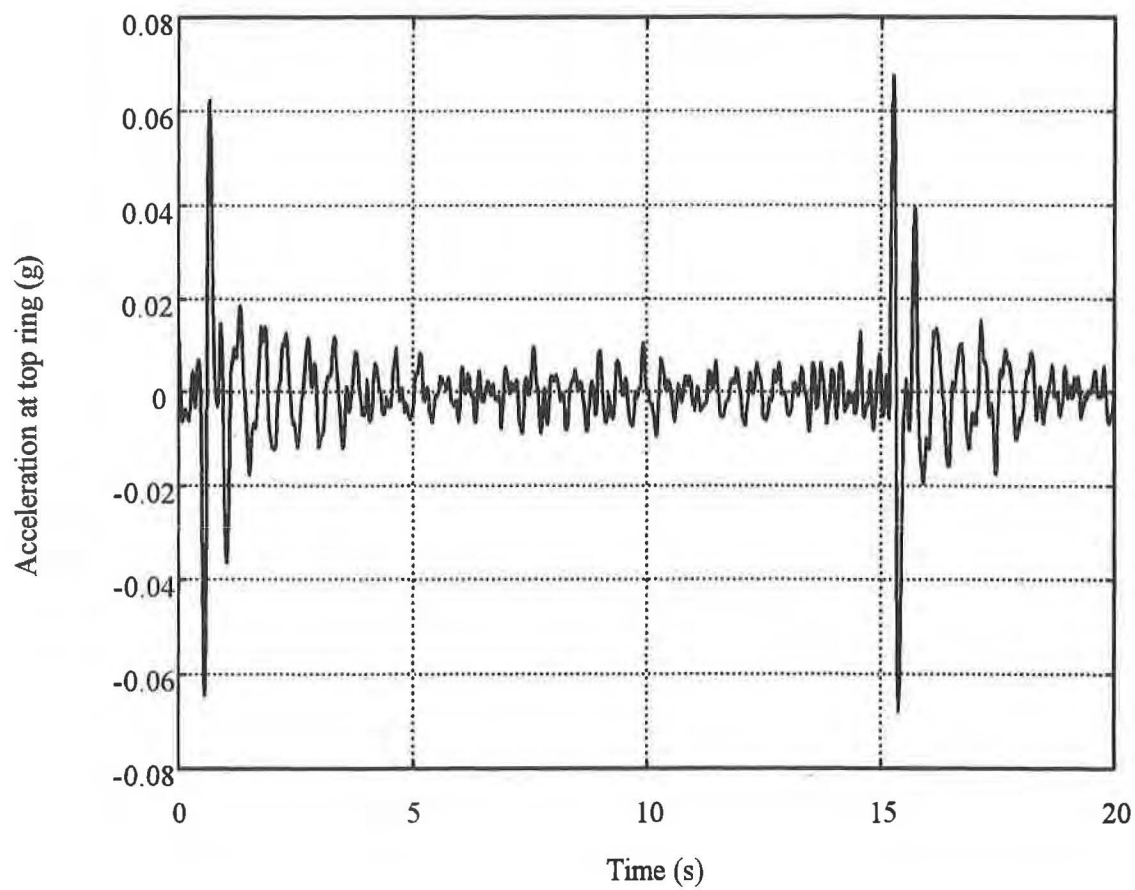
Figure C-57. Example 6: Top Ring Acceleration in Centrifuge Test, SP
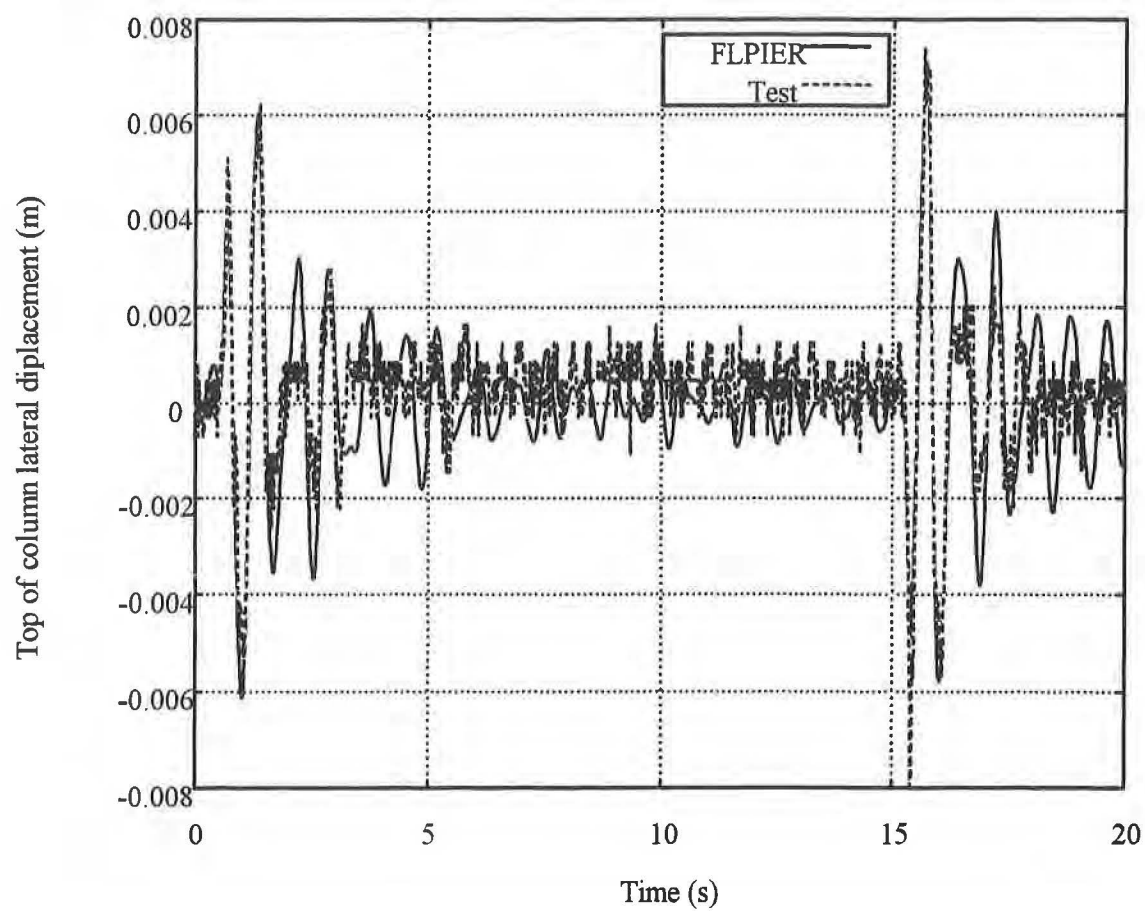
Figure C-57. Example 6: Comparison of Pile Top Displacements, SP
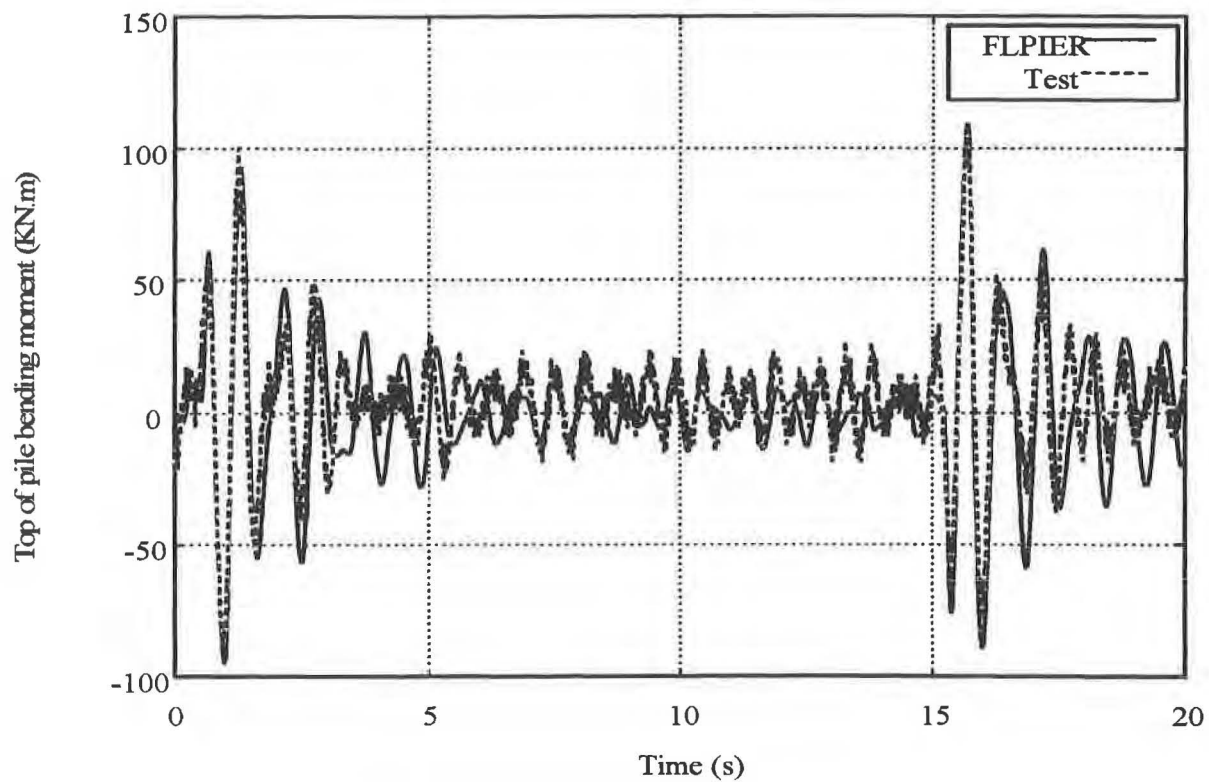
Figure C-58. Example 6: Comparison of Bending Moments, SP
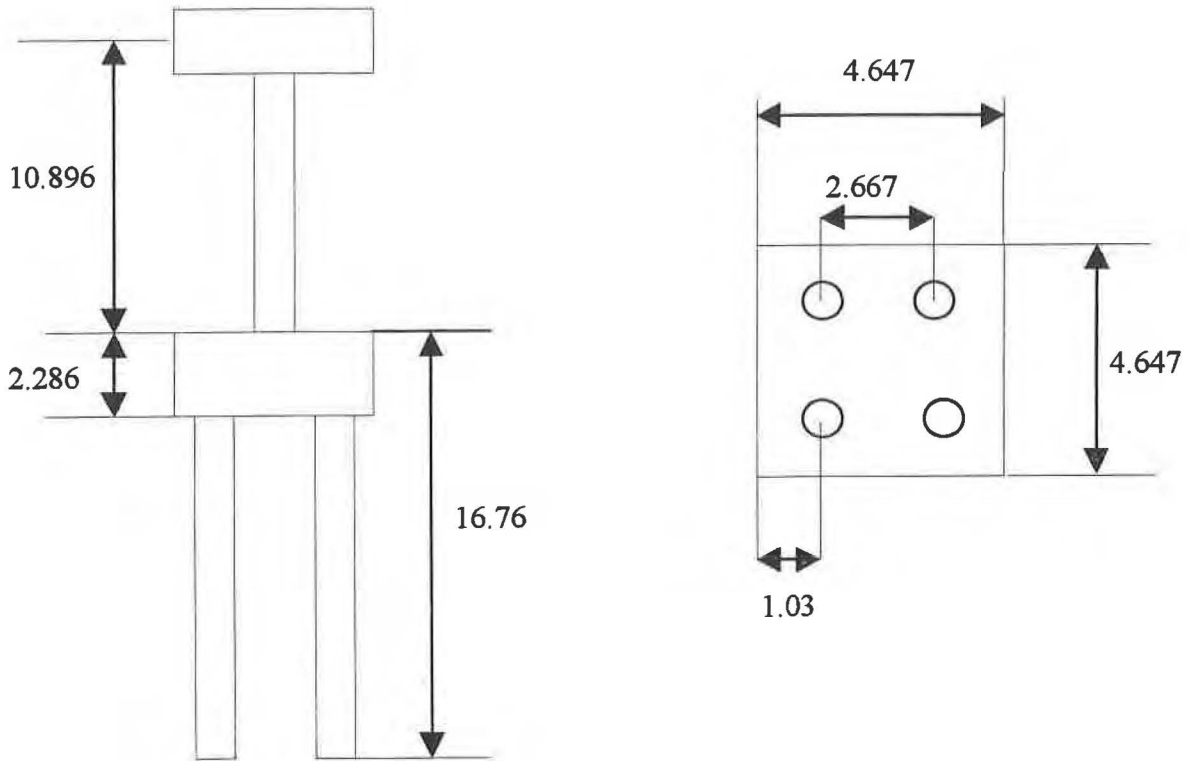
Figure C-59. Example 6: Scaled Dimensions (m) for 2 x 2 pile group in sand (PG2)
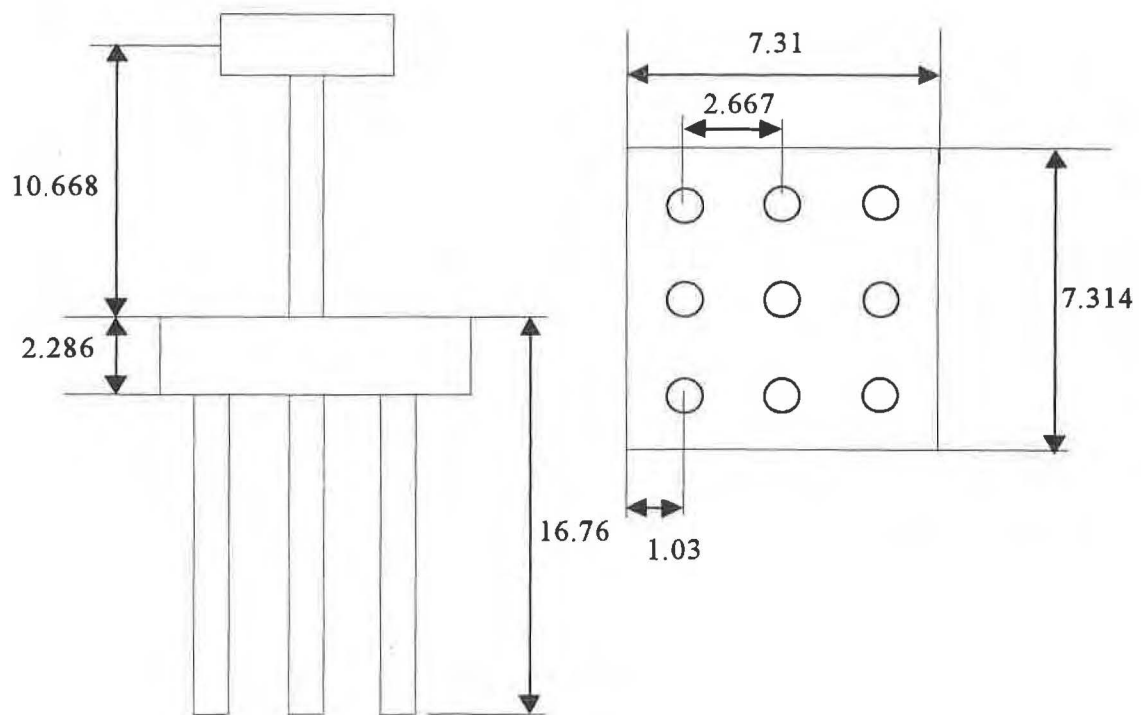
Figure C-60. Example 6: Scaled Dimensions (m) for 3 x 3 pile group in sand (PG2)
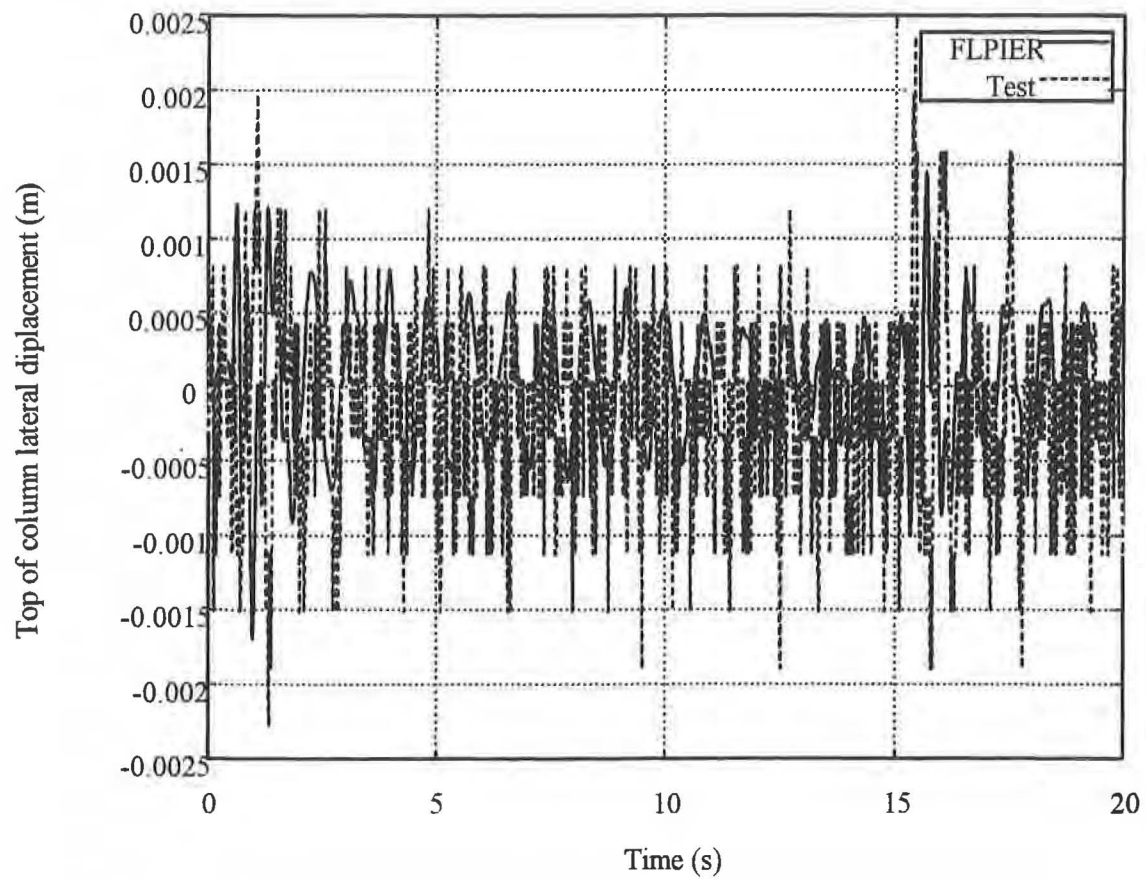
*Figure C-61.   Example 6: Lateral Displacement at Top of Pile, 2 x 2 Group (PG2) —
Comparison of FLPIER and Physical Test Results*
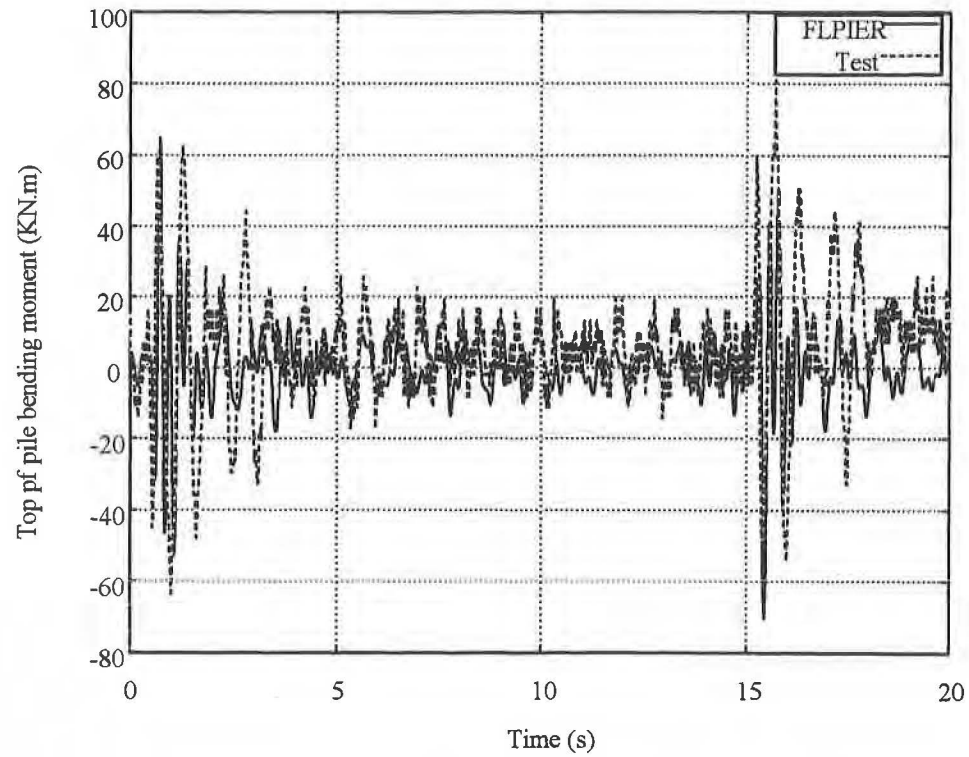
*Figure C- 62. Example 6: Bending Moment at Top of Pile, 2 x 2 Group (PG2) —
Comparison of FLPIER and Physical Test Results*
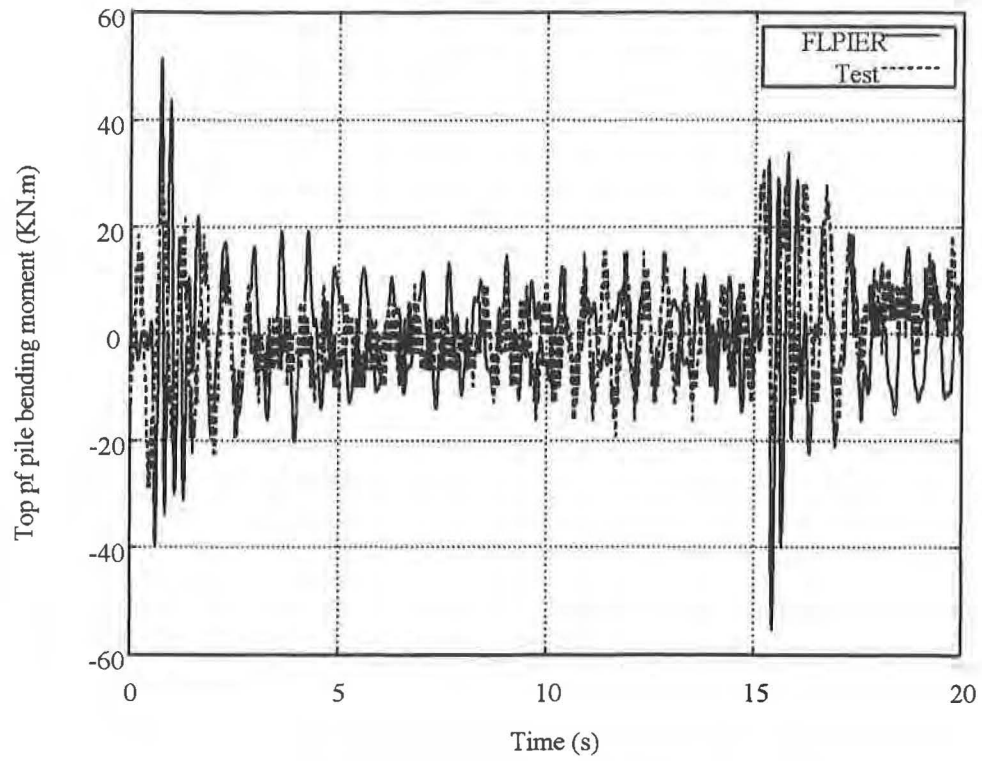
Figure C- 63. Example 6: Bending Moment at Top of Pile, 3 x 3 Group (PG3) — Comparison of FLPIER and Physical Test Results

Elevation Schematic - Dimensions in Inches

Elevation (in.) / Soil Type

X →	
Z ↓	

96

0

Water

-216

Sand: Reese p-y criteria

-312

Soft clay below water table - Matlock p-y criteria

-520

Soft clay below water table - Matlock p-y criteria

-720

1284

Sand - Reese p-y criteria

1

0.25

-1640

Plan View - Dimensions in Inches

Y

Load

X

45
45
45
45

30 x 30 Prestressed Concrete Piles

Concrete Cap

30 | 45 | 45 | 45 | 45 | 30
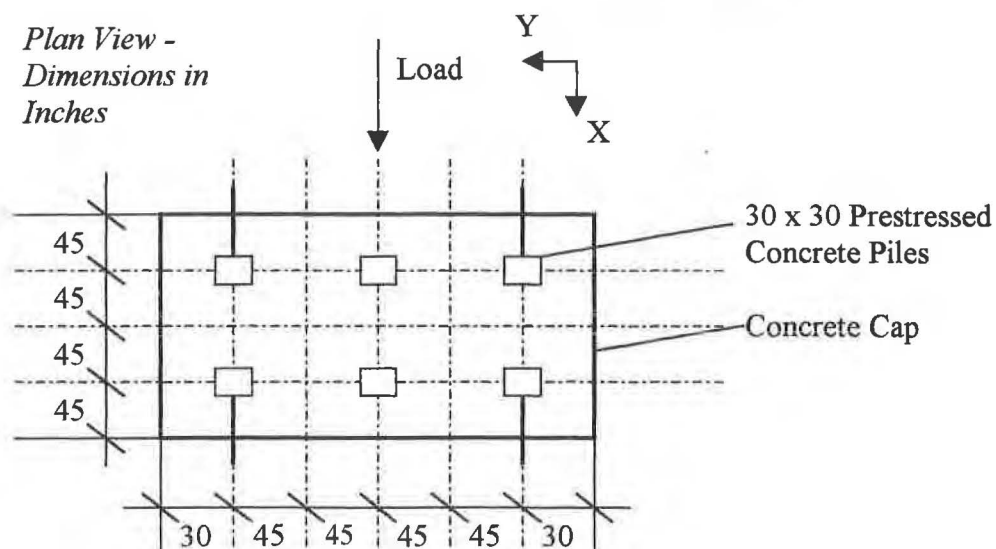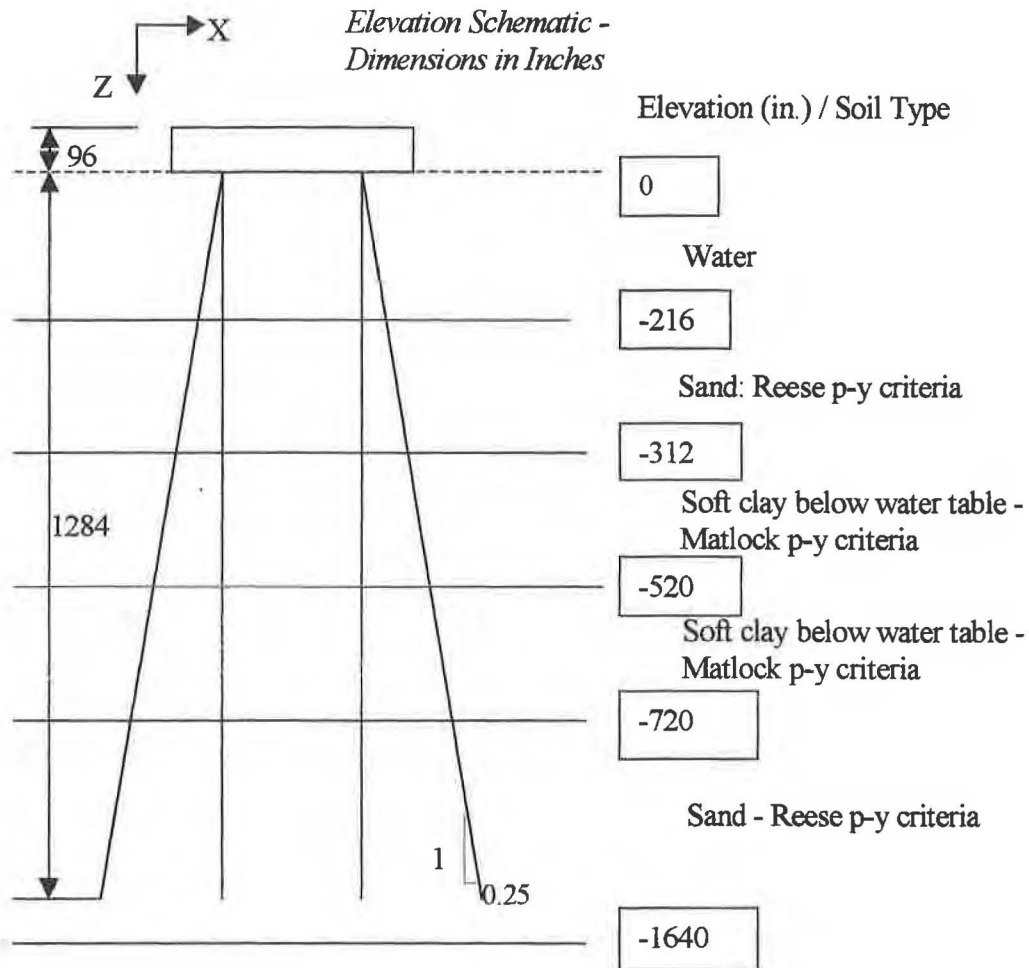
Figure C-64. Example 7: Pascagoula, Mississippi, Test Structure

C-125
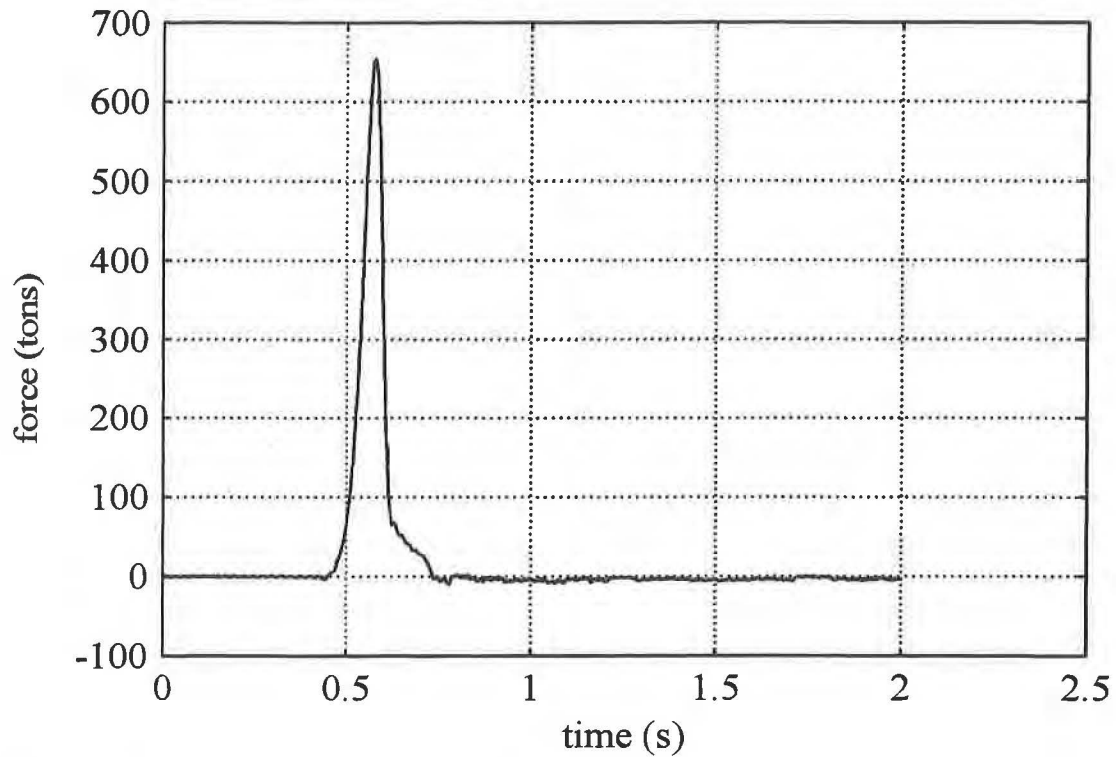
Figure C-65. Example 7: Cap Load Time History for Pascagoula, Mississippi, Test
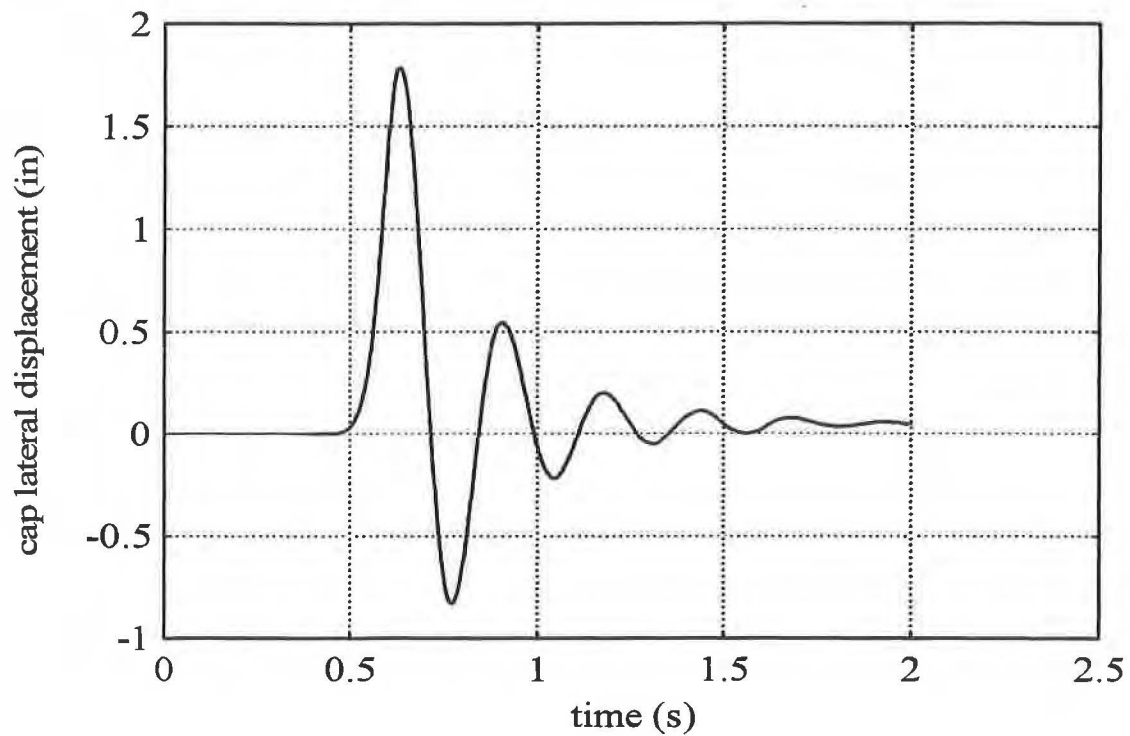
Figure C-66. Example 7: Measured Displacement Time History for Pascagoula, Mississippi Test, under Load Shown in Figure C-65

C-126
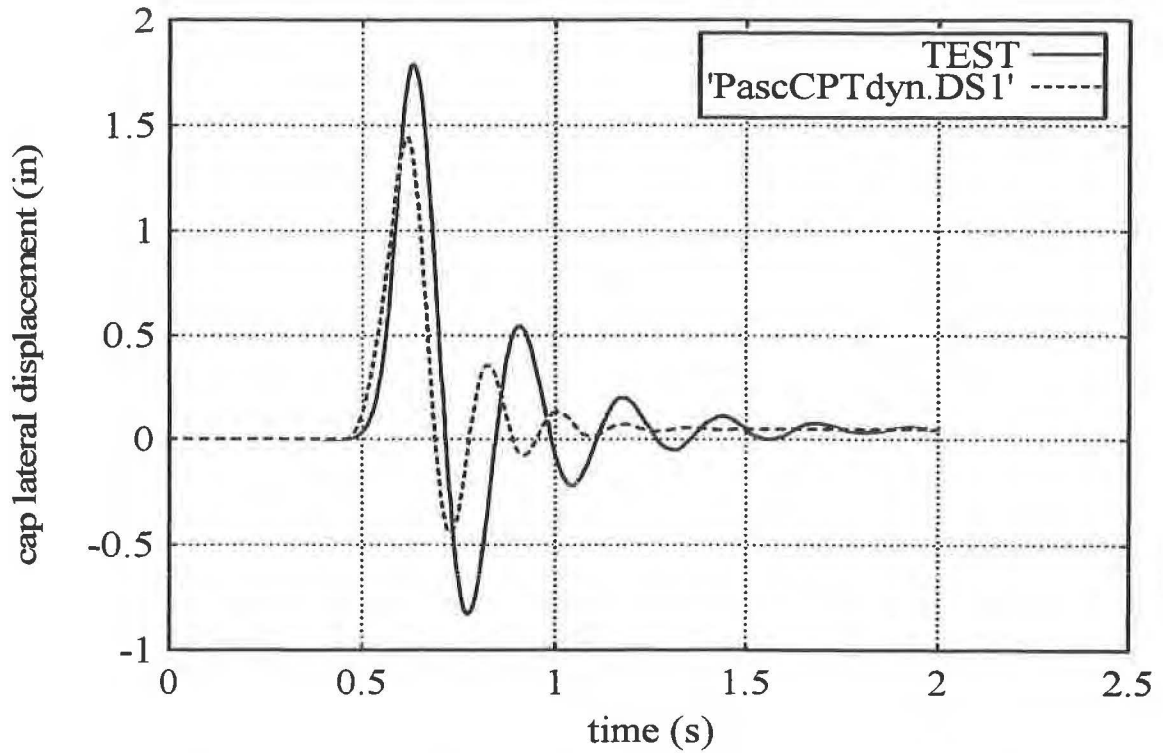
Figure C-67. Example 7: Comparison of Test and FLPIER with Soil Properties from CPT
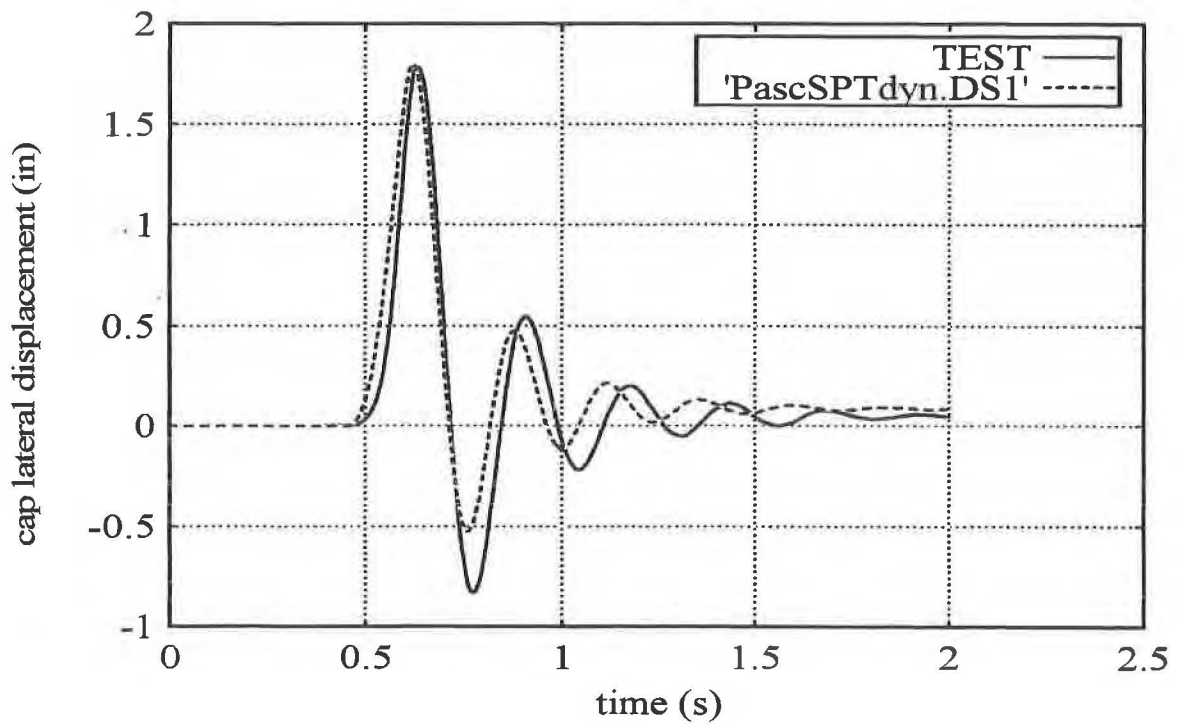
Figure C-68. Example 7: Comparison of Test and FLPIER with Soil Properties from SPT
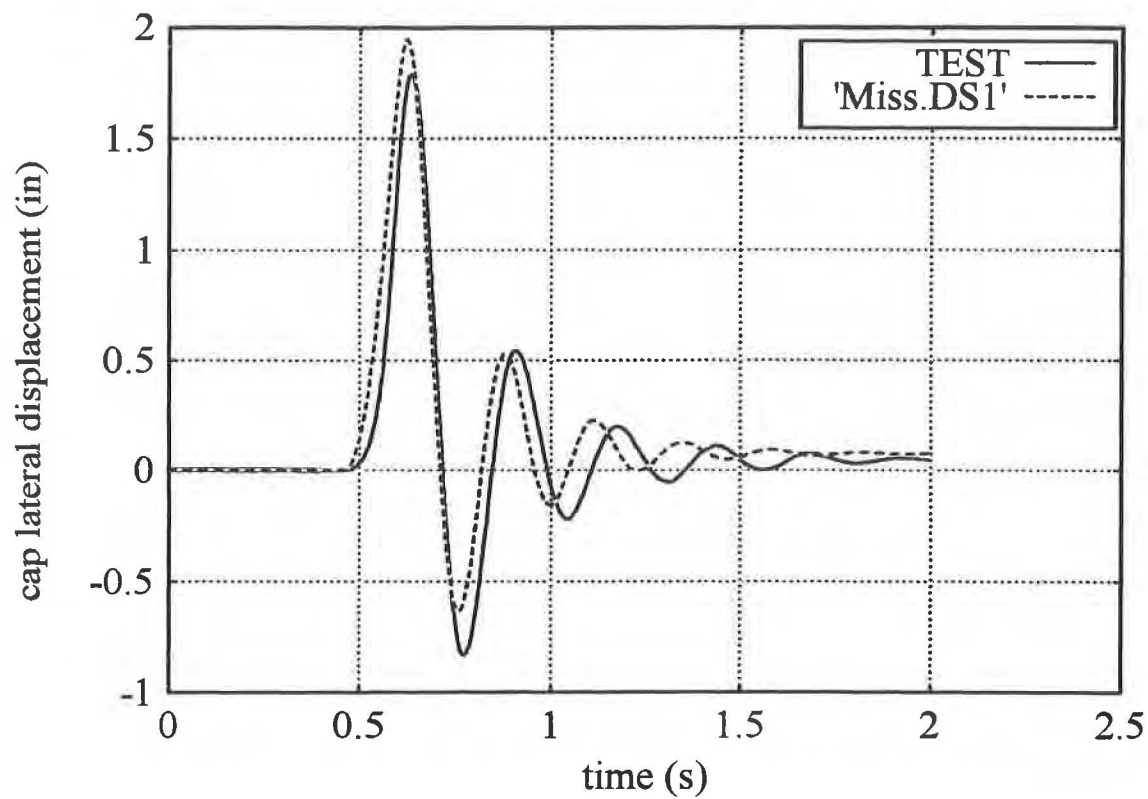
Figure. C-69. Example 7: Comparison of Test and FLPIER with Soil Properties Interpreted by Brown [71]

120"

120"

F

60"

Plan View
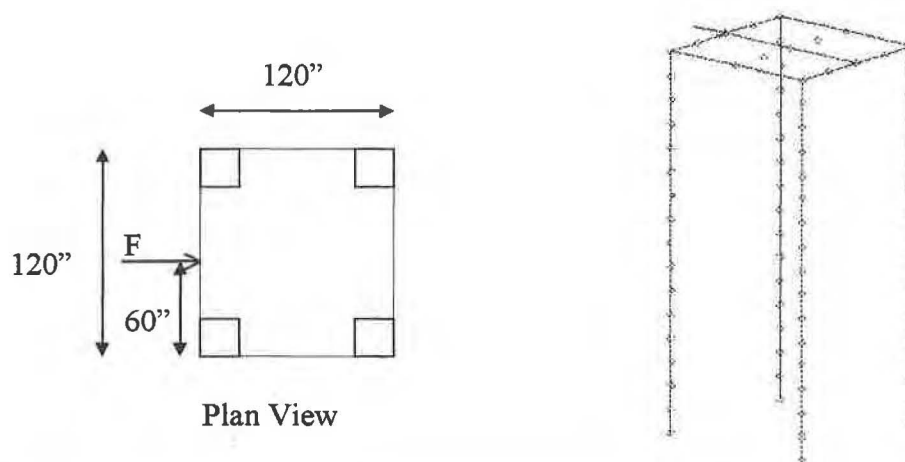
Piles:	12" x 12" L=384"	**Cap**:	120" x 120" x 48"	**Soil**:	O'Neill sand
	Ecp=4415 ksi		Ec=4000 ksi		ϕ=41°
	ν=0.3		ν=0.3		k=0.13k/in³
	ρ=2.25x10⁻⁷ks²/in⁴		ρ=2.25x10⁻⁷ks²/in⁴		γ=2.17x10⁻⁵k/in³

Figure C-70. Model for FLPIER Validation Problem
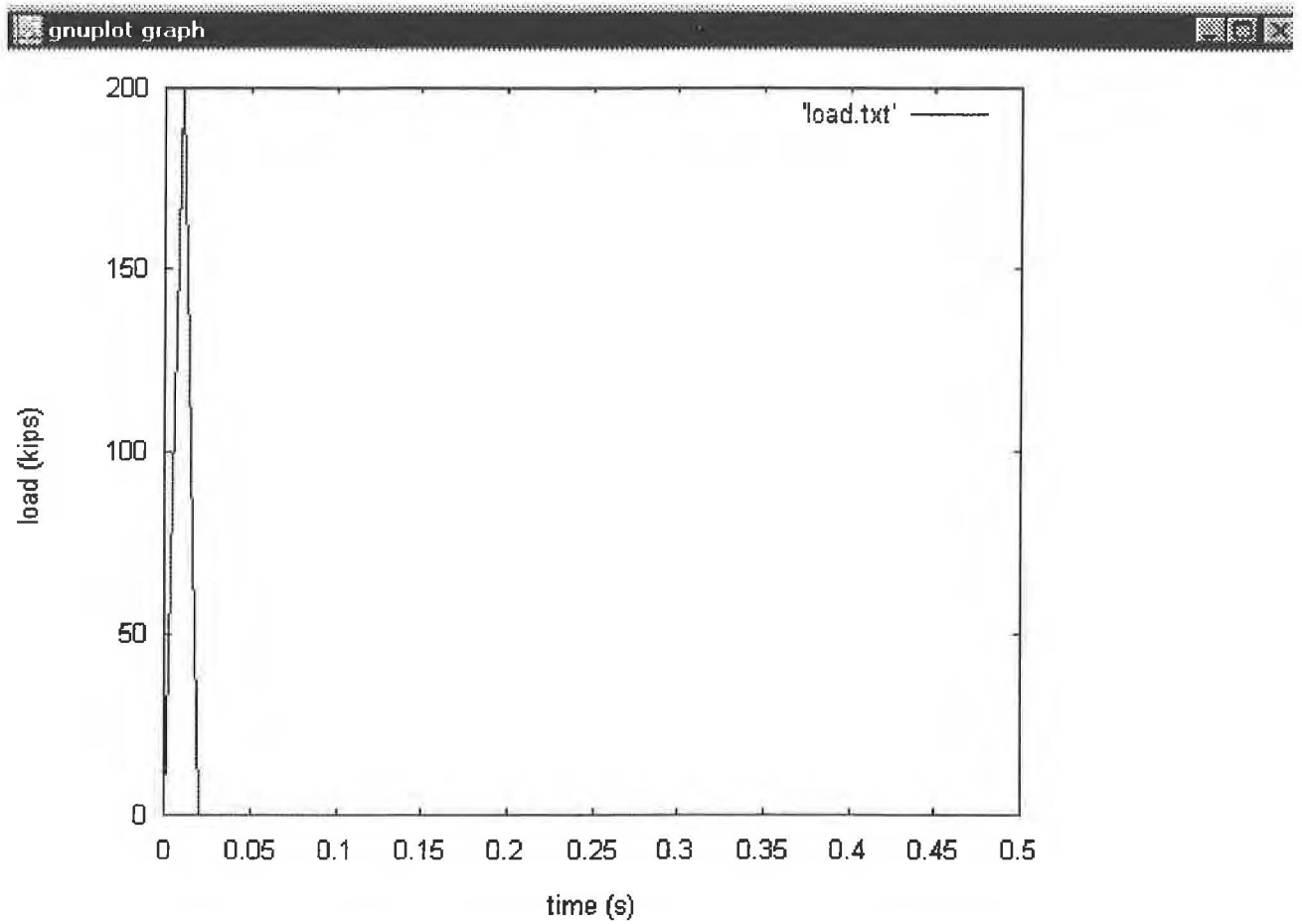
Figure C-71. Loading Time History for FLPIER Validation Problem
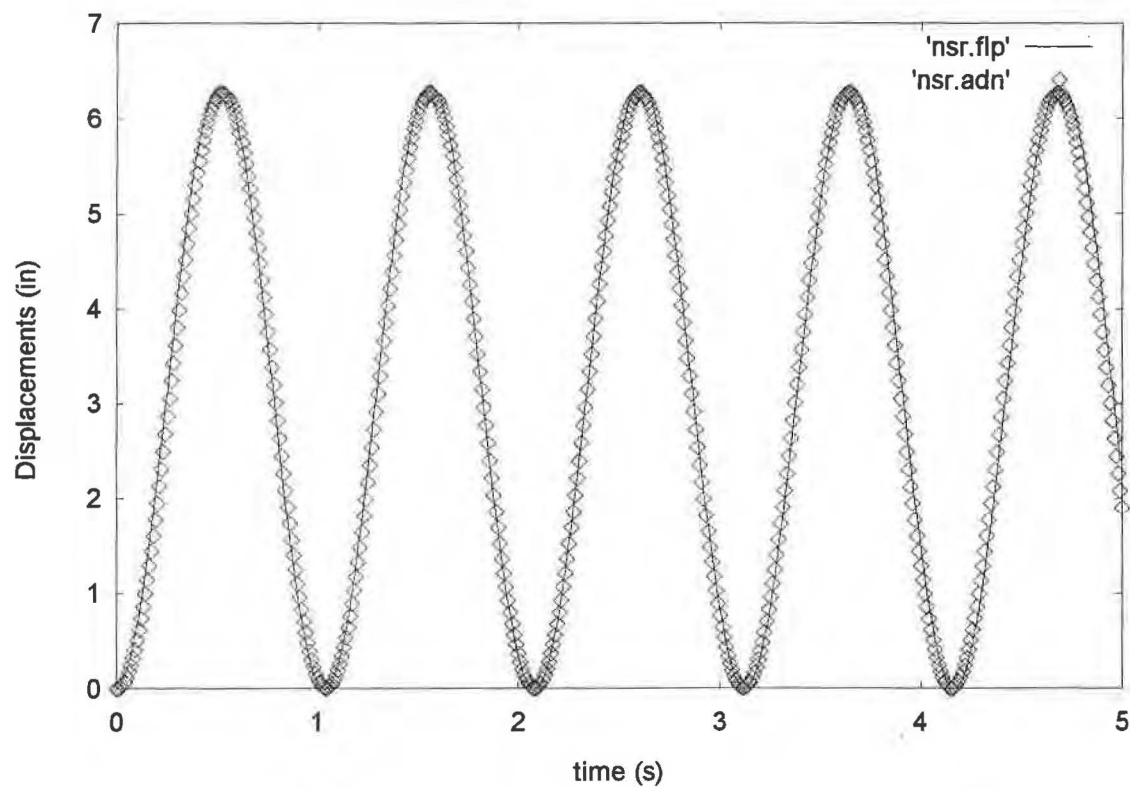
Figure C-72. Comparison of Results from FLPIER and ADINA —
Pile Cap Displacements (No Soil)
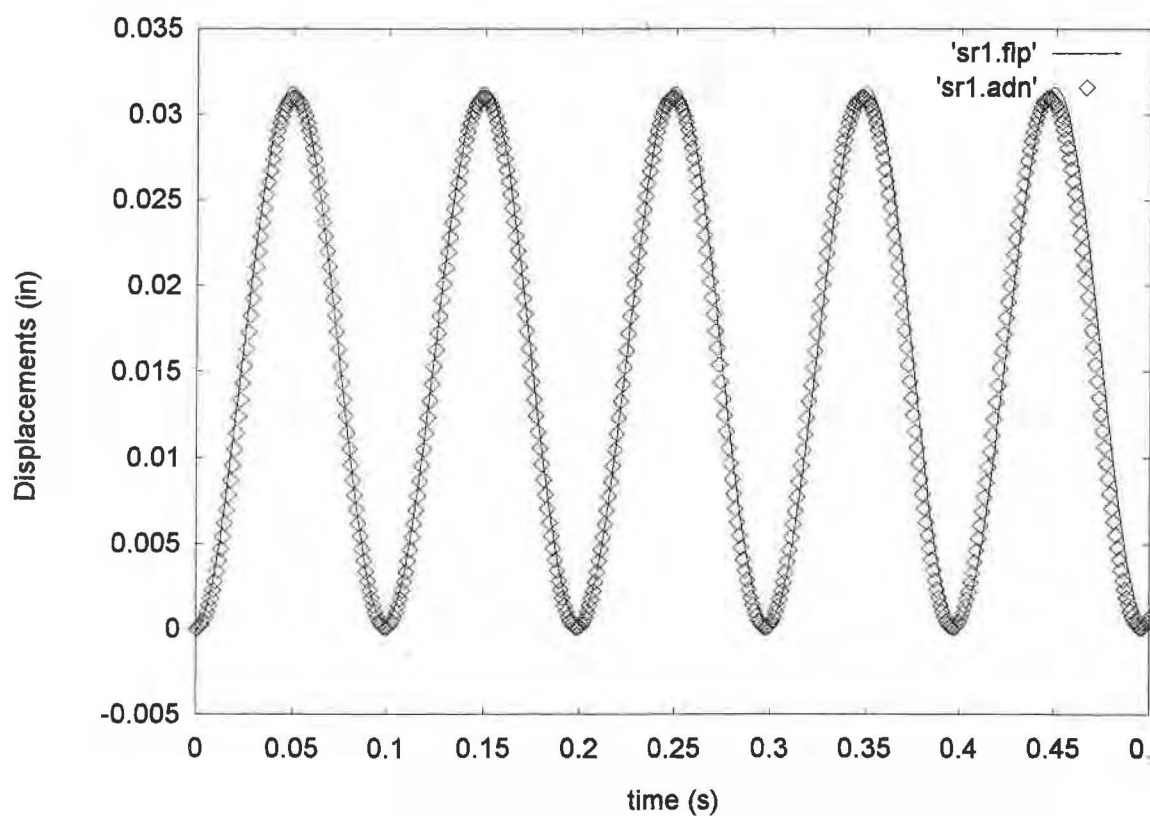
*Figure C-73. Comparison of Results from FLPIER and ADINA —
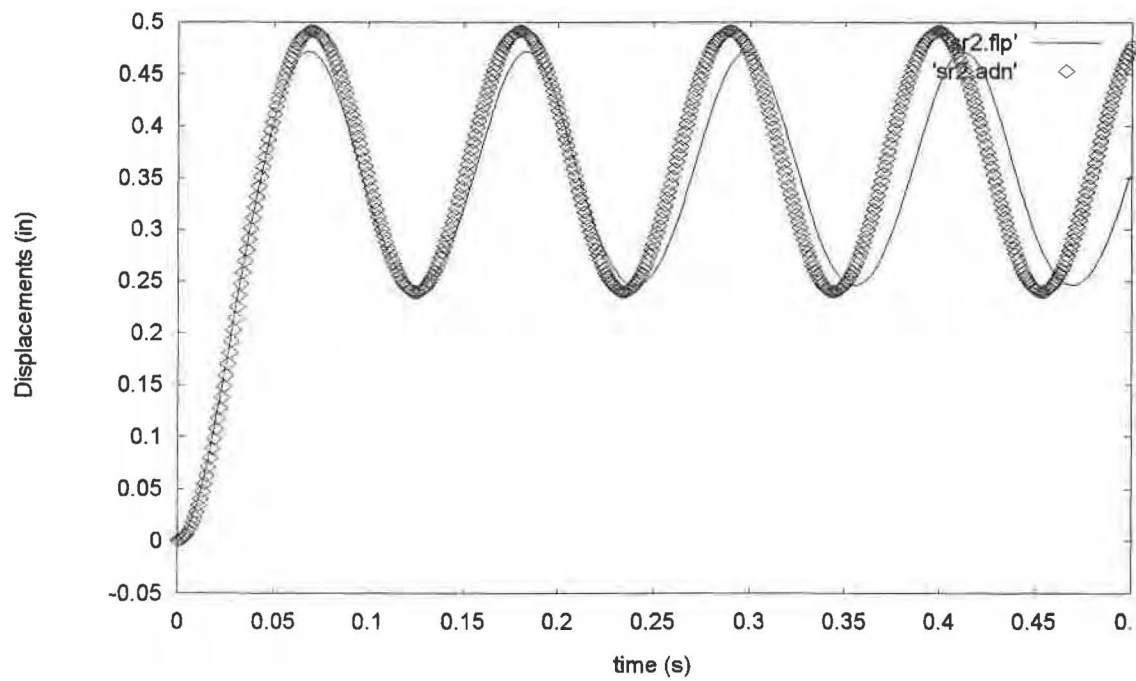Pile Cap Displacements (with Soil)*
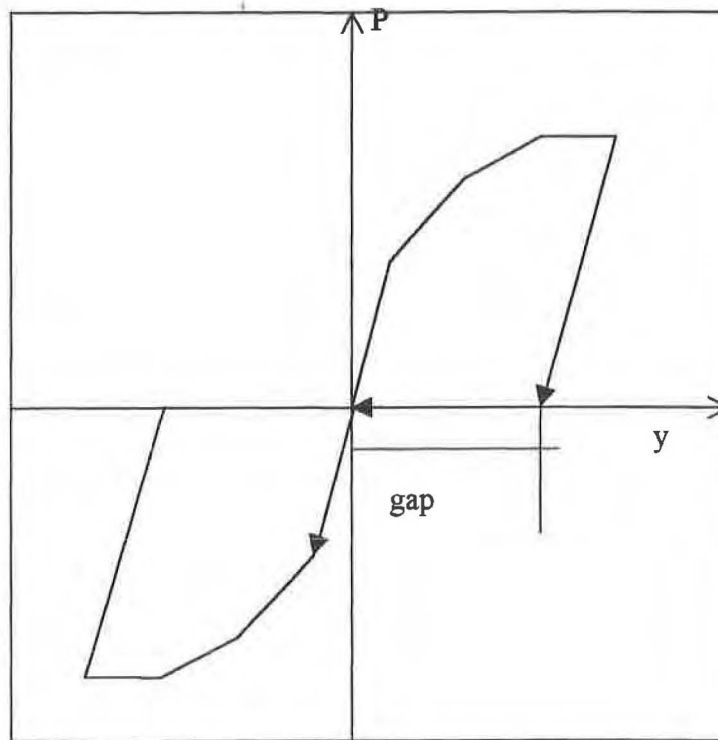
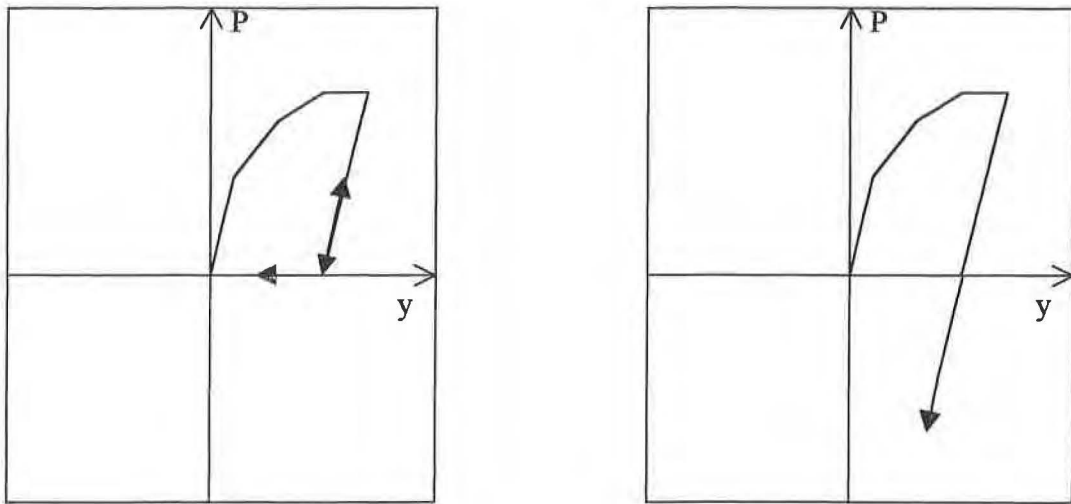*Figure C-74. Nonlinear Soil Model Used in FLPIER in Verification Problem*
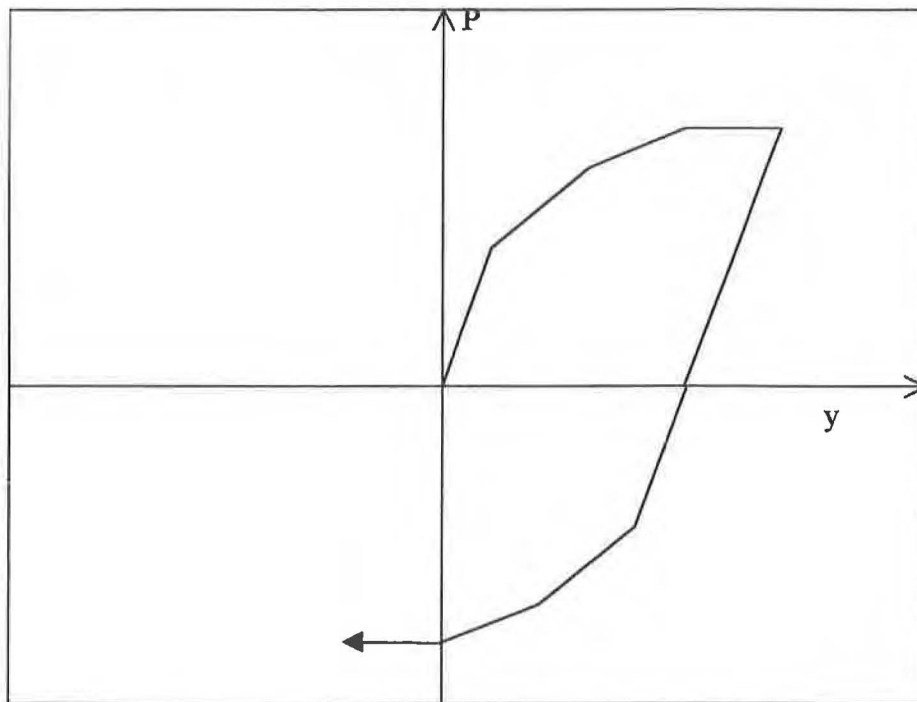
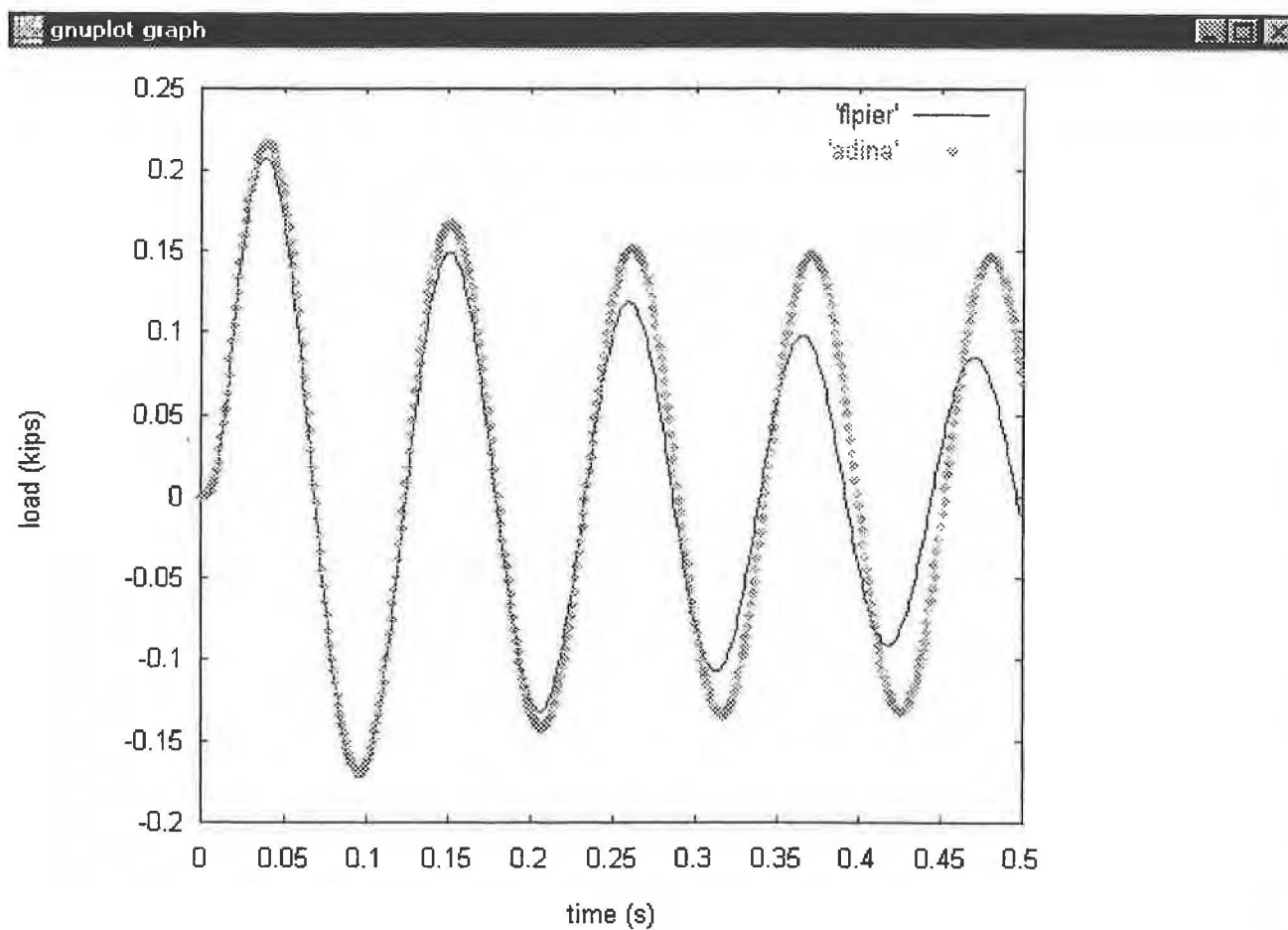*Figure C-75. Nonlinear Soil Model Used in ADINA in Verification Problem*

Figure C-76. Pile-Head Displacements for FLPIER and ADINA for Validation Problem, Nonlinear Test 1

Figure C-77. Nonlinear p-y Behavior for FLPIER (Left) and ADINA (Right) in Validation Problem — Nonlinear Test 1

Figure C-78. Pile Cap Displacements for FLPIER and ADINA for Validation Problem, Nonlinear Test 2
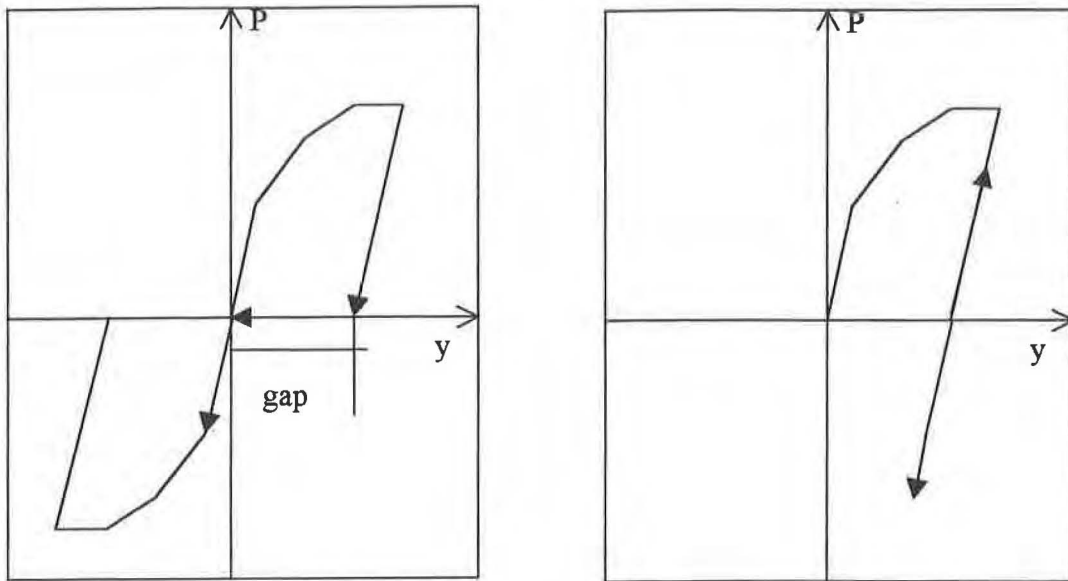
Figure C-79. Nonlinear p-y Behavior for FLPIER (Left) and ADINA (Right) in Validation Problem —Nonlinear Test 2